Dynamics of a biaised tracer in crowded environment

Pierre Rizkallah

Sorbonne Université

PHENIX & LPTMC

THÈSE DE DOCTORAT

Pour l'obtention du titre de

Docteur en Sciences de Sorbonne Université

Dynamique d'un traceur en milieu encombré

Pierre Rizkallah

Sous la direction de Pierre Illien et Olivier Bénichou

Soutenue le 29 juin 2023 devant un jury composé de :

M. Jean-François Joanny ..... Président
Mme. Oriane Blondel ..... Examinatrice
M. Eric Bertin ..... Rapporteur
M. David Dean ..... Rapporteur
M. Pierre Illien ..... Directeur de thèse
M. Olivier Bénichou ..... Invité

Contents

Remerciements

Ces trois années de thèse furent pour moi riches en enseignements scientifiques. J'ai eu la chance que ce doctorat se déroule dans d'excellentes conditions, grâce à l'ensemble des gens dont j'ai croisé la route.

Je tiens à remercier tout particulièrement mes directeurs de thèse Pierre et Olivier. J'ai énormément apprécié réaliser ma thèse sous votre supervision. J'ai pu, à vos côtés, à la fois apprendre beaucoup de science, et m'initier à la recherche avec un accompagnement idéal, le tout dans une ambiance toujours bienveillante et joyeuse. Je souhaite également remercier tout autant Aurélien, qui m'a beaucoup appris (par exemple qu'il est possible de trouver $f(x)$ pour tout x en connaissant uniquement $f(0)$), en plus d'être le plus sympa des co-bureau.

Je remercie enfin tous ceux avec qui j'ai pu collaborer sur différents projets de recherche.

Plus généralement, j'adresse un immense merci à tous les membres de PHENIX et du LPTMC. J'ai eu la chance d'y trouver une atmosphère accueillante et chaleureuse, et d'y faire de nombreuses belles rencontres !

Résumé en français

Dans de nombreuses situations d'intérêt biologique (moteurs moléculaires, molécules en milieu intracellulaire, bactéries...) ou issues de la physico-chimie (particules auto-propulsées, colloïdes dans une solution de polymères...), les outils classiques d'étude de la diffusion (loi de Fick, mouvement brownien) n'offrent pas une description adéquate du transport de la matière. En effet, les milieux biologiques constituent généralement des environnement complexes, encombrés et parfois géométriquement contraints (pores, membranes, capillaires...). De plus, dans de nombreux cas, les particules ne sont pas seulement soumises à des fluctuations thermiques, mais peuvent également convertir localement de l'énergie en travail mécanique, comme par exemple la bactérie *E. Coli* qui utilise des flagelles pour se déplacer ; on parle alors de particules actives.

Ainsi dans ce contexte, à cause des interactions diverses (avec d'autres particules, un champ électromagnétique externe, ou dues à l'écoulement d'un solvant), de possibles contraintes géométriques, ou encore de la présence d'activité, le comportement d'une particule marquée, appelée un *traceur*, peut se révéler très différent de ce qui serait prédit par la théorie classique du mouvement brownien. L'objet de cette thèse est l'étude des propriétés statistiques d'un traceur (actif ou non) évoluant dans un milieu complexe. Nous chercherons également à caractériser la réponse de l'environnement au déplacement du traceur, et réciproquement.

En première partie, un modèle microscopique, accessible à un traitement analytique, est proposé pour modéliser le transport et la diffusion d'un traceur actif (de type "run-and-tumble") en présence d'obstacles. Nous montrons ensuite que ce modèle explique l'émergence de propriétés spécifiques résultant de l'interaction entre la particule active et son environnement : dépendance complexe de la diffusivité en fonction des paramètres contrôlant l'activité et mobilité négative. Dans une seconde partie, nous traitons le cas où des particules (non nécessairement actives) diffusent dans une géométrie confinée unidimensionnelle, particulièrement adaptée pour modéliser par exemple les pores. Dans ce cas, les particules ne peuvent pas se dépasser ; leurs déplacements sont fortement corrélés. Cela conduit à une diffusion de traceur anormale. Partant du processus d'exclusion simple, nous chercherons à caractériser ces corrélations de manière plus générale dans ces systèmes unidimensionnels.

0.1 Particule active persistante en milieu encombré dynamique

De nombreux modèles théoriques de particules actives ont été introduits et étudiés pour décrire la dynamique d'un grand nombre de systèmes réels, allant des objets biologiques (moteurs moléculaires, bactéries, micro-nageurs, algues...) aux particules artificielles autopropulsées telles que les colloïdes actifs [1, 2]. Parmi ces modèles, les particules run-and-tumble et les particules browniennes actives ont suscité beaucoup d'intérêt : dans les deux cas, les particules s'autopropulsent avec une vitesse fixe, dont l'orientation change aléatoirement. Pour les particules run-and-tumble, l'orientation change brusquement, pour les particules

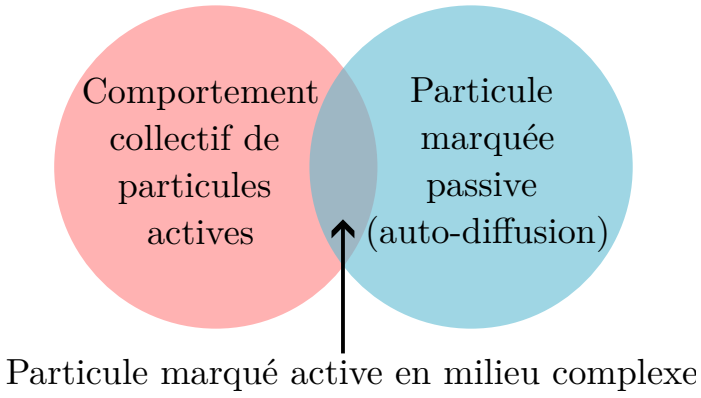

Figure 1: Il existe peu de résultats analytiques concernant le comportement individuel d'une particule active dans un environnement dynamique complexe.

browniennes actives, elle varie continûment. La dynamique des particules actives isolées, ou sans interaction, a fait l'objet de nombreuses études récentes [3–11].

0.1.1 Motivations : interaction entre une particule active et son environnement

Au-delà des propriétés à une particule, la dynamique des particules actives lorsqu'elles interagissent entre elles a reçu beaucoup d'attention. Il a été démontré que des effets surprenants pouvaient se produire, tels que le mouvement collectif à grande échelle [12, 13], ou une séparation de phases malgré l'absence d'interactions attractives [1, 14].

Un traceur dans un environnement dynamique

Ici, nous nous intéresserons à l'effet des *environnements complexes*. Comment le comportement d'une particule active marquée, appelé un traceur, est-il affecté par les interaction entre ce traceur et son environnement complexe ? Cette question se pose par exemple dans le transport d'objets biologiques, qui s'effectue souvent dans des conditions d'encombrement, comme les moteurs moléculaires à l'intérieur d'une cellule [15] ou les bactéries dans des milieux poreux [16]. Jusqu'à présent, c'est principalement le cas d'un environnement désordonné gelé qui a été étudié, par des expériences (sur des systèmes biologiques [17–21] et synthétiques [22]) et des approches théoriques (essentiellement numériques) [4, 23–33].

Le cas du désordre dynamique, qui a reçu beaucoup moins d'attention, est pourtant particulièrement pertinent, puisque les fluctuations thermiques affectent généralement l'environnement aussi bien que le traceur [34]. Des situations d'intérêt biologique ont ainsi été décrites par des modèles impliquant des traceurs dans des environnements avec obstacles mobiles [35–37]. La diffusion d'un traceur *passif* dans un environnement mobile (auto-diffusion du traceur), a été étudié sur réseau, avec la théorie de Nakazato et Kitahara [38] (voir également [39, 40]), et également en espace continu [41].

Le cas d'un traceur *actif* dans un environnement dynamique (Fig. 1) n'a fait l'objet que de quelques études théoriques de modèles sur réseau (voir cependant [42] pour une approche "mode-coupling" récente en espace continu), qui se sont principalement concentrées sur la limite de basse densité du problème, avec une description en temps discret, un traceur qui ne saute jamais latéralement par rapport à la direction de propulsion, et une dynamique spécifique [43]. Il n'existe pas de cadre analytique général qui permettrait de déterminer les propriétés statistiques de la position d'un traceur actif dans un environnement dynamique

pour une large gamme de paramètres, et en particulier pour une densité arbitraire d'obstacles.

Des effets surprenants résultant de l'activité et l'encombrement

L'élaboration d'une telle théorie est particulièrement intéressante car elle permettrait de mieux comprendre les caractéristiques atypiques qui peuvent être observées lorsqu'une particule active diffuse dans un environnement encombré. Par exemple, il a été observé expérimentalement que le coefficient de diffusion de particules actives peut dépendre de manière non monotone des paramètres d'activité (tels que le temps moyen de réorientation), conduisant à une diffusivité optimisée, ou à un piégeage du traceur par son environnement [16, 18, 20, 44–46].

En outre, la prédiction de la réponse d'un traceur soumis à une force extérieure et évoluant dans un environnement complexe est un défi central de la physique statistique [47, 48]. La relation entre la force appliquée au traceur et sa vitesse peut présenter un certain nombre d'anomalies frappantes, en particulier lorsque le traceur évolue très loin de l'équilibre. L'un des comportements les plus intrigants est l'apparition d'un courant inverse, qui est opposé à la force motrice, et qui a été mis en évidence par exemple dans le cadre très simple d'une particule brownienne évoluant dans un potentiel modulé périodiquement [49]. Dans le contexte spécifique du transport de particules, cet effet est connu sous le nom de mobilité négative absolue (MNA). De nombreuses approches théoriques ont été développées pour décrire ce phénomène : par une persistance effective du traceur [50], via des obstacles fixes anisotropes périodiques [49, 51–53], des interactions effectives entre le traceur et le bain [54], des forces thermodynamiques couplées [55], ou des champs de vitesse constants et périodiques [56–58]). Le cas d'un environnement complexe formé d'obstacles mobiles n'a pas été traité, malgré l'importance (cf. plus haut 0.1.1) de l'étude des environnements désordonnés dynamiques.

Plan. Dans un premier temps, nous développons une théorie microscopique dans le but d'étudier le coefficient de diffusion d'une particule active en milieu encombré. Dans un second temps, nous étendrons cette étude au cas où le traceur est également soumis à une force extérieure, où notre résultat majeur sera de montrer que la MNA est prédite par notre modèle, fournissant une description explicite de l'environnement.

0.1.2 Diffusion d'une particule run-and-tumble

Dans cette première partie, nous développons une théorie microscopique pour le coefficient de diffusion d'un traceur actif dans un environnement encombré sur un réseau, à une densité et une activité arbitraires. La dynamique du traceur et des obstacles constitue un problème à plusieurs corps, dont les équations font classiquement intervenir une hiérarchie (de type BBGKY). Nous recourons alors à une approximation de fermeture, permettant de calculer le coefficient de diffusion d'un traceur actif en termes des profils de densité du bain et des fonctions de corrélation entre le traceur et le bain. Notre résultat clé est que l'approximation proposée, en plus d'être traitable analytiquement (impliquant néanmoins, en général, des équations implicites), présente une grande précision dans une large gamme de paramètres (vérifiée via des simulation numériques).

Il est important de noter qu'en plus de la détermination du coefficient de diffusion du traceur, notre approche nous permet de calculer la perturbation de l'environnement due au déplacement du traceur actif et les corrélations entre la position du traceur et l'occupation des différents sites du réseau. Enfin, l'expression analytique du coefficient de diffusion devient explicite dans les régimes de basse et de haute densité, dans lesquels notre approximation de fermeture devient exacte (justification en section 3.3.1).

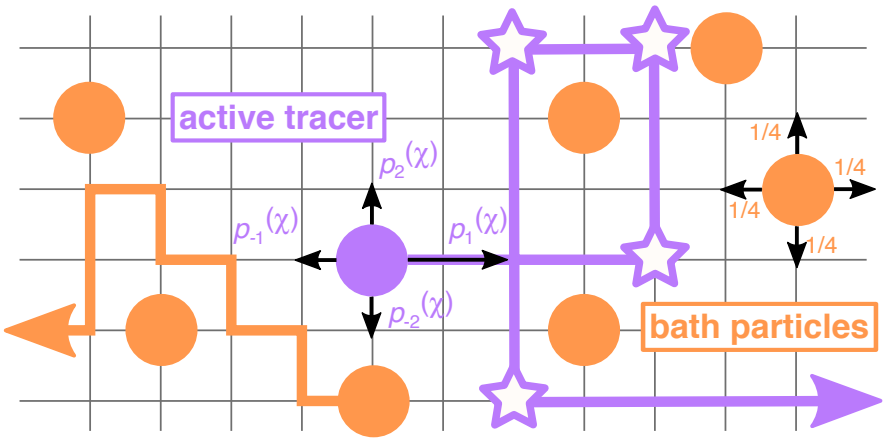

Figure 2: Schéma du modèle : un traceur actif effectue une marche aléatoire persistante dans un bain de particules effectuant des marches aléatoires symétriques simples. Le traceur actif saute préférentiellement dans la direction χ (ici par exemple $\chi = 1$). La direction χ change aléatoirement, et les événements de réorientation sont représentés par des étoiles. Toutes les particules interagissent par des interactions de cœur dur.

Modèle

Nous considérons un traceur actif dans un environnement encombré et dynamique (Fig. 2). Les particules du bain (présentes en densité ρ), et le traceur évoluent sur un réseau cubique à $d \geq 2$ dimensions, de pas unitaire. Le système évolue en temps continu, ce qui est la façon naturelle et habituelle de décrire les systèmes avec des effets de blocage de site, à la fois en dimension un, comme dans les processus d'exclusion simple (asymétriques) [59, 60], et en dimensions supérieures [38–40]. Les particules du bain effectuent des marches aléatoires symétriques (avec un temps caractéristique τ^*), et le traceur effectue une marche aléatoire (avec un temps caractéristique τ) biaisée dans la direction d'une force active dont l'orientation, notée χ, change de manière aléatoire. La variable $\chi \in \{\pm 1, \ldots, \pm d\}$ sera appelée "l'état" du traceur (qui correspond donc la direction actuelle de la force active). Le traceur passe d'un état χ à un autre état $\chi' \neq \chi$ avec un taux $\frac{\alpha}{2d\tau^*}$, où α est sans dimension. Le temps de persistance est alors $\tau_\alpha = \frac{2d\tau^*}{\alpha}$. Nous désignons par $p_\mu^{(\chi)}$ la probabilité pour le traceur de sauter dans la direction $\mu \in \{\pm 1, \ldots, \pm d\}$ lorsqu'il est dans l'état χ. Nous choisissons $p_\mu^{(\chi)} \propto \exp[F_A \boldsymbol{e}_\chi \cdot \boldsymbol{e}_\mu/2]$ avec une normalisation appropriée (où $\boldsymbol{e}_{\pm 1}, \ldots, \boldsymbol{e}_{\pm d}$ sont les vecteurs de base du réseau et nous utilisons la notation $\boldsymbol{e}_{-\mu} = -\boldsymbol{e}_\mu$). La force active F_A est liée à la vitesse du traceur en l'absence d'interactions (*i.e.* $\rho = 0$)[1] $v_0 = (p_1^{(1)} - p_{-1}^{(1)})/\tau$. La dynamique du traceur est une version sur réseau de la dynamique "run-and-tumble", qui est un modèle central dans la théorie de la matière active et qui a été largement utilisé pour décrire le transport et la diffusion des bactéries, voir par exemple [7]. Enfin, toutes les particules évoluent sur le réseau avec la restriction qu'il ne peut y avoir qu'une seule particule par site.

L'état du système à l'instant t est décrit par $P_\chi(\boldsymbol{R}, \eta; t)$, qui est la probabilité jointe de trouver le traceur dans l'état χ, au site $\boldsymbol{R}$, avec le réseau dans la configuration $\eta = (\eta_{\boldsymbol{r}})$, où $\eta_{\boldsymbol{r}} = 1$ si le site $\boldsymbol{r}$ est occupé par une particule de bain et 0 sinon. L'équation maîtresse à

[1] v_0 est l'analogue de la vitesse de propulsion dans les modèles habituels en espace continu de particules browniennes actives ou de particules "run-and-tumble". Ici, étant donné que la particule évolue sur un réseau, v_0 est limitée par $1/\tau$. Notons que, compte tenu de notre choix de $p_\mu^{(\chi)}$, la force active $\boldsymbol{F}$ contrôle v_0 mais aussi l'amplitude des fluctuations dans la direction perpendiculaire à $\boldsymbol{F}$.

laquelle obéit la probabilité jointe traceur-bain est :

$$2d\tau^*\partial_t P_\chi(\boldsymbol{R},\eta;t) = \mathcal{L}_\chi P_\chi - \alpha P_\chi + \frac{\alpha}{2d-1}\sum_{\chi'\neq\chi} P_{\chi'}, \tag{1}$$

où $\mathcal{L}_\chi$ l'opérateur d'évolution quand la force active est dans la direction $\boldsymbol{e}_\chi$ (voir (2.3)), décrivant le déplacement des particules du bain et du traceur. Les autres termes rendent compte de la réorientation de la force active.

A $t = 0$, nous supposons que toutes les directions de la force active sont équiprobables, de telle sorte que la position moyenne du traceur reste nulle, et qu'à tout moment tous les états ont la même probabilité $\frac{1}{2d}$. Nous nous intéressons aux fluctuations de la position du traceur le long d'une direction, par exemple $X_t = \boldsymbol{X}_t \cdot \boldsymbol{e}_1$. En multipliant l'équation maîtresse par X_t^2 et en calculant la moyenne, on obtient une expression de la dérivée temporelle de $\langle X_t^2\rangle$, où $\langle\cdot\rangle$ représente la moyenne sur la position du traceur, son état et la configuration du réseau. Le coefficient de diffusion du traceur, défini comme $D \equiv \lim_{t\to\infty} \frac{1}{2}\frac{\mathrm{d}}{\mathrm{d}t}\langle X_t^2\rangle$, est donné par

$$D = \frac{1}{4d\tau}\sum_\chi\sum_{\epsilon=\pm1}\left\{p_\epsilon^{(\chi)}\left[1-k_\epsilon^{(\chi)}\right] - 2\epsilon p_\epsilon^{(\chi)}\widetilde{g}_\epsilon^{(\chi)}\right\} + \frac{2d-1}{2d}\frac{\tau^*}{\tau^2\alpha}\sum_\chi\left\{\sum_{\epsilon=\pm1}\epsilon p_\epsilon^{(\chi)}\left[1-k_\epsilon^{(\chi)}\right]\right\}^2. \tag{2}$$

Cette expression fait intervenir les profils de densité dans le référentiel du traceur notés $k_{\boldsymbol{r}}^{(\chi)} = \langle\eta_{\boldsymbol{X}_t+\boldsymbol{r}}\rangle_\chi$ et les fonctions de corrélations traceur-bain $\widetilde{g}_{\boldsymbol{r}}^{(\chi)} = \langle\eta_{\boldsymbol{X}_t+\boldsymbol{r}}(X_t - \langle X_t\rangle_\chi)\rangle_\chi$, où $\langle\cdot\rangle_\chi = 2d\sum_{\boldsymbol{R},\eta}\cdot P_\chi(\boldsymbol{R},\eta;t)$ désigne la moyenne sachant que le traceur est dans l'état χ.

Approximation de découplage

Les équations d'évolution de $k_{\boldsymbol{r}}^{(\chi)}(t)$ et $\widetilde{g}_{\boldsymbol{r}}^{(\chi)}(t)$, obtenues en multipliant l'équation maîtresse [Eq. (1)] respectivement par $\eta_{\boldsymbol{X}_t+\boldsymbol{r}}$ et $X_t\eta_{\boldsymbol{X}_t+\boldsymbol{r}}$, ne sont pas fermées et impliquent des fonctions de corrélation d'ordre supérieur, dont les équations d'évolution impliquent à leur tour des fonctions de corrélation d'ordre encore plus élevé, et ainsi de suite. Dans le but de fermer la hiérarchie infinie d'équations qui en résulte, nous proposons l'approximation de type champ moyen suivante :

$$\langle\eta_{\boldsymbol{r}}\eta_{\boldsymbol{r}'}\rangle_\chi \simeq k_{\boldsymbol{r}}^{(\chi)}k_{\boldsymbol{r}'}^{(\chi)}, \tag{3}$$

$$\langle\delta X_t\eta_{\boldsymbol{r}}\eta_{\boldsymbol{r}'}\rangle_\chi \simeq k_{\boldsymbol{r}}^{(\chi)}\widetilde{g}_{\boldsymbol{r}'}^{(\chi)} + k_{\boldsymbol{r}'}^{(\chi)}\widetilde{g}_{\boldsymbol{r}}^{(\chi)}, \tag{4}$$

que l'on obtient en écrivant chaque variable aléatoire sous la forme $x = \langle x\rangle + \delta x$ et en négligeant les termes d'ordre 2 et 3 en les fluctuations. On note que cela va au-delà du champ moyen trivial, dans lequel l'occupation moyenne des sites du réseau serait supposée uniforme et égale à ρ. Cette approximation a été appliquée avec succès pour étudier la vitesse [61] et la diffusivité [62] d'un traceur biaisé (limite de $\alpha \to 0$) et il a été démontré dans ce cas qu'elle devenait exacte dans les régimes de basse et de haute densité [63].

De cette approximation de fermeture découlent des équations d'évolution non linéaires portant sur les quantités $h_{\boldsymbol{r}}^{(\chi)} \equiv k_{\boldsymbol{r}}^{(\chi)} - \rho$ (défini de telle sorte que $\lim_{|\boldsymbol{r}|\to\infty} h_{\boldsymbol{r}} = 0$) et $\widetilde{g}_{\boldsymbol{r}}^{(\chi)}$ (voir équations (3.5, 3.6)). Ces équations constituent l'élément central de notre résolution : dans le cadre de notre approximation de fermeture, elles permettent de déterminer les quantités $h_{\boldsymbol{r}}^{(\chi)}$ et $\widetilde{g}_{\boldsymbol{r}}^{(\chi)}$, et donc le coefficient de diffusion du traceur par l'intermédiaire de l'Eq. (2), pour tout choix de paramètres, et en particulier pour une densité arbitraire d'obstacles ρ.

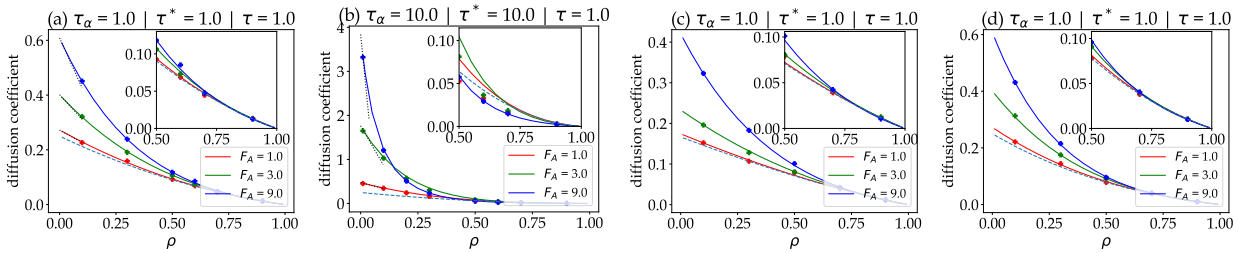

Figure 3: Coefficient de diffusion d'un traceur actif sur un réseau 2D (a,b), un réseau 3D (c) et un capillaire 2D de largeur $L = 3$ (d), en fonction de la densité ρ, pour plusieurs valeurs de la force active F_A et du temps de persistance τ_α. Symboles : Simulations Monte Carlo (voir appendice A.3 pour plus de détails sur les simulations numériques). Lignes continues : approche analytique [equation (2) et section 0.1.2]. Lignes pointillées : développement asymptotique dans le régime de basse densité. Lignes en tirets : cas d'un traceur passif [38].

Résolution analytique

La résolution analytique des équations issues du découplage repose sur l'invariance par translation du système, qui nous permet d'utiliser la transformée de Fourier pour inverser l'opérateur différentiel discret intervenant dans les équations (section 3.2).

Nous résolvons d'abord le cas d'un réseau infini en 2D. Nous calculons les valeurs de $h_\mu^{(\chi)}$ et $\widetilde{g}_\mu^{(\chi)}$ dans l'état stationnaire. On en déduit la valeur du coefficient de diffusion en utilisant l'Eq. (2). Nous étudions la dépendance de D en la densité de particules sur le réseau ρ, pour différentes valeurs de τ, τ^*, τ_α et F_A. La Fig. 3 montre un très bon accord entre les simulations Monte Carlo et notre approximation de découplage. Comme dans la théorie pour un traceur passif [38], la précision de notre approximation de découplage s'améliore lorsque l'environnement est plus mobile (typiquement $\tau^*/\tau \lesssim 10$) ou lorsque la dimension du réseau est plus élevée. Dans le cas où il n'y a pas de propulsion ($F_A = 0$), notre approximation correspond au résultat de Nakazato et Kitahara [38], qui fournit une expression explicite du coefficient de diffusion en fonction de la densité. Notre étude peut donc être considéré comme une généralisation de ce résultat classique sur la diffusion de traceurs dans les gaz sur réseau au cas d'une particule active. Notons également que dans la limite $\alpha \to 0$, nous retrouvons les résultats obtenus précédemment pour la vitesse et le coefficient de diffusion d'un traceur passif [62].

Ce calcul peut facilement être étendu à d'autres géométries sur réseau, à condition qu'elles restent invariantes par translation. En particulier, nous considérons le cas d'un réseau 2D en forme de bande (infini dans une direction et fini de largeur L avec des conditions aux limites périodiques dans l'autre direction ; une géométrie qui peut modéliser des canaux étroits ou des systèmes confinés), et celui d'un réseau 3D infini (Fig. 3).

Enfin, nous soulignons que notre approche permet d'aller au-delà de la détermination du seul coefficient de diffusion du traceur, et donne accès à la dépendance spatiale complète des profils de densité $h_{\boldsymbol{r}}^{(\chi)}$ et des fonctions de corrélation $\widetilde{g}_{\boldsymbol{r}}^{(\chi)}$. Ces quantités décrivent l'interaction entre le déplacement du traceur actif et la réponse de son environnement – un aspect non couvert par les descriptions précédentes [64]. En particulier, nous observons et quantifions une accumulation de particules du bain devant le traceur.

Non monotonie en fonction des paramètres contrôlant l'activité

Nous étudions maintenant la dépendance du coefficient de diffusion en le temps de persistance τ_α. Les limites asymptotiques $\tau_\alpha \to 0$ et $\tau_\alpha \to \infty$ sont connues : lorsque le

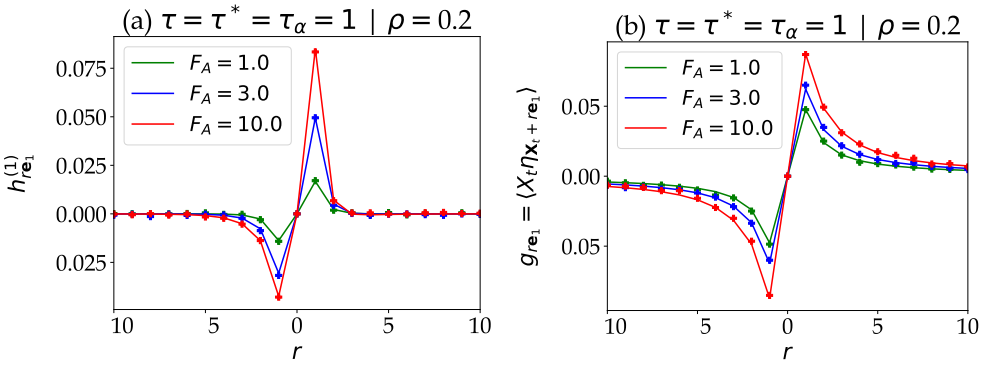

Figure 4: (a) Profils de densité (sachant que le traceur est dans l'état $\chi = 1$) et (b) fonctions de corrélation traceur-bain (moyennées sur tous les états) en fonction de la distance au traceur, sur un réseau 2D. Symboles : simulations Monte Carlo. Lignes : approche analytique 0.1.2.

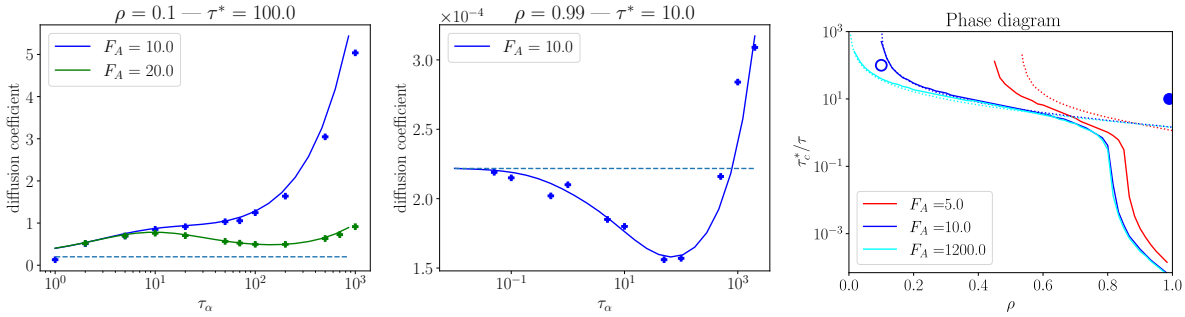

Figure 5: Non-monotonie de D en fonction du temps de persistance τ_α, aux densité $\rho = 0,1$ (gauche) et $\rho = 0,99$ (milieu). Symboles : simulations de Monte-Carlo. Lignes continues : approche analytique 0.1.2. Diagramme de phase (droite) : au-dessus des courbes, D est une fonction non-monotone de τ_α. Lignes continues : approche analytique 0.1.2. Symboles : Simulations Monte Carlo ; un cercle rempli signifie que la non-monotonie est observée en ce point, un cercle vide signifie qu'elle ne l'est pas. Lignes pointillées : argument qualitatif 0.1.3.

temps de persistance devient très petit, le coefficient de diffusion est fini et égal à celui d'un traceur passif [38], tandis que dans la limite d'un traceur infiniment persistant, le coefficient de diffusion diverge (sauf dans la limite spécifique d'obstacles fixes $\tau^* = \infty$). Notre analyse révèle que le coefficient de diffusion peut présenter un comportement non monotone entre ces deux limites, comme observé précédemment dans la limite de basse densité et de force active infinie ($F_A = \infty$) [43]. Ici, nous allons plus loin, notre modèle nous permettant de considérer une force active F_A et une densité ρ arbitraires. Pour une valeur donnée de ρ et τ^*/τ, la non-monotonie du coefficient de diffusion persiste tant que la force active est suffisamment grande, comme le montre la Fig. 5. Cet effet résulte de la compétition entre les différentes échelles de temps régissant la diffusion du traceur et peut être analysé à l'aide d'arguments analytiques simples (voir plus bas 0.1.3).

Conclusion

En conclusion, notre approche s'appuie sur un modèle sur réseau, étudié à l'aide d'une approximation de découplage, qui se révèle très performante à toute densité (Fig. 3). Cela nous permet de mettre en lumière la dépendance complexe du coefficient de diffusion d'un traceur actif en fonction des différents paramètres d'activité et d'encombrement.

Enfin, nos résultats pourraient permettre d'étudier et d'éclairer de récentes observations

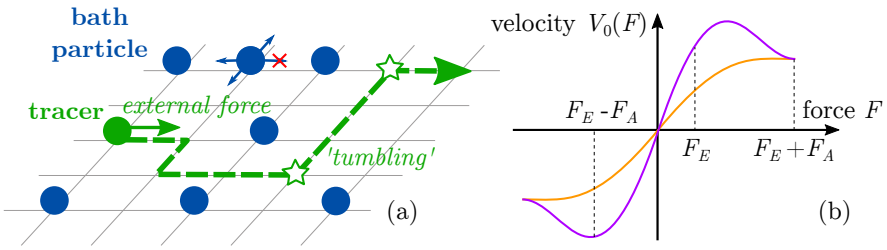

Figure 6: (a) Schéma du système étudié : le tracer (en vert) actif est soumis également à une force externe. (b) Courbe force-vitesse typique d'un traceur passif avec et sans mobilité différentielle négative (en violet et orange, respectivement).

expérimentales d'organismes vivants [16] ou de particules auto-propulsée [65] en milieu encombré. En effet, notre modèle constitue un modèle minimal, possédant les mêmes caractéristiques qualitatives que ces systèmes ("run-and-tumble", obstacles).

0.1.3 Réponse à un champ extérieur et mobilité négative

Dans cette section, nous étendons notre modèle au cas où le traceur est soumis à une force extérieure F_E constante en plus de la force active F_A (dont la direction χ varie au cours du temps). Nous obtenons des résultats dans une large gamme de paramètres. Le résultat principal de cette section est la mise en évidence, dans notre modèle, d'un effet surprenant, impossible dans le régime de la réponse linéaire : la mobilité négative absolue (MNA), c'est à dire une vitesse du traceur opposée à la direction de la force externe.

Nous présentons également un argument qualitatif valable à basse densité, qui explique le mécanisme physique à l'origine de la MNA en termes d'échelles de temps caractéristiques pertinentes : la MNA émerge d'un phénomène de piégeage du traceur par les obstacles passifs. Enfin, notre approche clarifie la relation entre la MNA et la mobilité différentielle négative (une autre caractéristique des systèmes maintenus loin de la réponse linéaire).

Afin de tenir compte de l'effet de la force extérieure, nous modifions la définition des taux de saut du traceur en posant $p_\mu^{(\chi)} = \frac{\exp[(F_A \boldsymbol{e}_\chi + F_E \boldsymbol{e}_1)\cdot \boldsymbol{e}_\mu/2]}{Z}$ (voir 0.1.2 pour la définition du modèle et Fig. 6(a) pour une représentation). En conséquence, pour $F_E \neq 0$, la vitesse atteinte par le traceur (le long de la direction 1) dans l'état stationnaire est non nulle. Elle sera notée $V \equiv \lim_{t\to\infty} \frac{\mathrm{d}\langle X_t\rangle}{\mathrm{d}t}$.

Argument simple pour la MNA

Nous présentons tout d'abord un argument expliquant l'émergence de la MNA comme découlant de la mobilité différentielle négative (MDN). Cette dernière désigne la situation où un traceur passif (cela correspond, dans notre modèle, à $F_A = 0$ et/ou $\tau_\alpha = 0$) soumis à une force extérieure constante F_E peut présenter une vitesse qui décroît avec l'intensité de la force, tout en restant positive [61, 63, 66–72].

A titre d'illustration, nous considérons la situation simple où le traceur est soumis à une force active F_A qui ne peut pointer que dans les directions $\pm\boldsymbol{e}_1$. Dans la limite où le temps de persistance τ_α est supérieur aux autres échelles de temps, la vitesse moyenne du traceur peut être estimée comme la moyenne des vitesses conditionnées à ces deux états $V \simeq \frac{1}{2}[V_0(F_E+F_A)+V_0(F_E-F_A)]$, où $V_0(F)$ est la vitesse stationnaire d'une particule passive soumise à une force externe F. Comme illustré sur la Fig. 6(b), V peut être négative pour un F_E positif dès lors que la $V_0(F)$ est non monotone (MDN).

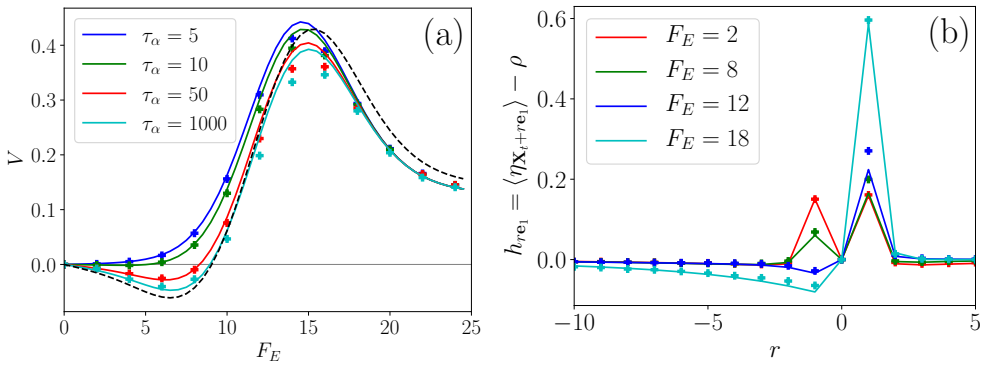

Figure 7: (a) Vitesse stationnaire du traceur le long de la direction de la force externe F_E sur un réseau 2D. Lignes continues : approximation de découplage [Eq. (5) et section 0.1.2] ; symboles : simulations Monte Carlo ; ligne pointillée : argument qualitatif dans la limite de persistance infinie (Eq. (7) pour $\tau_\alpha = \infty$). (b) Profils de densité (par rapport à la valeur de référence ρ) le long de la direction de F_E dans le référentiel du traceur, en fonction de la distance au traceur r. Dans les deux graphiques, $\rho = 0, 1, \tau^* = 30, \tau = 1, F_A = 12$.

Calcul de la vitess du traceur

A partir de l'équation maîtresse (1), nous pouvons exprimer la vitesse du traceur en fonction des profils conditionnels de densité $k_{\boldsymbol{r}}^{(\chi)} = \langle \eta_{\boldsymbol{X}_t + \boldsymbol{r}} \rangle_\chi$:

$$\frac{\mathrm{d}\langle X_t \rangle}{\mathrm{d}t} = \frac{1}{2d\tau} \sum_\chi \left\{ p_1^{(\chi)} \left[1 - k_{\boldsymbol{e}_1}^{(\chi)} \right] - p_{-1}^{(\chi)} \left[1 - k_{\boldsymbol{e}_{-1}}^{(\chi)} \right] \right\}. \tag{5}$$

A l'aide de la méthode de résolution présentée en section 0.1.2, nous calculons cette vitesse pour différents choix de paramètres. Nous observons que, pour un temps de persistance suffisamment grand τ_α, lorsque la force active est suffisamment grande et que les particules du bain sont suffisamment lentes par rapport au traceur ($\tau^* \gg \tau$), la vitesse peut devenir une fonction négative de la force externe (Fig. 7(a)), ce qui est la signature de la MNA. Nous comparons la valeur de la vitesse prédite par notre théorie analytique avec les résultats des simulations Monte Carlo de la dynamique microscopique, et observons un très bon accord, ce qui confirme la pertinence de notre approximation de découplage pour étudier la dynamique d'un traceur actif en présence d'une force externe.

Enfin, nous explorons plus en détail le domaine d'existence de la MNA à l'aide d'un diagramme de phase (Fig. 8). Nous en déduisons que la MNA peut se produire pour un nombre de Péclet Pe $\sim \sqrt{\tau_\alpha \tau^{-1}}$ supérieur à 3 environ (plus ce nombre est grand, plus l'effet de la propulsion active est grand devant l'effet des fluctuations thermiques). Cette condition est atteinte par de nombreux systèmes expérimentaux [1].

En outre, notre cadre analytique, qui rend pleinement compte des détails microscopiques de l'environnement du traceur, nous permet de quantifier la perturbation induite par son déplacement. En effet, comme sous-produit de notre calcul 0.1.2, nous obtenons les profils de densité dans le référentiel traceur. Leur dépendance spatiale typique est représentée sur la Fig. 7(b). On observe que la MNA a une signature sur la réponse de l'environnement : un petit excès de densité peut se développer derrière le traceur ($r < 0$) lorsque sa vitesse moyenne devient négative.

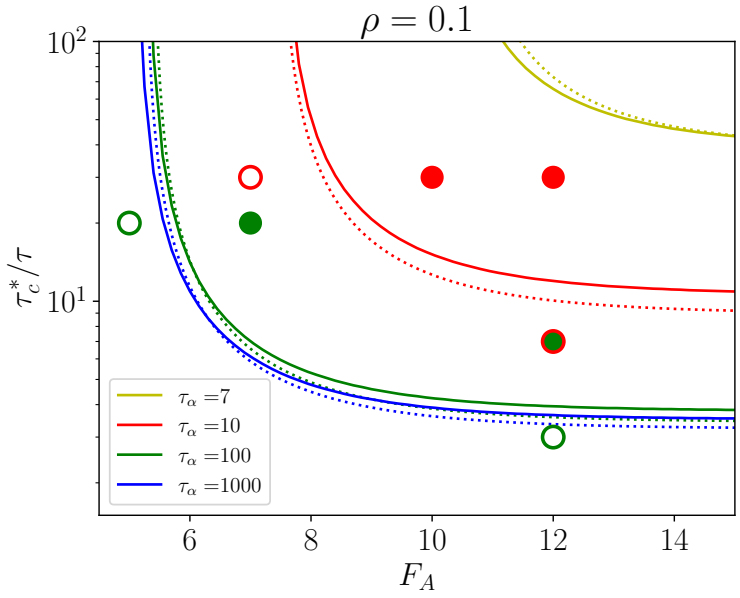

Figure 8: Diagramme de phase pour la MNA. Au-dessus des lignes, la théorie prévoit une mobilité négative absolue. Lignes continues : approximation de découplage [Eq. (5) et section 0.1.2]. Lignes pointillées : argument qualitatif de basse densité [Eq. (7)]. Symboles : Simulations Monte Carlo ; un cercle rempli signifie que la MNA est observée, un cercle vide signifie qu'elle ne l'est pas.

Argument qualitatif

Nous donnons enfin une interprétation physique du phénomène, qui éclaire qualitativement le mécanisme à l'origine de la MNA et de la non monotonie du coefficient de diffusion en l'absence de force externe (section 0.1.2). A basse densité de particules de bain, on peut supposer que ces dernières diffusent de manière indépendante. Pour une orientation donnée de la force active χ, le temps moyen entre deux sauts du traceur est $\tau + \rho\tau_p^{(\chi)}$, où $\tau_p^{(\chi)}$ est le temps moyen que le traceur passe bloqué derrière une particule du bain. Nous pouvons évaluer ce temps typique en considérant que, lorsque le traceur se trouve sur un site donné $\boldsymbol{R}$ et qu'il est bloqué par un obstacle situé sur le site $\boldsymbol{R} + \boldsymbol{e}_1$, le traceur peut avancer si l'un de ces trois événements indépendants, qui suivent des lois exponentielles, se produit : (i) l'obstacle se déplace dans une direction transversale avec un temps caractéristique $\frac{2d\tau^*}{(2d-2)}$; (ii) la force active change de direction avec un temps caractéristique τ_α ; (iii) le traceur se déplace dans une direction transversale avec un temps caractéristique $\tau/(1 - p_1^{(\chi)} - p_{-1}^{(\chi)})$. Le temps moyen passé piégé par un obstacle suit donc une loi exponentielle de temps caractéristique $\tau_p^{(\chi)}$ donné par

$$\frac{1}{\tau_p^{(\chi)}} = \frac{(2d-2)}{2d\tau^*} + \frac{1}{\tau_\alpha} + \frac{(1 - p_1^{(\chi)} - p_{-1}^{(\chi)})}{\tau}. \tag{6}$$

La vitesse du traceur est ensuite estimée comme une moyenne sur les directions de la force active χ :

$$V \simeq \frac{1}{2d} \sum_\chi \frac{p_1^{(\chi)} - p_{-1}^{(\chi)}}{\tau + \rho\tau_p^{(\chi)}}, \tag{7}$$

et la condition d'existence d'une mobilité négative absolue est donnée par $\left.\frac{\mathrm{d}V}{\mathrm{d}F_E}\right|_{F_E=0} < 0$. Ces considérations physiques montrent comment, dans la limite de basse densité, les différentes

échelles de temps du problème s'associent et conduisent, dans certains régimes, à un piégeage du traceur par les particules du bain pouvant amener à une MNA.

Conclusion

Nous avons montré que la MNA peut être observée dans un modèle minimal d'une particule active soumise à une force externe constante, en conséquence des interactions avec les autres particules de son environnement. La description explicite de l'environnement et du traceur dans notre modèle constitue une nouveauté par rapport aux approches théoriques précédentes utilisée pour décrire ce phénomène.

Dans cette première partie, les profils de densité et de corrélation $k_{\boldsymbol{r}}^{(\chi)}$ et $\widetilde{g}_{\boldsymbol{r}}^{(\chi)}$ se sont révélés être des quantités importantes puisqu'ils caractérisent les propriétés de transport du traceur. Dans la partie suivante, nous verrons que leur généralisation, les profils généralisés, jouent un rôle encore plus important, car ils se révéleront être des objets centraux pour caractériser le transport en une dimension.

0.2 Corrélations dans les systèmes diffusifs unidimensionnels

Dans la partie précédente, nous avons étudié le comportement d'une particule marquée dans un environnement encombré en dimension $d \geq 2$. Nous avons pu proposer une fermeture approximative (mais très précise) que nous avons utilisée pour analyser les propriétés de transport du traceur. Comme notre approximation repose sur des hypothèses de type champ moyen, il s'avère qu'elle est moins performante pour décrire le transport unidimensionnel, aussi appelé transport en ligne ou en file, car ce dernier présente de fortes corrélations.

0.2.1 Motivation et approche de notre étude

Une théorie valable pour le cas unidimensionnel serait néanmoins d'une grande valeur car cette géométrie intervient dans de nombreux contextes biologiques. En effet, différents processus reposent sur le transfert d'eau et d'ions à travers les nano-pores des protéines transmembranaires [73, 74]. En outre, la structure en file unique est celle naturellement adoptée par les fluides confinés dans des canaux étroits [75], comme cela a été démontré numériquement [76, 77], et plus récemment expérimentalement [78].

La singularité de la dimension 1

Le transport en file (Fig. 9) correspond à des particules qui diffusent dans des canaux étroits avec la contrainte qu'elles ne peuvent pas se contourner les unes les autres. Le fait que l'ordre initial soit maintenu à tout moment conduit au comportement sous-diffusif $\langle X_t^2 \rangle \propto \sqrt{t}$ pour la position X_t d'un traceur [79], en contraste avec la diffusion normale $\langle X_t^2 \rangle \propto t$. Cette prédiction, qui confère à la diffusion en file un grand intérêt théorique, a été observée expérimentalement dans les zéolithes et dans des systèmes de colloïdes dans des canaux étroits [80–82].

Dans cette thèse nous considérons le cas où les particules diffusent sur une ligne infinie (le cas fini a également fait l'objet d'un grand nombre de travaux [83–89]). Nous considérerons tout d'abord le cas d'un traceur identique aux autres particules, puis au cas d'un traceur biaisé (traceur soumis à une force extérieure constante, mais pas les autres particules). Cette dernière situation se rencontre par exemple en microrhéologie active [90, 91] et constitue un

modèle unidimensionnel minimal pour le transport hors d'équilibre dans des environnements confinés et encombrés [63, 67, 89, 92–95].

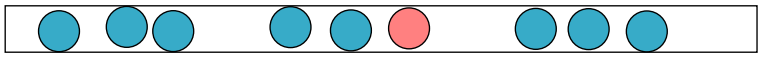

Figure 9: Particules confinées dans un canal plus étroit que le double de la taille des particules.

Le SEP : un modèle paradigmatique de diffusion en file

Le processus d'exclusion symétrique (SEP) est un modèle fondamental de diffusion en file. Les particules, présentes à une densité ρ, effectuent des marches aléatoires symétriques en temps continu sur un réseau infini unidimensionnel avec un taux de saut unitaire, et avec la contrainte qu'il y a au plus une particule par site (Fig. 10). Le SEP a atteint le statut de modèle paradigmatique de la physique statistique et a généré un nombre considérable de travaux dans la littérature mathématique et physique (voir, par exemple, Refs. [96–99]), c'est pourquoi il prendra une place centrale dans notre étude. Le calcul de la fonction de grande déviation de la position X_t d'un traceur dans la limite de temps long a constitué une avancée majeure récente [100, 101]. Elle donne accès à tous les cumulants au temps long de X_t, dont on constate en particulier qu'ils ont un comportement anormal en $\sqrt{t}$ [100, 102]. De même, il a été montré que les cumulants du courant intégré dans le temps à travers l'origine, Q_t, croissent également comme $\sqrt{t}$, et sa fonction de grandes déviations a été déterminée [99].

Cet ensemble de comportements anormaux dans le SEP et les systèmes en ligne en général, trouve son origine dans les fortes corrélations spatiales dans la géométrie unidimensionnelle, ce qui en fait des quantités déterminantes. Même si cela est compris qualitativement depuis longtemps, jusqu'à présent ces corrélations bain-traceur n'ont été déterminées quantitativement que dans des cas particuliers, tels que les limites de haute et de basse densité du SEP [103]. En effet, le calcul de ces corrélations constitue en fait un problème ouvert, à plusieurs corps.

Plan. Dans un premier temps, nous centrons notre étude sur le SEP à densité arbitraire. Notre résultat majeur est la détermination complète des corrélations bain-traceur à l'aide d'une équation fermée exacte d'une simplicité remarquable. Ensuite, nous montrerons que ce résultat s'applique à de nombreux autres systèmes au-delà du SEP, grâce à des correspondances générales dont nous développons la théorie complète dans une description hydrodynamique. Ainsi, les corrélations bain-traceur apparaîtraient comme des quantités fondamentales et générales pour analyser la diffusion en file. Enfin, nous présenterons, dans le cas du SEP, les premiers résultats que nous avons obtenus dans le cas où l'on considère un traceur biaisé. Un résultat central est l'obtention, de manière analytique, de la première correction de la variance du traceur au delà de la réponse linéaire, à densité arbitraire.

0.2.2 Fermeture exacte pour les corrélations dans le SEP

Dans le cas du SEP, nous montrons que nous pouvons caractériser, de manière exacte, les corrélations entre le traceur et son environnement à l'aide d'une équation fermée vérifiée par des quantités appelées profils de densité généralisés, que nous définissons ci-dessous. Nous soulignons ensuite le rôle central de cette équation en montrant qu'elle s'applique également à des situations hors d'équilibre, ainsi qu'à l'étude d'autres observables, telles que le courant intégré à travers l'origine.

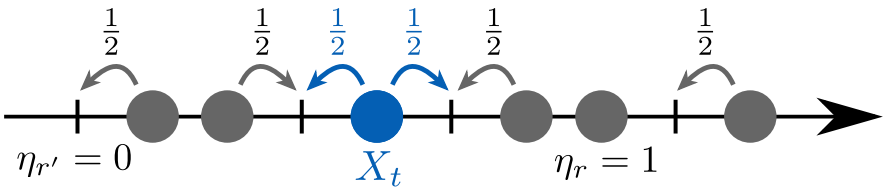

Figure 10: Le processus d'exclusion simple (SEP). Le traceur est situé à la position X_t. Les nombres d'occupation des sites sont notés η_r.

Profils de densité généralisés

Nous considérons le SEP, à densité moyenne ρ (chaque site est initialement occupé par une particule avec probabilité ρ), avec un traceur, de position X_t au temps t, initialement à l'origine. Les particules du bain sont décrites par l'ensemble des nombres d'occupation $\eta_r(t)$ de chaque site $r \in \mathbb{Z}$ au temps t, avec $\eta_r(t) = 1$ si le site est occupé et $\eta_r(t) = 0$ sinon (voir Fig. 10). Le système est entièrement déterminé par sa configuration (X, η). La distribution statistique de la position du traceur est décrite par la fonction génératrice des cumulants, dont le développement définit les cumulants κ_n de la position :

$$\psi(\lambda, t) \equiv \ln \left\langle \mathrm{e}^{\lambda X_t} \right\rangle \equiv \sum_{n=1}^{\infty} \frac{\lambda^n}{n!} \kappa_n(t). \tag{8}$$

Son équation d'évolution est donnée par :

$$\frac{\mathrm{d}\psi}{\mathrm{d}t} = \frac{1}{2} \left[(\mathrm{e}^{\lambda} - 1)(1 - w_1) + (\mathrm{e}^{-\lambda} - 1)(1 - w_{-1}) \right], \tag{9}$$

où la fonction génératrice des profils de densité généralisés (PDG) est définie par

$$w_r(\lambda, t) \equiv \langle \eta_{X_t + r} \mathrm{e}^{\lambda X_t} \rangle / \langle \mathrm{e}^{\lambda X_t} \rangle. \tag{10}$$

Notons qu'en plus de contrôler l'évolution temporelle de la fonction génératrice des cumulants, w_r (avec ψ) caractérise complètement la fonction génératrice des cumulants joints de (η_{X_t+r}, X_t) et donc les corrélations bain-traceur [103]. La fonction génératrice des PDG est donc une quantité clé, et l'étape suivante consisterait à écrire son équation d'évolution à partir de l'équation maîtresse décrivant le système. Cependant, de manière semblable à l'Eq. (9), elle implique des fonctions de corrélations d'ordre supérieur. Tout comme dans la première partie (0.1), ou dans les systèmes à plusieurs corps en général [85, 100, 104], ces fonctions de corrélations vérifient une hiérarchie infinie d'équations. Parvenant à fermer cette hiérarchie, nous donnons ci-dessous une équation fermée qui permet de déterminer la fonction génératrice des PDG dans la limite hydrodynamique (grand temps, grande distance).

Dans cette limite, la position du traceur satisfait un principe de grande déviation [100, 101, 105], ce qui implique que la fonction génératrice des cumulants se comporte comme $\psi \sim \hat{\psi}\sqrt{2t}$. Ce comportement anormal provient de la forme plus générale

$$w_r(\lambda, t) \underset{t \to \infty}{\sim} \Phi\left(\lambda, v = \frac{r}{\sqrt{2t}}\right) \equiv \sum_{n=0}^{\infty} \frac{\lambda^n}{n!} \Phi_n(v) \tag{11}$$

de la fonction génératrice des PDG, où le coefficient Φ_n donne la limite hydrodynamique du cumulant joint $\langle \eta_{X_t+r} X_t^n \rangle_c$ de la position X_t du traceur et du nombre d'occupation η_{X_t+r} mesuré dans son référentiel. Dans ce qui suit, nous ne noterons pas l'argument λ de Φ pour alléger les notations.

Fermeture exacte

Nous résumons ici les résultats obtenus en chapitres 7 et 8. Les deux fonctions (dérivées normalisées des profils)

$$\Omega_{\pm}(v) \equiv \mp 2\hat{\psi}\frac{\Phi'(v)}{\Phi'(0^{\pm})} \quad \text{définis pour} \quad v \gtrless 0 \tag{12}$$

sont entièrement déterminées par les équations intégrales *fermées* de type Wiener-Hopf [106] avec un noyau gaussien :

$$\boxed{\Omega_{\pm}(v) = \mp\omega\, \mathrm{e}^{-(v+\xi)^2+\xi^2} - \omega \int_{\mathbb{R}^{\mp}} \Omega_{\pm}(z)\mathrm{e}^{-(v-z+\xi)^2+\xi^2}\mathrm{d}z}, \tag{13}$$

où $\xi \equiv \frac{\mathrm{d}\hat{\psi}}{\mathrm{d}\lambda}$ et nous avons considéré la continuation analytique de Ω_+ pour $v < 0$ et de Ω_- pour $v > 0$. Le paramètre ω est déterminé par les conditions aux limites (voir Eq.(12))

$$\Omega_+(0) = -\Omega_-(0) = -2\hat{\psi}, \tag{14}$$

de sorte que les fonctions $\Omega_{\pm}(v)$ sont paramétrées par $\hat{\psi}$. A ce stade, l'expression de $\hat{\psi}(\lambda)$ n'a pas encore été déterminée explicitement, mais elle peut être obtenue de la manière suivante. Tout d'abord, Φ est déduit par intégration de $\Omega_{\pm}$, avec

$$\Phi(\pm\infty) = \rho, \tag{15}$$

par définition [Eq. (11)] (puisque $w_{|r|} \underset{r\to\infty}{\to} \rho$), et les conditions aux limites suivantes, qui découlent de considérations microscopiques :

$$\Phi'(0^{\pm}) \pm 2\frac{\hat{\psi}}{\mathrm{e}^{\pm\lambda} - 1}\Phi(0^{\pm}) = 0. \tag{16}$$

Le Φ obtenu est à ce stade paramétré par $\hat{\psi}$ et λ. Ensuite, en utilisant la limite de temps long de l'Eq.(9),

$$\frac{1 - \Phi(0^-)}{1 - \Phi(0^+)} = \mathrm{e}^{\lambda}, \tag{17}$$

$\hat{\psi}$ peut être écrit comme une fonction de λ, et nous obtenons finalement la fonction génératrice des PDG recherchée $\Phi(\lambda, v)$.

Les équations de Wiener-Hopf (13) peuvent être résolues explicitement en termes de transformées de Fourier [106] :

$$\int_{\mathbb{R}^{\pm}} \Omega_{\pm}(v)\mathrm{e}^{\mathrm{i}kv}\mathrm{d}v = \pm\left(1 - \exp[-Z_{\pm}]\right), \tag{18}$$

où

$$Z_{\pm} \equiv \frac{1}{2}\sum_{n\geq 1}\frac{(-\omega\sqrt{\pi}\,\mathrm{e}^{-\frac{1}{4}(k+2\mathrm{i}\xi)^2})^n}{n}\,\mathrm{erfc}\left(\pm\sqrt{n}\left(\xi - \frac{\mathrm{i}k}{2}\right)\right). \tag{19}$$

Notre approche permet d'obtenir la fonction génératrice de cumulants $\hat{\psi}$ (ou, de manière équivalente, la fonction de grandes déviations de la position du traceur),

$$\hat{\psi} = -\frac{1}{2\sqrt{\pi}}\mathrm{Li}_{\frac{3}{2}}(-\sqrt{\pi}\omega), \quad \mathrm{Li}_{\nu}(x) \equiv \sum_{n\geq 1}\frac{x^n}{n^{\nu}}, \tag{20}$$

dont on montre (chapitre 8) qu'elle est identique à l'expression exacte obtenue dans [100, 101] en utilisant l'arsenal des probabilités intégrables. En outre, nous obtenons une caractérisation complète des corrélations spatiales bain-traceur via les expressions analytiques des Φ_n en utilisant la procédure décrite ci-dessus (voir la Fig. 11 pour la comparaison avec les simulations numériques).

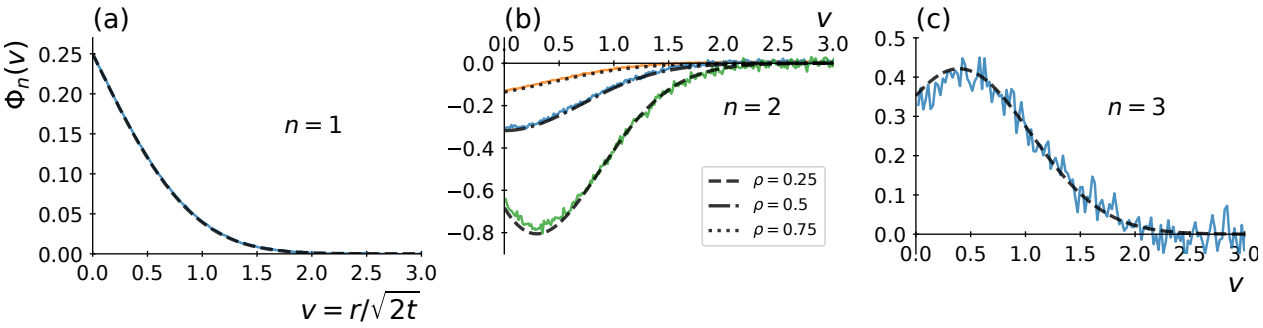

Figure 11: **SEP.** Profils de densité généralisés (PDG) d'ordre **(a)** $n = 1$ à la densité $\rho = 0.5$, **(b)** $n = 2$ aux densités $\rho = 0.25$, 0.5 et 0.75, et **(c)** $n = 3$ à la densité $\rho = 0.5$. Les lignes continues correspondent à des simulations du SEP (voir l'annexe A), temps final $t = 3000$, sur un réseau de 5000 sites. La moyenne est effectuée sur 10^8 réalisations. Les lignes en pointillés correspondent aux prédictions théoriques (18).

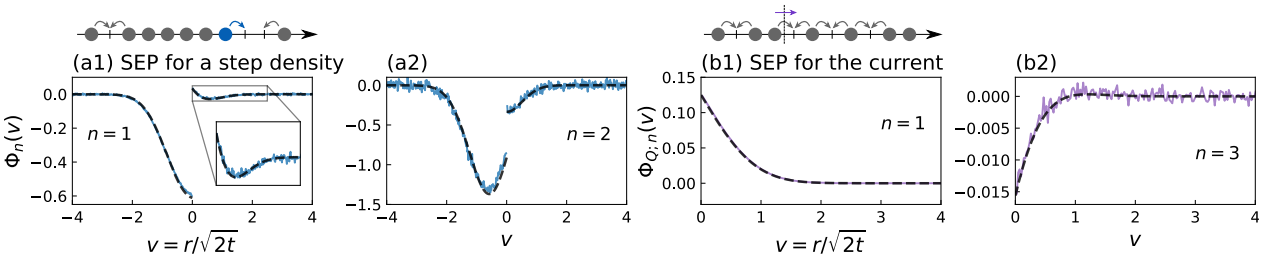

Figure 12: **Extensions: (a)** La situation, hors d'équilibre, d'une marche de densité initiale. **(b)** Autre observable, le courant passant par l'origine. Les lignes en pointillés correspondent aux prédictions obtenues à partir de l'équation centrale (8.47). (a) PDG à l'ordre $n = 1$ et $n = 2$ pour le SEP avec une marche de densité initiale $\rho_- = 0.7$ et $\rho_+ = 0.2$. Simulations à $t = 1500$ avec 2000 sites. (b) PDG pour le courant $\langle \eta_r Q_t^n \rangle_c$ dans le SEP pour une densité $\rho = 0.5$, simulations à $t = 900$, pour les ordres $n = 1$ et $n = 3$ (le profil pour $n = 2$ est nul).

Extension à d'autres situations

Il est important de noter que l'Eq. (13) décrit plusieurs autres situations d'importance physique dans le SEP. D'une part, elle s'applique à la situation hors équilibre d'une marche initiale de densité ρ_+ pour $x > 0$ et ρ_- pour $x < 0$, avec le traceur initialement à l'origine. Cette configuration a suscité beaucoup d'intérêt [99–101, 107, 108] car elle reste transitoire à tout moment et n'atteint jamais un état stationnaire. La fonction génératrice des PDG Φ est alors obtenue à partir de la solution (18) en suivant la procédure décrite ci-dessus, en changeant seulement la condition limite (15) en $\Phi(\pm\infty) = \rho_\pm$. Nous retrouvons les résultats de [100, 101] sur la fonction génératrice du cumulant $\hat{\psi}$. En outre, nous obtenons la structure spatiale complète des corrélations bain-traceur (voir Fig. 12(a)).

D'autre part, et de manière frappante, l'Eq. (13) donne également accès aux propriétés statistiques d'autres observables, comme par exemple le courant intégré à travers l'origine Q_t (voir chapitre 8 pour l'application au courant généralisé, qui est une observable plus générale), défini comme le flux total de particules entre les sites 0 et 1 pendant un temps t. Cette quantité a fait l'objet de nombreuses études, à la fois dans le contexte de la physique statistique [99, 104, 107, 109] et du transport mésoscopique [110, 111], en particulier dans la situation hors d'équilibre $\rho_- \neq \rho_+$ [99, 107]. Les quantités introduites précédemment (8)-(10)

sur l'exemple de la position du traceur sont naturellement adaptées en substituant Q_t à X_t. Les profils correspondants Φ_Q sont alors obtenus comme un cas particulier de l'Eq. (13) en fixant $\xi = 0$, complété par des conditions aux limites modifiées (16,17) obtenues par des considérations microscopiques (voir chapitre 7). En particulier, l'équation résultante (20) redonne la fonction génératrice des cumulants exacte de Q_t obtenue dans [99] par l'ansatz de Bethe, puisque dans ce cas, nous trouvons que

$$\omega_Q \sqrt{\pi} = \rho_-(1-\rho_+)(\mathrm{e}^{\lambda}-1) + \rho_+(1-\rho_-)(\mathrm{e}^{-\lambda}-1), \tag{21}$$

qui coïncide avec le paramètre réduit impliqué dans [99, 107]. En outre, le Φ_Q déterminé ici fournit la structure spatiale associée (voir Fig. 12(b)). Ces profils ont été introduits et étudiés numériquement dans [112] pour un système infini (voir aussi [85] pour un système fini entre deux réservoirs), mais aucune expression analytique n'était disponible jusqu'à présent.

Conclusion

En bref, nous avons déterminé analytiquement les corrélations spatiales dans le SEP, ce qui nous a permis de quantifier pleinement la réponse du bain à la perturbation induite par un traceur. En plus d'être de leur intérêt physique, ces corrélations se sont révélées être des quantités techniques fondamentales, car elles satisfont une équation fermée étonnamment simple. Cette même équation s'applique à une variété de situations dans le SEP. Dans la section suivante, nous avançons l'idée que cette équation peut en fait constituer un outil nouveau et prometteur pour aborder les systèmes de particules en interaction en général, puisqu'on verra qu'elle s'applique en fait à un grand nombre de systèmes.

0.2.3 Extension à des systèmes diffusifs unidimensionnels plus généraux

Au-delà du processus d'exclusion simple (SEP), divers modèles microscopiques de systèmes unidimensionnels ont été étudiés (voir Fig. 13 pour des exemples). Le résultat majeur de cette section est l'analyse et la caractérisation des relations qui peuvent exister, au niveau hydrodynamique, entre ces différents modèles, résumées dans le tableau 1.

Par exemple, il est connu que le SEP est lié à un autre modèle de particules sur réseau : le processus de portée nulle (ZRP, en anglais "Zero Range Process", voir les revues [117, 118]). Cette relation s'obtient en considérant la dynamique de l'écart de position entre deux particules consécutives dans le SEP. Elle a été utilisée explicitement dans plusieurs travaux, par exemple [119–122].

Nous montrons ici que, dans la limite hydrodynamique, tout système diffusif (*i.e.* satisfaisant une loi de Fourier) unidimensionnel peut être mis en correspondance avec d'autres systèmes reliés, que nous caractérisons. Ces relations de dualité générales nous permettent par la suite d'obtenir de nouveaux résultats pour différents modèles, en exploitant les solutions disponibles pour leur dual.

Hydrodynamique fluctuante et théorie macroscopique des fluctuations (MFT)

Nous nous plaçons dans le formalisme de l'hydrodynamique fluctuante [104, 123, 124], qui offre une description unifiée des systèmes diffusifs (voir chapitre 6). Dans ce cadre, en dimension un, les systèmes sont décrits par une densité macroscopique ρ qui satisfait une relation de continuité

$$\partial_t \rho(x,t) + \partial_x j(x,t) = 0\,, \tag{22}$$

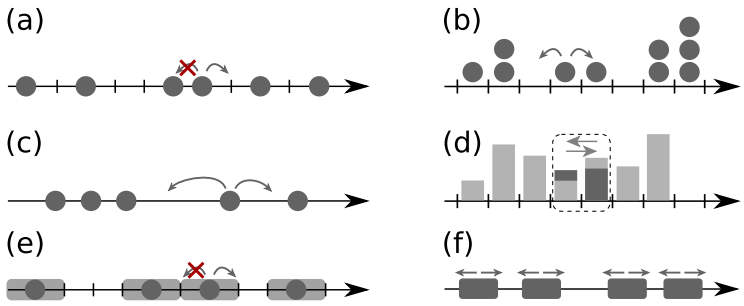

Figure 13: Les différents modèles de systèmes en ligne considérés ici. **(a)** le processus d'exclusion simple (SEP). **(b)** le processus de portée nulle (ZRP) [86, 107], où les particules peuvent sauter sur un site voisin avec un taux qui ne dépend que du nombre de particules sur leur site actuelle (d'où le nom de portée zéro, l'interaction se fait entre particules de même site uniquement). **(c)** le processus de moyenne aléatoire (RAP) [113, 114]. Les particules, sur une ligne continue, peuvent sauter à une fraction aléatoire de la distance qui les sépare de la particule suivante. **(d)** le modèle de Kipnis Marchioro Presutti (KMP) [115]. Chaque site héberge une variable continue (une masse). A des moments aléatoires, la masse totale de deux sites voisins est redistribuée aléatoirement entre eux. **(e)** le processus de double exclusion [116]. Une particule peut sauter sur un site voisin si le site de destination et le suivant sont vides. C'est un processus d'exclusion avec des particules qui occupent le volume de deux sites (zone assombrie sur le schéma). **(f)** [82] le gaz de bâtonnets durs. Des particules de longueur ℓ (bâtonnets) effectuent un mouvement brownien, avec la condition que les bâtonnets ne se chevauchent pas.

où $j(x,t)$ est le courant à la position x au temps t. Le comportement stochastique du modèle microscopique sous-jacent peut être pris en compte dans la description macroscopique en supposant que le courant j est aléatoire et prend la forme [123]

$$j(x,t) = -D(\rho)\partial_x\rho(x,t) + \sqrt{\sigma(\rho)}\,\eta(x,t)\,, \tag{23}$$

où η est un bruit blanc gaussien en espace et en temps avec une variance unitaire.

La force de cette approche, appelée hydrodynamique fluctuante, est que tous les détails microscopiques du modèle (déplacement, interaction, ...) sont encodés dans deux coefficients de transport : le coefficient de diffusion $D(\rho)$ et la mobilité $\sigma(\rho)$.

En pratique, ces deux coefficients peuvent être difficiles à calculer analytiquement [125]. Néanmoins, ils ont été obtenus pour différents modèles microscopiques (voir par exemple le tableau 6.1), notamment le SEP, où $D(\rho) = D_0$ et $\sigma(\rho) = 2D_0\rho(1-\rho)$, où D_0 est le taux de saut d'une particule (dans le cas de la Fig. 10, $D_0 = 1/2$). D'après la théorie macroscopique des fluctuations (MFT) [104, 124], tout système unidimensionnel diffusif (satisfaisant une loi de Fourier) peut être décrit, dans la limite hydrodynamique (temps long, grandes distances), par ses deux coefficients de transport.

Relations entres systèmes à l'échelle hydrodynamique

En nous appuyant sur la description hydrodynamique, nous mettons en lumière une relation de dualité, ainsi que 3 autres transformations, agissant sur les champs ρ et j (solutions de (22) et (23)), qui, combinées ensemble, génèrent toutes les correspondances possibles entre les systèmes diffusifs unidimensionnels (ce point est montré en annexe H.1).

Pour chacune des transformations données ci-dessous, les nouveaux champs $(\tilde{\rho}, \tilde{j})$ vérifient les équations de l'hydrodynamique fluctuante (22, 23) avec de nouveaux coefficients de transport $\tilde{D}, \tilde{\sigma}$, qui s'exprime en fonction des coefficients originaux D, σ de ρ et j. Les expressions sont résumées dans le tableau 1.

- **Relation de dualité (Du).** Cette relation est directement inspirée de la correspondance SEP-ZRP [117, 118]. Partant du champ de densité macroscopique $\rho(x,t)$, nous pouvons définir des "positions de particules" $x_k(t)$ (où k est un réel) en s'appuyant sur la conservation du nombre de particule à droite d'une particule donnée [102] :

$$\int_0^{x_k(t)} \rho(x,t)\mathrm{d}x - k = \int_0^{\infty} (\rho(x,t) - \rho(x,0))\mathrm{d}x \,. \tag{24}$$

  On définit alors le champs de densité $\tilde{\rho}(k,t)$, qui exprime la "distance moyenne entre la particule k et ses voisines", comme simplement l'inverse de la densité :

$$\tilde{\rho}(k,t) = \frac{1}{\rho(x_k(t),t)} \,, \qquad \tilde{j}(k,t) = -\frac{j(x_k(t),t)}{\rho(x_k(t),t)} \,, \tag{25}$$

  où $\tilde{j}$ est le "courant d'écart entre particules" associé.

- **Translation de la densité (T).** Cette transformation consiste à décaler la densité d'une constante c. Nous définissons les nouveaux champs de densité et de courant :

$$\tilde{\rho}(x,t) = \rho(x,t) + c \,, \qquad \tilde{j}(x,t) = j(x,t) \,. \tag{26}$$

- **Dilatation des champs (Di).** Cette transformation multiplie les deux champs par une constante c. Nous définissons

$$\tilde{\rho}(x,t) = c\,\rho(x,t) \,, \qquad \tilde{j}(x,t) = c\,j(x,t) \,. \tag{27}$$

- **Changement d'échelle du temps (Rt).** La dernière transformation correspond à la multiplication de l'échelle de temps par une constante τ. Nous introduisons

$$\tilde{\rho}(x,t) = \rho(x,\tau t) \,, \qquad \tilde{j}(x,t) = \tau\, j(x,\tau t) \,. \tag{28}$$

A partir de la densité hydrodynamique $\rho(x,t)$, on peut obtenir les observables de courant intégré et de position de traceur qui font l'objet de notre étude.

- Le courant intégré à travers un point x, $Q_t(x)$, qui compte le nombre total de particules qui ont traversé x de gauche à droite (moins le nombre de particules de droite à gauche, et moins le nombre de particules initialement entre 0 et x) jusqu'au temps t,

$$Q_t(x) = \int_0^t j(x,t')\mathrm{d}t' - \int_0^x \rho(x',0)\mathrm{d}x' = \int_x^{\infty} (\rho(x',t) - \rho(x',0))\mathrm{d}x' - \int_0^x \rho(x',0)\mathrm{d}x' \,. \tag{29}$$

- La position $x_k(t)$ de la k-ième particule (un traceur) (24). Par convention, la 0-ième particule a été initialement placée à l'origine $x_0(0) = 0$.

$$\int_0^{x_k(t)} \rho(x,t)\mathrm{d}x - k = \int_0^{\infty} (\rho(x,t) - \rho(x,0))\mathrm{d}x \,. \tag{30}$$

Les transformations introduites ci-dessus agissent sur ces observables de la manière indiquée dans le tableau 1, qui constitue le résultat clé de cette section.

Original	Dualité (Du)	Dilatation (Di)	Translation (T)	Temps (Rt)
$D(\rho)$	$\tilde{D}(\rho) = \frac{1}{\rho^2} D\left(\frac{1}{\rho}\right)$	$\tilde{D}(\rho) = D(\rho/c)$	$\tilde{D}(\rho) = D(\rho - c)$	$\tilde{D}(\rho) = \tau\, D(\rho)$
$\sigma(\rho)$	$\tilde{\sigma}(\rho) = \rho\, \sigma\left(\frac{1}{\rho}\right)$	$\tilde{\sigma}(\rho) = c^2\, \sigma(\rho/c)$	$\tilde{\sigma}(\rho) = \sigma(\rho - c)$	$\tilde{\sigma}(\rho) = \tau\, \sigma(\rho)$
ρ	$\tilde{\rho} = \frac{1}{\rho}$	$\tilde{\rho} = c\, \rho$	$\tilde{\rho} = \rho + c$	$\tilde{\rho} = \rho$
$x_k(t)$	$\tilde{x}_k(t) = -Q_t(k)$	$\tilde{x}_k(t) = x_{\frac{k}{c}}(t)$	$\tilde{x}_k(t) = x_{k - c\tilde{x}_k(t)}(t)$	$\tilde{x}_0(t) = x_0(t\tau)$
$Q_t(x)$	$\tilde{Q}_t(k) = -x_k(t)$	$\tilde{Q}_t(x) = c\, Q_t(x)$	$\tilde{Q}_t(x) = Q_t(x) - cx$	$\tilde{Q}_t(x) = Q_{t\tau}(x)$

Table 1: Transformation des coefficients de transport $D(\rho)$ et $\sigma(\rho)$, de la densité moyenne ρ, et des observables (i) position d'un traceur $x_k(t)$ et (ii) courant intégré à travers x, noté $Q_t(x)$, sous l'action de (Du), (Di), (T) et (Rt).

Extension des résultats sur le SEP à d'autre modèles

En chapitre 9, nous montrons que nos résultats pour le SEP peuvent s'appliquer à l'ensemble des modèles de la Fig. 13. Ici nous nous contentons d'illustrer notre démarche sur l'exemple du ZRP dual du SEP [117, 118] (voir Fig. 13 pour une description sommaire du ZRP au niveau microscopique, qu'il n'est pas nécessaire de connaître ici, puisque dans la description hydrodynamique, nous avons uniquement besoin des coefficients de transport).

Nous considérons ici un ZRP spécifique, qui correspond au cas le plus simple, dans lequel le taux de saut depuis un site est constant, et ne dépend donc ni du site ni du nombre de particules qui s'y trouvent. Au niveau macroscopique, ce système est décrit par les coefficients de transport [86, 119] (notez qu'ils sont invariants par (Du))

$$D(\rho) = \frac{D_0}{(1+\rho)^2}\,, \qquad \sigma(\rho) = \frac{2D_0\rho}{1+\rho}\,. \tag{31}$$

Au niveau hydrodynamique, le SEP peut être obtenu à partir du ZRP en combinant la translation de densité (T) et la relation de dualité (Du) :

$$\begin{aligned} D(\rho) = \frac{D_0}{(1+\rho)^2} &\xrightarrow[c=1]{\text{(T)}} \frac{D_0}{\rho^2} \xrightarrow{\text{(Du)}} D_0 = \tilde{D}(\rho)\,, \\ \sigma(\rho) = \frac{2D_0\rho}{1+\rho} &\xrightarrow[c=1]{\text{(T)}} \frac{2D_0}{\rho}(\rho - 1) \xrightarrow{\text{(Du)}} 2D_0\rho(1-\rho) = \tilde{\sigma}(\rho)\,. \end{aligned} \tag{32}$$

Sous ces transformations, les observables (position du traceur $x_0(t)$ et courant intégré à travers l'origine $Q_t(0)$) ainsi que la densité moyenne du systèmes sont transformés comme indiqué dans le tableau 1, nous permettant de relier les observables du ZRP à une densité donnée aux observables correspondantes du SEP à la densité associée ρ_{SEP} ($= \frac{1}{\rho+1}$ ici).

Ainsi, le n-ième cumulant du courant intégré à travers l'origine dans le ZRP à la densité ρ est égal à celui de la position du traceur dans le SEP à la densité ρ_{SEP} multiplié par $(-1)^n$. Par exemple, de (20), on tire:

$$\left\langle Q_t(0)^2 \right\rangle = 2\rho\sqrt{\frac{D_0 t}{\pi}}\,, \qquad \left\langle Q_t(0)^4 \right\rangle_c = 2\rho\frac{12\rho^2 + \pi(1 + 3(2-\sqrt{2})\rho - 3\rho^2)}{\pi}\sqrt{\frac{D_0 t}{\pi}}\,. \tag{33}$$

Au chapitre 9, nous montrons que cette méthode permet également d'obtenir les profils de densité généralisés, pour d'autres systèmes que le SEP.

Conclusion

En conclusion, nous avons introduit des transformations générales reliant différents systèmes diffusifs unidimensionnels. Nous utilisons ensuite ces transformations ainsi que nos résultats sur le SEP pour étudier d'autres systèmes. Cela souligne la portée de notre équation fermée (13) au-delà du SEP.

De plus, ces transformations décrivent la structure des symétries respectées par les systèmes unidimensionnels. A ce titre, elles apportent des renseignement précieux pour l'étude générale de la diffusion en ligne.

0.2.4 Etude d'un traceur biaisé

Au chapitre 10, nous développons une méthode générale pour décrire, à l'échelle hydrodynamique (en s'appuyant sur l'hydrodynamique fluctuante 0.2.3), les systèmes avec un traceur biaisé. Ici, nous illustrons cette méthode dans le cas particulier du SEP avec un traceur biaisé (Fig. 14). Jusqu'ici, les seuls résultats analytiques à densité arbitraire portent sur les moyennes de la position du traceur et de l'occupation du réseau dans le référentiel du traceur (c'est-à-dire les profils de densité) [119, 126, 127], qui ont récemment été déterminés également sur des systèmes périodiques finis [122, 128]. Depuis les travaux pionniers [119, 126, 127] qui remontent à près de trois décennies, les résultats concernant les cumulants d'ordre supérieur ont été limités au régime de haute densité [129, 130], et à des situations spécifiques [131][2]. A densité arbitraire, même la détermination de la variance de la position du traceur, qui est cruciale pour quantifier ses fluctuations, reste un problème entièrement ouvert.

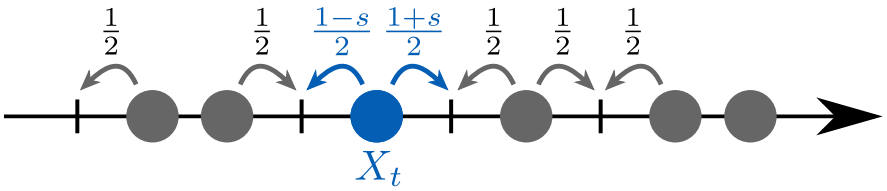

Figure 14: Le processus d'exclusion symétrique (SEP) avec un traceur biaisé (bleu) à la position X_t. La différence avec le cas du traceur non biaisé (Fig. 10) se situe au niveau des taux de saut du traceur (et uniquement du traceur), qui sont ici affectés par le biais s.

Nous considérons le SEP avec traceur biaisé (biais s, Fig. (14)) à la densité moyenne ρ. Nous déterminons la limite de temps long des profils de densité bain-traceur et des cumulants de la position du traceur à l'ordre linéaire en le biais s et à une densité arbitraire. Nous allons également au-delà de la réponse linéaire en déterminant le second cumulant de la position du traceur et le profil de densité correspondant à l'ordre deux en s. Notre résultat majeur est ainsi l'obtention de la première contribution non triviale du biais s à la variance de la position du traceur à une densité arbitraire.

[2]La situation spécifique dans [131] correspond au cas où la force subie par le traceur est compensée par une marche de densité résultant en une position moyenne nulle

Description hyrodynamique avec un traceur biaisé

Afin de décrire le SEP avec traceur biaisé dans la limite de temps long, nous nous appuyons sur l'hydrodynamique fluctuante (section 0.2.3), qui reste valable, excepté au voisinage du traceur (puisque c'est uniquement au niveau du traceur que la dynamique du système est altérée par le biais). Le biais introduit deux principales difficultés techniques : (i) la force subie par le traceur crée une discontinuité du champ de densité $\rho(x,t)$ à l'endroit où se trouve le traceur, car le traceur "pousse" les particules, qui s'accumulent devant lui ; (ii) l'endroit où se trouve cette discontinuité se déplace dans le temps.

Nous contournons la difficulté (ii) en utilisant la relation de dualité (Du) (introduite en 0.2.3), transposant le problème original sur un problème dual tel que la position du traceur du problème original X_t correspond au flux à l'origine $\tilde{Q}_t$ du problème dual (voir les deux premières colonnes du tableau 1, où X_t et $\tilde{Q}_t$ correspondent à $x_0(t)$ et $\tilde{Q}_t(0)$ apparaissant dans le tableau), transformant ainsi la discontinuité mobile en une condition aux limites statique située en zéro. Une approche similaire a été utilisée dans [114, 132]. Les équations hydrodynamiques fluctuantes pour le problème dual sont obtenues en appliquant la dualité (Du) au SEP, dont les coefficients de transport sont $D(\rho) = 1/2$ et $\sigma(\rho) = \rho(1-\rho)$. Les coefficients de transport du système dual sont donc $\tilde{D}(\tilde{\rho}) = 1/(2\tilde{\rho}^2)$ et $\tilde{\sigma}(\tilde{\rho}) = 1 - 1/\tilde{\rho}$. Nous notons $\tilde{\rho}(k,t)$ le champ de densité macroscopique pour le problème dual. Puisque le biais du traceur dans le SEP y est traduit en un biais fixe au point $k = 0$, l'équation suivante est vérifiée pour $k \neq 0$:

$$\partial_t \tilde{\rho} = \partial_k \left(\tilde{D}(\tilde{\rho}) \partial_k \tilde{\rho} + \sqrt{\tilde{\sigma}(\tilde{\rho})}\, \eta(k,t) \right), \tag{34}$$

où η est le bruit blanc gaussien de variance unitaire.

L'élément clé permettant de rendre compte au niveau macroscopique du biais implémenté dans la dynamique microscopique est une condition aux limites vérifiée par le champ de densité $\tilde{\rho}$. Cette relation s'obtient en étudiant les mesures stationnaires du système microscopique biaisé. La méthode est détaillée au chapitre 10. L'idée générale est que la possibilité de définir une densité macroscopique $\tilde{\rho}$ repose sur l'existence d'équilibres locaux au niveau microscopique, c'est-à-dire que localement, autour d'un point k et au temps t, le système microscopique est distribué selon sa mesure stationnaire de densité $\tilde{\rho}(k,t)$ (variant lentement avec k). Dans le cas du système dual du SEP avec traceur biaisé, nous trouvons la condition suivante:

$$(1+s)\left(1 - \frac{1}{\tilde{\rho}(0^+,t)}\right) = (1-s)\left(1 - \frac{1}{\tilde{\rho}(0^-,t)}\right). \tag{35}$$

Les équations (34, 35) peuvent être reformulées, dans la limite de temps long, en un principe de grandes déviations (les détails de la démarche sont donnés au chapitre 10), qui permet d'exprimer les profils généralisés Φ (même définition (10, 11)) du SEP avec traceur biaisé :

$$\Phi\left(v = \frac{y(k)}{\sqrt{2}}\right) = \frac{1}{\tilde{q}(k,1)}, \quad y(k) = \int_0^k \tilde{q}(k',1)\mathrm{d}k', \tag{36}$$

en fonction de la solution $\tilde{q}$ d'équations de diffusion couplées, appelées équations de MFT [102, 107]. La condition implémentant le biais (35) donne lieu dans ce formalisme à des conditions au limites à l'origine, dont nous déterminons la forme générale (voir chapitre 10). A partir de Φ (36), nous déduisons la fonction génératrice des cumulants de la position du traceur à l'aide de la formule (16), qui, remarquablement, reste valable dans le cas d'un traceur biaisé [133].

Ces équations caractérisent donc entièrement la dynamique d'un traceur biaisé dans le SEP. Cependant, leur résolution analytique pour une densité et un biais arbitraires est hors de portée. Nous proposons deux lignes d'investigation de ces équations : (i) une résolution numérique pour des ensembles arbitraires de paramètres ; (ii) un développement perturbatif, qui donne

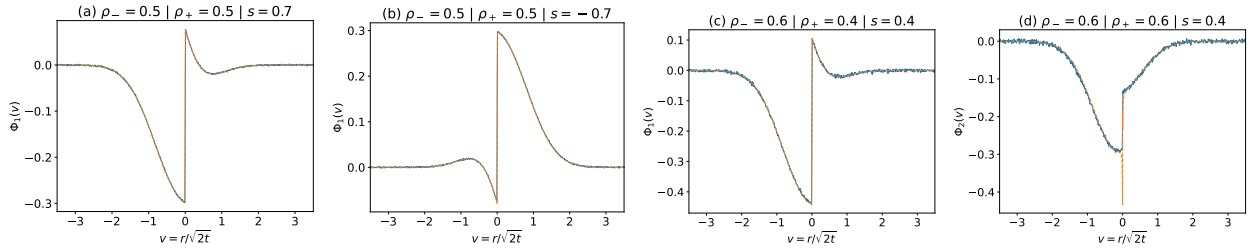

Figure 15: Profils Φ_1 et Φ_2 obtenus à partir de la résolution numérique des équations de MFT (cf. section 0.2.4) (lignes pointillées orange), comparés aux simulations Monte Carlo du SEP avec un traceur biaisé (lignes continues bleues), au temps final $t = 6000$, avec 10^7 simulations pour (a), (b) et (c) et $9 \cdot 10^7$ pour (d).

des résultats explicites, à *densité arbitraire*, valables pour les premiers coefficients $\Phi_n(v)$ définis par le développement de la limite hydrodynamique des profils de densité généralisés (11) : $\Phi(v) = \sum_{n=0}^{\infty} \frac{\lambda^n}{n!} \Phi_n(v)$.

Résolution numérique

Nous montrons en Fig. 15 les profils à l'ordre 1 et 2 en λ obtenus à partir de la résolution numérique des équations de MFT (cf. section 0.2.4), qui sont en parfait accord avec les résultats des simulations Monte Carlo du SEP, pour une large gamme de paramètres. En particulier, nous considérons des biais importants et des densités qui sont loin des limites de basse et haute densité. Notons que l'approche peut être étendue au cas important où la densité initiale de particules forme une marche ($\rho = \rho_+$ devant le traceur et $\rho = \rho_-$ derrière le traceur) [99, 100].

Résolution analytique

Nous remarquons tout d'abord que, pour tout biais, à l'ordre zéro en λ, nous retrouvons les résultats exacts obtenus précédemment dans [119, 126]. Pour les ordres suivants (Φ_n avec $n \geq 1$), nous avons recours à un développement en puissances du biais s. Nous définissons pour chaque ordre n :

$$\Phi_n(v) \underset{s\to 0}{=} \Phi_n^{(0)}(v) + s\Phi_n^{(1)}(v) + s^2\Phi_n^{(2)}(v) + \dots \tag{37}$$

où $\Phi_n^{(0)}$ correspond au cas symétrique connu (section 0.2.2).

Ordre linéaire en s. À l'ordre linéaire en le biais s, on détermine analytiquement $\Phi_1^{(1)}$ et $\Phi_2^{(1)}$ (voir section 10.3.2). Un point essentiel que nous remarquons est que $\Phi_2^{(1)}$ est une fonction *non analytique* de la variable v, présentant une singularité logarithmique à l'origine. Cela semble être une spécificité du cas biaisé, puisque, dans le cas symétrique, tous les Φ_n sont des fonctions analytiques de v (section 0.2.2). Les fonctions $\Phi_1^{(1)}(v)$ et $\Phi_2^{(1)}(v)$ sont représentées sur la Fig. 16 et sont en parfait accord avec la résolution numérique des équations de MFT.

En plus de caractériser entièrement les corrélations entre le bain et le traceur, les profils de densité généralisés Φ_n donnent accès aux cumulants de la position du traceur grâce à la relation (16). Nous obtenons les cumulants normalisés par le temps $\hat{\kappa}_n \equiv \lim_{t\to\infty}[\kappa_n/\sqrt{2t}]$:

$$\hat{\kappa}_1 = s\frac{1-\rho}{\rho\sqrt{\pi}} + \mathcal{O}(s^2), \quad \hat{\kappa}_2 = \frac{1-\rho}{\rho\sqrt{\pi}} + \mathcal{O}(s^2), \tag{38}$$

$$\hat{\kappa}_3 = \frac{s}{\pi^{3/2}\rho^3}\left[(1-\rho)\left(12(1-\rho)^2 - \pi\left(\left(8-3\sqrt{2}\right)\rho^2 - 3\left(4-\sqrt{2}\right)\rho + 3\right)\right)\right] + \mathcal{O}(s^2)\,. \tag{39}$$

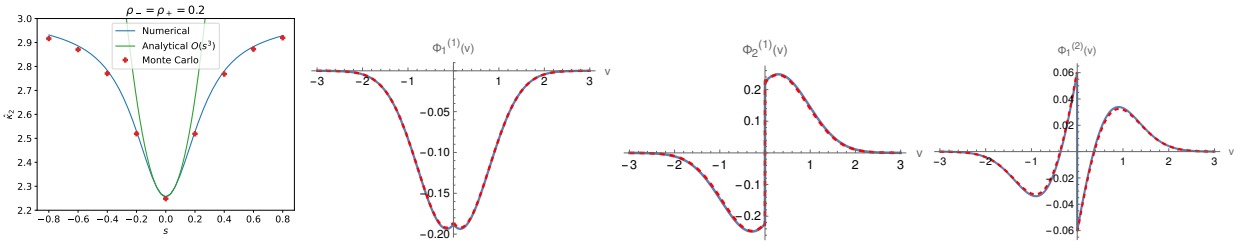

Figure 16: À gauche : cumulant $\hat{\kappa}_2$ en fonction du biais s, obtenu à partir de la résolution numérique des équations de MFT (cf. section 0.2.4) (courbe bleue), comparé au développement à petit biais (40) (courbe verte). Les points rouges sont obtenus à partir de simulations Monte Carlo (15,8 millions de simulations, temps final 100000). Les trois autres graphiques : profils de densité généralisés $\Phi_n^{(m)}(v)$, à la densité $\rho = 0.6$, obtenus à partir de la résolution numérique des équations de MFT (cf. section 0.2.4) (ligne pointillée rouge), comparés aux expressions analytiques, section 0.1.2 (ligne continue bleue).

Au-delà de la réponse linéaire. Nous allons maintenant plus loin, avec des résultats analytiques explicites au-delà de la réponse linéaire. On note que, même si nos expressions précédentes décrivent l'effet du biais s au premier ordre, elles n'apportent pas d'informations non triviales pour les cumulants pairs, puisque la première correction non nulle par rapport au cas sans biais intervient en fait à l'ordre s^2 pour des raisons de symétrie. Nous calculons donc le profil Φ_1 à l'ordre quadratique en s, $\Phi_1^{(2)}$. On retrouve de même le comportement non-analytique. On obtient l'ordre s^2 de $\hat{\kappa}_2 = \hat{\kappa}_2|_{s=0} + s^2\, \Delta\hat{\kappa}_2^{(2)} + \mathcal{O}(s^3)$, avec

$$\boxed{\Delta\hat{\kappa}_2^{(2)} = \frac{(1-\rho)^2(7-5\rho-\pi((\sqrt{2}-3)\rho+2))}{\pi^{3/2}\rho^3}}\,. \tag{40}$$

Ce résultat constitue la première détermination de la dépendance en le biais de la variance d'un traceur biaisé dans le SEP pour une densité arbitraire, un problème qui est resté ouvert pendant plus de 25 ans.

La fonction $\Phi_1^{(2)}(v)$ est représentée en Fig. 16. Nous montrons également la dépendance du second cumulant en fonction du biais pour une valeur donnée de la densité $\rho = 0.2$. Ce cumulant présente une variation importante avec le biais ($\sim 30\%$), soulignant l'importance quantitative de l'étude du problème au-delà de la réponse linéaire (qui prédirait une variation nulle).

Conclusion

En résumé, nous avons développé une description hydrodynamique pour le SEP avec un traceur biaisé. Ceci nous a permis de déterminer les premiers cumulants des corrélations bain-traceur et de la position du traceur à l'ordre linéaire en le biais et à une densité arbitraire – un régime de paramètres non étudié jusqu'à présent. Nous sommes également allés au-delà de la réponse linéaire en déterminant, pour la première fois, la dépendance de la variance à l'ordre 2 en le biais s. Notre approche est générale, nous l'étendons à l'étude d'autres modèles de transport unidimensionnels au chapitre 10.

En ouverture de cette partie, on peut s'interroger s'il serait possible de trouver une équation fermée, dans l'esprit de SEP sans biais (13), qui s'appliquerait à un système général (22, 23) ou bien au SEP en présence d'un biais (section 0.2.4. Le comportement non-analytique que nous avons mis en lumière indique que si une telle équation existe, alors elle devrait nécessairement faire intervenir d'autres objets que des convolutions, ou bien un autre noyau que le noyau gaussien (un noyau déjà non analytique par exemple).

Introduction

The great success at the foundation of statistical physics [134] is the interpretation of all the laws of thermodynamics in term of properties of the Boltzmann probability distribution, which is the universal distribution of the microscopic states of matter. Any isolated system, or subsystem of an isolated system, eventually reaches equilibrium. Equilibrium statistical physics, whose cornerstone is the Boltzmann distribution, successfully describes the behaviour of systems which have got the time to reach equilibrium. For instance, it explains the origin of the different phases of matter, or the way different species coexist together, with the law of mass action. However, many systems of high significance are maintained out-of-equilibrium. This is the case for instance of the atmosphere, which is subject to a constant injection of energy from the sun; waiting for the atmosphere to reach equilibrium would mean waiting for the death of the solar system. Another example lies in living cells, which are a complex machinery, continuously consuming energy (in the form of ATP) to survive. Consequently, the techniques of equilibrium statistical physics are not appropriate to study such systems; non-equilibrium statistical physics aims at developing new tools adequately describing their properties.

In this thesis, we will focus on an important physical mechanism, that has been first identified by Fourier in 1807 in the context of heat conduction and later generalised by Fick (1855) to solute molecules in a solvent: diffusion. Diffusion usually refers to the spontaneous process of displacement and homogenisation of matter in a medium. It is involved in a wide range of phenomena: formation of mixtures of gas or liquids, current of electrons in semi-conductors, permeation of porous media, osmosis through semi-permeable membranes, diffusion-controlled reactions (*i.e.* the reaction's characteristic time is much smaller than the characteristic time between encounters of reactants) etc... The theoretical explanation of diffusion relies on the atomistic view of matter and the kinetic theory of gas: due to thermal energy, any particle in a media is subject to random collisions with other particles in its environment. These collisions are at the origin of the random displacement ΔX_t of the particle over a time t, whose mean square is characterised by the diffusion coefficient D through

$$\left\langle \Delta X_t^2 \right\rangle = 6Dt, \tag{41}$$

according to the classical theory by Einstein [135] (also Langevin [136] and Smoluchowski [137]). This theory is very efficient to describe particles which are free to diffuse in the three dimensions of space and are at equilibrium with their environment (for example, a molecule in a solvent). Indeed, under these assumptions, the increments of the particle's position $\Delta X_{t+\mathrm{d}t} - \Delta X_t$ are stationary and isotropic, resulting in equation (41).

In this thesis, we will be interested in systems where this property of stationary and isotropic increments of position is not verified. This concerns, for example, biological transport, which often takes place in complex, crowded environments [34], with only a fraction of the space being accessible to the particle. Another important feature of biological environments is confinement: biological objects may be subject to strong geometrical constraints. For example, many membranes contain nano-pores (which constitute a confined geometry with

a longitudinal dimension much longer than the transverse ones) through which proteins travel [73, 74]. In such complex environments, more sophisticated descriptions (such as non-Markovian dynamics, effective time-varying potential, explicit description of the solvent molecules etc...) are necessary to properly model the behaviour of a particle.

Moreover, many biological objects evolve in an out-of-equilibrium context. For example, bacteria *E. Coli* [138] are able to propel themselves using flagella, in addition to being subject to the thermal noise from their environment. Furthermore, such objects may evolve under a gradient of temperature, of concentration or of other physical quantity. This non-equilibrium aspect of biological transport is intimately related to the complexity of the environment. We will see for example in part I that the displacement of a biased or active particle impacts significantly the structure of its environment, and reciprocally the environment affects the dynamics of the particle.

The object of this thesis is to investigate how the diffusion and transport properties of a tagged particle, called a *tracer*, are affected in an out-of-equilibrium context and in complex environments. It is mainly the diffusion properties of one particle (the tracer) that will interest us. The collective motion of matter in a complex medium is also an important aspect of diffusion, but it will not be the focus of our study (although we will consider this aspect in part II, in particular with the integrated current in a diffusive system). In order to study the dynamics of a tracer particle, we will often rely on lattice model descriptions.

Lattice models have proven to be very useful tools in physics, from d'Alembert's discrete mass model for vibrating strings to lattice QCD for high-energy particle physics. In statistical mechanics, Ising's model for ferromagnetism is the basic model to study phase transitions and critical phenomena. Lattice models offer a simple framework, where it is relatively easy to perform analytical computations and numerical simulations. At the same time, they remain sufficiently rich to capture the most important physical features (phase transitions, hydrodynamic behaviour...), which can be subsequently generalised to more realistic continuous descriptions. The lattice models used to describe fluids, called lattice gases, have received a lot of attention [139–142], and constitute a particularly relevant framework for the study of diffusion. Notably, they have been employed to compute the diffusion coefficient of a passive tracer in a crowded environment [38–40]. That is why in this thesis, in order to gain insight into the basic physics of tracer diffusion, we will most of the time study lattice models. As an illustration of the generality and relevance of these type of models, in part II, we will show that some results we obtained for a lattice model, the Simple Exclusion Process (SEP), can be generalised to other systems in continuous space. The SEP is a minimal model of interacting particles, where particles evolve on a lattice and interact through hard core interactions (via an exclusion rule). We will see that the theory we developed for the SEP applies to systems with various phenomenology, including for instance the hard-sphere gas in one dimension (also called hard-rod gas), which is a model in continuous space where particles cannot interpenetrate each other.

Since detailed introductions can be found in the first chapter of each part, we here simply sketch the outline of the thesis. In the first part, a microscopic lattice model is proposed to model the transport and diffusion of an active particle (of the "run-and-tumble" type) in the presence of mobile obstacles (chapter 2). Resorting to a mean-field-type approximation, we determine analytically the velocity and diffusion coefficient of the active tracer, and in addition, we characterise the spatial response of the environment to the displacement of the tracer (chapter 3). We then show that this model explains the emergence of specific properties resulting from the interaction between the active particle and its crowded environment, and we provide a heuristic explanation of the underlying physical mechanisms. In chapter 4, we highlight the complex, non-monotonic, dependence of the diffusivity on the parameters

controlling the activity. In chapter 5, we study the response of the active tracer to a drive imposed by an external force field, and we unveil a striking phenomenon, specific to out-of-equilibrium systems: absolute negative mobility, namely the fact that the tracer may have a velocity opposed to the direction of the external force.

In the second part, we deal with the case where the tracer particle (not necessarily active) diffuse in a one-dimensional confined geometry, under crowded conditions. In this case, the particles cannot overtake each other; their displacements are strongly correlated. This leads to anomalous diffusion. Our study first focuses on the Simple Exclusion Process (SEP, chapter 7), which is a paradigmatic lattice model for one-dimensional diffusion. Contrary to the first part, where we resort to an approximation, here we manage to provide an *exact* solution for the whole probability distribution of position of a tracer particle and fully characterise the response of its environment (chapter 8); it is striking that, despite its many-body nature, this problem admits a closed-form analytical solution. In chapter 9, building on a hydrodynamic description of one-dimensional systems, we determine and classify all possible mappings between such systems. This enables us to extend our results for the SEP to other models. Finally, in chapter 10, we develop a procedure to describe, at the hydrodynamic level, one-dimensional systems of particles with a biased tracer. This leads us to new results, beyond linear response, on the well-known problem of the SEP with a driven tracer.

Part I

Run-and-tumble particle in a crowded environment

This part is based on and adapted from the following articles.

- [143] P. Rizkallah, A. Sarracino, O. Bénichou, and P. Illien, *Microscopic Theory for the Diffusion of an Active Particle in a Crowded Environment.* Physical Review Letters 128, 038001 (2022).
- [144] P. Rizkallah, A. Sarracino, O. Bénichou, and P. Illien, *Absolute negative mobility of an active tracer in a crowded environment.* Physical Review Letters 130, 218201 (2023).

Chapter 1

Active particles in complex environments

1.1 What are active particles ?

In 1828, R. Brown [145] observed in a microscope that particles of pollen are subject to erratic, random, discontinuous and isotropic displacements. Almost a century after that, Einstein [135] proposed a theoretical model, based on statistical mechanics: particles which are at equilibrium with their environment perform what is referred to as "Brownian motion" as a result of the random collisions they undergo. Since then, Brownian motion has been used with great success to describe the motion of particles in various contexts: solute molecules, molecules composing a gas, colloids in suspension... Since these particles move only because of the collisions with their neighbours, they are called passive.

Active particles are characterised by the fact that, in addition to being subject to random collisions with particles from their surroundings, they are also able to extract energy from their environment and transform it into mechanical work. As a consequence, these particles are subject to a propulsion force that may vary over time, which maintains them out of equilibrium. Contrary to passive particles, active particles have a non vanishing mean displacement on short time scales (hence display a speed which can be measured, figure 1.1), whereas Brownian particles are characterised by their mean squared displacement. Active particles, also known as micro or nano-swimmers when they have the ability to propel themselves in a (viscous) fluid environment, are observed at different scales (see figure 1.1) in the biological realm and in artificial systems.

Many theoretical models of active particles have been introduced and studied during the past decades. They were proven to be particularly powerful to describe the dynamics of a large number of real systems, ranging from biological objects (molecular motors, bacteria, micro-swimmers, algae...) to artificial self-propelled particles such as active colloids [1, 2]. Among these models, run-and-tumble particles and active Brownian particles have attracted a lot of interest: in both cases, the particles self-propel with a fixed velocity, whose orientation changes randomly either abruptly or continuously, respectively. The dynamics of isolated or non-interacting active particles has been the subject of numerous recent studies [3–11].

1.2 Context and motivations

Beyond single-particle properties, the dynamics of active particles when they interact with each other has attracted a lot of attention, and was shown to display numerous surprising

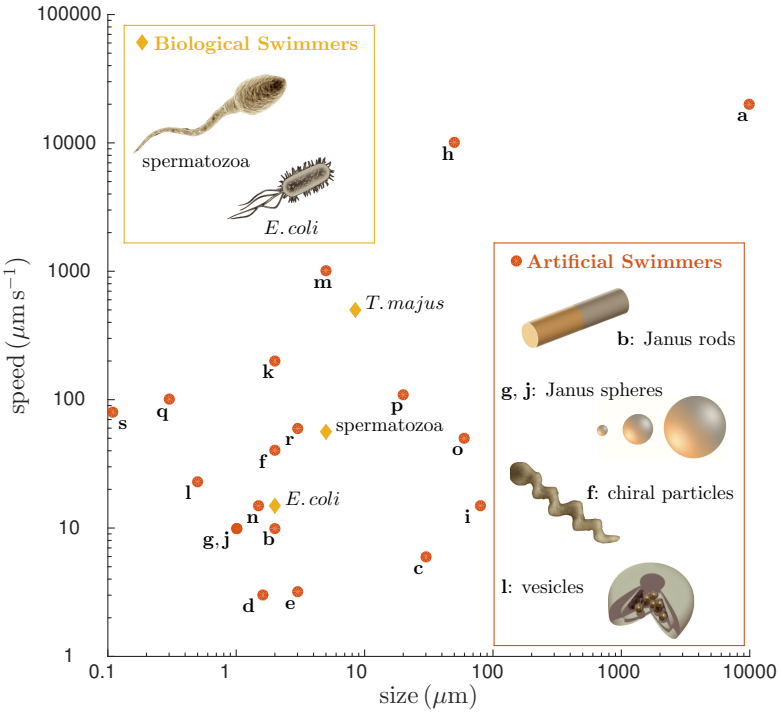

Figure 1.1: Figure taken from [1]. Examples of active particles, by size and maximal speed.

effects, such as large-scale collective motion [12, 13], clustering, or phase separation in the absence of attractive interactions [1, 14].

1.2.1 Tagged particle (tracer) in a crowded environment

Here, we focus on the effects of the interactions between a complex environment and a tagged active particle, called a tracer. This is relevant for example for the transport of biological objects, which often takes place under crowded conditions, such as motor proteins inside a cell [15] or bacteria in porous materials [16]. So far, the case of a frozen disordered environments was studied through experiments (on living [17–21] and synthetic [22] microswimmers) and theoretical approaches (essentially numerical) [4, 23–33].

The case of dynamic disorder, which has received much less attention, is however particularly relevant, since thermal fluctuations generally affect the environment as well as the tracer [34]. Models involving tracers in environments of mobile obstacles have therefore been employed to describe situations of biological interest [35–37]. For the case of a *passive* tracer, the theory by Nakazato and Kitahara [38] (see also [39, 40]) gives an expression of the corresponding diffusion coefficient as a function of the density of crowders, in a continuous-time description on a lattice. Due to the many-body nature of the problem, this expression is approximate but has been shown to be exact in the low and high density regimes, and offers very good quantitative estimates for arbitrary density, as soon as the environment is mobile enough [39, 40]. In continuous space, self-diffusion of passive tracers have also been investigated analytically in the context of hard sphere gases [41].

The case of an *active* tracer in a dynamic environment (figure 1.2) has been the subject of only a few theoretical studies of particles evolving on a lattice (see however [42] for a recent mode-coupling approach in continuous space), which focused mainly on the low-density limit of the problem, with a discrete-time description, with a tracer that never jumps sideways from the direction of propulsion, and with a specific dynamics [43]. Particular interactions between particles (third-neighbor exclusion) have also been studied through numerical simulations

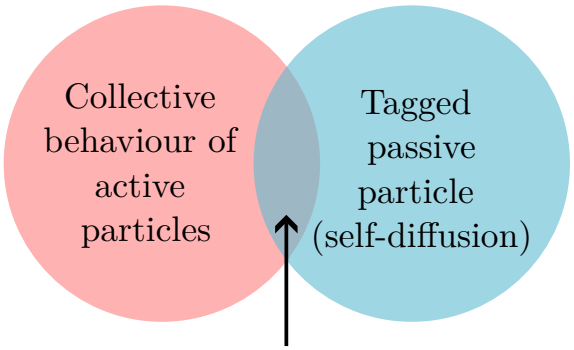

Figure 1.2: There are still few analytical results for the individual behaviour of an active particle in a complex, dynamical, environment.

and mean-field approximations [146]. A generic analytical framework, that would allow the calculation of the diffusivity of an active tracer in a dynamic environment for a wide range of parameters, and in particular for arbitrary density, is missing.

1.2.2 Surprising effects arise when activity meets crowding

Developing such a theory is of particular interest since it would help gaining insight into atypical features that can be observed when an active particle diffuses in a crowded environment. For example, it has been observed experimentally that the diffusion coefficient of active swimmers can be non-monotonous in the activity parameters (such as the tumbling rate), leading to optimised diffusivity, or efficient trapping of the tracer [16, 18, 20, 44–46].

Moreover, predicting the response of a tracer particle submitted to an external driving, and evolving in a complex environment, is a central challenge in statistical physics [47, 48]. The relation between the force applied to the tracer and its velocity can display a number of striking anomalies, in particular when the tracer evolves very far from equilibrium. One of the most intriguing behaviors is the onset of an inverse current, which is opposite to the driving force, and which was evidenced for instance in the very simple setting of a Brownian particle forced in a periodically modulated potential [49]. In the specific context of particle transport, this effect is known as absolute negative mobility (ANM). In figure 1.3, we show an example of an experimental setup where ANM is observed [147].

This intriguing effect actually finds important applications in sorting micrometric particles. Relying on this counter-intuitive response, microfluidic chips that allow efficient separations of particles have been successfully designed [147–149], and recent developments may even allow tunable mass separation [150]. At the theoretical level, understanding ANM is a challenge. Indeed, this effect emerges from the interactions between the tracer and its environment, which needs to be modulated in space and/or in time for ANM to emerge. This has motivated a whole field of research in the past, and different ways to model such an environment have been explored so far: through an effective persistence of the tracer [50], periodic ratchets [49, 51–53], effective tracer-bath interactions [54], coupled thermodynamic forces [55], or steady and periodic velocity fields [56–58]. However, the case of an environment made of mobile crowders (and the possibility for ANM to emerge in such a setting) has not been addressed, in spite of its importance in the modeling of transport in biological context, for instance. This is a particularly difficult theoretical problem, since it requires the treatment of a many-body problem.

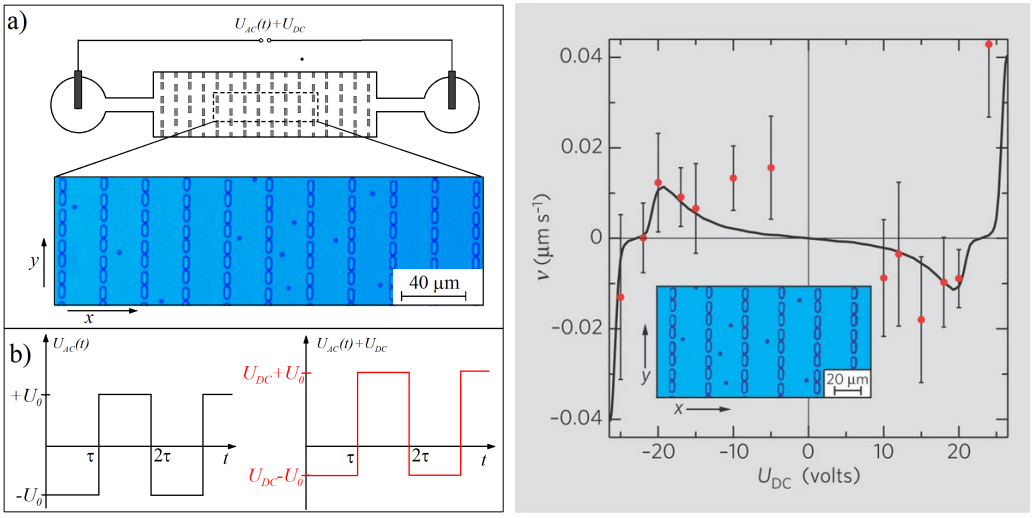

Figure 1.3: Experimental setting from [147] where a) negatively charged beads are placed in a 2D environment with fixed obstacles and subject to b) an alternating voltage $\pm U_0$ to which is added an constant voltage U_{DC}. The plot on the right shows that when the average electric force felt by the beads points towards the right ($U_{\mathrm{DC}} > 0$), their velocity may be in the opposite direction.

1.3 Microscopic theory for an active tracer in a crowded environment

The goal of the first part of this thesis is to provide a microscopic theory describing an active tracer in a dynamical crowded environment on a lattice, at arbitrary density and activity. We consider an active tracer particle submitted to a variable force, which evolves in a dynamical environment of mobile hardcore crowders on a lattice, whose dynamics is accounted for explicitly (chapter 2). Then, we resort to a closure approximation and calculate the velocity and diffusion coefficient of the active tracer in terms of the bath density profiles, and of tracer-bath correlation functions. We also present a qualitative argument valid at low density, which explains the main phenomenons in terms of the relevant characteristic timescales (chapter 3).

On top of providing an explicit description of the environment of the tracer, which allows us to characterize the response of the environment to the displacement of the tracer, this model is analytically tractable, gives accurate results in a wide range of parameters, and elucidates the conditions under which the surprising effects mentioned earlier are observed (chapters 4 and 5). In particular, we show how these effects emerge from the trapping of the tracer particle by the passive crowders.

Chapter 2

Microscopic lattice model

We introduce a lattice model based on the simple exclusion process, which has reached a paradigmatic status in non-equilibrium physics, both in one dimension [60, 151], and in higher dimensions [38, 39, 63, 67, 94, 152–154]. We adapt it in order to provide a lattice representation of the run-and-tumble motion. Then, we define the observables of interest and derive their evolution equations.

Key results.

- Section 2.1: definition of the model and its parameters.
- Definition of the central quantities: density (2.13) and correlation (2.17) profiles. Derivation of the expressions of the velocity (2.15) and diffusion coefficient (2.19).

2.1 Definition of the model

We consider an active tracer subject to an internal active force of random direction and fixed magnitude on a d-dimensional infinite cubic lattice $\mathbb{Z}^d$. Possibly, the tracer can also be subject to an additional external force. In addition, obstacle particles perform symmetric random walks on the lattice. Particles interact together through hardcore repulsion, meaning that there can be only one particle per site. The system evolves in continuous time. A sketch of the model is given in figure 2.1.

2.1.1 Parameters

We denote by $(\boldsymbol{e}_\mu)_{\mu\in[\![1,d]\!]}$ the vectors of the canonical basis of $\mathbb{Z}^d$. We adopt the convention that if $\mu \in [\![-d,-1]\!]$, then $\boldsymbol{e}_\mu = -\boldsymbol{e}_{-\mu}$. When nothing is specified, the sums $\sum_\mu$ are assumed to run over $\mu \in \{\pm 1, \dots, \pm d\}$. We introduce the following parameters:

- The distance between two sites is denoted σ, and the inverse temperature is denoted $\beta = 1/(kT)$.
- The characteristic time between two jumps of the tracer particle is noted τ, and the one for the obstacle particles (also called bath particles) is noted τ^*.
- The intensity of the external force is noted F_E. The external force is always along the horizontal axis: $F_E\boldsymbol{e}_1$.

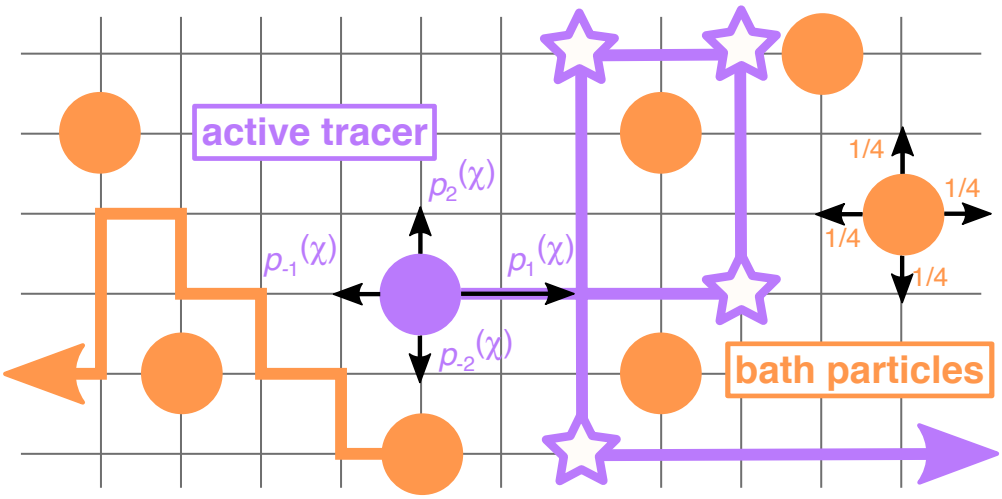

Figure 2.1: An active tracer performs a persistent random walk in a bath of particles performing simple symmetric random walks. Here the external force F_E is zero, so the active tracer jumps preferentially in direction χ (here, the case $\chi = 1$ is shown for illustration). The direction χ changes randomly along time, and the re-orientation events are represented by stars. All the particles interact via hardcore repulsion.

- The intensity of the active force is F_A, and $\chi \in \{\pm 1, \dots, \pm d\}$ is its current direction, also called the "state" of the tracer. The active force in state χ is therefore $F_A \boldsymbol{e}_\chi$.
- The tracer switches randomly from a state χ to any other state $\chi' \neq \chi$ with rate $\dfrac{\alpha}{2d\tau^*}$. The persistence time is therefore $\tau_\alpha = \dfrac{2d\tau^*}{\alpha}$.
- $p_\mu^{(\chi)}$ is the probability for the tracer to jump in direction $\mu \in \{\pm 1, \dots, \pm d\}$ when it is in state χ. Given that the active force is in a random direction χ, we choose (see discussion 2.1.3):
$$p_\mu^{(\chi)} = \frac{\exp\left[\beta\sigma(F_A \boldsymbol{e}_\chi + F_E \boldsymbol{e}_1) \cdot \boldsymbol{e}_\mu / 2\right]}{\sum_\nu \exp\left[\beta\sigma(F_A \boldsymbol{e}_\chi + F_E \boldsymbol{e}_1) \cdot \boldsymbol{e}_\nu / 2\right]}. \tag{2.1}$$
- The density of obstacle particles is denoted $\rho \in [0, 1]$.
- $P_\chi(\boldsymbol{R}, \eta; t)$ is the probability to find the tracer in state χ, at site $\boldsymbol{R}$, with the lattice in configuration η, at time t. The map $(\eta_{\boldsymbol{r}}) \in \{0, 1\}^{(\mathbb{Z})^d}$ associates each point of the lattice with 1 if it is occupied by a bath particle, and 0 otherwise.

We will denote by $\boldsymbol{X}_t$ the random variable describing the position of the tracer particle at time t and $X_t = \boldsymbol{X}_t \cdot \boldsymbol{e}_1$ its projection along the horizontal axis. The random variable $\eta_{\boldsymbol{r}}(t)$ describes the occupation of site $\boldsymbol{r}$ at time t ($\eta_{\boldsymbol{r}}(t) = 1$ if there is an obstacle, 0 otherwise).

According to (2.1), we can absorb β and σ in F_A and F_E (up to a re-scaling of $\boldsymbol{X}_t$ by σ). Thus, we will choose most of the time $\beta = \sigma = 1$.

2.1.2 Master equation

The dynamics of the model is described in the following way. Each bath particle (and the tracer) is equipped with an independent clock ringing at intervals of time drawn from an exponential distribution of rate $1/\tau^*$ ($1/\tau$ for the tracer). Each time its clock rings, a particle chooses a direction μ at random with probability $1/(2d)$ if it is a bath particle, $p_\mu^{(\chi)}$ if

is the tracer (where χ is the current state). If the corresponding neighbouring site in this direction is empty, the particle jumps onto it, otherwise, nothing happens. In addition, the tracer is equipped with a second clock ringing at intervals of time drawn from an exponential distribution of rate $1/\tau_\alpha$. Each time this clock rings, the state χ changes and is redistributed uniformly among the $2d-1$ other directions.

The corresponding master equation obeyed by the joint tracer-bath probability is:

$$2d\tau^*\partial_t P_\chi(\boldsymbol{R},\eta;t) = \mathcal{L}_\chi P_\chi - \alpha P_\chi + \frac{\alpha}{2d-1}\sum_{\chi'\neq\chi} P_{\chi'}, \tag{2.2}$$

where $\mathcal{L}_\chi$ is the evolution operator in state χ, accounting for the displacement of the particles:

$$\begin{aligned}\mathcal{L}_\chi P_\chi =& \sum_{\nu=1}^{d}\sum_{\boldsymbol{r}\neq\boldsymbol{R}-\boldsymbol{e}_\nu,\boldsymbol{R}} [P_\chi(\boldsymbol{R},\eta^{\boldsymbol{r},\nu};t) - P_\chi(\boldsymbol{R},\eta;t)] \\ &+ \frac{2d\tau^*}{\tau}\sum_\mu p_\mu^{(\chi)}[(1-\eta_{\boldsymbol{R}})\,P_\chi(\boldsymbol{R}-\boldsymbol{e}_\mu,\eta;t)\left(1-\eta_{\boldsymbol{R}+\boldsymbol{e}_\mu}\right)P_\chi(\boldsymbol{R},\eta;t)].\end{aligned} \tag{2.3}$$

We denoted by $\eta^{\boldsymbol{r},\nu}$ the configuration obtained from η by switching the occupations of sites $\boldsymbol{r}$ and $\boldsymbol{r}+\boldsymbol{e}_\nu$. The first term describes the displacements of the obstacle particles, and the second term the displacements of the tracer. The other terms in equation (2.2) account for the random reorientation of the active force.

Initially, the tracer is placed on the origin $\mathbf{0}$, and on every other site, there is a particle with probability ρ (for each $\boldsymbol{r}\in\mathbb{Z}^d\setminus\{\mathbf{0}\}$, $\eta_{\boldsymbol{r}}(0)$ follows a Bernoulli law of parameter ρ). The initial state χ (direction of the active force) is initially uniformly distributed among all directions. In terms of probability:

$$P_\chi(\boldsymbol{R},\eta;0) = \frac{\delta_{\boldsymbol{R},\mathbf{0}}}{2d}\prod_{\boldsymbol{r}}\rho^{\eta_{\boldsymbol{r}}}(1-\rho)^{1-\eta_{\boldsymbol{r}}}. \tag{2.4}$$

2.1.3 Detailed balance and activity

Here, we consider the case were there are no obstacles ($\rho=0$) and the active force is in a given direction χ. Before any reorientation of the active force, the tracer therefore evolves in a potential of the form

$$U(\boldsymbol{r}) = -(F_A\boldsymbol{e}_\chi + F_E\boldsymbol{e}_1)\cdot\boldsymbol{r}. \tag{2.5}$$

In this particular case where the direction χ of the active force is fixed, our choice of jump rates $p_\mu^{(\chi)}/\tau$ verifies detailed balance with respect to the Boltzmann measure. If the tracer is at a position $\boldsymbol{X}$, the ratios of rates to go to a neighbouring site and rates to come back verify:

$$\frac{p_\mu^{(\chi)}}{p_{-\mu}^{(\chi)}} = \frac{\exp\left[\beta\sigma(F_A\boldsymbol{e}_\chi + F_E\boldsymbol{e}_1)\cdot\boldsymbol{e}_\mu/2\right]}{\exp\left[\beta\sigma(F_A\boldsymbol{e}_\chi + F_E\boldsymbol{e}_1)\cdot\boldsymbol{e}_{-\mu}/2\right]} \tag{2.6}$$

$$= \exp\left[-\beta(U(\boldsymbol{X}+\sigma\boldsymbol{e}_\mu) - U(\boldsymbol{X}))\right] \tag{2.7}$$

This means that, when the active force is fixed, the tracer performs an equilibrium dynamics. Nevertheless, the overall dynamics of our tracer is fundamentally out-of-equilibrium precisely because the active force changes direction; the potential $U(\boldsymbol{r})$ varies over time.

2.2 Observables and evolution equations

We study our model through observables $\mathcal{O}[\boldsymbol{R}, \eta, \chi]$ which are functions of the configuration of the system $\boldsymbol{R}, \eta, \chi$. An average of an observable at time t is denoted by

$$\langle \mathcal{O}_t \rangle = \sum_{\boldsymbol{R},\eta,\chi} \mathcal{O}[\boldsymbol{R}, \eta, \chi] P_\chi(\boldsymbol{R}, \eta; t). \tag{2.8}$$

The average conditioned to the tracer being in state χ' is denoted by

$$\langle \mathcal{O}_t \rangle_{\chi'} = \frac{\sum_{\boldsymbol{R},\eta,\chi} \mathcal{O}[\boldsymbol{R}, \eta, \chi] \delta_{\chi,\chi'} P_\chi(\boldsymbol{R}, \eta; t)}{\sum_{\boldsymbol{R},\eta,\chi} \delta_{\chi,\chi'} P_\chi(\boldsymbol{R}, \eta; t)} = 2d \sum_{\boldsymbol{R},\eta} \mathcal{O}[\boldsymbol{R}, \eta, \chi] P_{\chi'}(\boldsymbol{R}, \eta; t). \tag{2.9}$$

We have used the fact that all directions of the active force have the same probability: for any $\chi \in \{\pm 1, ..., \pm d\}$, $\sum_{\eta,\boldsymbol{R}} P_\chi(\boldsymbol{R}, \eta; t) = 1/(2d)$.

To characterise the motion of our run-and-tumble tracer, the observables that will interest us are the first moments of its position X_t along the horizontal axis. Also, to quantify the interaction between the tracer and its environment, we will consider the average of the occupations of obstacles in the reference frame of the tracer $(\eta_{\boldsymbol{X}_t+\boldsymbol{r}})_{\boldsymbol{r}}$ and their correlations with the horizontal displacement of the tracer $(\widetilde{g}_{\boldsymbol{r}})_{\boldsymbol{r}}$ where $\widetilde{g}_{\boldsymbol{r}} = \langle \eta_{\boldsymbol{X}_t+\boldsymbol{r}} (X_t - \langle X_t \rangle) \rangle$.

2.2.1 Evolution of the position of the tracer

Velocity of a biased tracer

The mean position of the tracer is defined by

$$\langle X_t \rangle = \sum_{\chi,\boldsymbol{R},\eta} (\boldsymbol{R} \cdot \boldsymbol{e}_1) P_\chi(\boldsymbol{R}, \eta; t). \tag{2.10}$$

If we take the time derivative of $\langle X_t \rangle$ and use the master equation (2.2), we get:

$$\frac{\mathrm{d}\langle X_t \rangle}{\mathrm{d}t} = \frac{1}{2d\tau^*} \sum_{\chi,\boldsymbol{R},\eta} R \left(\mathcal{L}_\chi P_\chi - \alpha P_\chi + \frac{\alpha}{2d-1} \sum_{\chi' \neq \chi} P_{\chi'} \right) (\boldsymbol{R}, \eta; t), \tag{2.11}$$

where we denote $R = (\boldsymbol{R} \cdot \boldsymbol{e}_1)$. Simplifying the right-hand side (see appendix B.1 for details), we find:

$$\begin{aligned} \frac{\mathrm{d}\langle X_t \rangle}{\mathrm{d}t} &= \sum_\chi \sum_{\mu=\pm 1} \frac{1}{\tau} p_\mu^{(\chi)} \mu \sum_{\eta,\boldsymbol{R}} \left(1 - \eta_{\boldsymbol{R}+\boldsymbol{e}_\mu}\right) P_\chi(\boldsymbol{R}, \eta; t) \\ &= \frac{1}{2d\tau} \sum_\chi \sum_{\mu=\pm 1} p_\mu^{(\chi)} \mu \left(1 - k_{\boldsymbol{e}_\mu}^{(\chi)}(t)\right). \end{aligned} \tag{2.12}$$

The mean position of the tracer is therefore controlled by the mean occupations of obstacles in the vicinity of the tracer conditioned on the different possible directions χ of the active force:

$$\boxed{k_{\boldsymbol{e}_\mu}^{(\chi)}(t) = \left\langle \eta_{\boldsymbol{X}_t+\boldsymbol{e}_\mu} \right\rangle_\chi}. \tag{2.13}$$

Note the $1/(2d)$ in the last line of (2.12) which comes from the definition of $\langle \bullet \rangle_\chi$ and $\sum_{\eta,\boldsymbol{R}} P_\chi(\boldsymbol{R}, \eta; t) = 1/(2d)$.

The velocity of the tracer is defined as the long time limit of the derivative of its mean position:

$$V = \lim_{t\to\infty} \frac{\mathrm{d}\langle X_t\rangle}{\mathrm{d}t} \tag{2.14}$$

If we define $k^{(\chi)}_{\boldsymbol{e}_\mu} = \lim_{t\to\infty} k^{(\chi)}_{\boldsymbol{e}_\mu}(t)$, we find from the above

$$\boxed{V = \frac{1}{2d\tau}\sum_\chi \sum_{\mu=\pm1} p^{(\chi)}_\mu \mu \left(1 - k^{(\chi)}_{\boldsymbol{e}_\mu}\right)}. \tag{2.15}$$

The determination of the velocity thus relies on the knowledge of the conditional density profiles $k^{(\chi)}_{\boldsymbol{e}_\mu}$ in the vicinity of the tracer.

Diffusion coefficient of a symmetric tracer

We here consider that the external force is zero: $F_E = 0$. The mean position of the tracer remains at the origin $\langle \boldsymbol{X}_t\rangle = \boldsymbol{0}$, because the active force is in all directions with the same probability. To characterise the dynamics of the tracer, we look at the variance of its position. Its evolution equation is derived (in appendix B.1) from the master equation (2.2):

$$\begin{aligned}\frac{\mathrm{d}}{\mathrm{d}t}\left\langle {X_t}^2\right\rangle =& \frac{1}{2d}\sum_\chi \frac{1}{\tau}\left\{p^{(\chi)}_1\left[1 - k^{(\chi)}_{\boldsymbol{e}_1}(t)\right] + p^{(\chi)}_{-1}\left[1 - k^{(\chi)}_{\boldsymbol{e}_{-1}}(t)\right]\right\} - \frac{2}{\tau}\left[p^{(\chi)}_1 \widetilde{g}_{\boldsymbol{e}_1}(t) - p^{(\chi)}_{-1}\widetilde{g}_{\boldsymbol{e}_{-1}}(t)\right] \\ &+ \frac{1}{2d}\sum_\chi \frac{2\langle X_t\rangle_\chi}{\tau}\left[p^{(\chi)}_1\left(1 - k^{(\chi)}_{\boldsymbol{e}_1}(t)\right) - p^{(\chi)}_{-1}\left(1 - k^{(\chi)}_{\boldsymbol{e}_{-1}}(t)\right)\right].\end{aligned} \tag{2.16}$$

We defined the conditional correlation profiles in the reference frame of the tracer, which appear to control the diffusivity of the tracer:

$$\boxed{\widetilde{g}^{(\chi)}_{\boldsymbol{r}}(t) = \left\langle \left(X_t - \langle X_t\rangle_\chi\right)\eta_{\boldsymbol{X}_t+\boldsymbol{r}}\right\rangle_\chi}. \tag{2.17}$$

The diffusion coefficient of the symmetric tracer is defined as follows:

$$D = \lim_{t\to\infty}\frac{1}{2}\frac{\mathrm{d}\langle X_t^2\rangle}{\mathrm{d}t}. \tag{2.18}$$

It involves $k^{(\chi)}_{\boldsymbol{r}}$, $\widetilde{g}^{(\chi)}_{\boldsymbol{r}} = \lim_{t\to\infty}\widetilde{g}^{(\chi)}_{\boldsymbol{r}}(t)$, but also the mean position of the tracer when the active force is in direction χ, $X_\chi = \lim_{t\to\infty}\langle X_t\rangle_\chi$. Its value is determined in appendix B.1. Finally, the diffusion coefficient of the symmetric ($F_E = 0$) run-and-tumble tracer reads:

$$\boxed{D = \frac{1}{4d\tau}\sum_\chi\sum_{\epsilon=\pm1}\left\{p^{(\chi)}_\epsilon\left[1 - k^{(\chi)}_{\boldsymbol{e}_\epsilon}\right] - 2\epsilon p^{(\chi)}_\epsilon \widetilde{g}^{(\chi)}_\epsilon\right\} + \frac{2d-1}{2d}\frac{\tau^*}{\tau^2\alpha}\sum_\chi\left\{\sum_{\epsilon=\pm1}\epsilon p^{(\chi)}_\epsilon\left[1 - k^{(\chi)}_{\boldsymbol{e}_\epsilon}\right]\right\}^2}. \tag{2.19}$$

In addition to the conditional density profiles $k^{(\chi)}_{\boldsymbol{e}_\mu}$, the determination of the diffusion coefficient also requires the conditional correlation profiles $\widetilde{g}^{(\chi)}_{\boldsymbol{e}_\mu}$ in the vicinity of the tracer.

2.2.2 Density and correlation profiles

We now determine the evolution equations of the quantities $k^{(\chi)}_{\boldsymbol{e}_\mu}(t), \widetilde{g}^{(\chi)}_{\boldsymbol{r}}(t)$ introduced above. The conditional density profiles $k^{(\chi)}_{\boldsymbol{e}_\mu}(t) = \left\langle \eta_{\boldsymbol{X}_t+\boldsymbol{e}_\mu} \right\rangle_\chi$ express how the mean density at a given distance of the tracer differs from the average density ρ because of the activity of the tracer. The correlation profiles $\widetilde{g}^{(\chi)}_{\boldsymbol{r}}(t) = \left\langle (X_t - \langle X_t \rangle_\chi \, \eta_{\boldsymbol{X}_t+\boldsymbol{r}} \right\rangle_\chi$ describe the correlation between the displacement of the tracer and the density at a given distance of it. Therefore these quantities naturally characterise the impact of the tracer on its environment. Reciprocally, the results above show that, in turn, they control the displacement of the tracer. Therefore, these quantities are central in the study of tracer diffusion. From the master equation, in the same way as previously, we derive the evolution equation for the profiles (we recall that $\eta_{\boldsymbol{X}_t} = 0$ by convention):

$$\begin{aligned} 2d\tau^* \partial_t k^{(\chi)}_{\boldsymbol{r}}(t) = &\sum_\mu (\nabla_\mu - \delta_{\boldsymbol{r},\boldsymbol{e}_\mu} \nabla_{-\mu}) k^{(\chi)}_{\boldsymbol{r}}(t) + \frac{2d\tau^*}{\tau} \sum_\mu p^{(\chi)}_\mu \left\langle (1 - \eta_{\boldsymbol{X}_t+\boldsymbol{e}_\mu}) \nabla_\mu \eta_{\boldsymbol{X}_t+\boldsymbol{r}} \right\rangle_\chi \\ &+ \frac{\alpha}{2d-1} \sum_{\chi' \neq \chi} k^{(\chi')}_{\boldsymbol{r}}(t) - \alpha k^{(\chi)}_{\boldsymbol{r}}(t), \end{aligned} \tag{2.20}$$

where ∇_μ is the difference operator ($\nabla_\mu f(\boldsymbol{r}) = f(\boldsymbol{r}+\boldsymbol{e}_\mu) - f(\boldsymbol{r})$) and the one for the correlation profiles:

$$\begin{aligned} 2d\tau^* \partial_t \widetilde{g}^{(\chi)}_{\boldsymbol{r}}(t) = &\sum_\mu (\nabla_\mu - \delta_{\boldsymbol{r},\boldsymbol{e}_\mu} \nabla_{-\mu}) \widetilde{g}^{(\chi)}_{\boldsymbol{r}}(t) + \frac{2d\tau^*}{\tau} \sum_\mu p^{(\chi)}_\mu \left\langle (X_t - \langle X_t \rangle_\chi)(1 - \eta_{\boldsymbol{X}_t+\boldsymbol{e}_\mu}) \nabla_\mu \eta_{\boldsymbol{X}_t+\boldsymbol{r}} \right\rangle_\chi \\ &+ \frac{\alpha}{2d-1} \sum_{\chi' \neq \chi} \left[\widetilde{g}^{(\chi')}_{\boldsymbol{r}}(t) - \widetilde{g}^{(\chi)}_{\boldsymbol{r}}(t) + (\langle X_t \rangle_{\chi'} - \langle X_t \rangle_\chi)(k^{(\chi')}_{\boldsymbol{r}}(t) - k^{(\chi)}_{\boldsymbol{r}}(t)) \right] \\ &+ \sum_{\epsilon=\pm 1} \epsilon p^{(\chi)}_\epsilon \left\langle (1 - \eta_{\boldsymbol{X}_t+\boldsymbol{e}_\epsilon}) \left(\eta_{\boldsymbol{X}_t+\boldsymbol{r}+\boldsymbol{e}_\epsilon} - k^{(\chi)}_{\boldsymbol{r}} \right) \right\rangle_\chi, \end{aligned} \tag{2.21}$$

We adopted the convention $k^{(\chi)}_{\boldsymbol{0}}(t) = \widetilde{g}^{(\chi)}_{\boldsymbol{0}}(t) = 0$. As usual in many-body problems, the evolution of these one site quantities ($k^\chi_{\boldsymbol{r}}(t)$ and $\widetilde{g}^\chi_{\boldsymbol{r}}(t)$) involves two site correlations:

$$\left\langle (1 - \eta_{\boldsymbol{X}_t+\boldsymbol{e}_\mu}) \nabla_\mu \eta_{\boldsymbol{X}_t+\boldsymbol{r}} \right\rangle_\chi \text{ and } \left\langle (X_t - \langle X_t \rangle_\chi)(1 - \eta_{\boldsymbol{X}_t+\boldsymbol{e}_\mu}) \nabla_\mu \eta_{\boldsymbol{X}_t+\boldsymbol{r}} \right\rangle_\chi .$$

The evolution of these quantities involves in turn three site quantities, etc... This leads to an infinite hierarchy of equations, similar to the BBGKY hierarchy in the theory of fluids [155]. In the next chapter, we present how we tackle this problem.

Chapter 3

Approximate closure of the hierarchy

In the previous chapter, we derived the expressions of the velocity (equation (2.15)) and diffusivity (equation (2.19)) of the tracer in terms of the conditional density and correlation profiles. In order to compute these quantities, we need to circumvent the infinite hierarchy generated by the many body interactions in our system. In this chapter, we introduce an approximation, a "decoupling" scheme, which makes it possible to close the hierarchy. We then present an analytical solution to the resulting equations.

Finally, we introduce a qualitative argument which is only valid under some hypothesis on the parameters (low density, strong active force), which is based on a reduction of the problem onto the free diffusion of an active particle. This argument will be useful to understand physically how the interplay between the different timescales of the problem, giving rise to the surprising phenomena that will be discussed in chapters 4 and 5.

Key results.

- Section 3.1: introduction of a decoupling approximation, amenable to an analytical treatment (section 3.2), which will prove to be very accurate in a broad range of parameters (chapters 4 and 5).
- Subsection 3.3.1: we argue that our resolution yields the exact linear dependence on the density ρ in the low and high density limits, which are given explicitly (in subsection 3.3.2 and 3.3.3).
- Section 3.4: qualitative analysis of the different competing timescales in the model.

3.1 Decoupling approximation

A decoupling approximation was introduced previously in the context of a biased tracer (no activity, $F_A = 0$ in the present framework) to compute its velocity [156, 157] and diffusion coefficient [61, 62], on the infinite lattice $\mathbb{Z}^d$ with $d \geq 2$, and also in more general geometries. It showed a great accuracy in a wide range of parameters, and proved to give predictions which coincide with exact approaches in specific limits:

- In low-density, its predictions coincide, at linear order in ρ, with those of another approach in which the diffusion of the tracer is seen as a succession of scattering events due to interactions with independent obstacle [67, 94].
- In high-density, its predictions coincide, at linear order in $1 - \rho$, with another approach

in which the diffusion of the tracer is mediated by the diffusion of vacancies, which explore the lattice independently [129, 158, 159].

In the case of a symmetric passive tracer ($F_A = F_E = 0$), the decoupling approximation gives the same self-diffusion coefficient for the tracer as the theory of Nakazato and Kitahara [38] which relies on projection operator techniques, and reads:

$$D = \frac{1}{2d\tau}(1-\rho)\left[1 - \frac{2\rho\frac{\tau^*}{\tau}\gamma}{2d\left[1+\frac{\tau^*}{\tau}(1-\rho)\right] - \left[1+\frac{\tau^*}{\tau}(1-3\rho)\gamma\right]}\right]. \tag{3.1}$$

It applies to different geometries (we will see that our present treatment is also adaptable to different geometries), where the effect of the chosen geometry is encoded in the constant γ:

$$\gamma = \begin{cases} 4 - \dfrac{8}{\pi} & \text{for a 2D infinite lattice,} \\ \dfrac{4}{(2\pi)L}\displaystyle\sum_{k=0}^{L-1}\int_0^{2\pi} \frac{\sin(q)^2}{2-\cos(q)-\cos\left(\frac{2\pi k}{L}\right)}\mathrm{d}q & \text{for a 2D stripe-like lattice,} \\ \dfrac{6}{(2\pi)^3}\displaystyle\int_0^{2\pi}\int_0^{2\pi}\int_0^{2\pi} \frac{\sin(q_1)^2}{3-\cos(q_1)-\cos(q_2)-\cos(q_3)}\mathrm{d}q_1\mathrm{d}q_2\mathrm{d}q_3 & \text{for a 3D infinite lattice.} \end{cases} \tag{3.2}$$

Now, we extend the decoupling approximation in the presence of activity ($F_A \neq 0$).

3.1.1 Basic principle

The decoupling is a mean-field-type approximation which consists in neglecting the second order fluctuations of occupation numbers $\eta_{\boldsymbol{r}}(t)$ around their conditional average with respect to the direction χ of the active force. More precisely, in a given state χ, we write an occupation number $\eta_{\boldsymbol{r}}(t) = k_{\boldsymbol{r}}^{(\chi)}(t) + \delta\eta_{\boldsymbol{r}}(t)$, then:

$$\begin{aligned} \langle \eta_{\boldsymbol{r}}(t)\eta_{\boldsymbol{e}}(t)\rangle_\chi &= \left\langle (k_{\boldsymbol{r}}^{(\chi)}(t) + \delta\eta_{\boldsymbol{r}}(t))(k_{\boldsymbol{e}}^{(\chi)}(t) + \delta\eta_{\boldsymbol{e}})(t)\right\rangle_\chi \\ &= k_{\boldsymbol{r}}^{(\chi)}(t)k_{\boldsymbol{e}}^{(\chi)}(t) + \langle \delta\eta_{\boldsymbol{r}}(t)\delta\eta_{\boldsymbol{e}}(t)\rangle_\chi \\ &\simeq k_{\boldsymbol{r}}^{(\chi)}(t)k_{\boldsymbol{e}}^{(\chi)}(t). \end{aligned} \tag{3.3}$$

We used the fact that, by definition, $\langle \delta\eta_{\boldsymbol{r}}(t)\rangle_\chi = 0$. For the correlations with the tracer's position, we get:

$$\begin{aligned} \left\langle (X_t - \langle X_t\rangle_\chi)\eta_{\boldsymbol{r}}(t)\eta_{\boldsymbol{e}}(t)\right\rangle_\chi &= \left\langle (X_t - \langle X_t\rangle_\chi)(k_{\boldsymbol{r}}^{(\chi)}(t) + \delta\eta_{\boldsymbol{r}}(t))(k_{\boldsymbol{e}}^{(\chi)}(t) + \delta\eta_{\boldsymbol{e}})(t)\right\rangle_\chi \\ &= \widetilde{g}_{\boldsymbol{r}}^{(\chi)}(t)k_{\boldsymbol{e}}^{(\chi)}(t) + k_{\boldsymbol{r}}^{(\chi)}(t)\widetilde{g}_{\boldsymbol{e}}^{(\chi)}(t) + \left\langle (X_t - \langle X_t\rangle_\chi)\delta\eta_{\boldsymbol{r}}(t)\delta\eta_{\boldsymbol{e}}(t)\right\rangle_\chi \\ &\simeq \widetilde{g}_{\boldsymbol{r}}^{(\chi)}(t)k_{\boldsymbol{e}}^{(\chi)}(t) + k_{\boldsymbol{r}}^{(\chi)}(t)\widetilde{g}_{\boldsymbol{e}}^{(\chi)}(t). \end{aligned} \tag{3.4}$$

We used the fact that $\left\langle (X_t - \langle X_t\rangle_\chi)\delta\eta_{\boldsymbol{r}}(t)\right\rangle_\chi = \left\langle (X_t - \langle X_t\rangle_\chi)\eta_{\boldsymbol{r}}(t)\right\rangle_\chi = \widetilde{g}_{\boldsymbol{r}}^{(\chi)}$.

Since this approximation is based on the assumption that we can neglect some correlations, we expect it to be more accurate as the dimension of the space increases. In this part, we will focus on dimension $d \geq 2$.

3.1.2 New closed equations for the conditional profiles

We then use these assumptions to close equations (2.20, 2.21). This yields nonlinear, but closed, equations. We introduce the quantity $h_{\boldsymbol{r}}^{(\chi)} = k_{\boldsymbol{r}}^{(\chi)} - \rho$ (with the convention $h_{\boldsymbol{0}}^{(\chi)} = 0$),

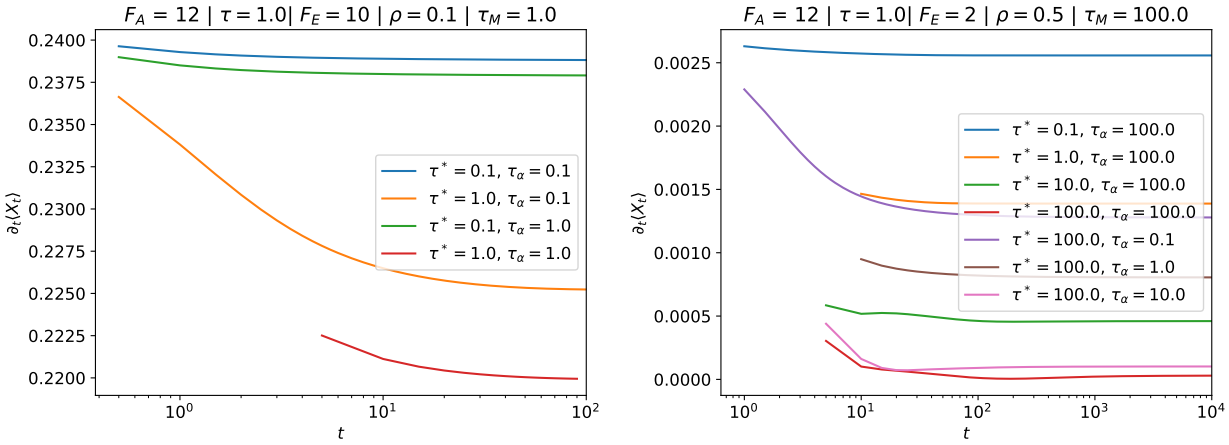

Figure 3.1: Resolution of (3.5) with an Euler method and plot of $\frac{\mathrm{d}\langle X_t \rangle}{\mathrm{d}t}$ using (2.12). We use a time step equal to $\min(\tau, \tau^*, \tau_\alpha)/100$. We observe that the stationary regime is reached for times $t \gtrsim 100\tau_M$ where $\tau_M = \max(\tau, \tau^*, \tau_\alpha)$.

which has the advantage to vanish for large $\boldsymbol{r}$ (this will be useful for the resolution of the equations). The closed equations read (we omit the dependence on t to lighten notations):

$$2d\tau^* \partial_t h_{\boldsymbol{r}}^{(\chi)} = \sum_\mu A_\mu^{(\chi)} (\nabla_\mu + \delta_{\boldsymbol{r},\boldsymbol{e}_\mu}) h_{\boldsymbol{r}}^{(\chi)} + \rho \sum_\mu \delta_{\boldsymbol{r},\boldsymbol{e}_\mu} (A_\mu - A_{-\mu}) - \alpha h_{\boldsymbol{r}}^{(\chi)} + \frac{\alpha}{2d-1} \sum_{\chi' \neq \chi} h_{\boldsymbol{r}}^{(\chi')}, \quad (3.5)$$

where we defined $A_\mu^{(\chi)}(t) = 1 + \frac{2d\tau^*}{\tau} p_\mu^{(\chi)} [1 - \rho - h_{\boldsymbol{e}_\mu}^{(\chi)}(t)]$. For the correlation profiles:

$$\begin{aligned} 2d\tau^* \partial_t \widetilde{g}_{\boldsymbol{r}}^{(\chi)} = {} & \sum_\mu A_\mu^{(\chi)} (\nabla_\mu + \delta_{\boldsymbol{r},\boldsymbol{e}_\mu}) \widetilde{g}_{\boldsymbol{r}}^{(\chi)} + \frac{\alpha}{2d-1} \sum_{\chi' \neq \chi} \left[\widetilde{g}_{\boldsymbol{r}}^{(\chi')} - \widetilde{g}_{\boldsymbol{r}}^{(\chi)} + (\langle X_t \rangle_{\chi'} - \langle X_t \rangle_\chi)(h_{\boldsymbol{r}}^{(\chi')} - h_{\boldsymbol{r}}^{(\chi)}) \right] \\ & + \sum_\mu \delta_{\boldsymbol{r},\boldsymbol{e}_\mu} \left[\left(A_{-\mu}^{(\chi)} - 1 \right) \rho (\boldsymbol{e}_\mu \cdot \boldsymbol{e}_1) - \frac{2d\tau^*}{\tau} \left(p_\mu^{(\chi)} \widetilde{g}_{\boldsymbol{e}_\mu}^{(\chi)} \left(h_{\boldsymbol{e}_\mu}^{(\chi)} + \rho \right) - \rho p_{-\mu}^{(\chi)} \widetilde{g}_{\boldsymbol{e}_{-\mu}}^{(\chi)} \right) \right] \\ & + \frac{2d\tau^*}{\tau} \sum_{\mu = \pm 1} \mu p_\mu^{(\chi)} \nabla_\mu h_{\boldsymbol{r}}^{(\chi)} \left(1 - \rho - h_{\boldsymbol{e}_\mu}^{(\chi)} \right) - \frac{2d\tau^*}{\tau} \sum_\mu p_\mu^{(\chi)} \widetilde{g}_{\boldsymbol{e}_\mu}^{(\chi)} \nabla_\mu h_{\boldsymbol{r}}^{(\chi)}, \end{aligned} \quad (3.6)$$

These equations can first be solved numerically with an Euler method. To perform this numerical resolution, we choose a cut-off length $L \in \mathbb{N}$, and we consider only the $h_{\boldsymbol{r}}^{(\chi)}(t)$ and $\widetilde{g}_{\boldsymbol{r}}^{(\chi)}(t)$ such that $\boldsymbol{r}$ has no component greater than L. We add the boundary condition that $h_{\boldsymbol{r}}^{(\chi)}(t) = \widetilde{g}_{\boldsymbol{r}}^{(\chi)}(t) = 0$ whenever $\boldsymbol{r}$ has a component equal to L. This choice of boundary condition is coherent with the fact that $h_{\boldsymbol{r}}^{(\chi)}(t)$ and $\widetilde{g}_{\boldsymbol{r}}^{(\chi)}(t)$ vanish when $\boldsymbol{r}$ goes to infinity. In figure 3.1, we give an illustration of the evolution of the derivative of the mean position of the tracer according to this resolution.

In the following, we will only be interested in the long time limits of h and g since we study the stationary velocity and diffusion coefficient. To get a quick convergence to this final value in the Euler method, we choose a time step as big as possible while keeping the scheme stable:

$$\mathrm{d}t = \frac{r}{\frac{1}{\tau_\alpha} + \frac{1}{\tau} + \frac{1}{\tau^*}}, \quad (3.7)$$

where $r \lesssim 1$ is chosen empirically. An important future development would be to study the features of the transient regime.

In the next section, we derive closed form implicit expressions for the stationary velocity and diffusion coefficient.

3.2 Analytical resolution

In the stationary regime, the left-hand-side of equations (3.5, 3.6) vanishes. The long time limits of $h_{\boldsymbol{r}}^{(\chi)}$ and $\widetilde{g}_{\boldsymbol{r}}^{(\chi)}$ therefore verify a nonlinear system of equations (with an infinite number of unknowns). We can rephrase this system in terms of a closed nonlinear system of equation for the quantities $h_{\boldsymbol{e}_\mu}^{(\chi)}$ and $\widetilde{g}_{\boldsymbol{e}_\mu}^{(\chi)}$ (profiles and correlations in the vicinity of the tracer, which are the one involved in the expressions (2.15, 2.19) of the velocity and diffusion coefficient, and are in finite number) using Fourier transforms:

$$H^{(\chi)}(\boldsymbol{q}) = \sum_{\boldsymbol{r}} e^{\mathrm{i}\boldsymbol{q}\cdot\boldsymbol{r}} h_{\boldsymbol{r}}^{(\chi)}, \tag{3.8}$$

$$G^{(\chi)}(\boldsymbol{q}) = \sum_{\boldsymbol{r}} e^{\mathrm{i}\boldsymbol{q}\cdot\boldsymbol{r}} \widetilde{g}_{\boldsymbol{r}}^{(\chi)}. \tag{3.9}$$

3.2.1 Equations in Fourier space

These Fourier transforms in the stationary regime ($t \to \infty$) verify the following equations:

$$0 = K^{(\chi)} H^{(\chi)} + K_0^{(\chi)} - \alpha H^{(\chi)} + \frac{\alpha}{2d-1} \sum_{\chi' \neq \chi} H^{(\chi')} \tag{3.10}$$

$$\begin{aligned} 0 =& K^{(\chi)} G^{(\chi)} + J_H^{(\chi)} H^{(\chi)} + J_0^{(\chi)} + \frac{\alpha}{2d-1} \sum_{\chi' \neq \chi} (X_{\chi'} - X_\chi) \left(H^{(\chi')} - H^{(\chi)} \right) \\ & - \alpha G^{(\chi)} + \frac{\alpha}{2d-1} \sum_{\chi' \neq \chi} G^{(\chi')}. \end{aligned} \tag{3.11}$$

If we denote $h_\mu^{(\chi)} = h_{\boldsymbol{e}_\mu}^{(\chi)}$ and $\widetilde{g}_\mu^{(\chi)} = \widetilde{g}_{\boldsymbol{e}_\mu}^{(\chi)}$, the functions involved in the Fourier transform are (we also denote $q_\mu = \boldsymbol{q} \cdot \boldsymbol{e}_\mu$ and $\boldsymbol{e}_{-\mu} = -\boldsymbol{e}_\mu$):

$$K^{(\chi)}(\boldsymbol{q}) = \sum_{\mu} \left(e^{-\mathrm{i}q_\mu} - 1 \right) A_\mu^{(\chi)} \tag{3.12}$$

$$K_0^{(\chi)}(\boldsymbol{q}) = \sum_{\mu} \left(e^{\mathrm{i}q_\mu} - 1 \right) A_\mu^{(\chi)} h_\mu^{(\chi)} + 2\mathrm{i} \sum_{j=1}^{d} \left[A_j^{(\chi)} - A_{-j}^{(\chi)} \right] \sin(q_j) \tag{3.13}$$

$$J_H^{(\chi)}(\boldsymbol{q}) = \sum_{\mu=\pm 1} \mu \left(A_\mu^{(\chi)} - 1 \right) \left(e^{-\mathrm{i}q_\mu} - 1 \right) - \frac{2d\tau^*}{\tau} \sum_{\mu} p_\mu^{(\chi)} \widetilde{g}_\mu^{(\chi)} (e^{-\mathrm{i}q_\mu} - 1) \tag{3.14}$$

$$\begin{aligned} J_0^{(\chi)}(\boldsymbol{q}) =& \sum_{\mu} (e^{\mathrm{i}q_\mu} - 1) \left(A_\mu^{(\chi)} - \frac{2d\tau^*}{\tau} p_\mu^{(\chi)} h_\mu^{(\chi)} \right) \widetilde{g}_\mu^{(\chi)} - \rho \frac{2d\tau^*}{\tau} 2\mathrm{i} \sum_{j=1}^{d} \sin(q_j) (p_j^{(\chi)} \widetilde{g}_j^{(\chi)} - p_{-j}^{(\chi)} \widetilde{g}_{-j}^{(\chi)}) \\ & - \sum_{\mu=\pm 1} \mu (A_\mu^{(\chi)} - 1) \left(\rho e^{-\mathrm{i}q_\mu} + h_\mu^{(\chi)} \right). \end{aligned} \tag{3.15}$$

We introduce the following matrix $\boldsymbol{M}(\boldsymbol{q})$ indexed by $(\chi, \chi') \in \{\pm 1, ..., \pm d\}^2$, that we will use to rephrase the above equations in a matrix form:

$$[\boldsymbol{M}(\boldsymbol{q})]_{\chi,\chi'} = \left(-\alpha + \sum_{\mu} \left(e^{-\mathrm{i}q_\mu} - 1 \right) A_\mu^{(\chi)} \right) \delta_{\chi,\chi'} + \frac{\alpha}{2d-1} (1 - \delta_{\chi,\chi'}). \tag{3.16}$$

3.2.2 Non driven active tracer

We first study the case where $F_E = 0$. Thanks to symmetries, detailed in appendix B.2, we have only 3 independent values for $h_\mu^{(\chi)}$ and 4 for $\widetilde{g}_\mu^{(\chi)}$. Therefore, the following vectors contain all the values of interest:

$$\boldsymbol{h} = \begin{pmatrix} h_1^{(1)} \\ h_1^{(-1)} \\ h_1^{(2)} \\ h_1^{(-2)} \end{pmatrix} \quad \text{and} \quad \boldsymbol{g} = \begin{pmatrix} \widetilde{g}_1^{(1)} \\ \widetilde{g}_{-1}^{(1)} \\ \widetilde{g}_2^{(1)} \\ \widetilde{g}_1^{(2)} \end{pmatrix}. \tag{3.17}$$

Now for simplicity we focus on dimension $d = 2$. Using symmetries, the matrix equation verified by $\boldsymbol{H} = \left(H^{(\chi)}(\boldsymbol{q})\right)_{\chi\in\{\pm1,\pm2\}}$ can be written in the following form (to lighten notations, we do not write dependencies on $\boldsymbol{q}$):

$$\boldsymbol{M}\cdot\boldsymbol{H} + \boldsymbol{\Lambda}\cdot\boldsymbol{h} + \boldsymbol{S} = 0. \tag{3.18}$$

The different matrices are precised in appendix B.3.1. Finally we can perform the inverse Fourier transform and get the following nonlinear system of unknowns $h_\mu^{(\chi)}$ (we recall that the unknowns also appear in the definition of $\boldsymbol{M}$ through $A_\mu^{(\chi)}$):

$$\boxed{\left(\mathbf{1} + \int_{\boldsymbol{q}} e^{-\mathrm{i}q_1}\boldsymbol{M}^{-1}\boldsymbol{\Lambda}\right)\cdot\boldsymbol{h} = -\int_{\boldsymbol{q}} e^{-\mathrm{i}q_1}\boldsymbol{M}^{-1}\boldsymbol{S}}, \tag{3.19}$$

where we use the shorthand notation $\int_{\boldsymbol{q}} = \int_{[-\pi,\pi]^d}\frac{\mathrm{d}\boldsymbol{q}}{(2\pi)^d}$ for the inverse Fourier transform. This nonlinear system can be solved numerically. Similarly, the matricial equation on $\boldsymbol{G} = \left(G^{(\chi)}(\boldsymbol{q})\right)_{\chi\in\{\pm1,\pm2\}}$ can be written with matrices defined in appendix B.3.1:

$$\boldsymbol{M}\cdot\boldsymbol{G} + \boldsymbol{\Lambda}_{\boldsymbol{G}}\cdot\boldsymbol{g} + \boldsymbol{X}\cdot\boldsymbol{H} + \boldsymbol{E} + \boldsymbol{F} = 0. \tag{3.20}$$

We can perform an inverse Fourier transform of this system, to get the final linear system on $\widetilde{g}_\mu^{(\chi)}$:

$$\boxed{(\mathbf{1} + \boldsymbol{L})\cdot\boldsymbol{g} = -\boldsymbol{B}}. \tag{3.21}$$

The matrices involved in equations (3.20, 3.21) are directly obtained from the Fourier transforms (3.10) and (3.11), and are given in appendix B.3.1.

3.2.3 Driven active tracer

In the general case $F_E \neq 0$, we will be interested only in the mean velocity of the tracer. That is why we tackle only the density profiles, which are necessary to compute it. In this case, there are less symmetries, leading to 11 (10 if $d = 2$) independent values for the $h_\mu^{(\chi)}$ (see below). We explain how to get the non-linear system on these values, but we do not give it explicitly under a 10×10 matrix form. Equation (3.10) can be written in the $2d\times2d$ matrix form:

$$\boldsymbol{M}(\boldsymbol{q})\boldsymbol{H}(\boldsymbol{q}) + \mathbf{S}_D(\boldsymbol{q}) = 0, \tag{3.22}$$

with the $2d$ dimensional vector $\mathbf{S}_D$ defined by:

$$\mathbf{S}_D(\boldsymbol{q})_\chi = \sum_\mu \left(e^{\mathrm{i}q_\mu} - 1\right) A_\mu^{(\chi)} h_\mu^{(\chi)} + 2\mathrm{i}\sum_{j=1}^{d}\left[A_j^{(\chi)} - A_{-j}^{(\chi)}\right]\sin(q_j). \tag{3.23}$$

By inverting this matricial equation $\boldsymbol{H}(\boldsymbol{q}) = -\boldsymbol{M}^{-1}(\boldsymbol{q})\mathbf{S}_D(\boldsymbol{q})$, we get an expression of $H^{(\chi)}$ in function of the quantities $\left(h_\mu^{(\chi)}\right)_{(\mu,\chi)\in\{\pm1,\dots,\pm d\}^2}$ and the parameters of the problem. By taking the inverse Fourier transform of $H^{(\chi)}$ at the point $\boldsymbol{e}_\mu$, we get the following equation:

$$h_\mu^{(\chi)} = -\int_{[-\pi,\pi]^d} \frac{\mathrm{d}\boldsymbol{q}}{(2\pi)^d} e^{-i\boldsymbol{q}\cdot\boldsymbol{e}_\mu} [\boldsymbol{M}^{-1}(\boldsymbol{q})\mathbf{S}_D(\boldsymbol{q})]_\chi \tag{3.24}$$

This is a non-linear equation (because $h_\mu^{(\chi)}$ also appears in $A_\mu^{(\chi)}$) involving only the densities in the vicinity of the tracer $\left(h_\mu^{(\chi)}\right)_{(\mu,\chi)\in\{\pm1,\dots,\pm d\}^2}$ and the parameters of the model. At first sight, it may seem that we need to perform $(2d)^2$ Fourier integrals in order to get enough equations to solve for the $h_\mu^{(\chi)}$, but in fact the number of independent unknowns is reduced to 10 for $d = 2$ and 11 for $d \geq 3$ thanks to symmetries, given in appendix B.2.

As a consequence, the following nonlinear system is closed and constitutes the analytical solution of the equations for the mean density in the vicinity of the tracer in the permanent regime, within our approximation scheme:

$$\boxed{h_\mu^{(\chi)} = -\int_{[-\pi,\pi]^d} \frac{\mathrm{d}\boldsymbol{q}}{(2\pi)^d} e^{-i\boldsymbol{q}\cdot\boldsymbol{e}_\mu} [\boldsymbol{M}^{-1}(\boldsymbol{q})\mathbf{S}_D(\boldsymbol{q})]_\chi, \text{ for } (\chi,\mu) \in \{\pm1\}\times\{\pm1,2\}\cup\{2\}\times\{\pm1,\pm2,3\}}. \tag{3.25}$$

Matrices $\boldsymbol{M}$ and $\mathbf{S}_D$ are defined in (3.16, 3.23).

Finally, note that we can get the whole density profiles once the systems are solved and the $h_\mu^{(\chi)}$ are known. We use $\boldsymbol{H}(\boldsymbol{q}) = -\boldsymbol{M}^{-1}(\boldsymbol{q})\mathbf{S}_D(\boldsymbol{q})$ (the right-hand side only depends on $\left(h_\mu^{(\chi)}\right)_{(\mu,\chi)\in\{\pm1,\dots,\pm d\}^2}$ and the parameters of the problem) from where we can compute any $h_{\boldsymbol{r}}^{(\chi)}$ by taking the inverse Fourier transform:

$$h_{\boldsymbol{r}}^{(\chi)} = -\int_{[-\pi,\pi]^d} \frac{\mathrm{d}\boldsymbol{q}}{(2\pi)^d} e^{-i\boldsymbol{q}\cdot\boldsymbol{r}} [\boldsymbol{M}^{-1}(\boldsymbol{q})\mathbf{S}_D(\boldsymbol{q})]_\chi. \tag{3.26}$$

The same method can give $h_{\boldsymbol{r}}^{(\chi)}$ and $\widetilde{g}_{\boldsymbol{r}}^{(\chi)}$ in the symmetric case once $h_\mu^{(\chi)}$ and $\widetilde{g}_\mu^{(\chi)}$ are known.

Comparison with the Euler method

In order to get numerical values for the conditional profiles using the implicit solutions above (3.19, 3.20, 3.25), we must find (numerically) the root of matrix expressions involving matrix inversion, and inverse Fourier transforms. As a consequence, it is not always more efficient than the Euler method presented before (in section 3.1.2), even though the latter method requires the computation of all the $h_{\boldsymbol{r}}^{(\chi)}$ and $\widetilde{g}_{\boldsymbol{r}}^{(\chi)}$ at different time steps (whereas the implicit solutions directly gives the solution for the profiles in the vicinity of the tracer $h_\mu^{(\chi)}$ and $\widetilde{g}_\mu^{(\chi)}$ which control the velocity and diffusivity of the tracer).

The main interest of these implicit solutions (3.19, 3.20, 3.25) is rather the fact that they become exact and explicit to leading order in the density ρ at low density and to leading order in $1-\rho$ in high density, as we will see in the next section (3.3).

3.3 Low and high density regimes

Here, we argue that our decoupling approach is exact at linear order in the density. Then, we show how to solve explicitly the equations (3.19) and (3.20) in the low and high-density regimes.

3.3.1 Closure of the hierarchy at linear order

If we look at the non closed terms in equations (2.20, 2.21) $\left\langle (1-\eta_{\boldsymbol{X}_t+\boldsymbol{e}_\mu})\eta_{\boldsymbol{X}_t+\boldsymbol{r}}\right\rangle_\chi$ and $\left\langle (X_t-\langle X_t\rangle_\chi)(1-\eta_{\boldsymbol{X}_t+\boldsymbol{e}_\mu})\eta_{\boldsymbol{X}_t+\boldsymbol{r}}\right\rangle_\chi$, we expect that in the low and high density limits, these terms become closed at first order. Indeed, let us write at low density:

$$\begin{aligned}\left\langle (1-\eta_{\boldsymbol{X}_t+\boldsymbol{e}_\mu})\eta_{\boldsymbol{X}_t+\boldsymbol{r}}\right\rangle_\chi &= k^{(\chi)}_{\boldsymbol{r}} - \left\langle \eta_{\boldsymbol{X}_t+\boldsymbol{e}_\mu}\eta_{\boldsymbol{X}_t+\boldsymbol{r}}\right\rangle_\chi \\ &= k^{(\chi)}_{\boldsymbol{r}} + O_{\rho\to 0}(\rho^2),\end{aligned} \tag{3.27}$$

and at high density:

$$\begin{aligned}\left\langle (1-\eta_{\boldsymbol{X}_t+\boldsymbol{e}_\mu})\eta_{\boldsymbol{X}_t+\boldsymbol{r}}\right\rangle_\chi &= (1-k^{(\chi)}_{\boldsymbol{e}_\mu}) - \left\langle (1-\eta_{\boldsymbol{X}_t+\boldsymbol{e}_\mu})(1-\eta_{\boldsymbol{X}_t+\boldsymbol{r}}\right\rangle_\chi) \\ &= (1-k^{(\chi)}_{\boldsymbol{e}_\mu}) + O_{\rho\to 1}((1-\rho)^2).\end{aligned} \tag{3.28}$$

We have supposed that the occupation numbers are not too much correlated so that we can suppose that N site correlations are of order ρ^N. As a consequence, equations (2.20, 2.21) become closed and linear to leading order in these regimes. The decoupling approximation gives the same first order expansion as in (3.27, 3.28), so we expect it to be exact at this order.

In the following subsections, we show, in the case of a non driven active tracer ($F_E = 0$) that the analytical solution presented above becomes explicit to leading (linear) order in the density ρ (*i.e.* does not require the resolution of an implicit equation).

3.3.2 Low density limit

In the low-density limit, the density profiles $h^{(\chi)}_\mu$ and the correlation functions $\widetilde{g}^{(\chi)}_\mu$ are expanded as $h^{(\chi)}_\mu =_{\rho\to 0} \rho h^{(\chi)}_{0,\mu} + O(\rho^2)$ and $\widetilde{g}^{(\chi)}_\mu =_{\rho\to 0} \rho \widetilde{g}^{(\chi)}_{0,\mu} + O(\rho^2)$. The diffusion coefficient (2.19) is expanded as $D = D_0 + \rho\mathcal{D}_0 + O(\rho^2)$, with

$$D_0 = \frac{1}{2d\tau} + \frac{2d-1}{d}\frac{\tau^*}{\tau^2\alpha}[p^{(1)}_1 - p^{(1)}_{-1}]^2, \tag{3.29}$$

$$\mathcal{D}_0 = -\frac{1}{4d\tau}\sum_\chi \sum_{\epsilon=\pm 1} p^{(\chi)}_\epsilon (1+h^{(\chi)}_{0,\epsilon}) + 2\epsilon p^{(\chi)}_\epsilon \widetilde{g}^{(\chi)}_{0,\epsilon} - 2\frac{2d-1}{d}\frac{\tau^*}{\tau^2\alpha}[p^{(1)}_1 - p^{(1)}_{-1}]\sum_{\epsilon=\pm 1}\epsilon p^{(1)}_\epsilon (1+h^{(1)}_{0,\epsilon}). \tag{3.30}$$

In this limit, the linear dependence on ρ of the profiles is contained in:

$$\boldsymbol{h}_0 = \begin{pmatrix} h^{(1)}_{0,1} \\ h^{(-1)}_{0,1} \\ h^{(2)}_{0,1} \\ h^{(-2)}_{0,1}\end{pmatrix} \quad \text{and} \quad \boldsymbol{g}_0 = \begin{pmatrix} \widetilde{g}^{(1)}_{0,1} \\ \widetilde{g}^{(1)}_{0,-1} \\ \widetilde{g}^{(1)}_{0,2} \\ \widetilde{g}^{(2)}_{0,1}\end{pmatrix}. \tag{3.31}$$

As for the density profiles, $\boldsymbol{h}_0$ is obtained by solving the following linear system:

$$\boldsymbol{\mathcal{M}}_{\boldsymbol{h},0}\boldsymbol{h}_0 = \boldsymbol{x}_{\boldsymbol{h},0} \tag{3.32}$$

with $\boldsymbol{\mathcal{M}}_{\boldsymbol{h},0} \equiv \mathbf{1} + \int_{\boldsymbol{q}} e^{-\mathrm{i}q_1}\boldsymbol{M_0}^{-1}\boldsymbol{\Lambda_0}$ and $\boldsymbol{x}_{\boldsymbol{h},0} \equiv -\int_{\boldsymbol{q}} e^{-\mathrm{i}q_1}\boldsymbol{M_0}^{-1}\boldsymbol{S_0}$. We denoted $\boldsymbol{M_0}(\boldsymbol{q})$ is the $\rho\to 0$ limit of $\boldsymbol{M}(\boldsymbol{q})$, with off-diagonal coefficients all equal to $\alpha/3$, and diagonal coefficients given by $[\boldsymbol{M_0}(\boldsymbol{q})]_{\chi\chi} = -\alpha + \sum_\mu \left(e^{-\mathrm{i}\boldsymbol{q}\cdot\boldsymbol{e}_\mu} - 1\right) a^{(\chi)}_\mu$, with $a^{(\chi)}_\mu = 1 + 4\frac{\tau^*}{\tau}p^{(\chi)}_\mu$. We recall the shorthand notation $\int_{\boldsymbol{q}} = \int_{[-\pi,\pi]^d}\frac{\mathrm{d}\boldsymbol{q}}{(2\pi)^d}$ for the inverse Fourier transform. The expressions of the

matrix $\boldsymbol{\Lambda_0}$ and of the vector $\boldsymbol{S_0}$ are given in appendix B.3.2. Contrary to the arbitrary-density case, here the matrices are given explicitly in function of the parameters, with no dependence on the unknown $\boldsymbol{h}_0$.

Similarly, we get the linear dependence on ρ of the correlation profiles by solving the linear system $\boldsymbol{\mathcal{M}}_{\widetilde{\boldsymbol{g}},0}\widetilde{\boldsymbol{g}}_0 = \boldsymbol{x}_{\widetilde{\boldsymbol{g}},0}$ with matrices defined in appendix B.3.2.

The predictions of this low-density expansion for the diffusion coefficient are plotted in figure 4.1. Even though this result is explicit (it simply requires the resolution of a linear system), the expressions obtained involve inverse Fourier transforms of complicated rational functions. In the high-density limit, we will be able to even simplify these inverse Fourier transforms by expressing them in terms of generating functions of propagators of isolated random walkers.

3.3.3 High density limit

In the high-density limit $\rho \to 1$, writing the expansions $h_\mu^{(\chi)} =_{\rho\to 1} (1-\rho) h_{1,\mu}^{(\chi)} + O[(1-\rho)^2]$, $\widetilde{g}_\mu^{(\chi)} =_{\rho\to 1} (1-\rho)\widetilde{g}_{1,\mu}^{(\chi)} + O[(1-\rho)^2]$, and using equation (2.19) yields the asymptotic form of the diffusion coefficient $D =_{\rho\to 1} (1-\rho)\mathcal{D}_1 + O[(1-\rho)^2]$ with

$$\mathcal{D}_1 = \frac{1}{4d\tau} \sum_{\chi} \sum_{\epsilon=\pm 1} p_\epsilon^{(\chi)} (1 - h_{1,\epsilon}^{(\chi)}) - 2\epsilon p_\epsilon^{(\chi)} \widetilde{g}_{1,\epsilon}^{(\chi)}. \tag{3.33}$$

We introduce the vectors of the linear dependencies in $(1-\rho)$ for the 3 independent values of $h_\mu^{(\chi)}$ (thanks to symmetries (B.10)) and the 4 of $\widetilde{g}_\mu^{(\chi)}$(B.11):

$$\boldsymbol{h}_1 = \begin{pmatrix} h_{1,1}^{(1)} \\ h_{1,1}^{(-1)} \\ h_{1,1}^{(2)} \end{pmatrix} \quad \text{and} \quad \boldsymbol{g}_1 = \begin{pmatrix} \widetilde{g}_{1,1}^{(1)} \\ \widetilde{g}_{1,-1}^{(1)} \\ \widetilde{g}_{1,2}^{(1)} \\ \widetilde{g}_{1,1}^{(2)} \end{pmatrix}. \tag{3.34}$$

Interestingly, in the high-density regime, the matrix $\boldsymbol{M}(\boldsymbol{q})$ (3.16) simplifies even further than in the low-density regime, and has all off-diagonal coefficients equal to $-\alpha/(2d-1)$, and all diagonal coefficients equal to $-\alpha + 2d[\lambda(\boldsymbol{q}) - 1]$ where $\lambda(\boldsymbol{q}) = \sum_\mu \frac{1}{2d} e^{-\mathrm{i}q_\mu}$ is the structure factor associated to the random walk of an isolated symmetric random walker [160]. The high density limit of the matrix $\boldsymbol{M}(\boldsymbol{q})$ can be explicitly reduced for any value of the dimension d by noticing that its eigenvalues are $2d(\lambda(\boldsymbol{q}) - 1)$, associated to the eigenvector $(1)_{i\in[\![1,2d]\!]}$ and $2d[\lambda(\boldsymbol{q}) - 1 - \alpha/(2d-1)]$ associated to the space orthogonal to $(1)_{i\in[\![1,2d]\!]}$.

Thanks to this diagonalisation of $\boldsymbol{M}(\boldsymbol{q})$ at high density, we can derive from (3.10) and (3.11) linear systems $\boldsymbol{\mathcal{M}}_{\boldsymbol{h},1}\boldsymbol{h}_1 = \boldsymbol{x}_{\boldsymbol{h},1}$ and $\boldsymbol{\mathcal{M}}_{\widetilde{\boldsymbol{g}},1}\widetilde{\boldsymbol{g}}_1 = \boldsymbol{x}_{\widetilde{\boldsymbol{g}},1}$. These systems are derived in a generic manner for any dimension d and the matrices involved are given in appendix B.3.2.

Remarkably, these matrices only depend on $\widehat{Q}(\boldsymbol{r}|\boldsymbol{0};\zeta) = \int_{\boldsymbol{q}} e^{-\mathrm{i}\boldsymbol{q}\cdot\boldsymbol{r}}/[1-\zeta\lambda(\boldsymbol{q})]$, which is the generating function associated with the propagator of an isolated random walk starting from $\boldsymbol{0}$ and arriving at site $\boldsymbol{r}$ on a d-dimensional lattice [160]. The lattice geometry is encoded in this fundamental quantity, and it is remarkable that the solution to a many-body problem is expressed in terms of these single-body quantities in the high-density limit.

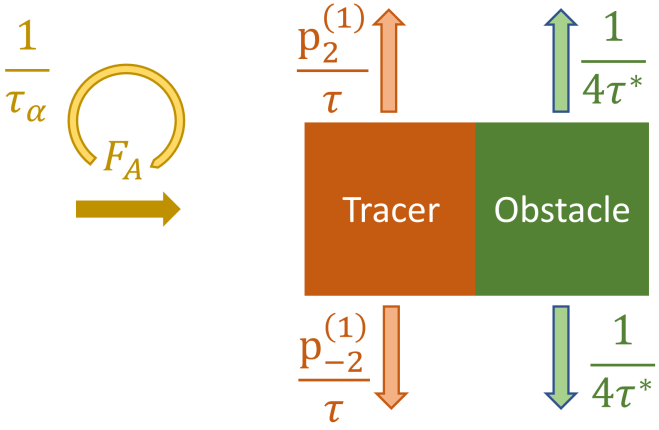

Figure 3.2: Illustration of the three possible ways for the tracer to circumvent an obstacle along the horizontal axis and associated rates in a two dimensional geometry.

Note that the solution of the system $\boldsymbol{\mathcal{M}}_{\boldsymbol{h},1}\boldsymbol{h}_1 = \boldsymbol{x}_{\boldsymbol{h},1}$ is surprisingly simple:

$$h_{\pm 1}^{(1)} \underset{\rho\to 1}{=} \pm(1-\rho)\frac{\frac{2d\tau^*}{\tau}b\left(p_1^{(1)} - p_{-1}^{(1)}\right)}{\frac{2d\tau^*}{\tau}b\left(p_1^{(1)} + p_{-1}^{(1)}\right) + 2d - b} + O[(1-\rho)^2], \tag{3.35}$$

$$h_{\pm 2}^{(1)} \underset{\rho\to 1}{=} O[(1-\rho)^2], \tag{3.36}$$

$$b = \zeta[\widehat{Q}(\mathbf{0}|\mathbf{0};\zeta) - \widehat{Q}(2\boldsymbol{e}_1|\mathbf{0};\zeta)].$$

It is very similar to the formula obtained for a passive driven tracer in [62], where the same expression is obtained, but with $\zeta = 1$ in the definition of b. Here the activity is taken into account in the expression through taking $\zeta < 1$.

Finally, we stress the fact that the solutions in low and high-density limits presented here are explicit, and exact at linear order according to our argument (3.27, 3.28).

3.4 Qualitative argument

In order to better understand physically the mechanisms at work in our model, we present here a qualitative argument which makes it possible to compute directly the stationary velocity and diffusion coefficient of the tracer. The major drawbacks of this argument compared to the decoupling approximation is that (i) it does not give access to the density and correlation profiles and that (ii) it fails in dense regimes ($\rho \gtrsim 0.1$).

At low density, the obstacles can be assumed independent and the probability for the tracer to find an obstacle at a given site is ρ. For a given orientation of the active force χ, the average waiting time of the tracer between two jumps is therefore approximated by $\tau + \rho\tau_p^{(\chi)}$, where $\tau_p^{(\chi)}$ is the mean time that the tracer spends with a bath particles on one of its neighboring sites along the horizontal axis (since we are interested in velocity and diffusivity along this axis), and accounts for the trapping effect caused by the passive crowders.

We can evaluate the mean trapping time by considering that the escape from a trap can be caused by three independent events following exponential laws (see figure 3.2):

- the obstacle moves in a transverse direction (there are $2d-2$ such directions) with characteristic time $\frac{2d\tau^*}{(2d-2)}$,

- the active force changes direction with characteristic time τ_α (this makes sense especially if $F_A \gg 1$ and $\tau_\alpha \gg \tau$),
- the tracer moves in a direction transverse to the horizontal axis with characteristic time $\frac{\tau}{(1-p_1^{(\chi)}-p_{-1}^{(\chi)})}$.

Consequently the mean trapping time follows an exponential law of characteristic time $\tau_p^{(\chi)}$ given by

$$\frac{1}{\tau_p^{(\chi)}} = \frac{(2d-2)}{2d\tau^*} + \frac{1}{\tau_\alpha} + \frac{(1-p_1^{(\chi)}-p_{-1}^{(\chi)})}{\tau}. \tag{3.37}$$

Under these hypotheses, the tracer behaves like an isolated tracer (*i.e.* absence of obstacles) with a characteristic jump time that depends on the state χ and equal to $\tau + \rho\tau_p^{(\chi)}$ and with unchanged jump probabilities $p_\mu^{(\chi)}$. For an isolated tracer ($\rho = k_{\boldsymbol{r}}^{(\chi)} = \widetilde{g}_{\boldsymbol{r}}^{(\chi)} = 0$), formulas for the velocity (2.15) and diffusion coefficient (2.19) become explicit. The qualitative argument then yields:

$$V \simeq \frac{1}{2d}\sum_\chi \frac{p_1^{(\chi)} - p_{-1}^{(\chi)}}{\tau + \rho\tau_p^{(\chi)}}, \tag{3.38}$$

$$D \simeq \frac{1}{4d}\sum_\chi \frac{p_1^{(\chi)} + p_{-1}^{(\chi)}}{\tau + \rho\tau_p^{(\chi)}} + \frac{(2d-1)\tau_\alpha}{4d^2}\sum_\chi \left\{\frac{p_1^{(\chi)} - p_{-1}^{(\chi)}}{\tau + \rho\tau_p^{(\chi)}}\right\}^2 \quad \text{if } F_E = 0 \tag{3.39}$$

We would expect these expressions to only match qualitatively the results obtained by the other methods, but we will see that in fact this argument become very accurate as the density goes to zero.

3.5 Summary

In a nutshell, in order to close the infinite hierarchy associated to our many-body problem, we generalised the decoupling approximation, which was used with success in the case of a passive trace [61, 62, 156, 157]. It relies on a assumption that reduces the infinite hierarchy of equations to a finite set of nonlinear equations. We can express their analytical solution in terms of implicit equations that can be solved numerically at low computational cost. We argue in section 3.3.1 that our resolution becomes in fact exact in the dense and dilute limits, in which cases we computed explicitly the observables of interest.

In addition to the decoupling approximation, which provides a complete solution for the observables of interest (velocity (2.15) and density profiles (2.13), diffusion coefficient (2.19) and correlation profiles (2.17)), we also introduced a qualitative argument. This argument relies on several assumptions, being consequently acceptable only in a small range of parameters of the model. It does not give access to the density and correlation profiles. However, it makes it possible to get explicit analytical formulas for the velocity (3.38) and diffusion coefficient (3.39) of the tracer in function of the different timescales of the problem. This provides insight into the physical mechanisms at work in the interaction between the tracer and the bath.

Finally, we will also evaluate the observables of interest using Monte Carlo simulations. This method is computationally heavy (compared to the decoupling approximation), but needs no assumptions. It is an exact sampling of the master equation (2.2); the simulation method is presented in appendix A.3. We will use it as a standard for the assessment of the accuracy of the other methods.

Chapter 4

Non monotony of the diffusion coefficient

In this chapter we focus on the run-and-tumble tracer in the absence of an external force ($F_E = 0$). We compute its diffusion coefficient using the different methods presented in chapter 3 (namely decoupling approximation 3.1, qualitative argument 3.4 and Monte Carlo simulations) and we compare their results. Then we explore the space of parameters using the decoupling approximation, which has low computational cost, and, as we proceed to show, a good accuracy in a broad range of parameters (note that performing an extensive exploration using Monte Carlo simulations would be too costly computationally).

Importantly, we unveil counter intuitive behaviours of the diffusion coefficient when varying the activity parameters (intensity of the active force F_A and persistence time τ_α). Finally, using our qualitative argument, we interpret these phenomena in terms of the competing timescales of the model.

Key results.

- Section 4.1: check of the good accuracy of the decoupling approximation.
- Section 4.2: analysis and characterisation of the non-monotonic dependence of the diffusion coefficient on the activity parameters.

4.1 Validation of the decoupling approximations

We verify that our analytical predictions using the decoupling approximation (section 3.1) are reliable in a certain range of parameters by comparing them to Monte Carlo simulations.

4.1.1 Diffusion coefficient

Comparing Monte Carlo simulations to the decoupling approach (equations (2.19), (3.5), and (3.6)) on a two-dimensional infinite lattice (figure 4.1 (a) and (b)), the agreement is very good for all densities ρ for different values of the parameters F_A, τ^*, τ_α (we take $\tau = 1$, which fixes the unit of time in our model).

We also extend our resolution to other lattice geometries, provided that they remain translation-invariant. More specifically, we consider the case of a 2D stripe-like lattice (infinite in one direction and finite of width L with periodic boundary conditions in the other direction),

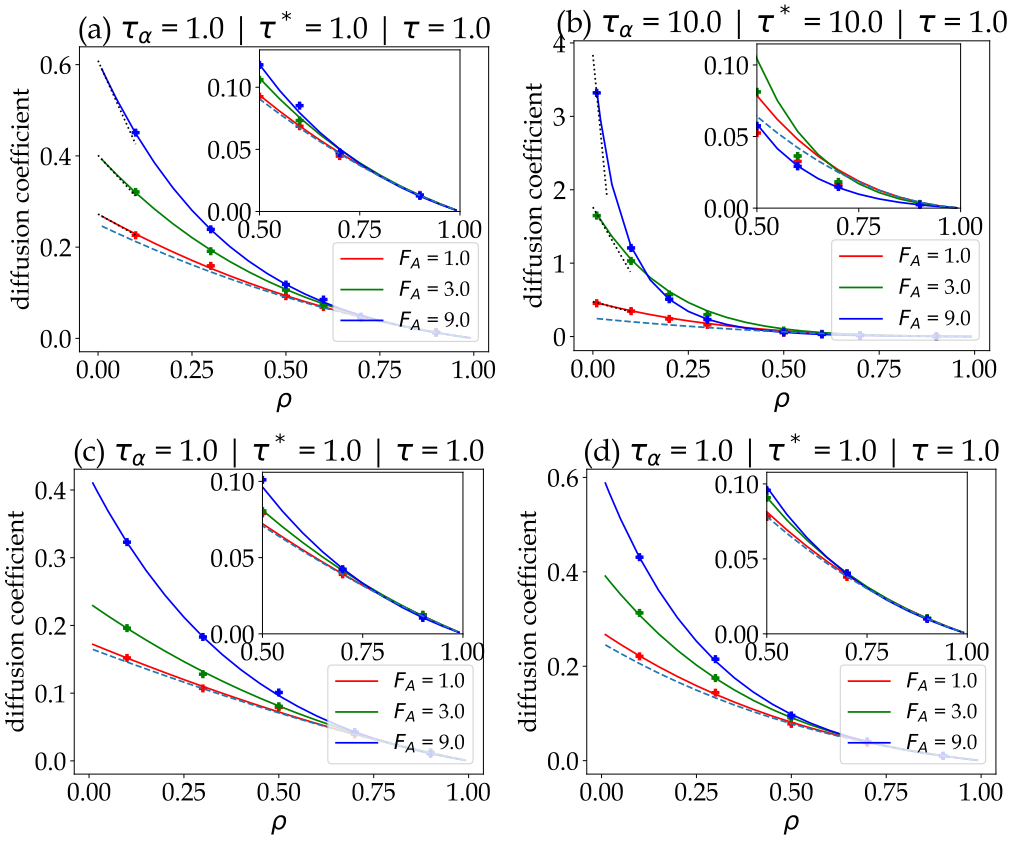

Figure 4.1: Diffusion coefficient of an active tracer on a 2D lattice (a,b), a 3D lattice (c) and a 2D capillary of width $L = 3$ (d), as a function of the density ρ, for several values of the active force F_A and the persistence time τ_α. Symbols: Monte-Carlo simulations. Solid lines: decoupling approach [Eqs. (2.19), (3.5), and (3.6)]. Dotted lines: asymptotic expansion in the low-density regime (see 3.3.2, equations (3.29, 3.30)). Dashed lines: case of a passive tracer [38].

which schematically mimics narrow channels and confined systems, and of a 3D infinite lattice (figure 4.1 (c) and (d)).

Like in the theory for a passive tracer [38], the accuracy of our decoupling approximation improves when the crowding environment is more mobile (typically $\tau^*/\tau \lesssim 10$) or when the dimension of the lattice is higher, which is what we expect from a mean-field type approximation.

4.1.2 Density profiles

Furthermore, we emphasize that our decoupling approach allows us to go beyond the determination of the only diffusion coefficient of the tracer, and gives access to the perturbation induced by the activity of the tracer on its environment, with good accuracy according to figure 4.2. The density profiles $h_{\boldsymbol{r}}^{(\chi)}$ and the correlation profiles $\widetilde{g}_{\boldsymbol{r}}^{(\chi)}$ unveil the interplay between the displacement of the active tracer and the response of its environment, which is major novelty compared to previous descriptions of a run-and-tumble tracer on a lattice [64].

In particular, we observe and quantify an accumulation of bath particles in front of the tracer and a depletion behind it. In figure 4.2, the plot (a) shows that when the active force is in direction +1, we observe an increase of the density of obstacles in this direction and a

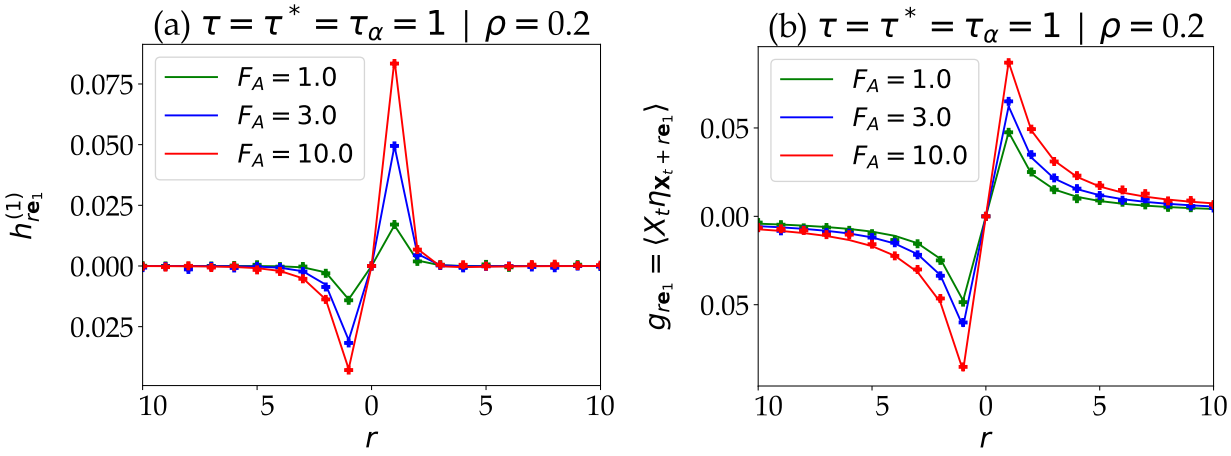

Figure 4.2: (a) Density profiles (conditioned on the activity being in state $\chi = 1$) and (b) tracer-bath correlation functions (averaged on all the states) as a function of the distance to the tracer, on a 2D lattice. The values of the forces F_A respectively correspond to transition probabilities $p_1^{(1)} = 0.39$, 0.67 and 0.99. Symbols: Monte-Carlo simulations. Solid lines: decoupling approach.

decrease in the opposite direction. The plot (b) displays $\widetilde{g}_{\boldsymbol{r}} = \langle X_t \eta_{\boldsymbol{X}_t + \boldsymbol{r}} \rangle = \frac{1}{2d} \sum_\chi \widetilde{g}^\chi_{\boldsymbol{r}} + X_\chi k^{(\chi)}_{\boldsymbol{r}}$. It is the correlation between the displacement of the tracer and the density of obstacles; as expected, it is positive in front of the tracer, and negative behind (the tracer "pushes" the obstacles when it moves). This local anisotropy of the environment of the tracer is a direct consequence of its activity, and increases when the active force is stronger.

4.2 Non monotonic dependence on the activity parameters

Before going into the counter intuitive effects we observe as a result of the interplay between activity and crowding, we recall what is predicted for an active run-and-tumble tracer in the absence of crowding.

4.2.1 Isolated run-and-tumble tracer

As already noticed before, the expression for the diffusion coefficient (2.19) ($k^{(\chi)}_{\boldsymbol{r}} = \widetilde{g}^{(\chi)}_{\boldsymbol{r}} = 0$) becomes explicit in the absence of obstacles.

$$D_{\text{isolated}} = \frac{1}{2d\tau} + \frac{2d-1}{2d^2} \frac{\tau_\alpha}{\tau^2} \left(p_1^{(1)} - p_{-1}^{(1)} \right)^2 \tag{4.1}$$

The first term corresponds to the diffusion coefficient of a passive tracer ($F_A = 0$) on a lattice. The second term expresses the effect of activity on the diffusion coefficient, and is always positive; activity can only lead to an enhanced diffusivity. Moreover, D_{isolated} is an increasing function of the active force F_A and the persistence time $\tau - \alpha$; the more directive the active tracer, the better it diffuses. We will see that this does not hold anymore in a crowded environment.

In a recent work [161], the free diffusion of an active tracer is studied extensively in a similar model.

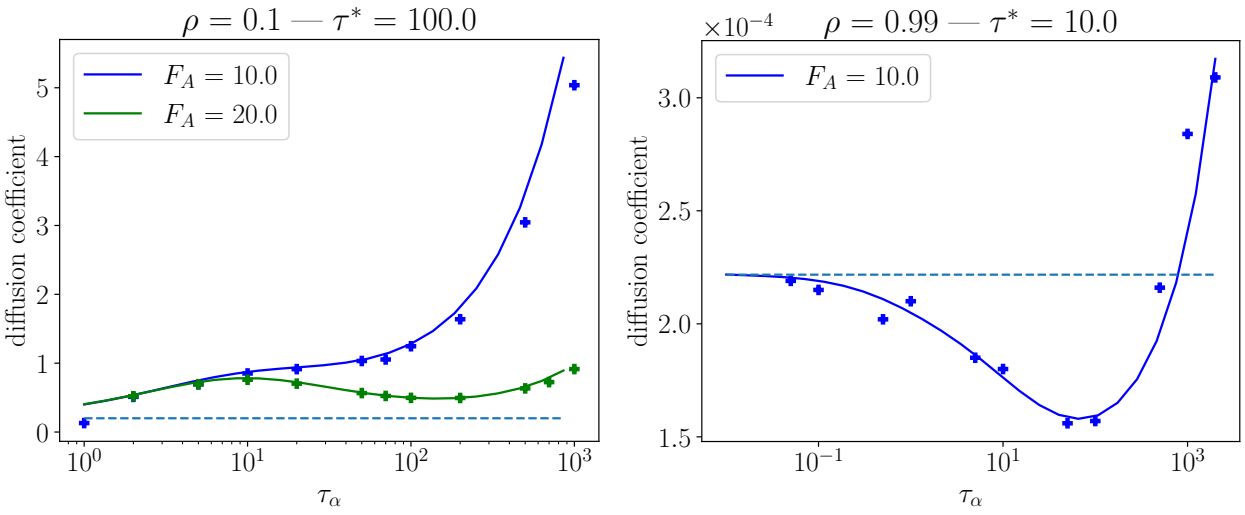

Figure 4.3: Non-monotony of D as a function of the persistence time τ_α, at density $\rho = 0.1$ and $\rho = 0.99$. As usual, $\tau = 1$. Symbols: Monte-Carlo simulations. Solid lines: analytical approach. Dashed lines: passive tracer.

4.2.2 Effect of crowding

Using our decoupling approach, we study the dependence of the diffusion coefficient on the persistence time τ_α in the presence of obstacles ($\rho > 0$). The asymptotic limits $\tau_\alpha \to 0$ and $\tau_\alpha \to \infty$ are known: when the persistence time becomes very small, the diffusion coefficient is finite and equal to that of a passive tracer [38], while in the limit of an infinitely persistent tracer, the diffusion coefficient is expected to diverge as the motion of a tracer becomes ballistic (except in the specific limit of fixed obstacles $\tau^* \to \infty$ and infinite active force $F_A \to \infty$ where the tracer remains forever blocked behind an obstacle and the diffusion coefficient goes to zero).

Our analysis reveals that the diffusion coefficient can exhibit a non monotonic behavior between these two limits, as previously observed in the low-density limit [43]. This effect remains when $\tau^*/\tau < \infty$, but was only studied in the situation of an infinite active force, i.e. in the limit where the tracer cannot step sideways from its persistence direction [43]. Here, we go further and consider the effect of a finite active force, and an arbitrary density. For a given value of ρ and τ^*/τ, the non-monotony of the diffusion coefficient persists as long as the active force is large enough, as shown in Fig. 4.3 (see also 4.2.3). This effect results from the competition between the different timescales governing the diffusion of the tracer (discussed in the next section 4.2.3). In some configurations (such as $\rho = 0.99$ in figure 4.3), the diffusion coefficient of the active tracer can even become smaller that the one of the passive tracer.

We build a phase diagram (figure 4.4 (a)) which represents the critical value of τ^*/τ above which D becomes a non-monotonic function of τ_α (for given density ρ and force F_A). Note that such a diagram (built by logarithmic dichotomy) would need much more computing power if built using Monte Carlo simulations.

We also observe a non-monotony of the diffusion coefficient with the active force F_A (figure 4.4 (b)), which is reminiscent of previous observations in the case of an infinitely persistent tracer [62]. As we can see in this plot (figure 4.4 (b)), the decoupling approximation is in quantitative agreement with Monte Carlo simulations, whereas the qualitative argument only qualitatively reproduces the real features of the model. Nevertheless, as we proceed to show in the next section, the qualitative argument is a valuable tool to understand the

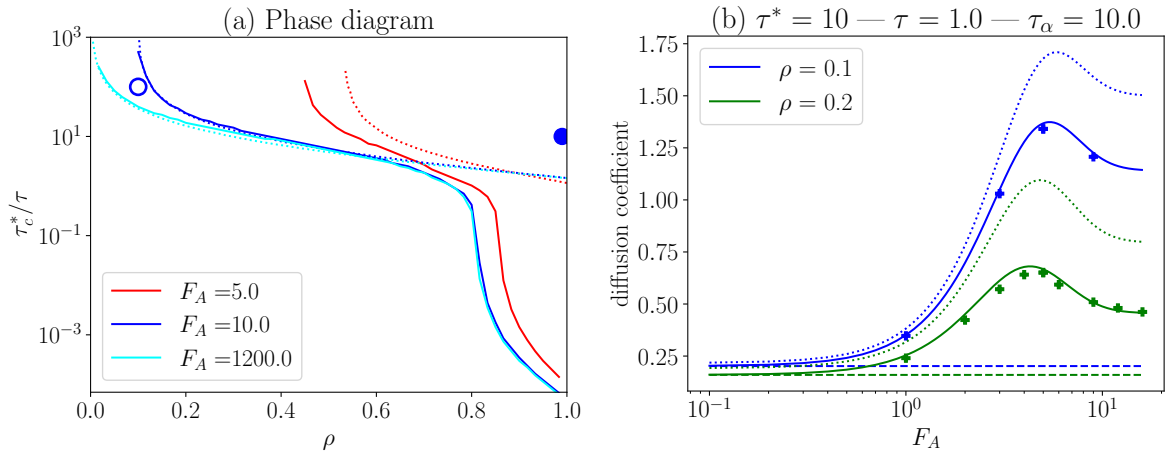

Figure 4.4: **Left (a).** Region of the non-monotony of the diffusion coefficient with τ_α in the plane $(\rho,\tau^*/\tau)$: above the curves, D is a non-monotonic function of τ_α. At low density and strong active force, the qualitative argument (equation (3.39)) (dotted lines) and the decoupling approximation (straight lines) coincide. Symbols: Monte Carlo simulations; filled circle means non monotony is observed at this point, an empty one means it is not. **Right (b).** Non-monotony of the diffusion coefficient as a function of the magnitude of the active force F_A. The symbols represent the results from Monte Carlo simulations, the solid lines are the results from our decoupling approach. Dotted lines: qualitative argument (3.39), less accurate as the density increases. Dashed lines: passive tracer.

physical mechanism at the origin of the non-monotonies we observed.

4.2.3 Qualitative analysis

The qualitative argument's formula for the diffusion coefficient (3.39) can give us meaningful insights into the behaviour of the tracer as a function of the parameters for any lattice dimension $d \geq 2$. For instance, we can use the formulas derived below to design, in first approach, an active tracer which will be trapped in certain media and diffuse quickly in others, and therefore target a specific medium for example. This analysis comes as a complement to the decoupling approximation approach, which outperforms it since (i) it describe the response of the environment (figure 4.2) (ii) it remains accurate in denser regimes (see figures 4.4 and 4.1).

Accuracy at very low density

In figure 4.5, we compare the diffusion coefficient computed using the decoupling approximation (equations (2.19), (3.5), and (3.6)) and the qualitative argument (equation (3.39)) with near infinite active force ($F_A = 10^4$), at low density and for low ($\tau^* = 10^6$) and high ($\tau^* = 0.1$) mobility of obstacles. When the density goes to zero, the qualitative argument turns out to be quantitatively equivalent to the decoupling approximation, even for arbitrarily slow obstacles.

Minimum and maximum of diffusion

We consider a fully directive run-and-tumble tracer ($F_A = \infty$) in the case where the tracer can remain trapped for a long time $\rho\tau_p \gg \tau$. For this regime to exist, we need a choice of parameters such that $\rho\tau^* \gg \tau$, namely slow obstacles. Precise formulas (with dependence on

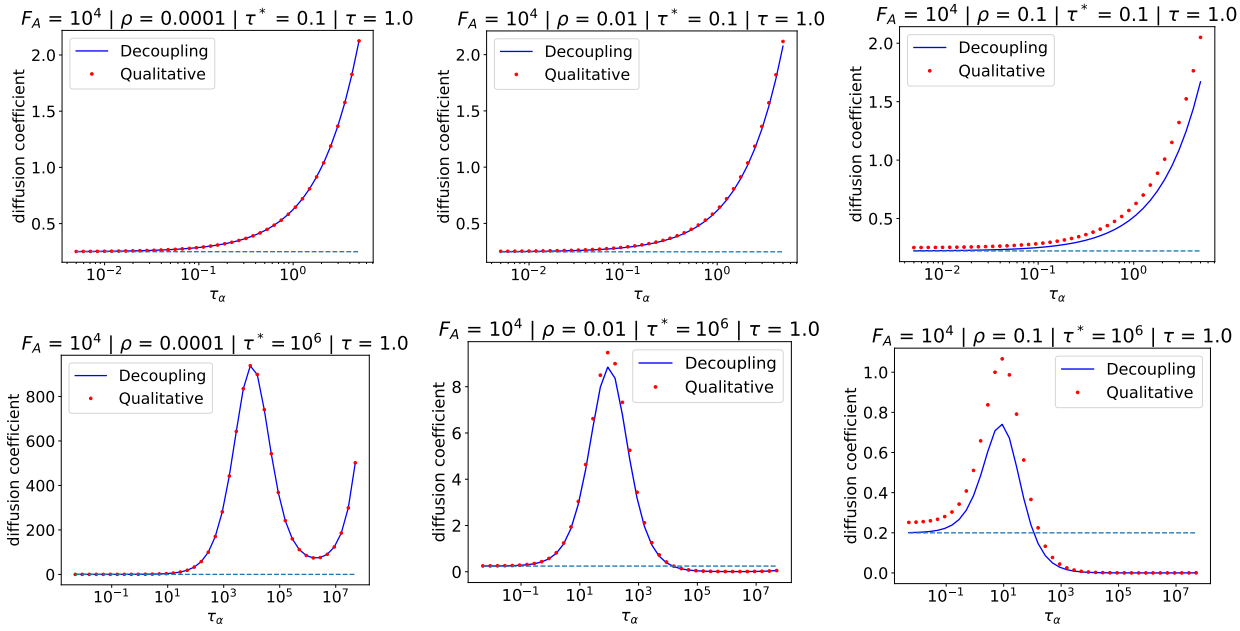

Figure 4.5: Comparison of the diffusion coefficients computed by the two methods: decoupling approximation 3.1 and qualitative argument [equation (3.39)] in the case of a very large active force. Remarkably, the agreement is almost perfect at very low density, whatever the mobility of obstacle (even for large τ^*). Dashed lines: case of a passive tracer [38] ($\tau_\alpha \to 0$ or $F_A = 0$).

the dimension d) and more details on the methods and hypothesis can be found in appendix C, here we summarise the results.

In this regime, the diffusion coefficient successively goes through a maximum $D_{\max}$ and minimum $D_{\min}$ before diverging (illustration in figure 4.5 at $\tau^* = 10^6$) as τ_α increases (except for fixed obstacles and infinite active force, $\tau^*, F_A = +\infty$, in which case the diffusion coefficient goes to zero). The scalings of $D_{\max}$, $D_{\min}$ and the persistence time for which they are reached τ_α^M and τ_α^m are given in table 4.1.

	Condition	Persistence time	Diffusion coefficient
Minimum of diffusion	$\rho\tau^* \gg \tau$	$\tau_\alpha^m \propto \tau^*$	$D_{\min} \propto \dfrac{1}{\rho^2\tau^*}$
Maximum of diffusion	$\rho\tau^* \gg \tau$	$\tau_\alpha^M \propto \dfrac{\tau}{\rho}$	$D_{\max} \propto \dfrac{1}{\rho\tau}$

Table 4.1: Scalings of the extreme diffusion coefficients as a function of the persistence time τ_α.

When the persistence time is close to the time between two jumps of obstacles, tumbling is useless in escaping obstacles (the obstacle would have moved anyway), so that it simply prevents the tracer from going forward and exploring new territory. We see that this can lead to a huge drop of diffusivity in certain media. On the contrary when the persistence time is smartly adjusted so that it is close to the mean duration the tracer will spend between two obstacles $\frac{\tau}{\rho}$, the diffusivity is optimised. By tuning the parameters, one could design an active tracer which would diffuse quickly in most environments until it reaches a target environment where its diffusivity will drop drastically (it will be trapped there).

Analytic criteria for existence of non monotony

In the case of an infinite active force $F_A \to \infty$, we find the following analytic expression for the critical timescale of displacement of obstacles τ_c^* (with $\tau = 1$) above which there exists non monotony of the diffusion coefficient as a function of the persistence time τ_α:

$$\boxed{\tau_c^* \simeq \left(8 - \frac{8}{d}\right)\frac{1}{\rho}}. \tag{4.2}$$

Non monotony exists for all lattice dimensions (we always consider $d \geq 2$), but requires slower obstacles as the dimension increases (more escape options in higher dimension).

In the case of a finite active force $F_A \gg 1$, there is a critical surface defined by an equation given in appendix C. The most interesting consequence is that under some critical density ρ_C, there cannot be non monotony anymore, whatever the value of τ^*:

$$\boxed{\rho_C \simeq \frac{16(d-1)}{2d - 2 + e^{F_A/2}}}. \tag{4.3}$$

It means that if the obstacle are too sparse, the small deviations of the tracer from the direction of the active force, which are allowed by $F_A < +\infty$, will always be enough for the tracer not to be trapped.

At first sight, the formulas (4.2,4.3) should hold only qualitatively since they are obtained from the qualitative argument 3.4, but, as we can see in figure 4.4 (a), they closely match the predictions of the decoupling approximation in the low-density limit. Since we believe the decoupling approximation to be exact in this limit (as argued in section 3.3.1), equations (4.2,4.3) can be regarded as very accurate in this limit.

Conclusion

In conclusion, we checked that the decoupling approximation is accurate in wide range of parameters to compute the profiles and diffusion coefficient of a symmetric run-and-tumble tracer. Relying on this approximation, we explored extensively the space of parameters of the model, and we characterised the conditions of existence of a counter-intuitive phenomenon: the diffusion coefficient may decrease when the activity of the tracer increases. This remarkable feature is the result of the complex interplay between activity and crowding, which our approach allows to characterise through the density and correlation profiles. The qualitative argument (part 3.4) displays a remarkable accuracy in low density, and makes it possible to determine analytically, in the dilute limit, how the diffusion coefficient behaves as a function of the other parameters of the model.

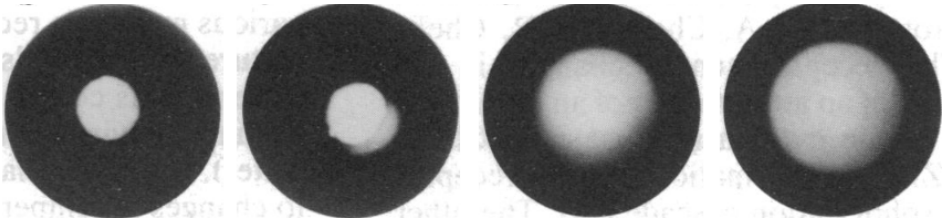

Figure 4.6: Left: observations of swarms of bacteria E. Coli (performing run-and-tumble motion) in semisolid agar, from [44]. The size of the swarm is related to the diffusion coefficient of the bacteria.

Finally, our theoretical model provides a minimal (very schematic) description of experimental settings such as the one in [44]. In this experiments, the authors put bacteria E. Coli (which would be represented by our active tracer in our model), performing a run-and-tumble motion, in an agar matrix. Agar is a porous media, it would correspond to fixed obstacles ($\tau^* \to \infty$) in our model. Then, the authors observe how a swarm of bacteria diffuses in the media (figure 4.6). Using chemicals and genetic engineering, they are able to tune the tumbling rate of the bacteria. In particular, they observe, like in our model, that decreasing the tumble frequency of bacteria (increasing τ_α in our model) may lead to smaller swarms (domain where the diffusion coefficient D is a decreasing function of τ_α in our model).

Since this first experimental observation of an optimised diffusivity for active particles, other experiments in different setups have focused on better understanding these features, including recent studies [16, 18, 20, 45, 46]. Our model may constitute a useful theoretical basis to understand and explain the feature of the diffusivity of active particles in various contexts.

Chapter 5

Absolute negative mobility

In the previous chapter, we focused on the case where the tracer is subject only to its internal active force (and thermal fluctuations). However, in many situations (figure 1.1), such as a swimmer in a flowing solvent, a massive active particle for which gravity cannot be neglected, or a charge particle subject to electromagnetic forces, the tracer is also subject to an external influence, which can modeled by an external force $F_E \neq 0$ in our framework.

In this case, the average velocity of the run-and-tumble tracer does not vanish anymore. We compute this velocity within our approximation scheme. One would expect, intuitively, that the velocity of the tracer should be in the same direction as the external force. Surprisingly, we predict that for some sets of parameters, the velocity may point in the opposite direction. This phenomenon, called absolute negative mobility (ANM), is only possible far for equilibrium, because it is in contradiction with linear response theory.

Key results.

- Overall, we observe that the decoupling approximation (section 3.1) remains accurate in the presence of an external drive ($F_E \neq 0$).
- Section 5.2: theoretical prediction of ANM in the context of an active particle in a complex environment made of mobile crowders described explicitly (the emergence of ANM in this situation constitutes an novelty compared to previous theoretical approaches reviewed in the introduction 1.2.2).

5.1 Relation with negative differential mobility

We begin by presenting a simple argument to explain the emergence of ANM in our model, and its relation to negative differential mobility (NDM). The latter refers to the situation where a particle submitted to a constant external force F_E may display a velocity which decreases with the intensity of the force while remaining positive [61, 63, 66–72].

For illustration, we consider the simple situation where the tracer is submitted to an active force F_A that may only point in directions $\pm\boldsymbol{e}_1$. In the limit where the persistence time is greater than other timescales, the average velocity of the tracer can therefore be estimated as the average of the velocities conditioned on these two states $V \simeq \frac{1}{2}[V_0(F_E+F_A)+V_0(F_E-F_A)]$, where $V_0(F)$ is the stationary velocity of a passive particle (i.e. with $F_A = 0$ and/or $\tau_\alpha = 0$) submitted to an external force F. We assume that $F_E > 0$, and we first consider the case where the tracer does not display negative differential mobility. Its velocity is then a monotonic function of the force undergone by the tracer (see Fig. 5.1 for a sketchy representation of

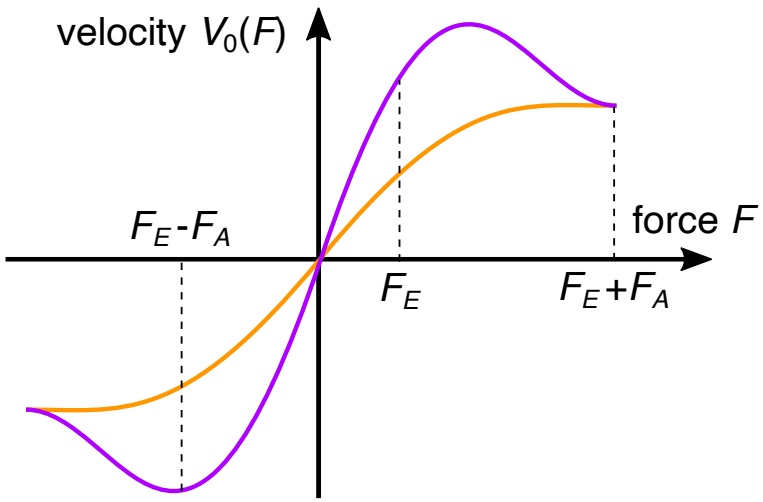

Figure 5.1: Typical force-velocity curve of a passive tracer with and without negative differential mobility (in purple and orange, respectively).

the force-velocity curves). In this situation, it is clear that V will be of the sign of F_E, and no absolute negative mobility can be observed. However, when the tracer displays negative differential mobility, one may observe the situation where $|V_0(F_E - F_A)| > |V_0(F_E + F_A)|$, therefore resulting in a situation where average velocity V is negative although $F_E > 0$.

These simple considerations clarify the relationship between ANM and NDM. To summarize, the velocity of the active tracer can be understood as an average over the velocities conditioned over the different possible orientations of the active force. If this conditional velocity is a non-monotonic function of the force (NDM), the average velocity can become negative (ANM) (necessary but not sufficient condition).

5.2 Negative mobility for a driven run-and-tumble tracer in a crowded environment

Beyond the simple argument given previously, our approach makes it possible to calculate the velocity (2.15) of the tracer and quantify the existence of ANM.

5.2.1 Observation of negative mobility

For a given value of the density, when the active force F_A is small enough or the bath particles are mobile enough compared to the tracer ($\tau^* \lesssim \tau$), the average velocity of the tracer remains positive at all values of the external force F_E. However, we observe that, for a sufficiently large persistence time τ_α, when the active force is large enough and when the bath particles are sufficiently slow compared to the tracer ($\tau^* \gg \tau$), the velocity can become a negative function of the external force (figure 5.2), which is the definition of ANM. We compare the value of the velocity predicted by our decoupling theory (equations (2.15,3.5)) with results from Monte Carlo simulations of the microscopic dynamics, and observe an excellent agreement, which confirms the relevance of our decoupling approximation to study the dynamics of an active, driven tracer. Compared to the previous chapter about the symmetric tracer, we note that here the decoupling approximation is less accurate when $F_E \sim F_A$.

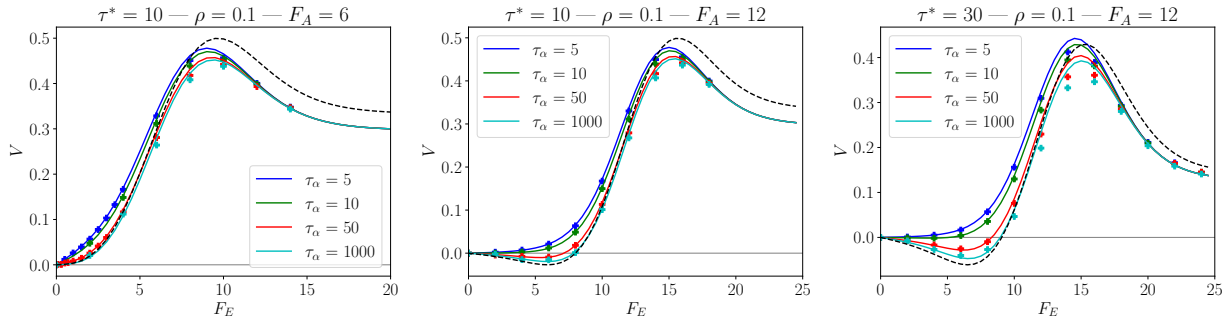

Figure 5.2: Stationary velocity of the tracer particle along the direction of the external force F_E on a 2D lattice. Lines: decoupling approximation (equations (2.15,3.5)); symbols: Monte Carlo simulations; dashed line: qualitative argument in the limite of infinite persistence (equation (3.38) for $\tau_\alpha = \infty$). As usual, the time unit is fixed by $\tau = 1$.

5.2.2 Phase diagram

Relying on our decoupling approach, which allows for the calculation of the velocity of the tracer at low computational cost, we explore the space of parameters to determine domains of existence of ANM.

NDM is needed for ANM to occur

According to previous studies on negative differential mobility (NDM) [61, 69], for a passive driven tracer (in the present formalism this corresponds to $F_A = 0$ and $F_E > 0$), this phenomenon occurs when, for a given value of the density, the ratio between the jump time of the obstacles and that of the tracer τ^*/τ is sufficiently large (see figure 5.3 (a)). Here, the emergence of ANM is also determined by the parameters that control the activity of the tracer (the magnitude of the active force F_A and the average persistence time of its orientation τ_α). In figure 5.3 (b), we show the critical value of the characteristic jump time of bath particles τ_c^* (rescaled by τ) above which ANM occurs, as a function of the active force F_A for different values of the persistence time τ_α and for a fixed value of the density of crowders ρ.

We can verify that the simple argument we put forward in 5.1 is plausible by comparing 5.3 (a) and (b): for large persistence ($\tau_\alpha = 1000$), as predicted by the argument, ANM appears for active force F_A (on (b) at $\tau^* = 10$ and $F_A = 6$ for instance) such that a passive tracer driven by a constant force of the same intensity (corresponding on (a) to $\tau^* = 10$ and $F_E = 6$) has a velocity which decreases when the intensity of the force increases.

Which swimmer can perform ANM ?

This phase diagram gives an insight into the range of parameters where ANM can be observed. For instance, for $F_A \simeq 10$ and $\tau^*/\tau \simeq 10$, it shows that ANM is observed as soon as τ_α reaches a critical value comprised between 10 and 100. In order to relate these values to real systems, we can compute a Péclet number for the active tracer as $\mathrm{Pe} \sim v_0/\sqrt{D_T D_R}$, where v_0 is the typical propulsion velocity, and D_T (resp. D_R) is the translational (resp. rotational) diffusion coefficient of the active particle. In our system of units, where σ is the lattice spacing, $D_T \sim \sigma^2\tau^{-1}$, $v_0 \sim \sigma\tau^{-1}$ (when F_A is large enough), and $D_R \sim \tau_\alpha^{-1}$, so that we simply get $\mathrm{Pe} \sim \sqrt{\tau_\alpha \tau^{-1}}$. In the example above, the condition for ANM to be observed becomes $3 \lesssim \mathrm{Pe} \lesssim 10$. Comparing to typical values reported in the experimental literature ([1], figure 1.1), we find that this condition can be easily reached for a wide range of microswimmers.

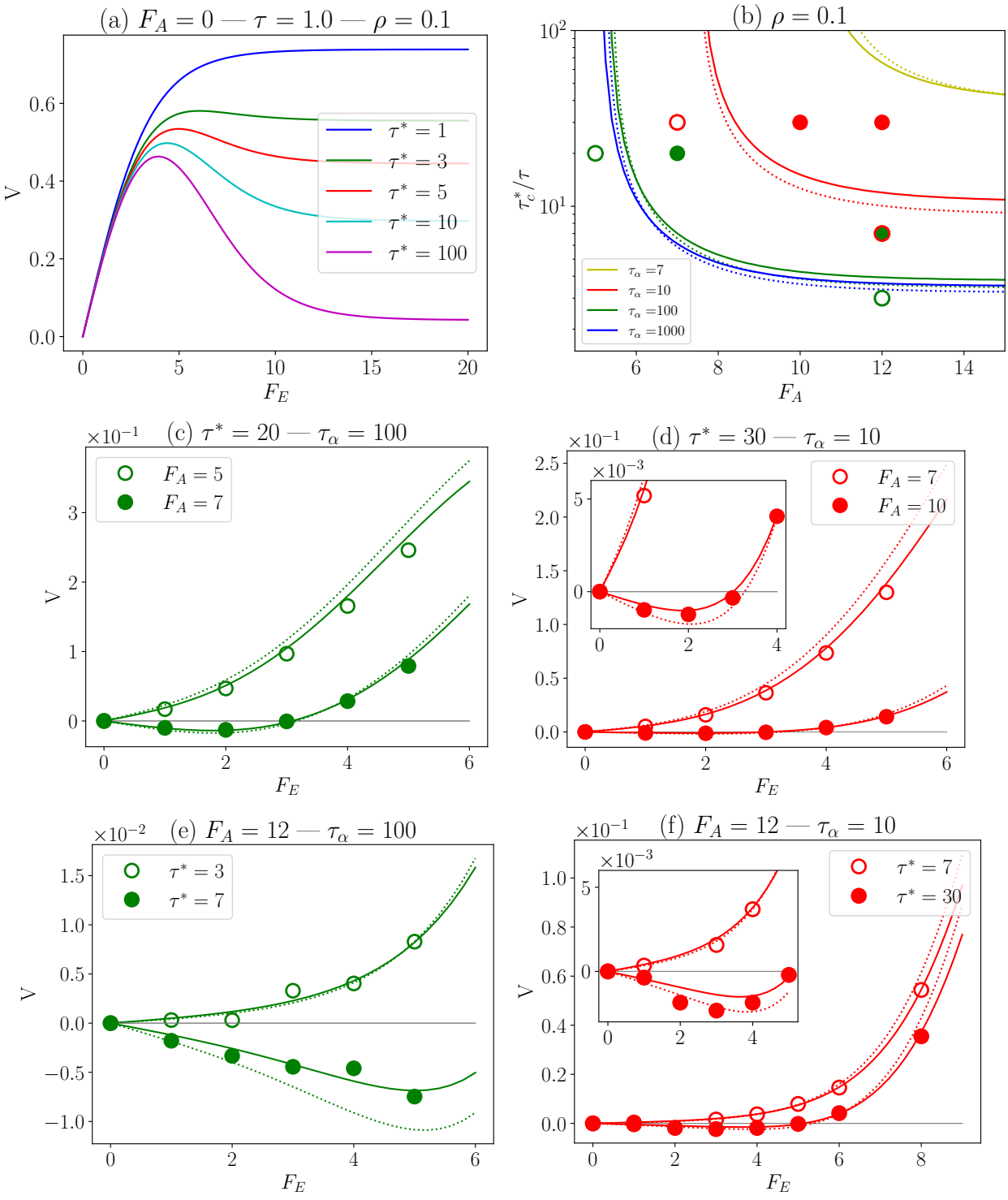

Figure 5.3: (a) Velocity of a passive driven tracer as a function of the driving force. (b) Phase diagram for ANM: above the lines, the theory predicts absolute negative mobility (straight line: decoupling approximation; dotted lines: qualitative argument condition (5.1)). The filled circles mean that ANM is observed in Monte Carlo simulations with the corresponding parameters, and the empty circles mean it is not. Each simulation point on the phase diagram corresponds to one of the curves below, representing the velocity of the tracer as a function of the external force. The plots (c) and (d) represent the situation where the critical line is crossed horizontally (by changing the active force). On the plots (e) and (f), the critical line is crossed vertically (by changing the mobility of the obstacles). On all plots, the obstacle density is $\rho = 0.1$, and the solid lines are obtained with the decoupling approximation, the dotted line with the low density argument, and the symbols with Monte Carlo simulations. In (b),(c),(d),(e),(f), red is $\tau_\alpha = 10$ and green $\tau_\alpha = 100$.

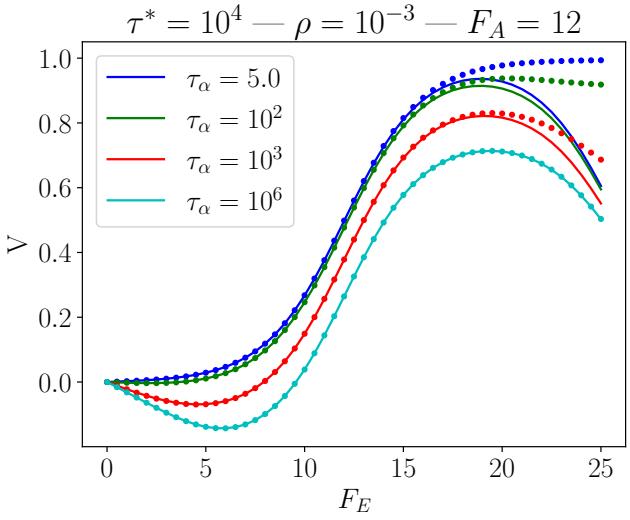

Figure 5.4: Stationary velocity of the tracer particle along the direction of the external force F_E on a 2D lattice. Lines: decoupling approximation; dots: qualitative argument (equation (3.38). As usual, the time unit is fixed by $\tau = 1$.

Qualitative argument

Finally, the qualitative argument (section 3.4) provides an analytical condition for ANM in terms of the different timescales of the problem. The condition is given by $\frac{\mathrm{d}V}{\mathrm{d}F_E}(F_E = 0) < 0$ with V computed from equation (3.38), and reads:

$$\frac{(2d-2)p_2}{\tau + \rho\tau'_p} + \frac{p_1 + p_{-1}}{\tau + \rho\tau_p} - \frac{(p_1 - p_{-1})^2}{\tau + \rho\tau_p}\left(1 + \rho\frac{(2d-2)p_2\tau_p^2}{\tau(\tau + \rho\tau_p)}\right) < 0, \tag{5.1}$$

where we use the following notations $p_\mu = p_\mu^{(1)}(F_E = 0)$ and

$$\frac{1}{\tau_p} = \frac{1}{\tau_p^{(1)}(F_E = 0)} = \frac{(2d-2)}{2d\tau^*} + \frac{1}{\tau_\alpha} + \frac{(1 - p_1 - p_{-1})}{\tau}, \tag{5.2}$$

$$\frac{1}{\tau'_p} = \frac{1}{\tau_p^{(2)}(F_E = 0)} = \frac{(2d-2)}{2d\tau^*} + \frac{1}{\tau_\alpha} + \frac{(1 - 2p_2)}{\tau}. \tag{5.3}$$

For the second line, we used the fact that when $F_E = 0$, symmetries imply that $p_1^{(2)} = p_{-1}^{(2)} = p_2^{(1)} = p_2$. As we can see in figure 5.4, when $\rho \to 0$, the qualitative argument and the decoupling approximation coincide, so we expect this analytic criteria to become very accurate in this limit.

5.2.3 Results at arbitrary density

Until now in this chapter, we have focused on results at low density, because in this limit, our decoupling approximation becomes exact for any values of the other parameters (as argued in section 3.3.1).

Nevertheless, the decoupling approximation provides results in quantitative agreement with Monte Carlo simulations at all densities, as long as the mobility of the obstacles is high enough (empirically $\tau^* \lesssim 10\tau$). As we can see on Fig. 5.5, in this regime, where the density of bath particles is expected to homogenize quickly on the timescale of displacement of the tracer, the decoupling approximation constitutes a sensible improvement compared to the

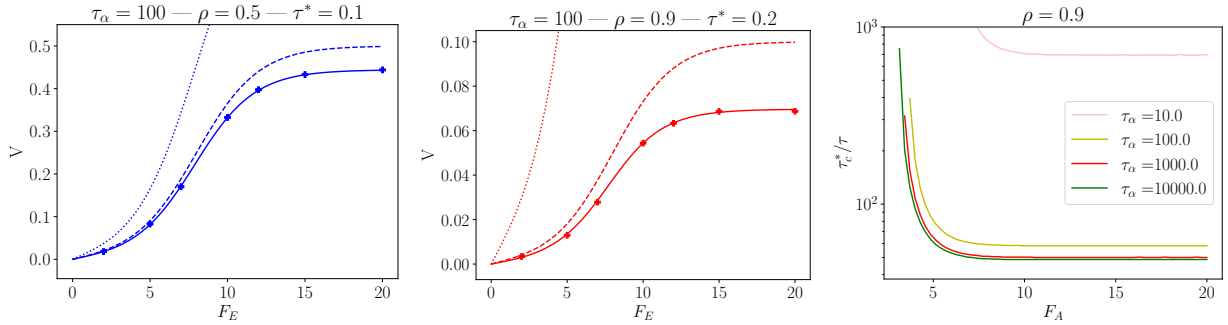

Figure 5.5: **Left and middle.** Velocity of the tracer as a function of the external force for different sets of parameters, calculated with different methods: decoupling approximation (solid lines), low-density qualitative argument (dotted lines), naive mean field (dashed lines). For both plots, the active force is $F_A = 8$. **Right.** Phase diagram from decoupling approximation. Above the lines, ANM is predicted.

naive mean-field approximation (which consists in supposing $k_{\boldsymbol{r}}^{(\chi)}(t) = \rho$ for any $\boldsymbol{r}, \chi, t$). As expected, the low density argument is irrelevant at higher densities.

However, for a higher characteristic time of displacement of the obstacles τ^*, the predictions of the decoupling approximation can only match qualitatively those obtained by Monte Carlo simulations (as opposed to the low density situation where the approximation is accurate even for large τ^*). This may be due to the fact that when the environment's density approaches the percolation threshold, the correlations neglected by the decoupling approximation become too strong. In figure 5.5, we show the phase diagram at density $\rho = 0.9$ predicted by the decoupling approximation (same aspect as in low density), but it is not in quantitative agreement agreement with results from Monte Carlo simulations.

5.3 Characterising the interplay between activity and crowding

Our approach to study tracer diffusion has the important feature to also give us access to the density profiles $k_{\boldsymbol{r}}^{(\chi)}$. This makes it possible to better understand how the activity of the tracer interacts with its environment, and reciprocally, in the present driven setting ($F_E \neq 0$).

5.3.1 Density profiles

We compute the global density profiles in the reference frame of the tracer $h_{\boldsymbol{r}} = \frac{1}{2d}\sum_\chi h_{\boldsymbol{r}}^{(\chi)}$. Their typical spatial dependence is plotted in figure 5.6. It suggests that ANM has a signature on the response of the environment, and that a small density excess may develop behind the tracer ($r < 0$) when its average velocity becomes negative, which is coherent with the idea that the tracer "pushes" obstacles in front of it (at $F_A = 12, \tau^* = 30, \tau_\alpha = 50$, this density excess is observed for F_E such that the velocity is negative and not when the velocity is positive). However this effect is not rigorously specific to ANM as it is also observed when ANM does not occur (*e.g.* $F_A = 6, \tau^* = 10, \tau_\alpha = 50$). The question to characterise entirely the behaviour of the tracer (ANM or not) only by looking at its environment (global density profiles $h_{\boldsymbol{r}}$) remains open, even though our results already provide valuable insight into this question.

Then density profiles describe how the structure of the crowded environment is affected by

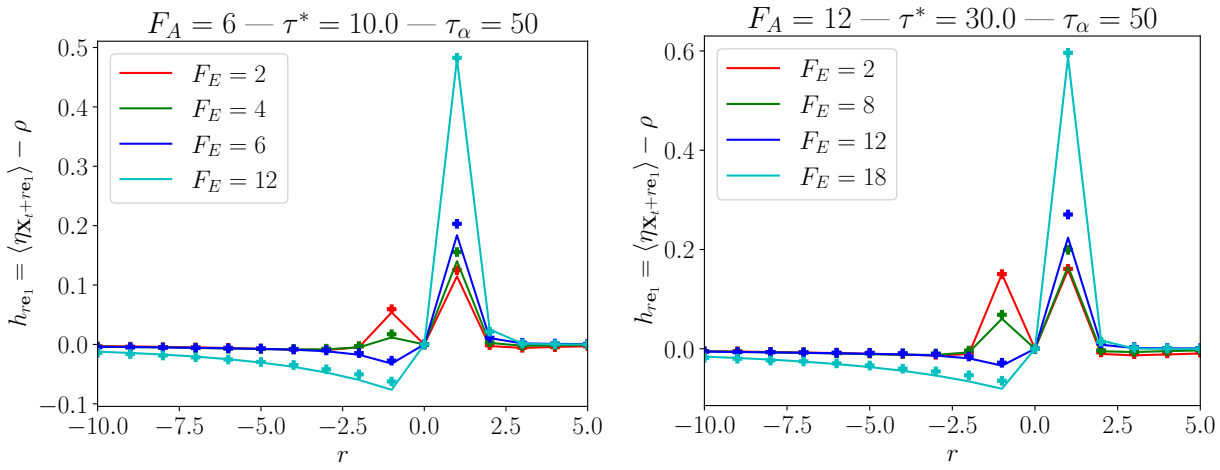

Figure 5.6: Density profiles (relatively to the reference value ρ) along the direction of F_E in the frame of reference of the tracer, as a function of the distance to the tracer r. In both plots, the parameters are $\rho = 0.1, \tau = 1$.

the activity of the tracer. Reciprocally, the environment impacts the properties of the active tracer.

5.3.2 Generalised Einstein relation

The way the crowded environment influences the dynamics of the tracer is illustrated by the following generalised Einstein relation, which involves density and correlation profiles $k_\mu^{(\chi)}$ (2.13) and $\widetilde{g}_\mu^{(\chi)}$ (2.17). In the absence of activity and crowding ($F_A = 0$ and $\rho = 0$), we recover the classical Einstein relation. From equation (2.15), we derive the expression of the mobility of the tracer in the limit of small external force:

$$\lim_{F_E \to 0} \frac{V}{F_E} = D_0 - \frac{1}{2d\tau} \left[\left(p_1^{(1)} - p_1^{(-1)} \right) v_1 + \frac{2(2d-1)\tau^*}{\alpha\tau} v_1^2 \right. \\ \left. + 2 \sum_{\epsilon \in \{-1,1,2\}} p_1^{(\epsilon)} \left(\frac{\mathrm{d}k_1^{(\epsilon)}}{\mathrm{d}F_E} - \widetilde{g}_1^{(\epsilon)} \right) (1 + (2d-3)\delta_{\epsilon,2}) \right], \tag{5.4}$$

where D_0 refers to equation (2.19) (the index 0 is here to recall that in (2.19), $F_E = 0$). We used the shorthand notation $v_1 = p_1^{(1)} \left(1 - k_1^{(1)}\right) - p_1^{(-1)} \left(1 - k_1^{(-1)}\right)$. All values are evaluated at $F_E = 0$.

The first term in equation (5.4) corresponds to the usual Einstein relation between the mobility of the tracer and its diffusion coefficient. The other term originates from the correlations between the displacement of the tracer and the dynamics of its environment (the first line involves the activity parameter α, and the second line involves the environment through the density and correlation profiles). Importantly, its value controls the emergence of ANM: if it exceeds D_0 in absolute value, the mobility of the tracer becomes negative.

Therefore, our approach also provides an analytical expression for the generalised Einstein relation [56, 162]; in particular we explicitly state the modified Einstein relation as a function of the conditional and correlation profiles.

Conclusion

In this chapter, we considered the case where an active run-and-tumble tracer is subject to an external drive ($F_E \neq 0$). Using our decoupling approximation 3.1, which proved to be in good agreement with Monte Carlo simulations, we explored the space of parameters of the model.

The emergence of ANM our minimal model for an active particle submitted to a constant external force as a result of its interactions with the other particles in its environment, constitutes a novelty compared to previous theoretical approaches. This context of an active particle in a media filled with mobile obstacles looks quite natural and common, and is striking that *ANM can emerge in such a situation made of simple ingredients* (no need of a periodic potential, of anisotropic obstacle or other structured set-up).

Finally, we determined the conditions for ANM to be observed, and studied the response of the environment to the non-equilibrium dynamics of the tracer.

Conclusion and open questions

In conclusion, we introduced a lattice model for a run-and-tumble tracer in a crowded dynamical environment. As a many-body problem, it involves an infinite hierarchy of equations for the determination of quantities of interest: velocity (2.15) and density profiles (2.13), diffusion coefficient (2.19) and correlation profiles (2.17). We proposed an approximate closure of this hierarchy based on a decoupling approximation 3.1. We also developed a qualitative argument 3.4, which makes it possible to understand the interplay between the different timescales of the model.

Then, we checked that the decoupling approximation is accurate in a broad range of parameters by comparing its predictions to results from Monte Carlo simulations. We argued that it even becomes exact, to leading order, in the dense and dilute limits. This approximation allowed us to explore extensively, at low computational cost, the space of parameters of the model and unveil counter-intuitive behaviours, which can arise because the system is far from equilibrium. Importantly, our approach makes it possible to characterise, through the density (2.13) and correlation (2.17) profiles, the interaction between the bath and the tracer. Finally, using our qualitative argument 3.4, we are able to explain the physical mechanisms at work in terms of the different timescales involved in the dynamics of the tracer (4.2.3, 5.2.2).

Many questions remain open, such as:

- **Higher order cumulants.** Extend the decoupling approximation to compute the cumulant generating function of the tracer.
- **Transitory regime.** Study of the features of the transitory regime.
- **Exactness of the qualitative argument.** Prove mathematically the concordance between the decoupling approximation and the qualitative argument at low density.
- **Decoupling and mode-coupling.** Can the decoupling approximation be rephrased in a mode-coupling [163, 164] framework?
- **Tracer-bath duality.** Is there a systematic signature of the counter intuitive behaviour of the tracer on its environment? In other words, can we determine if the tracer has a non monotonic diffusion coefficient or negative mobility only by observing the global density (and correlation in the symmetric case) profiles $h_{\boldsymbol{r}} = \langle \eta_{X_t+\boldsymbol{r}} \rangle$ (and $\widetilde{g}_{\boldsymbol{r}} = \langle X_t \eta_{X_t+\boldsymbol{r}} \rangle$). We recall that it is the conditional profiles which appear in the definitions of velocity (2.15) and diffusion coefficient (2.19); the global profiles mentioned here are not enough to compute them exactly.

In the one-dimensional case (part II), we will use rather different tools and methods, even though we will focus on the same observables. Addressing the open questions raised above could be of valuable interest, not only to better understand tracer diffusion in complex environments in dimension $d \geq 2$, but also to bridge the gap with the techniques we will use in dimension $d = 1$.

In this first part, the density and correlation profiles $k_{\boldsymbol{r}}^{(\chi)}$ and $\widetilde{g}_{\boldsymbol{r}}^{(\chi)}$ have proved to be important quantities since they characterise the transport properties of the tracer. In the next part, we will see that their generalisation, the generalised profiles, play an even more important role, as they will turn out to be central objects to characterise transport in one dimension.

Part II

Correlations in single-file diffusion

This part is based on and adapted from the following articles.

- [165] A. Grabsch, A. Poncet, P. Rizkallah, P. Illien, and O. Bénichou, *Exact closure and solution for spatial correlations in single-file diffusion.* Science Advances 8, eabm5043 (2022).
- [166] P. Rizkallah, A. Grabsch, P. Illien, and O. Bénichou, *Duality relations in single-file diffusion.* Journal of Statistical Physics 2023, 013202 (2023).
- [167] A. Grabsch, P. Rizkallah, P. Illien, and O. Bénichou, *Driven Tracer in the Symmetric Exclusion Process: Linear Response and Beyond.* Physical Review Letters 130, 020402 (2023).
- [168] A. Grabsch, P. Rizkallah, A. Poncet, P. Illien, and O. Bénichou, *Exact spatial correlations in single-file diffusion.* Physical Review E 107, 044131 (2023).

Chapter 6

Single-file diffusion

Single-file diffusion refers to the situation where particles diffuse on a line, with the geometrical constraint that they cannot bypass each other. After presenting the general context and introducing some theoretical models used to describe this situation, we briefly recall the framework of fluctuating hydrodynamics, which we will use in the following chapters. Then we discuss what was already known about these models, and introduce our contribution, which will be detailed in the next chapters.

Key ideas of the chapter.

- Subsection 6.1.1: in one-dimensional systems, tracer position and integrated current are closely related.
- Section 6.2: we will study diffusive systems (characteristic time and length scales τ and l related through a diffusion coefficient $D = l^2/\tau$), for which there is a unified description in the long time, large distance (*i.e.* hydrodynamic) limit.
- Section 6.3: the core of our approach will be to try to characterise the bath-tracer correlations.

6.1 Overview and models

In part I, we studied the behaviour of a tagged particle in a crowded environment in an unconstrained geometry (dimension $d \geq 2$). We were able to propose an approximate, yet accurate closure, that we used to unveil the transport properties of the tracer. Because our approximation relies on mean-field-type assumptions, it turns out that it does not properly describe one dimensional transport, which displays strong correlations (as argued below 6.1.1).

Nevertheless, a theory valid for the one-dimensional case would be of high value because single-file transport occurs in numerous biological contexts. Indeed, many processes rely on the transfer of water and ions through the nano-pores of trans-membrane proteins [73, 74]. Moreover, the single-file structure is the one naturally adopted by fluids confined in narrow channels [75], as demonstrated numerically [76, 77], and more recently experimentally [78].

In most of this second part (chapters 7, 8, 9), we will consider the simplest case where all particles are identical; there is no activity and the tracer particle performs the same dynamics as the other particles. In chapter 10, we will try to extend our study to the case of a biased tracer: the tracer has a different probability to move to the left than to the right.

We will consider infinite systems, which is relevant in real situations if the observation time is smaller than the characteristic time taken by the tracer to travel the system's length.

The situation of interest can be represented schematically as shown in figure 6.1. What is special about it? How to model it from a theoretical perspective?

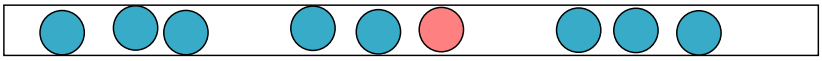

Figure 6.1: Particles confined in a channel narrower than twice the size of the particles.

6.1.1 The singularity of dimension one

The main feature of single-file diffusion which makes it of high theoretical interest is that a tagged particle (called a tracer, in red in figure 6.1) undergoes anomalous diffusion. If X_t denotes its position:

$$\langle X_t^2 \rangle \propto \sqrt{t}, \tag{6.1}$$

whereas in higher dimension, we would observe a classical diffusive behavior $\langle X_t^2 \rangle \propto t$. Direct observation of this anomalous scaling has been undertaken in different experimental contexts, at different scales of matter, from molecules in porous minerals (zeolites) to colloids in narrow channels (see figure 6.2) [80, 81, 169].

The very reason why 1D transport is anomalous is also the reason why there is a specific way to study tracer diffusion in this context: because the order of particles is preserved, one can recover the position of the tracer from the density of particles. For some systems, it will turn out that the positions of the particles can be computed easily, whereas for other systems, it is the density of particles which is easier to compute. Thanks to this property of preserved order, one can choose the most convenient quantity to compute (positions or density), and get results about the other.

More precisely, let us introduce the two observables (see figure 6.3 for illustration) which have been the focus of many studies in the context of single-file diffusion [99–103, 107, 165, 170–172]:

- **Position of a tracer** $x_k(t)$. Position at time t of the k-th particle. The 0-th particle is initially located at the origin ($x_0(0) = 0$).
- **Integrated current through a point** $Q_t(x)$. The number of particles in $]x, +\infty[$ at time t minus the number of particles in $]0, +\infty[$ at initial time $t = 0$.

The fundamental relation between these quantities, which is a consequence of the preserved order of particles, was used in [98] and in recent breakthroughs in the field [100, 101]. It reads

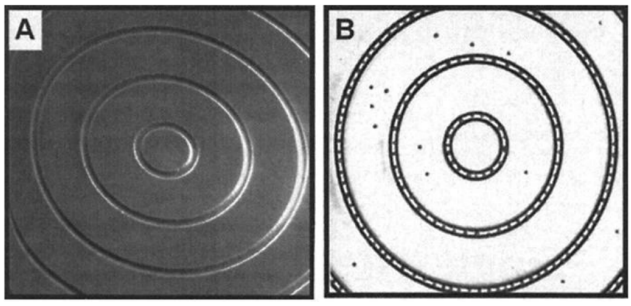

Figure 6.2: Images (A: scanning electron microscope, B: optical microscope) of narrow channels fabricated by photo-lithography where colloidal particles perform single-file diffusion [81]. They observe anomalous self-diffusion of the tracer.

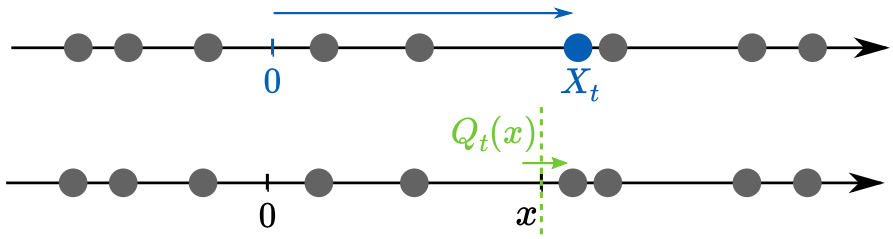

Figure 6.3: A single-file system with a tracer (top) initially at 0 ($X_t = x_0(t)$) and the same system with $Q_t(x)$, the integrated current through x. During the evolution of the system, at fixed x, $Q_t(x)$ is incremented by $+1$ when a particle crosses the green dashed line in the direction of the arrow and varies of -1 when a particle crosses the line in the opposite direction. If one fixes t and increases x, $Q_t(x)$ decreases by one each time x crosses a particle. In the single-file geometry, X_t never crosses a particle because of the constraint that particles cannot bypass each other, so $Q_t(X_t)$ remains zero at all time t, and $\forall \epsilon > 0, Q_t(X_t - \epsilon) \geq 1 > 0$ because the tracer is in $]X_t - \epsilon, +\infty[$ and not in $]X_t, +\infty[$.

(see explanation on figure 6.3):

$$\boxed{x_k(t) = \inf\{x \in \mathbb{R} | Q_t(x) + k \leq 0\}} \tag{6.2}$$

The remarkable point is that in order to compute $Q_t(x)$, we do not need to follow any particular particle (lagrangian description in the vocabulary of fluid mechanics), we only need to know how the density of particles evolves in time (eulerian description). Quite counter-intuitively, according to (6.2), the knowledge of $Q_t(x)$ makes it possible to recover the position of a given tagged particle.

We stress the fact that this reasoning is *specific* to the 1D case, and cannot be applied in higher dimensions: in this latter case, the knowledge of the currents at every points in space is not enough to recover the trajectory of a tracer, because, the geometry being unconstrained, the tracer is not forced to follow the current (the current only reflects the average displacement of all particles). This is why the hydrodynamic framework will be of great use for our study in one dimension.

Finally, from these considerations, it emerges that correlations between particles are key quantities in order to understand single-file diffusion: a particle cannot move if it does not push its neighbours (which is drastically different from other dimensions where particles can circumvent each other). In the second part of this thesis, we will present first results towards a general characterisation of these correlations.

6.1.2 Classical microscopic models

Many models have been designed in order to describe single-file diffusion from a theoretical point of view. We begin by presenting the Simple Exclusion Process, which has reached a paradigmatic status in the study of single-file diffusion [173]. Then, we introduce several important models from the literature of interacting particle systems that will fall under the scope of our analysis. We will always consider these models with annealed initial conditions, meaning that the system is initially distributed according to an equilibrium measure.

The last two models (KMP 6.1.2 and ZRP 6.1.2) do not directly describe single-file transport of particles, but we will see in chapter 9 that they are deeply related to respectively the RAP and the SEP because they describe the dynamics of the gaps between particles in these latter systems.

The SEP (Simple Exclusion Process)

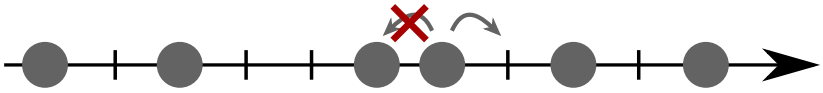

Figure 6.4: The Simple Exclusion Process.

The SEP [96, 173, 174] is the one dimensional version of the lattice model studied in part I. Each particle attempts a jump to a neighbouring site with a rate D_0 to the left and same rate D_0 to the right. The jump is performed only if the destination site is empty.

The N-EP (N-Exclusion Process)

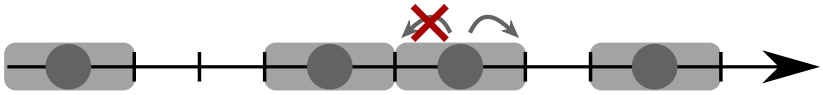

Figure 6.5: The DEP (Double Exclusion Process), corresponding to $N = 2$.

This lattice model [175, 176] is very similar to the SEP. The difference is that particles occupy N sites instead of 1: a jump is performed only if the N neighbouring sites in the direction of the jump are empty. It has for instance been considered for applications to biological systems [116].

The RBM (Reflecting Brownian Motion)

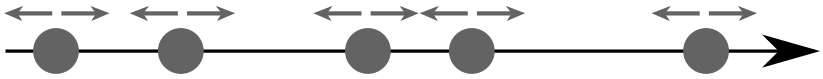

Figure 6.6: Reflecting Brownian particles.

This model [102, 171] in continuous space consists of point-like particles performing Brownian motion with the constraint that particles cannot bypass each other.

The RAP (Random Average Process)

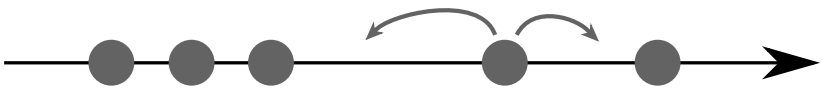

Figure 6.7: The random average process.

The RAP [113, 170, 177] is a model of point particles on the continuous line. Each particle performs jumps to the right with rate 1/2 or to the left with rate 1/2. The distance traveled by a particle which hops is a fraction $u \in [0, 1]$ of the distance separating it from the next particle in that direction. At each jump, u is drawn from an independent random variable $\mathcal{U}$ of a given law taking values in $[0, 1]$ (for example uniform law, or the law which weights a with probability one where $a \in [0, 1]$). We denote by μ_1 and μ_2 the first and second moments of $\mathcal{U}$.

The Hard Rods

Figure 6.8: Hard rods.

This model [82] is the hard sphere gas on the continuous line. Particle have a spatial extension $l > 0$ and interact through hard core interactions. They perform Brownian motion.

The KLS (Katz Lebowitz Spohn model)

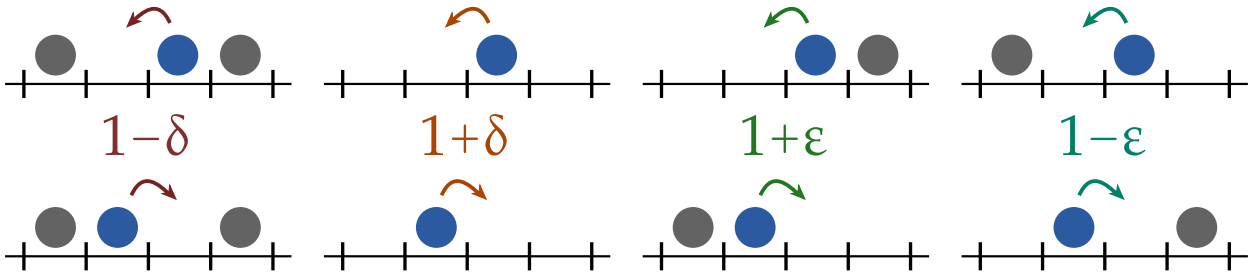

Figure 6.9: Jump rates in the KLS for the blue particle in function of its neighbouring configuration.

The KLS [178] is a lattice model with exclusion rule (at most one particle per site) featuring short-range interactions: the jump rates of each particle depend on its near environment in the way described in figure 6.9. The parameters δ and ϵ are in $[-1, 1]$. When $\epsilon < 0$, the particles feel attractive interaction, and when $\delta > 0$, particles are slower in the presence of neighbours.

The case $\delta = \epsilon = 0$ corresponds to the SEP (with jump rates $D_0 = 1$), and if $\epsilon = 1$ (fully repulsive interactions), it corresponds to the double exclusion process with jump rate $D_0 = 1 + \delta$. This model displays a rich phenomenology [175, 176].

The KMP (Kipnis Marchioro Presutti)

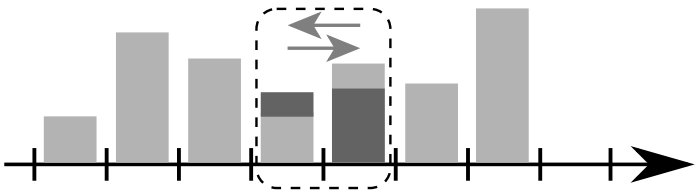

Figure 6.10: The KMP model.

This model [179, 180] is not strictly speaking a system of particles, and belongs to the class of mass transfer models [113, 181]. It is a lattice model where each site bears a mass which is a positive real number. With rate 1, each site exchanges mass with its right neighbour in the following way: the masses of the two sites are added up and the right site receives a random amount of the total mass drawn from a uniform distribution; the left site receives the rest.

The ZRP (Zero Range Process)

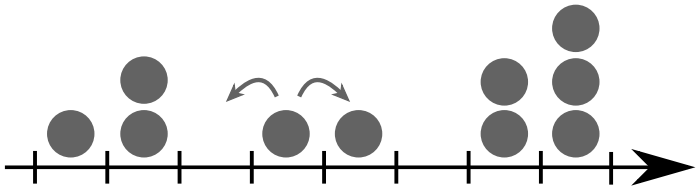

Figure 6.11: The zero range process.

This is a class of lattice models [86, 118] defined by a function $g : \mathbb{N}^* \longrightarrow \mathbb{R}^{+*}$. Sites can be empty, or occupied by one or more particles. Each site occupied by $k \in \mathbb{N}^*$ particles transfers one particle to its right neighbour with rate $g(k)/2$ and to its left neighbour with same rate $g(k)/2$. The name "zero range" comes from the fact that the jump rate depends only on the number of particles on the site of origin (interaction of range 0).

6.2 Hydrodynamic description

Although there is a broad diversity of models, with different features and phenomenology, there exists a powerful framework, which is recalled in this section, providing a unified description for all the models.

6.2.1 Macroscopic Fluctuation Theory

The Macroscopic Fluctuation Theory (MFT) takes its roots from a remarkable result of convergence in the SEP [182]. As it often happens in physics, this is an example where a simple theoretical model like the SEP was able to give insights leading to a general theory [124, 183, 184].

The large deviation principle

Relying on results for the SEP and further extensions to other models (notably "gradient models", see [124]), the MFT postulates a large deviation principle for *any* diffusive system. Let us first explain what we mean by diffusive system. Consider a system for which we can define a macroscopic density. If it is a system of particles, it can be defined through the formula, where N is the scaling parameter:

$$\rho^N(x,t) = \frac{1}{N}\sum_k \delta\left(x - \frac{x_k(tN^2)}{N}\right). \tag{6.3}$$

If it is a mass system such as the KMP, where each site $i \in \mathbb{Z}$ bears a mass $\eta_i(t) \in \mathbb{R}^+$ which depends on time t, one can define the rescaled mass:

$$\rho^N(x,t) = \frac{1}{N}\sum_k \eta_i(tN^2)\delta\left(x - \frac{i}{N}\right). \tag{6.4}$$

If it is already a fluctuating field $\rho(x,t)$ such as in the Dean-Kawasaki equation [185, 186], one can rescale the field $\rho^N(x,t) = \rho(Nx, N^2t)$. The system is said to be diffusive if ρ^N converges when $N \to \infty$ to the solution ρ of a diffusion equation:

$$\partial_t\rho(x,t) = \partial_x\left(D(\rho(x,t))\partial_x\rho(x,t)\right), \tag{6.5}$$

where the diffusion coefficient $D(\rho)$ is a positive function of ρ and depends on the system considered. In other words, the macroscopic current $j = -D(\rho)\partial_x\rho$ of the system satisfies a Fourier law. From the microscopic system, j is obtained as the limit of the rescaled current $j^N(x,t)$ defined as:

$$j^N(x,t) = N\ \partial_\tau Q_\tau(xN)|_{\tau=tN^2}\,. \tag{6.6}$$

The rescaling we have performed to define ρ^N, j^N is called diffusive (as opposed for instance to the ballistic scaling where space and time are multiplied by the same factor N); a diffusive system is a system which yields a non-trivial limit under a diffusive rescaling. Physically, we expect most non driven systems, only subject to symmetric noise (left/right) to be diffusive.

The MFT goes much beyond by specifying the associated large deviation principle (how the empirical density can deviate from the deterministic solution to the heat equation). The rescaled density and current $\rho^N(x,t), j^N(x,t)$ verify $\partial_t\rho^N + \partial_x j^N = 0$. For any density profile $\rho(x,t)$ and current $j(x,t)$ on $(x,t) \in \mathbb{R}\times[0,1]$ such that $\partial_t\rho + \partial_x j = 0$, the joint probability to observe them satisfies:

$$\boxed{\frac{1}{N}\ln \mathbb{P}\left(\left(\rho^N, j^N\right) \sim (\rho, j)\right) \underset{N\to\infty}{\longrightarrow} -F[\rho(x,0)] - \int_0^1 \mathrm{d}t \int_{-\infty}^{\infty} \mathrm{d}x \frac{\left(j(x,t) + D(\rho(x,t))\partial_x\rho(x,t)\right)^2}{2\sigma(\rho(x,t))}}, \tag{6.7}$$

where the mobility $\sigma(\rho)$ is a positive function which depends on the system considered. We will see a physical interpretation below 6.2.3. The functional F encodes the probability distribution on the initial condition. It expression, derived in appendix E.1 reads:

$$F[\rho(x,0)] = \int_{-\infty}^{+\infty} f(\rho(x,0)) - f(\rho_0(x)) - f'(\rho_0(x))(\rho(x,0) - \rho_0(x))\mathrm{d}x. \tag{6.8}$$

6.2.2 The transport coefficients

The diffusion coefficient $D(\rho)$ and the mobility $\sigma(\rho)$ are called the transport coefficients. They appear at the hydrodynamic level when performing the derivation of the MFT principle (6.7) from the microscopic dynamics. However, in most cases (notably in the case, of physical interest, of massive particles interacting through a Lennard-Jones or Coulomb potential), this derivation is out of reach. Fortunately, these coefficients can be computed or measured by other means at the microscopic level such as Green-Kubo relations or analysis of the steady states. Physically, we expect that the transport coefficients computed by different methods are

Figure 6.12: Transfer of matter between two reservoirs.

consistent [123], although in general this is a difficult mathematical problem. The broad scope of MFT allows one to apply (6.7) to any system for which one has computed or measured (experimentally or numerically for instance) the transport coefficients.

For theoretical models (such as those of 6.1.2), a convenient way to compute them is to consider a finite version of length L of the model we want to study, placed between two reservoirs at density ρ_a and ρ_b [125]. The coefficients $D(\rho)$ and $\sigma(\rho)$ are related to the first

Model	$D(\rho)$	$\sigma(\rho)$
Simple exclusion process [86, 107]	D_0	$2D_0\rho(1-\rho)$
Zero range processes [86]	$\frac{\sigma'(\rho)}{2}$	$\sigma(\rho)$
Random average process [113, 114]	$\frac{\mu_1}{2\rho^2}$	$\frac{1}{\rho}\frac{\mu_1\mu_2}{\mu_1-\mu_2}$
Kipnis-Marchioro-Presutti [115]	D_0	$\sigma_0\rho^2$
Hard Brownian particles [187]	D_0	$2D_0\rho$
Hard rod gas [82]	$\frac{D_0}{(1-\ell\rho)^2}$	$2D_0\rho$
Double exclusion process [175, 176]	$\frac{D_0}{(1-\rho)^2}$	$\frac{2D_0\rho(1-2\rho)}{1-\rho}$

Table 6.1: Transport coefficients $D(\rho)$ and $\sigma(\rho)$ for different models (see 6.1.2 for definitions).

two moments of the integrated current Q_t leaving the left reservoir (figure 6.12, matter going to the left reservoir is counted negatively):

$$\lim_{t\to\infty}\frac{\langle Q_t\rangle}{t}\underset{\substack{L\to\infty\\ \rho_a\to\rho_b=\rho}}{\sim}\frac{D(\rho)(\rho_a-\rho_b)}{L}\,,\quad \lim_{t\to\infty}\frac{\langle Q_t^2\rangle}{t}\bigg|_{\rho_a=\rho_b=\rho}\underset{L\to\infty}{\sim}\frac{\sigma(\rho)}{L}\,. \tag{6.9}$$

In practice, these two coefficients can be difficult to compute analytically. Nevertheless, they have been obtained for different microscopic models (see Table 6.1).

Finally, note that since they characterise fluctuations and linear response of the transfer of matter between the two reservoirs, the transport coefficients are related through equilibrium quantities (fluctuation-dissipation theorem), here the free energy per unit volume $f(\rho)$ as a function of the density ρ. This relation [104], proved in appendix E.2 reads:

$$2D(\rho) = f''(\rho)\sigma(\rho). \tag{6.10}$$

6.2.3 Stochastic heat equation

We can interpret equation (6.7) by recognising the Feynman measure of a Gaussian white noise in space and time $\sqrt{\frac{\sigma(\rho)}{N}}\times\eta$ with variance $\frac{\sigma(\rho)}{N}$. The noise η has unit variance and zero mean:

$$\langle\eta(x,t)\eta(x',t')\rangle = \delta(x-x')\delta(t-t')\,. \tag{6.11}$$

Then in the large N limit, the rescaled density and current ρ^N and j^N of a microscopic diffusive system evolve according to a conservation equation,

$$\partial_t\rho^N(x,t)+\partial_x j^N(x,t)=0\,, \tag{6.12}$$

and a stochastic Fourier law:

$$j^N(x,t) = -D\left(\rho^N\right)\partial_x\rho^N(x,t)+\sqrt{\frac{\sigma(\rho^N)}{N}}\,\eta(x,t)\,. \tag{6.13}$$

This interpretation is referred to as "fluctuating hydrodynamics", and can be compared to the central limit theorem in the sense that the gaussian noise for the current appears when we sum many weakly correlated microscopic currents (through the rescaling operation). From a physical point of view, equation (6.13) means that the systems remains *locally* (on a characteristic length N, supposed large enough) in the linear response regime, and that fluctuations can be considered Gaussian (like in Onsager's theory), with mean and variance given by the transport coefficients (6.9)).

As a side remark, note that we often encounter equation (6.13) without the N [102, 114]. For practical purpose (in particular in section 9.1), we will also consider such equations with a non weak noise:

$$\boxed{\partial_t \rho(x,t) + \partial_x j(x,t) = 0}\,, \tag{6.14}$$

associated to a stochastic Fourier law:

$$\boxed{j(x,t) = -D(\rho)\partial_x \rho(x,t) + \sqrt{\sigma(\rho)}\,\eta(x,t)}\,. \tag{6.15}$$

This is a convenient way to represent a single-file system with transport coefficients D and σ. Indeed, whatever the precise definition of equations (6.14, 6.15) (defining such equations is a difficult mathematical problem), it turns out that the rescaled density and current $\rho^N(x,t) = \rho(Nx, N^2 t)$ and $j^N(x,t) = Nj(Nx, N^2 t)$ verify equations (6.12,6.13), with the weak noise ($\propto 1/\sqrt{N}$). This is a consequence of the following formula:

$$\eta(f(x), g(t)) \overset{\text{(law)}}{=} \sqrt{\frac{1}{f'(x)g'(t)}}\,\eta(x,t)\,, \tag{6.16}$$

where f and g are monotonous functions. This formula stems from the composition rule $\delta(f(x)) = \frac{\delta(x)}{|f'(x)|}$.

By essence, because of the hydrodynamic scaling $(x,t) \mapsto (xN, tN^2)$, the MFT informs us only about the large scale and long time limit (which is one of the limitations of this theory). In short, if we care only about this limit, it is equivalent to consider a microscopic model or its fluctuating hydrodynamic description given by equations (6.14, 6.15) with the corresponding transport coefficients $D(\rho)$ and $\sigma(\rho)$.

6.3 Known results and outline

In this thesis, we are interested in systems on the infinite line. Note that there have been lots of studies about finite-size systems, in particular between two reservoirs [83–89]. A major difference is that, contrary to infinite systems, finite systems of size L usually reach a stationary regime after a time of order L^2.

Most studies of a tracer's position and integrated currents in single-file systems on the infinite line have focused on the SEP, which is a minimal model implementing non-trivial interactions between particles.

6.3.1 The SEP: the road to the tracer's position distribution

The first notable result is the analytical computation of an asymptotic equivalent of the mean-squared displacement of a tagged particle [98]:

$$\langle x_0(t)^2 \rangle \underset{t\to\infty}{\sim} \frac{1-\rho}{\rho}\sqrt{\frac{2t}{\pi}}. \tag{6.17}$$

The next major result is the computation of the cumulant generating function of the integrated current through the origin [99] (using Bethe Ansatz technique), yielding a surprisingly simple formula in the long-time limit:

$$\ln \left\langle e^{\lambda Q_t} \right\rangle = -\mathrm{Li}_{\frac{3}{2}}(-\omega)\sqrt{\frac{2t}{\pi}}, \tag{6.18}$$

where ω is a reduced variable combining the parameter λ and the initial densities on $\mathbb{Z}^-$ and $\mathbb{Z}^{+*}$ ("step" initial condition); $\mathrm{Li}_{\frac{3}{2}}$ refers to the polylogarithm function.

For the tracer, the cumulant generating function $\ln \left\langle e^{\lambda x_0(t)} \right\rangle$ was then determined in the dense ($\rho \to 1$) [188] limit, by considering the dynamics of vacancies, and in the dilute ($\rho \to 0$) [102, 171] limit, using a mapping to independent particles. Finally, the whole cumlant generating function at arbitrary density was computed a few years later [100, 101] using Bethe Ansatz.

In the case of a biased tracer (the tracer, and only the tracer, has a different jump rate to the right than the one to the left), the only known results at arbitrary density deal with the mean position of the tracer [119] and its variance in a specific case [131]. The cumulant generating in the biased case is known only in the dense limit [188].

6.3.2 More general systems

The hydrodynamic description introduced above (6.2) is a central tool in the study of more general single-file systems. It has been used to generalise the result for the integrated current in the SEP [99] to the integrated current in any one dimensional system with constant diffusion coefficient and quadratic mobility ($D(\rho) = D_0$ and $\sigma(\rho) = a\rho^2 + b\rho$). This includes the KMP model 6.1.2.

For arbitrary transport coefficients $D(\rho)$ and $\sigma(\rho)$, a general theory for tracer diffusion has been developed [102], based on MFT (equation (6.7)). The authors managed to recover the general formula for the variance of the tracer's position [189]. However, it is difficult to go beyond, because the equations obtained by this method are challenging.

In the context of tracer diffusion, it has been pointed out that the RAP model 6.1.2 is particularly well adapted because the evolution equations for the positions of the particles are naturally closed (which is an exceptional fact). We will give some insight into this fact in chapter 9. In the RAP, correlations between particles and the variance of the position of a biased tracer have been computed, by microscopic methods [89, 95] and using MFT [114]. Nevertheless, some of the methods employed are specific to the RAP (naturally closed equations).

6.3.3 Outline: understanding correlations in single-file diffusion

The anomalous scaling in $\sqrt{t}$ for all the cumulants of a tracer's position is ubiquitous in single-file diffusion. Although it is known that the anomalous scaling in $\sqrt{t}$ originates from the strong correlations between particles (preserved order in the one dimensional geometry), none of the approaches developed so far fully accounts for the interactions between the tracer (or the integrated current) and the bath.

In order to bridge the gap, a new approach has been introduced in [103, 133]. It is based on the introduction of a new observable of great physical significance, the generalised density profile (a generalisation of the density and correlation profiles studied in the first part), which precisely characterises the bath-tracer correlations. This approach makes it possible to recover

easily the known results in the dense and dilute limits, and in addition, to determine the bath-tracer correlations in these limits. We will extend this approach to an arbitrary density.

We begin in chapter 7 by a microscopic study of the SEP, where we extend the definition of the generalized density profile to the more general observable of the integrated current. We derive, from microscopic considerations, non trivial equations relating the density profiles and the cumulant generating function. Similarly to what we saw in chapter 2, the generalised density profiles are shown to be involved in a infinite hierarchy of equations resulting from the many-body nature of the problem.

In chapter 8, we break this infinite hierarchy by providing an exact closure; the availability of such a closure is very uncommon in many-body problems. We detail the steps that lead us to determine the closed equation verified by the generalised density profile. We then use this equation to study different observables, and different situations in the SEP. We stress the fact that, contrary to the approximate closure we used in the first part I, the closed equation we put forward in the case of the one dimensional SEP is exact.

The object of chapter 9 is to extend our result for the SEP to other single-file systems. The core of our approach is the introduction of very general mappings relating different single-file systems; we argue that these mappings are the only one that can exist relating different single-file systems at the hydrodynamic level. We use them to show that the results we obtained for the SEP can be extended to wide class of models of single-file diffusion, displaying a wide variety of phenomenology (see 6.1.2).

Finally, in chapter 10, we present first results towards an extension of our generalised-density-profile approach to the case of a biased tracer. We propose a general method to implement the bias in the hydrodynamic description 6.2, which we validate by comparing its predictions to Monte Carlo simulations of different models. The culmination of this chapter is the determination of new analytical results for the variance of the position of a biased tracer in the SEP, valid at any density.

Chapter 7

Microscopic study of the Simple Exclusion Process

We begin with a microscopic study of the SEP. The microscopic point of view gives results and strong indications which will guide our quest for a closed equation formula in the next chapter. We begin, in section 7.1, by recalling the definition [103] of the generalised density profiles and we derive their long-time scalings. The objects introduced here will be at the core of our study in the following chapters.

Key results.

- Paragraphs 7.2.1 and 7.2.2: boundary conditions verified by the generalised density profiles, which appear as central quantities to study the cumulant generating function of the tracer's position or the integrated current through a point (discussed in 6.1.1).
- Paragraph 7.2.2: application of the relation between integrated current through a point and tracer position (6.2) to the generalised density profiles.

7.1 The generalised density profiles

We consider the SEP on a 1D infinite lattice. Initially each site is filled independently with probability $\rho \in [0,1]$ (annealed initial conditions), which is the mean density of the system, except the origin which is always occupied by a particle, which we call the tracer. We denote X_t the position of the tracer at time t, with $X_0 = 0$. The other particles are described by a set of occupation numbers $\{\eta_i(t)\}_{i\in\mathbb{Z}}$, with $\eta_i(t) = 1$ if site i is occupied at time t and 0 otherwise. Contrary to what we did in part I, here we use the convention[1] that $\eta_{X_t}(t) = 1$.

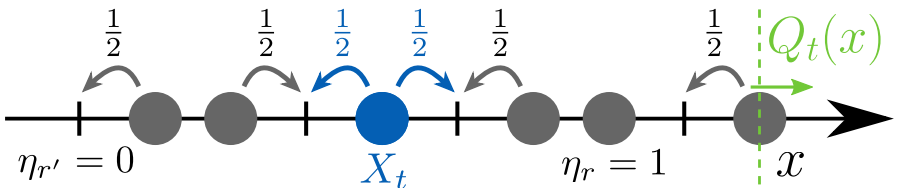

Figure 7.1: The SEP with a tracer. We recall the fundamental relation between tracer position and integrated current $X_t = \inf\{x \in \mathbb{R} | Q_t(x) \leq 0\}$ (6.2). We chose the jump rate $D_0 = 1/2$

[1] We make this choice here because we will also consider the integrated current (and we want the tracer to be counted in the current so we need $\eta_{X_t} = 1$ according to definition of the integrated current (7.15)).

The master equation of the SEP, which describes the time evolution of the probability $P_t(X,\eta)$ to observe the configuration $\{X,\eta\}$ with a tracer on site X at time t is

$$\begin{aligned}\partial_t P_t(X,\eta) =& \frac{1}{2}\sum_{r\neq X,X-1}\left[P_t(X,\eta^{r,+})-P_t(X,\eta)\right]\\ &+\frac{1}{2}\left\{(1-\eta_{X-1})P_t(X-1,\eta^{X-1,+})-(1-\eta_{X+1})P_t(X,\eta)\right\}\\ &+\frac{1}{2}\left\{(1-\eta_{X+1})P_t(X+1,\eta^{X,+})-(1-\eta_{X-1})P_t(X,\eta)\right\}\ ,\end{aligned} \tag{7.1}$$

where $\eta^{r,+}$ is the configuration obtained from η by exchanging the occupations of sites r and $r+1$. In (7.1), the terms of the first line corresponds to the jumps of the bath particles, while the other terms describe the displacement of the tracer.

In this section, we introduce the quantities, first defined in [103], that will be central in our analysis of the SEP, and we determine their long time limit scaling using the large deviation principle 6.7.

7.1.1 Bath-tracer correlations

Our main goal is to characterise the position of the tracer particle. Its statistical properties are encoded in the cumulant generating function

$$\psi(\lambda,t)=\ln\left\langle \mathrm{e}^{\lambda X_t}\right\rangle\ , \tag{7.2}$$

whose expansion in powers of λ give the cumulants $\kappa_n(t)$,

$$\psi(\lambda,t)=\sum_{n=1}^{\infty}\frac{\lambda^n}{n!}\kappa_n(t)\ . \tag{7.3}$$

The core of our approach to this problem, which will be developed in this section and in the next chapter, resides in the introduction of a physical observable which fully quantifies the bath-tracer correlations in the SEP

$$w_r(\lambda,t)=\frac{\langle \eta_{X_t+r}(t)\,\mathrm{e}^{\lambda X_t}\rangle}{\langle \mathrm{e}^{\lambda X_t}\rangle}\ . \tag{7.4}$$

Far from the tracer, sites do not feel its influence (independence of η_{X_t+r} and X_t), hence the large $|r|$ limit is equal to the mean density ρ: $w_r(\lambda,t)\underset{|r|\to\infty}{\longrightarrow}\rho$. We call $w_r(t)$ the generalised density profiles (GDP) generating function, since its expansion in powers of λ yields all the joint cumulants $\langle X_t^n\eta_{X_t+r}(t)\rangle_c$ between X_t and η_{X_t+r},

$$w_r(\lambda,t)=\sum_{n=0}^{\infty}\frac{\lambda^n}{n!}\langle X_t^n\eta_{X_t+r}(t)\rangle_c\ . \tag{7.5}$$

At 0-th order we recognise the density profiles $k_{\boldsymbol{r}}=\langle\eta_{X_t+r}\rangle$ of part I, and at first order the correlation profiles $\widetilde{g}_{\boldsymbol{r}}=\langle(X_t-\langle X_t\rangle)\eta_{X_t+r}\rangle$. The other orders are called the generalised density profiles.

7.1.2 Scaling functions

In this section, we use a path integral formulation and physical arguments to derive the scaling forms of the long time limit of the cumulant generating function of the tracer's position and integrated current in the SEP from the large deviation principle 6.7. This was done for example in [102]. A rigorous proof of these scalings is provided in [105].

In the large time limit, we can use the MFT large deviation principle to evaluate the probability of observing an evolution from time $t = 0$ to $t = T$ for the occupation numbers $(\eta_r(t))_{r\in\mathbb{Z},t\in[0,T]}$. Such an evolution corresponds to a macroscopic density (6.4) $(\rho^{\sqrt{T}}(x,t))_{x\in\mathbb{R},t\in[0,1]}$ and associated current (6.6), which probability is given by the MFT large deviation principle (6.7) in the limit $T\to\infty$ (we chose $N=\sqrt{T}$ in (6.7)). Summing over all possible evolutions $(\eta_r(t))_{r\in\mathbb{Z},t\in[0,T]}$, we evaluate the cumulant generating function of the tracer's position in the long time limit $T\to\infty$:

$$\ln\left\langle e^{\lambda X_T}\right\rangle \underset{T\to\infty}{\sim} \ln\int \mathcal{D}[\rho,j]\exp\left(-\sqrt{T}\mathcal{U}[\rho,j]+\sqrt{T}\lambda\xi_1[\rho]\right), \tag{7.6}$$

where the integral runs over $\rho(x,t), j(x,t)$ verifying $\partial_t\rho+\partial_x j=0$ and we expressed the position of the tracer $X_T=\sqrt{T}\xi_1[\rho]$ as a function of the macroscopic density ρ through the relation expressing the conservation of the number of particles on the right of the tracer[2] [102]:

$$\int_0^{\xi_1[\rho]}\rho(x,1)\mathrm{d}x=\int_0^{\infty}(\rho(x,1)-\rho(x,0))\mathrm{d}x\,. \tag{7.7}$$

We noted the large deviation functional

$$\mathcal{U}[\rho,j]=\int_0^1\mathrm{d}t\int_{-\infty}^{\infty}\mathrm{d}x\frac{\left(j+\frac{1}{2}\partial_x\rho\right)^2}{2\rho(1-\rho)}+F[\rho(x,0)]. \tag{7.8}$$

Using a saddle-point method in the path integral, we find that the following scaling holds:

$$\boxed{\hat{\psi}(\lambda)=\lim_{T\to\infty}\frac{\psi(\lambda,T)}{\sqrt{2T}}\,,\quad \hat{\psi}(\lambda)=\sum_{n\geq 1}\hat{\kappa}_n\frac{\lambda^n}{n!}}\,, \tag{7.9}$$

where $\hat{\kappa}_n$ is the n^{th} cumulant of the tracer's position (rescaled by $\sqrt{2t}$).

As shown in [103], the MFT can also be used to analyse the generalised density profiles. Here, we determine the large time scaling of the GDP-generating function (7.4). According to the MFT large deviation principle (identically to previously, taking $N=\sqrt{T}$ in equation (6.7)):

$$\frac{\left\langle \eta_{X_T+r}e^{\lambda X_T}\right\rangle}{\left\langle e^{\lambda X_T}\right\rangle}\underset{T\to\infty}{\sim}\frac{\displaystyle\int\mathcal{D}[\rho,j]\rho\left(\xi_1[\rho]+\frac{r}{\sqrt{T}}\right)\exp\left(-\sqrt{T}\left(\mathcal{U}[\rho,j]-\lambda\xi_1[\rho]\right)\right)}{\displaystyle\int\mathcal{D}[\rho,j]\exp\left(-\sqrt{T}\left(\mathcal{U}[\rho,j]-\lambda\xi_1[\rho]\right)\right)}, \tag{7.10}$$

[2]Here there is a little subtlety. Equation (7.7) defines the position X_T of the tracer by saying that $Q_T(X_T)=0$, where $Q_t(x)$ is the integrated current through x (defined in 6.1.1, see (7.15) for the definition in the case of the SEP). But there can be several x such that $Q_t(x)=0$ (see figure 6.3); the real position of the tracer is in fact the *minimal* x such that $Q_t(x)=0$ (7.2.2). Nevertheless, although $Q_T(X_T)=0$ does not uniquely define X_T, it does uniquely define $\xi_1[\rho]=\frac{X_T}{\sqrt{T}}$ for large T. Indeed, with high probability, we will have: diameter$\{x|Q_T(x)=0\}=o(\sqrt{T})$ (the zone where $Q_T(x)=0$ grows less quickly than $\sqrt{T}$). This is the kind of results proved rigorously in [105].

where we expressed the occupation $\eta_{X_T+r}(T)$ as a function of the hydrodynamic density[3] at position $\frac{X_T+r}{\sqrt{T}}$, $\rho\left(\xi_1[\rho]+\frac{r}{\sqrt{T}},1\right)$. Using the saddle-point method when $T\to\infty$ and noticing that the saddle-point is the same in both path integrals because $\rho\left(\xi_1[\rho]+\frac{r}{\sqrt{T}},1\right)$ is not involved in the exponential term $\exp(-\sqrt{T}(\mathcal{U}[\rho,j]-\lambda\xi_1[\rho]))$, we find that

$$w_r(\lambda,T)\underset{T\to\infty}{\sim}\rho^*\left(\xi_1[\rho^*]+\frac{r}{\sqrt{T}},1\right), \tag{7.11}$$

where (ρ^*,j^*) minimises, under the constraint $\partial_t\rho+\partial_x j=0$, the argument of the exponential:

$$\int_0^1 \mathrm{d}t\int_{-\infty}^{\infty}\mathrm{d}x\frac{\left(j+\frac{1}{2}\partial_x\rho\right)^2}{2\rho(1-\rho)}+F[\rho(x,0)]-\lambda\xi_1[\rho]. \tag{7.12}$$

We finally obtain that:

$$\boxed{w_r(\lambda,T)\underset{T\to\infty}{\sim}\Phi\left(v=\frac{r}{\sqrt{2T}},\lambda\right),\quad \Phi(v,\lambda)=\sum_{n\geq 1}\Phi_n(v)\frac{\lambda^n}{n!}}. \tag{7.13}$$

We have in particular $\Phi\left(v=\frac{r}{\sqrt{2t}},\lambda\right)=\rho^*\left(\xi_1[\rho^*]+v\sqrt{2},1\right)$. Hence the GDP-generating function can be seen as the most probable density observed at a site for the modified probability distribution $P_{\mathrm{mod}}(X,\eta,t)=P(X,\eta,t)\frac{e^{\lambda X}}{\langle e^{\lambda X_t}\rangle}$ (for instance, when $\lambda>0$, this distribution favors configurations where $X>0$). Note that the scaling (7.13) implies that $w_r(t)$ never reaches a stationary regime, and that the area of influence of the tracer grows like $\sqrt{t}$.

As a direct consequence of (7.4),

$$\lim_{v\to\pm\infty}\Phi(v,\lambda)=\rho\,. \tag{7.14}$$

7.1.3 Bath-current correlations

Thanks to (6.2), in order to study tracer diffusion, it is equivalent to consider the integrated current through a point x, whose microscopic definition in the SEP reads

$$Q_t(x)=\sum_{r\geq 1}\left(\eta_{r+x}(t)-\eta_r(0)\right)\,. \tag{7.15}$$

Because the long time limit follows a diffusive scaling (see the scaling limit above, *e.g.* equation (7.6)), we rather consider $Q_t(x_t)$ with $x_t=\lfloor\xi\sqrt{2t}\rfloor$, for an arbitrary real number ξ. Its statistical properties are encoded in the cumulant generating function

$$\psi_Q(\lambda,\xi,t)=\ln\left\langle \mathrm{e}^{\lambda Q_t(x_t)}\right\rangle\,, \tag{7.16}$$

The GDP are defined in the same way as the tracer, and they fully account for the correlations between the density of the bath and the integrated current

$$w_{Q;r}(\lambda,t)=\frac{\left\langle\eta_{x_t+r}(t)\,\mathrm{e}^{\lambda Q_t(x_t)}\right\rangle}{\left\langle\mathrm{e}^{\lambda Q_t(x_t)}\right\rangle}\,. \tag{7.17}$$

[3]The reason why it is legitimate to replace $\eta_{X_T+r}(T)$ by $\rho\left(\xi_1[\rho]+\frac{r}{\sqrt{T}},1\right)$ in the large T limit is not obvious and relies on the existence of local equilibriums in this limit. It is further discussed in appendices D, F.2.

Thanks to our choice of scaling for x_t, we can show from the large deviation principle (6.7), in the same way as for the tracer, that there exist scaling functions:

$$\boxed{\ln \left\langle \mathrm{e}^{\lambda Q_t(x_t)} \right\rangle \underset{t\to\infty}{\sim} \sqrt{2t}\, \hat{\psi}_Q(\xi,\lambda)}\,, \tag{7.18}$$

$$\boxed{w_{Q;r}(t) \underset{t\to\infty}{\sim} \Phi_Q\left(v=\frac{r}{\sqrt{2t}},\xi,\lambda\right)}\,. \tag{7.19}$$

And the scaling function Φ_Q is obtained from the (ρ^*, j^*) which minimise, under the constraint $\partial_t\rho + \partial_x j = 0$, the following expression arising from the large deviation principle

$$\int_0^1 \mathrm{d}t \int_{-\infty}^{\infty} \mathrm{d}x \frac{\left(j+\frac{1}{2}\partial_x\rho\right)^2}{2\rho(1-\rho)} + F[\rho(x,0)] - \lambda Q_1(\xi\sqrt{2})[\rho]. \tag{7.20}$$

The integrated current current through a point x is computed from the hydrodynamics profile as follows:

$$Q_1(x)[\rho] = \int_x^{\infty} \rho(x,1) - \rho(x,0)\mathrm{d}x - \int_0^x \rho(x,0)\mathrm{d}x. \tag{7.21}$$

We have the relation $\Phi_Q(v,\xi,\lambda) = \rho^*(\xi + v\sqrt{2}, 1)$. Also $\lim_{v\to\pm\infty} \Phi_Q(v,\xi,\lambda) = \rho$.

In the next section, we will derive valuable information about the scaling functions ($\hat{\psi}$, $\hat{\psi}_Q$, Φ, Φ_Q) from the master equation.

7.2 Evolution equations and boundary conditions

Similarly to our approach in the first part of this thesis, from the master equation (7.1), we derive evolution equations for the quantities introduced above. We will see that, strikingly, in the long-time limit, these evolution equations yield non trivial boundary conditions involving ($\hat{\psi}$, $\hat{\psi}_Q$, Φ, Φ_Q).

7.2.1 Integrated current

We first focus on the integrated current $Q_t(x_t)$. We fix a (positive for simplicity) value for ξ, with $x_t = \lfloor \xi\sqrt{2t} \rfloor$.

Microscopic evolution equations

The evolution equation for the cumulant generating function is computed in appendix F.1, it reads:

$$\begin{aligned}\partial_t \ln \left\langle \mathrm{e}^{\lambda Q_t(x_t)} \right\rangle =& \frac{1}{2}\left[(\mathrm{e}^{\lambda}-1)\frac{\left\langle \eta_{x_t}(1-\eta_{x_t+1})\mathrm{e}^{\lambda Q_t(x_t)}\right\rangle}{\left\langle \mathrm{e}^{\lambda Q_t(x_t)}\right\rangle} + (\mathrm{e}^{-\lambda}-1)\frac{\left\langle \eta_{x_t+1}(1-\eta_{x_t})\mathrm{e}^{\lambda Q_t(x_t)}\right\rangle}{\left\langle \mathrm{e}^{\lambda Q_t(x_t)}\right\rangle}\right] \\ &+ \sum_n \delta(t-t_n)\ln[1+(\mathrm{e}^{-\lambda}-1)w_{Q;1}(t)]\,.\end{aligned} \tag{7.22}$$

Note the sum of δ functions, which comes from the fact that x_t varies discontinuously at times $t_n = (n/\xi)^2/2$.

As for the evolution of the GDP-generating function $\partial_t w_{Q;r}$, it depends if we look in the bulk ($r \neq 0, 1$) or next to the point where the current is measured x_t ($r = 0, 1$). The details

of computation are given appendix F.1. At the boundary we find for example for $r = 0$:

$$\partial_t w_{Q;0} = \frac{\mathrm{e}^{-\lambda} - (\mathrm{e}^{-\lambda} - 1)w_{Q;0}}{\mathrm{e}^{-\lambda} - 1}\left(\partial_t \ln\left\langle \mathrm{e}^{\lambda Q_t(x_t)}\right\rangle - \sum_n \delta(t - t_n)\ln[1 + (\mathrm{e}^{-\lambda} - 1)w_{Q;1}(t)]\right) + \frac{w_{Q;-1} - w_{Q;0}}{2} + \sum_n \delta(t - t_n)\left(\frac{\mathrm{e}^{-\lambda} w_{Q;1}}{1 + (\mathrm{e}^{-\lambda} - 1)w_{Q;1}} - w_{Q;0}\right), \tag{7.23}$$

and in the bulk $r \neq 0, 1$:

$$\partial_t w_{Q;r} = \frac{1}{2}\Delta w_{Q;r} + \frac{\left\langle \eta_{x_t+r} e^{\lambda Q_t(x_t)}(e^{\lambda} - 1)(\eta_{x_t} - e^{-\lambda}\eta_{x_t+1} + (e^{-\lambda} - 1)\eta_{x_t}\eta_{x_t+1})\right\rangle}{2\left\langle e^{\lambda Q_t(x_t)}\right\rangle} + \sum_n \delta(t - t_n)\left(\frac{\left\langle \eta_{x_t+r+1}(1 + (e^{-\lambda} - 1)\eta_{x_t+1})e^{\lambda Q_t(x_t)}\right\rangle}{\left\langle \mathrm{e}^{\lambda Q_t(x_t)}\right\rangle (1 + (\mathrm{e}^{-\lambda} - 1)w_{Q;1}(t))} - w_{Q;r}(t)\right). \tag{7.24}$$

Three major remarks are in order. First, the evolution equation for $w_{Q;r}$ in the bulk is not closed since it involves higher order correlations between occupation numbers such as $\left\langle \eta_{x_t+r}\eta_{x_t}\eta_{x_t+1} e^{\lambda Q_t(x_t)}\right\rangle$. This is classically observed in many body problems, however, in the next chapter, we will be able to provide an exact closure in the long-time limit. Second, it is remarkable that, the way we wrote it, equation (7.23) is in fact closed since it only involves the cumulant generating function $\ln\left\langle \mathrm{e}^{\lambda Q_t(x_t)}\right\rangle$ and one site correlations $w_{Q;r}$; it provides a quite unexpected relation between these quantities. Third, equation (7.22) is not closed because it involves two site correlations $\left\langle \eta_{x_t+1}\eta_{x_t} e^{\lambda Q_t(x_t)}\right\rangle$, however, it will yield a closed relation (7.25) in the long-time limit.

Boundary conditions in the long time limit

Now, we take the long-time limit of the equations derived above by injecting the scaling forms we derived in section 7.1.2, in order to get information about the scaling functions ($\hat{\psi}$, $\hat{\psi}_Q$, Φ, Φ_Q). The method is detailed in appendix F.2, here we summarise the results. To lighten notations, we will simply write $\Phi_Q(v)$, instead of $\Phi_Q(v, \xi, \lambda)$.

Because of the scaling of the cumulant generating function (7.19), $\partial_t \ln\left\langle \mathrm{e}^{\lambda Q_t(x_t)}\right\rangle \underset{t\to\infty}{\longrightarrow} 0$, therefore, from equation (7.22), we deduce:

$$\boxed{\frac{\Phi_Q(0^+)(1 - \Phi_Q(0^-))}{\Phi_Q(0^-)(1 - \Phi_Q(0^+))} = \mathrm{e}^{\lambda}}. \tag{7.25}$$

In particular, this proves that the long time profile $\Phi_Q(v)$ is indeed discontinuous in 0 when $\lambda \neq 0$. This relation expresses the fact that choosing $\lambda > 0$ gives more weight to the configurations where $\eta_{x_t+1} > \eta_{x_t}$. One can heuristically see λ as a drive to the right imposed on particles at site x_t.

The equation for $\partial_t w_{Q;0}$ (7.23), together with the one on $\partial_t w_{Q;1}$ (which we did not write, because it is very similar) yields in the long-time limit:

$$\boxed{\Phi'_Q(0^{\pm}) = \mp 2\Psi\left(\frac{1}{1 - \mathrm{e}^{\mp\lambda}} - \Phi_Q(0^{\pm})\right)}, \tag{7.26}$$

where we have denoted

$$\Psi = \hat{\psi}_Q - \xi \ln[1 + (\mathrm{e}^{-\lambda} - 1)\Phi_Q(0^+)]. \tag{7.27}$$

The apparition of this quantity Ψ is surprising, but it will make a little bit more sense in the next subsection in the study of the tracer, with equation (7.40). These relations (7.26) constitute an unexpected relation between the density profiles and the cumulant generating function which is difficult to understand from a physical point of view.

Eventually, carrying a careful analysis of the microscopic equations, we have obtained the three non trivial relations (7.25, 7.26) in the long time limit between the cumulant generating function and the GDP generating function. This emphasizes the central role played by the GDP $w_{Q;r}$.

7.2.2 From integrated current to tracer position

The same microscopic analysis as above can be done for the tracer's position (*e.g.* [103, 133]) based on the same arguments (especially making use of the known scaling of the quantities). Alternatively, we will show here how to derive some of the equations for the tracer observable from the equations on the integrated current observables.

First boundary condition for the tracer's position

For the first boundary condition (tracer equivalent of (7.25)), we begin by deriving from the master equation (7.1) the evolution equation:

$$\partial_t \ln \left\langle e^{\lambda X_t} \right\rangle = \frac{1}{2} \left[(\mathrm{e}^{\lambda} - 1)(1 - w_1) + (\mathrm{e}^{-\lambda} - 1)(1 - w_{-1}) \right]. \tag{7.28}$$

In the long time limit, because of the scaling (7.9), the left-hand side vanishes and in a similar way as previously, we find:

$$\boxed{\frac{1 - \Phi(0^-)}{1 - \Phi(0^+)} = \mathrm{e}^{\lambda}}. \tag{7.29}$$

For the two other equations, we will rely on the following principle.

General principle relating integrated current and tracer observables

The starting point is the relation (6.2). It implies that

$$\mathbb{P}(X_t \leq x) = \mathbb{P}(Q_t(x) \leq 0). \tag{7.30}$$

We define the large deviation functions (still with $x_t = \lfloor \xi \sqrt{2t} \rfloor$)

$$\varphi(\xi) = -\lim_{t\to\infty} \frac{1}{\sqrt{2t}} \ln \mathbb{P}\left(\frac{X_t}{\sqrt{2t}} = \xi \right), \tag{7.31}$$

$$\varphi_Q(\xi, q) = -\lim_{t\to\infty} \frac{1}{\sqrt{2t}} \ln \mathbb{P}\left(Q_t(x_t) = q \right). \tag{7.32}$$

Then, equation (7.30) implies [100, 101, 171]:

$$\varphi(\xi) = \varphi_Q(\xi, 0). \tag{7.33}$$

Intuitively, this means that in the long time limit, the position of the tracer X_t, and any point $\tilde{x}$ where we observe a zero integrated current ($Q_t(\tilde{x}) = 0$) will almost always be separated by a distance negligible compared to $\sqrt{t}$.

Large deviation functions and cumulant generating functions in the long time limit are related through Legendre transforms:

$$\varphi(\xi) = \lambda\xi - \hat{\psi}(\lambda) \qquad \text{with} \qquad \hat{\psi}'(\lambda) = \xi, \tag{7.34}$$

$$\varphi_Q(\xi, q) = \lambda_Q q - \hat{\psi}_Q(\xi, \lambda_Q) \qquad \text{with} \qquad \partial_{\lambda_Q}\hat{\psi}_Q(\xi, \lambda_Q) = q. \tag{7.35}$$

In particular, if we take $q = 0$, then whenever $\hat{\psi}'(\lambda) = \xi$ and $\partial_{\lambda_Q}\hat{\psi}_Q(\xi, \lambda_Q) = 0$, we have

$$\lambda\xi - \hat{\psi}(\lambda) = -\hat{\psi}_Q(\xi, \lambda_Q). \tag{7.36}$$

A last important remark is in order. Since in the long time limit, observing $\frac{X_t}{\sqrt{2t}} = \xi$ is the same as observing a vanishing integrated current $Q_t(x_t) = 0$, the most probable hydrodynamic profiles (ρ^*, j^*) (7.12, 7.20) leading to these two events are the same. Hence, if $\hat{\psi}'(\lambda) = \xi$ and $\partial_{\lambda_Q}\hat{\psi}_Q(\xi, \lambda_Q) = 0$, then:

$$\boxed{\Phi(v, \lambda) = \Phi_Q(v, \xi, \lambda_Q)}. \tag{7.37}$$

Boundary equations for the tracer

Let us chose an arbitrary λ. Then we fix ξ and λ_Q by demanding that:

$$\hat{\psi}'(\lambda) = \xi, \quad \partial_{\lambda_Q}\hat{\psi}_Q(\xi, \lambda_Q) = 0 \tag{7.38}$$

In the equations for the integrated current (7.26), the quantity

$$\Psi = \hat{\psi}_Q(\xi, \lambda_Q) - \xi \ln[1 + (\mathrm{e}^{-\lambda_Q} - 1)\Phi_Q(0^+, \xi, \lambda_Q)], \tag{7.39}$$

is reminiscent of (7.36) $\hat{\psi}_Q(\xi, \lambda_Q) + \lambda\xi = \hat{\psi}(\lambda)$. Indeed we show that we have, as a consequence of (7.38):

$$\lambda = -\ln[1 + (\mathrm{e}^{-\lambda_Q} - 1)\Phi_Q(0^+, \xi, \lambda_Q)]. \tag{7.40}$$

More precisely, starting from (7.29) and using $\Phi(v, \lambda) = \Phi_Q(v, \xi, \lambda_Q)$ then replacing $\Phi_Q(0^-, \xi, \lambda)$ with (7.25), we get:

$$\begin{aligned} \mathrm{e}^{\lambda} &= \big(1 - \Phi_Q(0^-, \xi, \lambda_Q)\big)\, \frac{1}{1 - \Phi_Q(0^+, \xi, \lambda_Q)} \\ &= \frac{1 - \Phi_Q(0^+, \xi, \lambda_Q)}{1 + (e^{-\lambda_Q} - 1)\Phi_Q(0^+, \xi, \lambda_Q)}\, \frac{1}{1 - \Phi_Q(0^+, \xi, \lambda_Q)}, \end{aligned} \tag{7.41}$$

which gives (7.40) by simplifying and taking the logarithm. Hence it is remarkably true that $\Psi = \hat{\psi}(\lambda)$. Then to conclude, we start from (7.26):

$$\Phi_Q'(0^{\pm}, \xi\lambda_Q) = \mp 2\Psi \left(\frac{1}{1 - \mathrm{e}^{\mp\lambda_Q}} - \Phi_Q(0^{\pm}, \xi\lambda_Q) \right). \tag{7.42}$$

Then we use identities (7.37), $\Psi = \hat{\psi}(\lambda)$ and the inverse of (7.40):

$$\begin{aligned} e^{-\lambda_Q} - 1 &= \frac{e^{-\lambda} - 1}{\Phi(0^+, \lambda)}, \\ 1 - e^{\lambda_Q} &= \frac{1 - e^{\lambda}}{\Phi(0^-, \lambda)}. \end{aligned} \tag{7.43}$$

For the second line, we multiplied the first line by e^{λ_Q}, then used (7.25, 7.29) to simplify the right-hand side. Finally, we find the two other boundary conditions for the tracer

$$\boxed{\Phi'(0^{\pm}) \pm \frac{2\hat{\psi}}{\mathrm{e}^{\pm\lambda} - 1}\Phi(0^{\pm}) = 0}. \tag{7.44}$$

Conclusion

As we can see, the derivation of the boundary conditions (7.25, 7.26, 7.29, 7.44) requires a quite involved analysis of the microscopic equations. In particular, equation (7.44) (or (7.26) for the integrated current observable) shows that the knowledge of the density profiles Φ is enough to recover the cumulant generating function of the tracer's position. This is a very strong result, which until now has not been established from the sole hydrodynamic description (equations of section 6.2 with the transport coefficients of the SEP).

Chapter 8

Exact closure of the hierarchy

The generalised density profiles (GDP) introduced in the previous chapter 7 are central physical quantities, since they characterise the full joint distribution of an observable (tracer position or integrated current) and the occupation numbers in the bath. Strikingly, as we proceed to show, for the SEP, these quantities also verify a surprisingly simple closed equation. Focusing on the tracer position observable, we first recall (section 8.1) some results hinting at the existence of such an equation. Then, in section 8.2 we explain the approach that we followed to construct it.

Our major result, summarised in paragraph 8.2.3, is the existence of an *exact* closure for the infinite hierarchy verified by the GDP, despite the many-body nature of the problem.

In section 8.3, we recover known results thanks to our equation, and go beyond by fully characterising the bath-tracer correlations. Finally, we illustrate the broad scope of validity of this closure in the SEP by showing that it applies to different observables and also out-of-equilibrium settings.

Key result.

- Paragraph 8.2.3: existence of a closed equation for the GDP in the SEP. From this equation, we can easily derive numerous results for various observables in the SEP (section 8.3).

8.1 A closed equation ?

The intuition that the GDP-generating function may verify a simple equation originates from several observations. First, closed form formulas were found to describe N-site correlations in the SEP [190, 191], but also the cumulant generating function of the integrated current and tracer position [99–101]. In addition, closed equations were known for the GDP in some limiting cases [103, 133], which we recall here.

8.1.1 Insight from limiting cases

Here we recall known results from [103, 133]. The following notations for the cumulant generating function and GDP-generating function introduced in the last chapter (7) will be

extensively used here:

$$\psi(\lambda,t) = \ln\left\langle \mathrm{e}^{\lambda X_t}\right\rangle \underset{t\to\infty}{\sim} \hat{\psi}(\lambda)\sqrt{2t}\,, \qquad \hat{\psi}(\lambda) = \sum_{n\geq 1}\hat{\kappa}_n\frac{\lambda^n}{n!}\,, \tag{8.1}$$

$$w_r(\lambda,t) = \frac{\langle \eta_{X_t+r}(t)\,\mathrm{e}^{\lambda X_t}\rangle}{\langle \mathrm{e}^{\lambda X_t}\rangle} \underset{t\to\infty}{\sim} \Phi\left(v=\frac{r}{\sqrt{2t}},\lambda\right)\,, \qquad \Phi(v,\lambda) = \sum_{n\geq 1}\Phi_n(v)\frac{\lambda^n}{n!}\,. \tag{8.2}$$

Correlation profile (order 1 in λ of the GDP)

The correlation profile $g_r(t) = \langle \eta_{X_t+r}X_t\rangle$ converges to the scaling function $\Phi_1(v = r/\sqrt{2t})$ (order 1 in λ of Φ). It was shown that the equation for Φ_1 is closed, and can be written as

$$\Phi_1''(v) + 2v\Phi_1'(v) = 0\,. \tag{8.3}$$

The solution on the two domains $\mathbb{R}^{\pm}$ is $\Phi_1(v) = a_{\pm}\,\mathrm{erfc}(\pm v)$ for $v \gtrless 0$, where we have used the condition $\Phi_1(\pm\infty) = 0$ deduced from (7.14). We determine the integration constants $a_{\pm}$ by using the boundary conditions (7.44) at first order in λ,

$$\Phi_1'(v) + \hat{\kappa}_2\rho = 0 \Rightarrow a_{\pm} = \pm\frac{\sqrt{\pi}}{2}\hat{\kappa}_2\rho\,. \tag{8.4}$$

The second cumulant $\hat{\kappa}_2$ is determined by writing equation (7.29) at first order in λ, from which we recover the well-known expression [98]

$$\hat{\kappa}_2 = \frac{1-\rho}{\rho\sqrt{\pi}}\,, \tag{8.5}$$

and therefore

$$\Phi_1(v) = \mathrm{sign}(v)\frac{1-\rho}{2}\,\mathrm{erfc}(|v|)\,. \tag{8.6}$$

High density limit

We now consider the high density limit $\rho \to 1$. In this case, both the cumulants and the shifted GDP-generating function $\Phi(v) - \rho$ scale as $1-\rho$ (see for instance (8.5) and (8.6) for the scaling at lowest order in λ). This leads us to define

$$\check{\Phi}(v) = \lim_{\rho\to 1}\frac{\Phi(v)-\rho}{1-\rho}\,. \tag{8.7}$$

In this limit, identically to what we argued in 3.3.1, the microscopic equations become closed at linear order in ρ. In the long time limit (note that the microscopic equations can also be solved at all time in this case [103]) this yields

$$\check{\Phi}''(v) + 2v\check{\Phi}'(v) = 0. \tag{8.8}$$

Solving this equation on both domains $v > 0$ and $v < 0$, combined with the condition $\check{\Phi}(\pm\infty) = 0$ deduced from (7.14,8.7), we obtain $\check{\Phi}(v) = A_{\pm}\,\mathrm{erfc}(\pm v)$ for $v \gtrless 0$. The integration constants $A_{\pm}$ are then determined by the boundary conditions at zero (7.44) in the limit $\rho \to 1$,

$$\check{\Phi}'(0^{\pm}) = \frac{\mp 2\hat{\psi}}{\mathrm{e}^{\pm\lambda}-1} \Rightarrow A_{\pm} = \sqrt{\pi}\frac{\hat{\psi}}{\mathrm{e}^{\pm\lambda}-1}\,. \tag{8.9}$$

Finally, using the last condition (7.29), we determine $\hat{\psi}$ in terms of λ in the dense limit:

$$\hat{\psi}(\lambda) = \frac{2(1-\rho)}{\sqrt{\pi}} \sinh^2\left(\frac{\lambda}{2}\right) , \tag{8.10}$$

which coincides with the result obtained from a different approach in [188]. Additionally, we get the profile [103]

$$\Phi(v) = \rho + (1-\rho)\frac{1-\mathrm{e}^{\mp\lambda}}{2}\operatorname{erfc}(\pm v) . \tag{8.11}$$

Low density limit

In the SEP with a tracer, the low density limit is singular because when the bath particles are more and more sparse, the tracer recovers a classical diffusive behavior. This makes the rescaled cumulants diverge (see (8.5)). Therefore, in one dimension, the argument used in 3.3.1 does not hold in this limit.

In order to capture this divergence when $\rho \to 0$, a convenient way is to consider the limit $\rho \to 0$ with $z = \rho r$ and $\tau = \rho^2 t$ fixed. We still have the same scaling variable $v = r/\sqrt{2t} = z/\sqrt{2\tau}$. In this limit, the boundary conditions (7.44, 7.29) become

$$\Phi'(0^\pm) + \frac{\hat{\psi}}{\lambda}\Phi(0^\pm) = 0 , \tag{8.12}$$

$$\Phi(0^+) - \Phi(0^-) = \lambda . \tag{8.13}$$

Poncet et al. [103, 133], trying to reproduce the results of [171], found that, in this limit, the scaling function Φ associated to the generalised profiles verify the following instructive equation

$$\boxed{\Phi''(v) + 2(v+\xi)\Phi'(v) = 0 , \quad \xi = \frac{\mathrm{d}\hat{\psi}}{\mathrm{d}\lambda}} . \tag{8.14}$$

Solving this equation for $v > 0$ and $v < 0$ with the condition $\Phi(\pm\infty) = \rho$, we get $\Phi(v) = \rho + A_\pm \operatorname{erfc}(\pm(v+\xi))$ for $v \gtrless 0$. The integration constants $A_\pm$ are determined by the boundary conditions at zero (8.12),

$$A_\pm = \frac{\rho\hat{\psi}}{\pm\lambda\frac{\mathrm{e}^{-\xi^2}}{\sqrt{\pi}} - \hat{\psi}\operatorname{erfc}(\pm\xi)} . \tag{8.15}$$

Combined with the relation (8.13), this gives an implicit equation for the cumulant generating function (because $\xi = \frac{\mathrm{d}\hat{\psi}}{\mathrm{d}\lambda}$),

$$\frac{\rho\hat{\psi}\operatorname{erfc}(\xi)}{\lambda\frac{\mathrm{e}^{-\xi^2}}{\sqrt{\pi}} - \hat{\psi}\operatorname{erfc}(\xi)} + \frac{\rho\hat{\psi}\operatorname{erfc}(-\xi)}{\lambda\frac{\mathrm{e}^{-\xi^2}}{\sqrt{\pi}} + \hat{\psi}\operatorname{erfc}(-\xi)} = \lambda . \tag{8.16}$$

Expanding in powers of λ using (7.9), we obtain from (8.16) the cumulants (the odd cumulants vanish by symmetry)

$$\hat{\kappa}_2 = \frac{1}{\rho\sqrt{\pi}} , \quad \hat{\kappa}_4 = \frac{3(4-\pi)}{\rho^3\pi^{3/2}} , \quad \cdots \tag{8.17}$$

which coincides with those obtained previously [171]. Furthermore, we obtain the profiles Φ_n (7.13). The exact expressions can be obtained by expanding (8.16) in powers of λ and plugging the result into the solution of (8.14).

8.1.2 First orders by MFT

In order to generalise these closed equations (8.8) and (8.14) valid in some limiting cases to the case of arbitrary density, we begin by computing the long time limit of the GDP-generating function Φ at first orders in λ. Thanks to MFT, this can be achieved by solving the minimisation under linear constraint problem (7.12) on the hydrodynamics fields (ρ, j). This minimisation problem is usually rephrased using Martin-Siggia-Rose formalism [102, 107] or by comparing the probability to observe a fluctuation in a non driven system to the most probable evolution in the same system subject to a weak drive [124] (this latter approach gives a physical interpretation to the Lagrange multiplier $\hat{\rho}(x,t)$ that we are going to introduce: it is the driving force that we must apply at point x at time t in order to make a given evolution (ρ, j) the most probable; this is reminiscent of the Lagrange multipliers giving the constraint forces in Lagrangian mechanics).

Here we introduce a Lagrangian $\mathcal{L}(\rho, j, \hat{\rho})$, where $\hat{\rho}(x,t)$ is a Lagrange multiplier enforcing the conservation equation $\partial_t \rho + \partial_x j = 0$. We recall that $\xi_1[\rho]$ is the position of the tracer at time $t = 1$ for the hydrodynamic profile ρ (see equation (7.7)), and that the functional F encodes the initial condition (6.8). The Lagrangian reads:

$$\begin{aligned}\mathcal{L}(\rho, j, \hat{\rho}) &= \int_0^1 \int_{-\infty}^{\infty} \frac{\left(j + \frac{1}{2}\partial_x \rho\right)^2}{2\rho(1-\rho)} + \hat{\rho}(\partial_t \rho + \partial_x j)\mathrm{d}x\mathrm{d}t + F[\rho(x,0)] - \lambda \xi_1[\rho] \\ &= \int_0^1 \int_{-\infty}^{\infty} \frac{\left(j + \frac{1}{2}\partial_x \rho\right)^2}{2\rho(1-\rho)} - \rho \partial_t \hat{\rho} - j \partial_x \hat{\rho} \mathrm{d}x\mathrm{d}t \\ &\quad + \int_{-\infty}^{\infty} \hat{\rho}(x,1)\rho(x,1) - \hat{\rho}(x,0)\rho(x,0)\mathrm{d}x + F[\rho(x,0)] - \lambda \xi_1[\rho]. \end{aligned} \tag{8.18}$$

We performed an integration by parts with respect to t for $\hat{\rho}\partial_t \rho$ and one with respect to x for $\hat{\rho}\partial_x j$. We then differentiate this Laplacian with respect to $j(x,t)$ and $\rho(x,t)$, yielding (after another space integration by parts for the ρ derivative)

$$\frac{\delta \mathcal{L}}{\delta j(x,t)} = \frac{2j + \partial_x \rho}{2\rho(1-\rho)} - \partial_x \hat{\rho}, \tag{8.19}$$

$$\frac{\delta \mathcal{L}}{\delta \rho(x,t)} = -\partial_x \left(\frac{j + \frac{1}{2}\partial_x \rho}{2\rho(1-\rho)} \right) - \frac{\left(j + \frac{1}{2}\partial_x \rho\right)^2 (1-2\rho)}{2\left(\rho(1-\rho)\right)^2} - \partial_t \hat{\rho}. \tag{8.20}$$

At optimal $(\rho, j) = (q, j^*)$ under the conservation constraint, these two derivatives must vanish, in particular the first one gives $j^* = -\frac{1}{2}\partial_x q + q(1-q)\partial_x \hat{\rho}$. Injected in the conservation equation, this gives an equation for the corresponding Lagrange multiplier $\hat{\rho} = p$ ((q, j^*, p) refer to the fields which are solution of the minimisation problem). Together with the second vanishing derivative, this yields the MFT equations:

$$\partial_t q = \frac{1}{2}\partial_x^2 q - \partial_x \left(q(1-q)\partial_x p \right), \tag{8.21}$$

$$\partial_t p = -\frac{1}{2}\partial_x^2 p - \frac{1-2\rho}{2}(\partial_x p)^2. \tag{8.22}$$

Theses are coupled diffusion and anti-diffusion equations. To solve them, we need boundary conditions, which are obtained by differentiating the Lagrangian with respect to initial and final profiles $\rho(x,0)$ and $\rho(x,1)$; they read:

$$p(x,0) = \frac{\lambda}{q(\xi_1[q],1)}\Theta(x) + \ln\left(\frac{q(x,0)(1-\rho_0(x))}{(1-q(x,0))\rho_0(x)} \right), \tag{8.23}$$

$$p(x,1) = \frac{\lambda}{q(\xi_1[q],1)}\Theta(x - \xi_1[q]), \tag{8.24}$$

where $\rho_0(x)$ is the initial average density near position x, Θ is Heaviside's function. We will mainly focus on flat ($\rho_0(x) = \rho$ constant) and step ($\rho_0(x) = \rho_- + (\rho_+ - \rho_-)\Theta(x)$) initial conditions.

The procedure to solve these equations and perturbative solution at first orders in λ are described in [102]. We introduced the new idea that the solution for q has in fact a deep physical meaning since it corresponds to the long time limit of our GDP-generating function, as shown in the previous chapter 7.1.2. In addition, Grabsch et al. [165] were able to overcome many technical difficulties raised by these equations and compute the generalised density profiles at higher orders. We will give more details on the perturbative resolution of MFT equations in chapter 10.

In the case of initial flat density ρ, we computed the following expansion for the GDP-generating function for $v > 0$ ($v < 0$ is obtained by the symmetry $(v, \lambda) \to (-v, -\lambda)$ which leaves the system unchanged):

$$\begin{aligned}\Phi(v) = \rho + \lambda\frac{1-\rho}{2}\operatorname{erfc}(v) + \lambda^2\left(\frac{(1-\rho)(1-2\rho)}{4\rho}\operatorname{erfc}(v) - \frac{1-\rho}{\pi\rho}\mathrm{e}^{-v^2}\right)\\ + \lambda^3\left((1-\rho)\frac{2(3+\pi)\rho^2 - (12+\pi)\rho + 6 + \pi\rho(1-\rho)}{12\pi\rho^2}\operatorname{erfc}(v)\right.\\ \left. + (1-\rho)^2\frac{2(1-\rho)v - \sqrt{\pi}(1-2\rho)}{2\pi^{3/2}\rho^2}\mathrm{e}^{-v^2} - \frac{(1-\rho)^2}{8\rho}\operatorname{erfc}\left(\frac{v}{\sqrt{2}}\right)^2\right) + O(\lambda^4)\,, \quad (8.25)\end{aligned}$$

In the case of step density profile ($\rho_0(x) = \rho_- + (\rho_+ - \rho_-)\Theta(x)$), we get:

$$\begin{aligned}\Phi_0(v) =& \frac{\rho_+}{2}\operatorname{erfc}(-v - \hat{\kappa}_1) + \frac{\rho_-}{2}\operatorname{erfc}(v + \hat{\kappa}_1)\,,\\ \Phi_1(v > 0) =& \hat{\kappa}_2\Phi_0'(v) + \frac{1}{\Phi_0(0)}\Phi_0(v)(1 - \Phi_0(v)) - \frac{\rho_+(1-\rho_+)}{2\Phi_0(0)}\operatorname{erfc}(-v - \hat{\kappa}_1)\\ & - \frac{(\rho_+ - \rho_-)^2}{\Phi_0(0)}\int_0^\infty \frac{\mathrm{d}z}{2\sqrt{2\pi}}\mathrm{e}^{-\frac{1}{2}(v + 2\hat{\kappa}_1 + z)^2}\operatorname{erfc}\left(\frac{|v-z|}{\sqrt{2}}\right)\,. \quad (8.26)\end{aligned}$$

To get the formula for $v < 0$, we use the symmetry $(v, \lambda, \rho_-, \rho_+) \to (-v, -\lambda, \rho_+, \rho_-)$. We recall that $\hat{\kappa}_n \underset{t\to\infty}{\sim} \frac{\langle X_t^n\rangle_c}{\sqrt{2t}}$ are the rescaled cumulants of the tracer's position. From the formulas above, we derive implicit equations for the cumulants using the boundary conditions (7.44). For instance, we get for the first cumulant, that we will need below:

$$\frac{\rho_-}{1 + \sqrt{\pi}\,\kappa_1\mathrm{e}^{\kappa_1^2}\operatorname{erfc}(-\kappa_1)} = \frac{\rho_+}{1 - \sqrt{\pi}\,\kappa_1\mathrm{e}^{\kappa_1^2}\operatorname{erfc}(\kappa_1)}\,, \quad (8.27)$$

If we now compute the left-hand side of equation 8.14 using these expressions valid at any density, we get a non zero result (vanishing in the low-density limit). In the next section, we build a new closed equation verified by these first order expansions.

8.2 Construction of the closed equation

The closures obtained in the limiting cases presented above, and the rich structure of the SEP [99–101, 190, 191] convey the intuition that a similar closure can be obtained at arbitrary density. Here we present the approach we followed in order to build such an equation. The version developed here varies from the original one [165], but the principle is identical. It was mainly a trial-and-error process, and at each stage, we were mainly guided by the known exact results that we wanted to recover.

8.2.1 Structure of the sought equation

From the closed bulk equations we obtained at high density (8.8) and low density (8.14), we guess that the general equation at arbitrary density takes the form

$$\Phi''(v) + 2(v+\xi)\Phi'(v) = \textcircled{?}\,, \tag{8.28}$$

with $\textcircled{?}$ a right-hand side to be determined. For this new equation to be closed, $\textcircled{?}$ should be expressed in terms of the function $\Phi(v)$ only. From our previous results [103] recalled in section 8.1.1, $\textcircled{?}$ vanishes in both limits $\rho \to 0$ and $\rho \to 1$, as well as at first order in λ (because of (8.3)). For this latter reason, when expanding this equation in powers of λ, we expect that, at order n, the right-hand side $\textcircled{?}$ will act as a source term in the equation for Φ_n, by involving only the profiles Φ_m at lower orders $m < n$. Furthermore equation (8.28), combined with the boundary conditions (7.14,7.29,7.44), has to reproduce the known cumulants of the position of the tracer [100, 101].

Finally, we have some constraints on how the different parameters (λ, $\hat{\psi}$, ξ and ρ) should appear in $\textcircled{?}$:

(C1) The variable λ is explicitly involved in the microscopic equations and the boundary conditions of Section 7.2 only through expressions of the form $\mathrm{e}^{\pm\lambda} - 1$, so we expect that only these combinations appear.

(C2) In the low density equation (8.14), $\hat{\psi}$ does not appear explicitly, only its derivative $\xi = \frac{\mathrm{d}\hat{\psi}}{\mathrm{d}\lambda}$ is involved, so we expect the same to happen at arbitrary density. Similarly, we do not expect other parameters, such as the density ρ, to appear explicitly in the equation.

(C3) The equation we write should have a "proper scaling" with time. Indeed, the left-hand side of equation (8.28) originates from microscopic quantities which scale as $\frac{1}{t}$. For instance, $\Phi''(v)$ appears as the long time limit of the microscopic quantity

$$w_{r+1} + w_{r-1} - 2w_r \underset{t\to\infty}{\sim} \frac{\Phi''(r/\sqrt{2t})}{2t},$$

where we recall that $v = r/\sqrt{2t}$. Similarly, $v\Phi'(v)$ and $\xi\Phi'(v)$ originate from t^{-1} terms, respectively

$$\partial_t w_r(t) \underset{t\to\infty}{\sim} -\frac{r\Phi'(r/\sqrt{2t})}{2t\sqrt{2t}}, \text{ and } \partial_t(\partial_\lambda\psi(\lambda,t))(w_{r+1}(t) - w_r(t)) \underset{t\to\infty}{\sim} \frac{\hat{\psi}'(\lambda)}{\sqrt{2t}}\frac{\Phi'(r/\sqrt{2t})}{\sqrt{2t}}.$$

The same scalings should hold for the right-hand side $\textcircled{?}$.

8.2.2 Closed form for the right-hand side

As a starting point to infer the structure of $\textcircled{?}$, we use its lowest order in λ. In the case of flat initial density ρ, we compute the left-hand side of equation (8.28) with the formula for Φ obtained by solving the MFT equations up to order 3 in λ included (8.25). We get:

$$\textcircled{?} = \frac{2(1-\rho)^2}{\rho}\left(\frac{v}{4\sqrt{2\pi}}\mathrm{e}^{-\frac{v^2}{2}}\operatorname{erfc}\left(\frac{|v|}{\sqrt{2}}\right) - \operatorname{sign}(v)\frac{\mathrm{e}^{-v^2}}{4\pi}\right)\lambda^3 + O(\lambda^4)\,. \tag{8.29}$$

Closing the lowest order

The goal is now to rewrite this expression in terms of the lowest orders of Φ, as guessed above. Using that

$$\int_0^\infty \mathrm{d}z\, \Phi_1'(v+z)\Phi_1'(-z) = \frac{(1-\rho)^2}{\sqrt{2\pi}} \mathrm{e}^{-\frac{v^2}{2}} \operatorname{erfc}\left(\frac{v}{\sqrt{2}}\right), \tag{8.30}$$

we can rewrite the term of (8.29) at order 3 in λ as

$$\textcircled{?} = \begin{cases} -2\dfrac{\lambda}{\rho}\displaystyle\int_0^\infty \mathrm{d}z\, z\Phi'(-z)\Phi'(v+z) + O(\lambda^4) & \text{for } v>0\,, \\ 2\dfrac{\lambda}{\rho}\displaystyle\int_0^\infty \mathrm{d}z\, z\Phi'(z)\Phi'(v-z) + O(\lambda^4) & \text{for } v<0\,. \end{cases} \tag{8.31}$$

This rewriting is one of the simplest way we found to express (8.29) as a closed form function of Φ, which respect the constraint (C3). Indeed, this can be seen as originating from the following microscopic expression of scaling t^{-1}:

$$\begin{aligned} \sum_{u>0} \partial_t w_{-u}(t)(w_{r+u+1}(t) - w_{r+u}(t)) &\underset{t\to\infty}{\sim} \sum_{u>0} u \frac{\Phi'\left(\frac{-u}{\sqrt{2t}}\right)}{2t\sqrt{2t}} \frac{\Phi'\left(\frac{r+u}{\sqrt{2t}}\right)}{\sqrt{2t}} \\ &\underset{t\to\infty}{\sim} \int_{u>0} \frac{\mathrm{d}u}{\sqrt{2t}} \frac{u}{\sqrt{2t}} \frac{\Phi'\left(\frac{-u}{\sqrt{2t}}\right)\Phi'\left(v+\frac{u}{\sqrt{2t}}\right)}{2t} \\ &\underset{t\to\infty}{\sim} \frac{1}{t}\int_{z>0} \mathrm{d}z\, z\Phi'(-z)\,\Phi'(v+z)\,. \end{aligned} \tag{8.32}$$

We replaced the sum by an integral since the integrand is slowly varying when t is large then we performed a change of variable.

The constraint (C2) imposes to rewrite ρ in terms of Φ. Since $\Phi(v) = \rho + O(\lambda)$, we can for instance replace ρ by $\Phi(0^\pm)$. This guess is further confirmed by considering the case of a step initial condition (corresponding to an initial mean density ρ_- for $x<0$ and ρ_+ for $x>0$). Indeed, using the result (8.26) from the MFT computation at first order in λ in this case and using the same method as above, we get a similar expression, which takes the form

$$\textcircled{?} = -2\frac{\lambda}{\Phi_0(0)}\int_0^\infty \mathrm{d}z\, z\Phi'(-z)\Phi'(v+z) + O(\lambda^2)\,, \tag{8.33}$$

written for $v>0$. This equation reduces to (8.31) in the case of a uniform density ρ, since in that case $\Phi = \rho + \lambda\Phi_1 + O(\lambda^2)$. Using now the constraint (C1), we can rewrite $\lambda/\Phi_0(0)$ as $(\mathrm{e}^\lambda - 1)/\Phi(0^+)$ or $(\mathrm{e}^{-\lambda}-1)/\Phi(0^-)$ at lowest order in λ. Therefore, it leads us to propose an equation of the form

$$\Phi''(v) + 2(v+\xi)\Phi'(v) = \frac{\mathrm{e}^{-\lambda}-1}{\Phi(0^-)}\int_0^\infty \mathrm{d}z\, z\Phi'(-z)\Phi'(v+z) + O(\lambda^4)\,, \tag{8.34}$$

for $v>0$. Using this equation in the case of the uniform density, combined with the boundary conditions (7.29,7.44), we can compute the cumulants predicted by this equation. The first two cumulants $\hat\kappa_2$ and $\hat\kappa_4$ coincide with the ones computed previously [98, 100, 102], but not the following one $\hat\kappa_6$. This means that (8.34) must be refined in order to properly account for term of order λ^5 and higher.

Getting higher cumulants

Having introduced convolutions when going from order 2 to order 3 in λ, we conjectured that double convolutions would enable to go beyond these orders. After trying several possibilities, we found that the following equation (valid for $v > 0$) properly reproduces all the known cumulant $\hat{\kappa}_n$ for $n \leq 6$ [100]:

$$\begin{aligned}\Phi''(v) + 2(v+\xi)\Phi'(v) =& \frac{\mathrm{e}^{-\lambda}-1}{\Phi(0^-)}\int_0^\infty \mathrm{d}z\, z\Phi'(-z)\Phi'(v+z) \\ &- \frac{(\mathrm{e}^{-\lambda}-1)^2}{\Phi(0^-)^2}\int_0^\infty \mathrm{d}z \int_0^\infty \mathrm{d}z'\, z'\Phi'(-z)\Phi'(-z')\Phi'(z+z'+v) + O(\lambda^6).\end{aligned} \tag{8.35}$$

Using the symmetry $(v,\lambda) \to \Phi(-v,-\lambda)$ ($\Phi(v,\lambda) = \Phi(-v,-\lambda), \xi(\lambda) = -\xi(-\lambda)$), when $v < 0$:

$$\begin{aligned}\Phi''(v) + 2(v+\xi)\Phi'(v) =& \frac{\mathrm{e}^{\lambda}-1}{\Phi(0^+)}\int_0^\infty \mathrm{d}z\, z\Phi'(z)\Phi'(v-z) \\ &- \frac{(\mathrm{e}^{\lambda}-1)^2}{\Phi(0^+)^2}\int_0^\infty \mathrm{d}z \int_0^\infty \mathrm{d}z'\, z'\Phi'(z)\Phi'(z')\Phi'(v-z-z') + O(\lambda^6).\end{aligned} \tag{8.36}$$

The structure of these equations leads us to introduce the two functions

$$\Omega_\pm(v) = \mp\frac{\mathrm{e}^{\pm\lambda}-1}{\Phi(0^\pm)}\Phi'(v) = 2\hat{\psi}\frac{\Phi'(v)}{\Phi'(0^\pm)} \quad \text{for } v \gtrless 0\,, \tag{8.37}$$

where we have used the boundary condition (7.44) in the last equality. Equation (8.35) then takes the more compact form

$$\begin{aligned}\Omega_+'(v) + 2(v+\xi)\Omega_+(v) =& \int_0^\infty \mathrm{d}z\, z\Omega_-(-z)\Omega_+(v+z) + O(\lambda^6) \\ &- \int_0^\infty \mathrm{d}z \int_0^\infty \mathrm{d}z'\, z'\Omega_-(-z)\Omega_-(-z')\Omega_+(v+z+z').\end{aligned} \tag{8.38}$$

Now, the key point of our approach is to observe that to go from the convolution to the double convolution we have applied an operator $\mathscr{L}_-$ defined by:

$$\mathscr{L}_- f(v) = \int_0^\infty \mathrm{d}z\, \Omega_-(-z) f(v+z), \tag{8.39}$$

allowing us to rewrite equation (8.38) in the form:

$$\Omega_+'(v) + 2(v+\xi)\Omega_+(v) = (1-\mathscr{L}_-)\int_0^\infty \mathrm{d}z\, z\Omega_-(-z)\Omega_+(v+z) + O(\lambda^6). \tag{8.40}$$

Finally, we conjecture that the closed equation, at all orders in λ, is obtained by applying repeatedly the operator $\mathscr{L}_-$ to the right-hand side $1 - \mathscr{L}_- + {\mathscr{L}_-}^2 - {\mathscr{L}_-}^3 ...$, which can be written in the compact form:

$$\boxed{\Omega_+'(v) + 2(v+\xi)\Omega_+(v) = (1+\mathscr{L}_-)^{-1}\int_0^\infty \mathrm{d}z\, z\Omega_-(-z)\Omega_+(v+z)}. \tag{8.41}$$

For $v < 0$, we define similarly

$$\mathscr{L}_+ f(v) = \int_0^\infty \mathrm{d}z\, \Omega_+(z) f(v-z), \tag{8.42}$$

and the closed equation reads:

$$\boxed{\Omega'_-(v) + 2(v+\xi)\Omega_-(v) = (1+\mathscr{L}_+)^{-1} \int_0^\infty \mathrm{d}z\, (-z)\Omega_+(z)\Omega_-(v-z)}. \tag{8.43}$$

The original closure we proposed [165] required to identify more complicated operators $\mathscr{L}_\pm$, which had a matrix form because it coupled the equations on $\Omega_\pm$. We chose to present this version because it is simpler, allowing for a clearer exposition, while based on the same ideas and methodology. It also makes it possible to interpret our closure as a decomposition of the evolution of the density profiles onto a Markovian, linear dynamics, and a non-Markovian part, as argued in appendix G.1.

8.2.3 Compact form and summary

In fact, equations (8.41,8.43) can be put in a simple form. This was for us a strong indication that they may be exact.

Wiener-Hopf equations

Remarkably, the closed equations (8.41, 8.43) are in fact equivalent to much simpler Wiener-Hopf equations (8.45, 8.46). Indeed, if we apply $(1+\mathscr{L}_-)$ to equation (8.41):

$$\begin{aligned}
\int_0^\infty \mathrm{d}z\, z\Omega_-(-z)\Omega_+(v+z) =& (1+\mathscr{L}_-)\left[(\partial_v + 2(v+\xi))\Omega_+(v)\right] \\
\int_0^\infty \mathrm{d}z\, z\Omega_-(-z)\Omega_+(v+z) =& (\partial_v + 2(v+\xi))\Omega_+(v) \\
&+ \int_0^\infty \mathrm{d}z\, \Omega_-(-z)(\partial_v + 2(v+z+\xi))\Omega_+(v+z) \\
0 =& (\partial_v + 2(v+\xi))\left[\Omega_+(v) + \int_0^\infty \mathrm{d}z\, \Omega_-(-z)\Omega_+(v+z)\right]
\end{aligned} \tag{8.44}$$

Finally, since the only solutions to the differential equation $(\partial_v + 2(v+\xi))f(v) = 0$ are proportional to $e^{-(v+\xi)^2}$, there exists an integration constant, which we denote $\frac{\omega e^{\xi^2}}{\sqrt{\pi}}$ (it will be convenient later), such that:

$$\Omega_+(v) + \int_0^\infty \Omega_+(v+z)\Omega_-(-z)\mathrm{d}z = \frac{\omega}{\sqrt{\pi}}\, \mathrm{e}^{-(v+\xi)^2+\xi^2}, \tag{8.45}$$

And identically for Ω_-, with the same integration constant as a consequence of definition (8.37) (which in particular implies $\Omega_+(0) = \Omega_-(0)$):

$$\Omega_-(v) + \int_0^\infty \Omega_+(z)\Omega_-(v-z)\mathrm{d}z = \frac{\omega}{\sqrt{\pi}}\, \mathrm{e}^{-(v+\xi)^2+\xi^2}. \tag{8.46}$$

These two coupled equations can be mapped onto two independent linear equations, upon analytic continuation of Ω_+ to $v < 0$ and Ω_- to $v > 0$ [192]. We give a proof of this fact in

appendix G.2, adapting a remarkable probabilistic argument given in [193] in the case of KPZ equation with weak noise. This finally gives two Wiener-Hopf integral equations,

$$\Omega_+(v) + \int_{-\infty}^{0} \mathrm{d}z\, K(v-z)\, \Omega_+(z) = K(v)\,, \tag{8.47}$$

$$\Omega_-(v) + \int_{0}^{\infty} \mathrm{d}z\, K(v-z)\, \Omega_-(z) = K(v)\,, \tag{8.48}$$

with the Gaussian kernel

$$K(v) = \frac{\omega}{\sqrt{\pi}}\, \mathrm{e}^{-(v+\xi)^2+\xi^2}\,. \tag{8.49}$$

Summary of the equations

We will see just after that these closed equations, together with the boundary conditions obtained in the last chapter (7), can be solved to give the full GDP and cumulants of the tracer's position in function of ρ and λ. We have finally found that the rescaled derivatives of the generalised density profiles,

$$\Omega_\pm(v) = 2\hat{\psi}\frac{\Phi'(v)}{\Phi'(0^\pm)} \quad \text{for } v \gtrless 0\,, \tag{8.50}$$

obey the simple linear equation

$$\boxed{\Omega_\pm(v) + \int_{\mathbb{R}^\mp} \mathrm{d}z\, K(v-z)\, \Omega_\pm(z) = K(v)}\,, \tag{8.51}$$

with the kernel

$$K(v) = \frac{\omega}{\sqrt{\pi}}\, \mathrm{e}^{-(v+\xi)^2+\xi^2}\,, \tag{8.52}$$

where the parameter ω is determined from the boundary condition

$$\Omega_+(0) = \Omega_-(0) = 2\hat{\psi}\,, \tag{8.53}$$

which is a consequence of the definition (8.50). This equation is completed by the boundary relations, derived above from microscopic considerations (chapter 7),

$$\Phi'(0^\pm) \pm \frac{2\hat{\psi}}{\mathrm{e}^{\pm\lambda}-1}\Phi(0^\pm) = 0\,, \tag{8.54}$$

$$\lim_{v\to\pm\infty} \Phi(v) = \rho\,, \tag{8.55}$$

$$\frac{1-\Phi(0^-)}{1-\Phi(0^+)} = \mathrm{e}^{\lambda}\,. \tag{8.56}$$

In a nutshell, starting from the previously known closed equations for the GDP in the dense and dilute limits, and on the basis of the first orders in λ we computed at arbitrary density using MFT, we managed to build a closed equation that correctly accounts for these first orders. We then conjectured that this equation holds at all orders in λ. Initially [165], we supported our conjecture by showing that its predictions exactly matches all known results, in particular the cumulant generating function of the tracer's position. Since then, the closed equations (8.45,8.46) were proved by solving exactly the MFT equations (8.21) using the inverse scattering transform [172].

8.3 Results from the closed equation approach

First, we describe the resolution procedure, which makes it possible to get analytical expressions for the cumulants of the position of the tracer and the GDP. Then, we implement the procedure in the case of a flat initial density. Finally, we extend our results to the case of initial step density and to the integrated current observable (defined in section 7.1.3).

8.3.1 Solving the Wiener-Hopf equations for the profiles and the cumulants

The solution of the Wiener-Hopf equations (8.51) can be expressed in terms of the half Fourier transforms $\hat{\Omega}_{\pm}^{(\pm)}$ of $\Omega_{\pm}$, defined as

$$\hat{\Omega}_{\pm}^{(\pm)}(k) = \int_{\mathbb{R}^{\pm}} \mathrm{d}v\, \Omega_{\pm}(v)\, \mathrm{e}^{\mathrm{i}kv}\,. \tag{8.57}$$

The solution of (8.51) is described in [106] and is obtained by solving a Riemann problem. It reads:

$$\hat{\Omega}_{\pm}^{(\pm)}(k) = \exp\left[\int_{\mathbb{R}^{\pm}} \frac{\mathrm{d}x}{2\pi} \mathrm{e}^{\mathrm{i}kx} \int_{-\infty}^{\infty} \mathrm{d}u\, \mathrm{e}^{-\mathrm{i}ux} \ln(1+\hat{K}(u))\right] - 1\,, \tag{8.58}$$

where

$$\hat{K}(k) = \int_{-\infty}^{\infty} K(v)\mathrm{e}^{\mathrm{i}kv}\mathrm{d}v = \omega\, \mathrm{e}^{-\frac{1}{4}(k+2\mathrm{i}\xi)^2}\,. \tag{8.59}$$

Inserting the expression of $\hat{K}$ (8.59) and expanding in powers of ω, we get

$$\int_{\mathbb{R}^{\pm}} \frac{\mathrm{d}x}{2\pi} \mathrm{e}^{\mathrm{i}kx} \int_{-\infty}^{\infty} \mathrm{d}u\, \mathrm{e}^{\mathrm{i}ux} \ln(1+\hat{K}(u)) = -Z_{\pm}\left(\omega, \xi - \frac{\mathrm{i}k}{2}\right)\,, \tag{8.60}$$

with

$$Z_{\pm}(\omega,\xi) = \frac{1}{2}\sum_{n\geq 1} \frac{(-\omega\, \mathrm{e}^{\xi^2})^n}{n} \operatorname{erfc}\left(\pm\sqrt{n}\,\xi\right)\,. \tag{8.61}$$

With the definitions (8.57) of the Fourier transforms, this explicitly gives

$$\int_0^{\infty} \Omega_+(v)\mathrm{e}^{\mathrm{i}kv}\mathrm{d}v = \exp\left[-Z_+\left(\omega, \xi - \frac{\mathrm{i}k}{2}\right)\right] - 1\,, \tag{8.62}$$

$$\int_{-\infty}^{0} \Omega_-(v)\mathrm{e}^{\mathrm{i}kv}\mathrm{d}v = \exp\left[-Z_-\left(\omega, \xi - \frac{\mathrm{i}k}{2}\right)\right] - 1\,. \tag{8.63}$$

These expressions are convenient to get perturbative expansions in powers of λ, as we will see below. For arbitrary values of λ, the expressions (8.58) are more practical. For instance, setting $k = \pm\mathrm{i}s$ in (8.58) and letting $s \to \infty$, we get

$$\hat{\Omega}_{\pm}^{(\pm)}(\pm\mathrm{i}s) \underset{s\to\infty}{\simeq} \frac{1}{2\pi s} \int_{-\infty}^{\infty} \ln(1+\hat{K}(u))\mathrm{d}u\,, \tag{8.64}$$

while on the other hand, from the definition (8.57) we have

$$\hat{\Omega}_{\pm}^{(\pm)}(\pm\mathrm{i}s) \underset{s\to\infty}{\simeq} \frac{1}{s}\,\Omega_{\pm}(0) = \frac{1}{s}\,2\hat{\psi}\,, \tag{8.65}$$

where we have used that $\Omega_\pm(0) = 2\hat{\psi}$ from the definition of $\Omega_\pm$ (8.50). Combining these two asymptotic results, we get

$$\hat{\psi} = \frac{1}{4\pi}\int_{-\infty}^{\infty} \ln(1+\hat{K}(u))\mathrm{d}u\,. \tag{8.66}$$

Using the expression of $\hat{K}$ (8.59) and expanding in powers of ω, this becomes

$$\hat{\psi} = -\frac{1}{2\sqrt{\pi}}\mathrm{Li}_{\frac{3}{2}}(-\omega)\,, \tag{8.67}$$

where $\mathrm{Li}_\nu(z) = \sum_{n\geq 1} z^n/n^\nu$ is the polylogarithm function. It relates the parameter ω and the cumulant generating function $\hat{\psi}$. Since $\xi = \frac{\mathrm{d}\hat{\psi}}{\mathrm{d}\lambda}$, one can thus think of $\Omega_\pm$ as parametrised by $\hat{\psi}$. At this stage, the function $\hat{\psi}(\lambda)$ is not known. It can be determined in the following way:

1. The integration of $\Omega_\pm$ on $\mathbb{R}^\pm$ with the boundary conditions at infinity (8.55) gives a relation between $\Phi(0^+)$ and $\Phi'(0^+)$, and between $\Phi(0^-)$ and $\Phi'(0^-)$. It can be obtained by setting $k = 0$ in (8.62,8.63):

$$\int_0^\infty \Omega_+ = 2\hat{\psi}\frac{\rho - \Phi(0^+)}{\Phi'(0^+)} = \exp\left[-Z_+(\omega,\xi)\right] - 1\,, \tag{8.68}$$

$$\int_{-\infty}^0 \Omega_- = 2\hat{\psi}\frac{\Phi(0^-) - \rho}{\Phi'(0^-)} = \exp\left[-Z_-(\omega,\xi)\right] - 1\,. \tag{8.69}$$

2. Combining these relations with the boundary conditions (8.54) yield $\Phi(0^+)$ and $\Phi(0^-)$, parametrised by λ and $\hat{\psi}$ (via ω and ξ):

$$\Phi(0^+) = \rho\frac{\mathrm{e}^\lambda - 1}{\mathrm{e}^\lambda - \mathrm{e}^{-Z_+(\omega,\xi)}}\,, \tag{8.70}$$

$$\Phi(0^-) = \rho\frac{\mathrm{e}^{-\lambda} - 1}{\mathrm{e}^{-\lambda} - \mathrm{e}^{-Z_-(\omega,\xi)}}\,. \tag{8.71}$$

3. Using finally the relation (8.56) which relates $\Phi(0^+)$ and $\Phi(0^-)$, we obtain the cumulant generating function $\hat{\psi}(\lambda)$.

We now illustrate how this procedure can be applied to obtain the cumulants and the profiles Φ_n at lowest orders in λ.

8.3.2 Expansions in powers of λ

Here we compute the cumulants of the tracer and GDP following the procedure described above with initial density ρ, and check that they are in agreement with the known cumulants [100] and with Monte Carlo simulations of the SEP (figure 8.1).

For the cumulants

Inserting the expansion of $\hat{\psi}$ in powers of λ (7.9) into equation (8.67), we obtain the expansion of ω in powers of λ,

$$\omega = \sqrt{\pi}\hat{\kappa}_2\lambda^2 + \frac{\sqrt{\pi}}{12}(\hat{\kappa}_4 + 3\sqrt{2\pi}\hat{\kappa}_2^2)\lambda^4 + \cdots\,. \tag{8.72}$$

Note that the odd order cumulants vanish, as expected. We also have by definition

$$\xi = \frac{\mathrm{d}\hat{\psi}}{\mathrm{d}\lambda} = \hat{\kappa}_2\lambda + \hat{\kappa}_4\frac{\lambda^3}{6} + \cdots . \tag{8.73}$$

Plugging these expansions into the expressions (8.70,8.71) give $\Phi(0^{\pm})$ in terms of the cumulants. Inserting these results into the last relation (7.29), we obtain the cumulants

$$\hat{\kappa}_2 = \frac{1-\rho}{\rho\sqrt{\pi}} , \tag{8.74}$$

$$\hat{\kappa}_4 = \frac{(1-\rho)}{\pi^{3/2}\rho^3}\left(12(1-\rho)^2 - \pi(3 - 3(4-\sqrt{2})\rho + (8-3\sqrt{2})\rho^2)\right) . \tag{8.75}$$

$$\begin{aligned}\hat{\kappa}_6 = \frac{(1-\rho)}{\pi^{5/2}\rho^5}\Big(&30\pi\left(2\left(9\sqrt{2}-20\right)\rho^2 + \left(60-18\sqrt{2}\right)\rho - 15\right)(1-\rho)^2 \\ &- \pi^2\left(8\left(-17+15\sqrt{2}-5\sqrt{3}\right)\rho^4 + \left(480-300\sqrt{2}+80\sqrt{3}\right)\rho^3\right. \\ &\left.+5\left(-114+45\sqrt{2}-8\sqrt{3}\right)\rho^2 - 45\left(\sqrt{2}-6\right)\rho - 45\right) + 1020(1-\rho)^4\Big) .\end{aligned} \tag{8.76}$$

These expressions coincide with the cumulants computed by Bethe ansatz in Ref. [100]. This is expected, since we have constructed our starting equation (8.35) to reproduce these cumulants. We have computed the next cumulants, up to order 10, by implementing the procedure described above with Mathematica. These cumulants also coincide with those obtained from Ref. [100]. This provides a strong nontrivial validation of our integral equations (8.51). We have thus found an alternative parametrization for the cumulant generating function to the one obtained in [100]. We will show below that we can actually recover the exact same parametrization of Ref. [100].

For the generalised profiles

Having obtained the cumulant generating function $\hat{\psi}(\lambda)$, we can go further than [100] and obtain the profiles Φ_n which encode the bath-tracer correlations. Indeed, we have the expression of $\xi = \frac{\mathrm{d}\hat{\psi}}{\mathrm{d}\lambda}$ and ω in terms of λ, via equation (8.67). We thus have $\Omega_{\pm}(v)$ in terms of λ from the solution of (8.51). We then obtain $\Phi(v)$ by integration of $\Omega_{\pm}$, with the definition (8.50):

$$\Phi(v>0) = \rho + \frac{\Phi(0^+)}{\mathrm{e}^{\lambda}-1}\int_v^{\infty}\Omega_+(z)\mathrm{d}z , \tag{8.77}$$

$$\Phi(v<0) = \rho + \frac{\Phi(0^-)}{\mathrm{e}^{-\lambda}-1}\int_{-\infty}^{v}\Omega_-(z)\mathrm{d}z , \tag{8.78}$$

where we have used the boundary conditions at infinity (8.55). Note that we have already obtained the expressions of $\Phi(0^{\pm})$, given by (8.70,8.71), in the derivation of the cumulants. Therefore, expanding (8.77), we get the profiles, for example

$$\Phi_0(v>0) = \rho , \tag{8.79}$$

$$\Phi_1(v>0) = \frac{1-\rho}{2}\operatorname{erfc}(v) , \tag{8.80}$$

$$\Phi_2(v>0) = \frac{(1-\rho)(1-2\rho)}{2\rho}\operatorname{erfc}(v) - \frac{2}{\pi}\frac{(1-\rho)^2}{\rho}\mathrm{e}^{-v^2} , \tag{8.81}$$

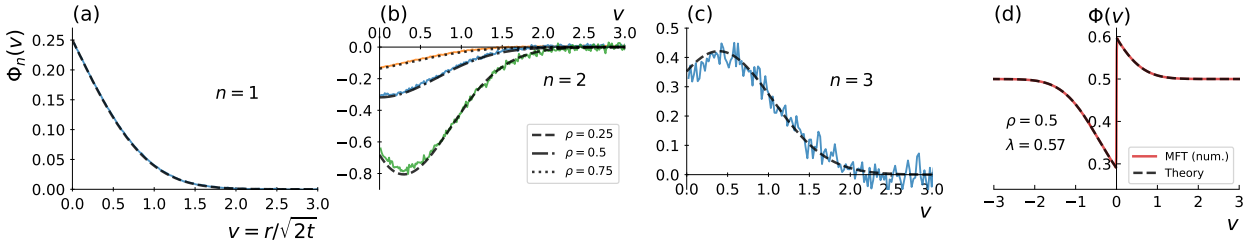

Figure 8.1: **SEP.** Generalised density profiles (GDP) of order **(a)** $n = 1$ at density $\rho = 0.5$, **(b)** $n = 2$ at densities $\rho = 0.25$, 0.5 and 0.75, and **(c)** $n = 3$ at density $\rho = 0.5$. The solid lines correspond to simulations of the SEP (see appendix A), performed at time $t = 3000$ on a lattice of 5000 sites. The averaging is performed over 10^8 realisations. The dashed lines are the theoretical predictions (8.80,8.81,8.82). **(d)** GDP-generating function at $\rho = 0.5$ and $\lambda = 0.57$, obtained from solving numerically the Wiener-Hopf equation (8.51) (dashed line, see Section 8.3.2), compared to the numerical solution (red solid line) of the MFT equations (8.21) obtained from the algorithm described in [108].

$$\begin{aligned}\Phi_3(v>0) =&(1-\rho)\frac{2(3+\pi)\rho^2-(12+\pi)\rho+6+\pi\rho(1-\rho)}{2\pi\rho^2}\operatorname{erfc}(v)\\ &+3(1-\rho)^2\frac{2(1-\rho)v-\sqrt{\pi}(1-2\rho)}{\pi^{3/2}\rho^2}\mathrm{e}^{-v^2}-\frac{3(1-\rho)^2}{4\rho}\operatorname{erfc}\left(\frac{v}{\sqrt{2}}\right)^2,\end{aligned}\tag{8.82}$$

The first few profiles Φ_n are represented in figure 8.1, compared to numerical simulations of the SEP.

The first order profile $\Phi_1(v)$ gives the long-time asymptotics of the covariance $\widetilde{g}_r(t) = \mathrm{Cov}(X_t, \eta_{X_t}+r)$ (correlation profile), with $v = r/\sqrt{2t}$. For $v > 0$, this covariance is positive, indicating that an increase of X_t (displacement towards the right) is correlated with an increase of the occupation of the sites in front of the tracer. The profile Φ_1 thus provides a quantitative measurement of the "jam" that forms in front of the tracer when it moves in a given direction (see figure 8.1(a)).

Similarly, the second order profile $\Phi_2(v)$ is the long time limit of $\mathrm{Cov}(X_t^2, \eta_{X_t+r})$. It measures the correlations between the amplitude of the fluctuations of the tracer, and the density around it. This function is negative, meaning that these two quantities are anti-correlated. This can be interpreted in the following way: a decrease of the occupation of the sites around the tracer gives more space for the tracer to fluctuate and thus increases its fluctuations. Surprisingly, when the mean density of particles becomes less than 1/2, Φ_2 becomes non-monotonic, indicating that this anti-correlation effect is stronger at a given distance (rescaled by $\sqrt{t}$) from the tracer.

Conservation relation and numerical resolution

Using the expressions above for the profiles, one can check that the conservation relation

$$\int_0^\infty(\Phi(v)-\rho)\mathrm{d}v-\int_{-\infty}^0(\Phi(v)-\rho)\mathrm{d}v=\rho\xi\tag{8.83}$$

holds up to $O(\lambda^6)$. We have further checked numerically that this relation holds non-perturbatively in λ.

This relation is particularly useful to implement a numerical computation of the profile $\Phi(v)$ from the closed Wiener-Hopf equation (8.51). Indeed, we have an explicit analytical

solution (8.62,8.63) only in Fourier space, and inverting it to real space can be difficult. Numerically, it is much more stable and faster to solve directly in real space by using the following procedure:

1. Select an initial "guess" for the values of ω and ξ;
2. Discretise the Wiener-Hopf equations (8.51) and solve them for $\Omega_\pm(v)$;
3. We then need to determine the parameters λ and ρ. They can be deduced from $\Omega_\pm(v)$ from (8.77,8.78), but that introduces two new parameters, $\Phi(0^+)$ and $\Phi(0^-)$. One relation between them is given by the cancellation of the velocity (8.56). In principle, the last relation needed is $\xi = \frac{\mathrm{d}\hat{\psi}}{\mathrm{d}\lambda}$, since $\hat{\psi} = \Omega_+(0)/2$ is known. However, this relation is not practical to use because we cannot easy compute the derivative with respect to λ. This last equation is however conveniently replaced by the conservation relation (8.83), which can be used straightforwardly;
4. Finally, having determined all the parameters, the profile $\Phi(v)$ is obtained from (8.77,8.78).

This procedure can be implemented easily thanks to the conservation relation (8.83). We have used it to plot the profile $\Phi(v)$ for an arbitrary value of λ, as shown in figure 8.1(d).

8.3.3 Extensions to other situations and observables in the SEP

Although we have focused on the example of tracer diffusion in the SEP with a mean density ρ, our closed equations (8.51) can be applied to various other situations. Here, we describe explicitly the extension to other situations and observables within the SEP, give exact expression for the profiles Φ and discuss some of the physical consequences of these results.

An out-of-equilibrium situation: SEP with an initial step density profile

We consider a SEP with a mean initial step density ρ_+ for $v > 0$ and ρ_- for $v < 0$, which constitutes a paradigmatic example of a system that remains out-of-equilibrium at all times. The tracer is initially placed at the origin. The microscopic evolution equations of section 7.2 are unchanged, and so are the boundary relations (8.54,8.56) deriving from them. Only the boundary condition at infinity (8.55) is changed into

$$\lim_{v\to\pm\infty} \Phi(v) = \rho_\pm \tag{8.84}$$

to take into account the imbalance of density.

In this case, we found that the closed equations (8.51) still apply. Indeed, by following the procedure described at the end of section 8.3.1, we obtain the cumulants $\hat{\kappa}_n$ of the position of the tracer, which coincide with those computed using Bethe ansatz in [100]. In this case, the left/right symmetry is broken by the difference of density on the two domains $x > 0$ and $x < 0$, so the odd cumulants are now nonzero. For instance, the first cumulant is obtained from the solution of the equation

$$\frac{\rho_-}{1 + \sqrt{\pi}\,\hat{\kappa}_1 \mathrm{e}^{\hat{\kappa}_1^2}\,\mathrm{erfc}(-\hat{\kappa}_1)} = \frac{\rho_+}{1 - \sqrt{\pi}\,\hat{\kappa}_1 \mathrm{e}^{\hat{\kappa}_1^2}\,\mathrm{erfc}(\hat{\kappa}_1)}\,, \tag{8.85}$$

and the higher order cumulants have explicit expressions in terms of $\hat{\kappa}_1$. For instance,

$$\hat{\kappa}_2 = \hat{\kappa}_1^2 \left(2\pi \mathrm{e}^{2\hat{\kappa}_1^2} \hat{\kappa}_1 \,\mathrm{erfc}\left(\sqrt{2}\hat{\kappa}_1\right) - \sqrt{2\pi} + \frac{4\pi \mathrm{e}^{2\hat{\kappa}_1^2} \hat{\kappa}_1 \rho_+ \left(\rho_+^2 - 3\rho_-\rho_+ + 2\rho_-\right)}{\left(\rho_- - \rho_+\right)^3} \right), \tag{8.86}$$

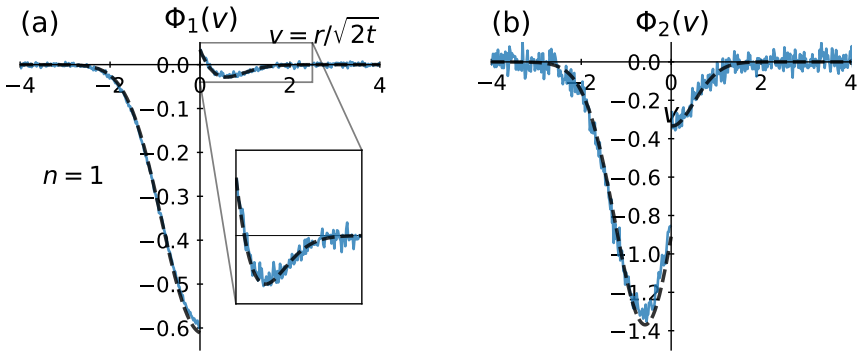

Figure 8.2: **SEP with an initial step density.** Generalised density profiles (GDP) of order **(a)** $n = 1$ and **(b)** $n = 2$ for a step of density $\rho_- = 0.7$ and $\rho_+ = 0.2$. Solid lines: result of the simulations, computed at $t = 1500$ on a lattice with 2000 sites, with the averaging performed over 10^8 realisations. Dashed lines: analytical predictions obtained from the resolution of the Wiener-Hopf equation (8.51). For instance $\Phi_1(v)$ is given by (8.88).

in agreement with [100].

Our procedure additionally yields the generalised density profiles, for instance

$$\Phi_0(v) = \frac{\rho_+}{2}\,\mathrm{erfc}(-v-\hat\kappa_1) + \frac{\rho_-}{2}\,\mathrm{erfc}(v+\hat\kappa_1)\,, \tag{8.87}$$

$$\begin{aligned}\Phi_1(v) = {}& \frac{2\sqrt{\pi}\mathrm{e}^{\hat\kappa_1^2}\hat\kappa_1\rho_-\left(1-\rho_+\right)-\left(\rho_-\rho_+\right)^2}{2\left(\rho_--\rho_+\right)}\,\mathrm{erfc}\left(\hat\kappa_1+v\right)\\ & - \frac{\mathrm{e}^{-(\hat\kappa_1+v)^2}\left(4\sqrt{\pi}\mathrm{e}^{2\hat\kappa_1^2}\hat\kappa_1^3\left(\left(\rho_--\rho_+\right)^3\mathrm{erfc}\left(\sqrt{2}\hat\kappa_1\right)+2\rho_+\left(\rho_+^2+\rho_-\left(2-3\rho_+\right)\right)\right)-2\sqrt{2}\hat\kappa_1^2\left(\rho_--\rho_+\right)^3\right)}{2\left(\rho_--\rho_+\right)^2}\\ & + \frac{1}{2}\sqrt{\pi}\mathrm{e}^{\hat\kappa_1^2}\hat\kappa_1\left(\rho_+-\rho_-\right)\left(4\mathrm{T}\left(\sqrt{2}\hat\kappa_1,\frac{\hat\kappa_1+v}{\hat\kappa_1}\right)-4\mathrm{T}\left(2\hat\kappa_1+v,\frac{v}{2\hat\kappa_1+v}\right)+\mathrm{erfc}\left(\frac{2\hat\kappa_1+v}{\sqrt{2}}\right)-\mathrm{erfc}\left(\hat\kappa_1\right)\right)\,,\end{aligned} \tag{8.88}$$

for $v > 0$ and $\hat\kappa_1 > 0$, and where T is Owen's T-function defined by [194]

$$\mathrm{T}(h,a) = \frac{1}{2\pi}\int_0^a \frac{\mathrm{e}^{-\frac{h^2}{2}(1+x^2)}}{1+x^2}\mathrm{d}x\,. \tag{8.89}$$

Similar expressions can be written for $\hat\kappa_1 < 0$. The values of $\Phi_n(v<0)$ can be obtained by the symmetry $\Phi(-v,\lambda,\rho_+,\rho_-) = \Phi(v,-\lambda,\rho_-,\rho_+)$. The first two profiles Φ_n for $n = 1$ and 2 are represented in Fig. 8.2.

Unlike the case of the flat initial density, the profiles Φ_n are no longer symmetric or anti-symmetric, but their physical meaning remains the same. $\Phi_1(v)$ again measures the covariance between X_t and η_{X_t+r} at large times. For $v > 0$ and close to 0, it is still positive, indicating that a displacement of the tracer towards the right leads to an increase of the density of particles in front of the tracer. Surprisingly, unlike the case of the flat density, $\Phi_1(v>0)$ changes sign at a given distance (rescaled by $\sqrt{t}$) from the tracer. This indicates that for v larger than this critical value, the effect is inverted: a displacement of the tracer towards the right is correlated with a *decrease* of the density. This unexpected behaviour is fully quantified by our computation of the generalised profile Φ_1, and is stressed by the inset in Fig. 8.2(a).

Another observable: the integrated current

We now consider the integrated current through a point $Q_t(x)$, that we introduced in the previous chapter 7, which was studied in [100, 101] and [99, 107, 108] in the case $x = 0$. We recall its definition:

$$Q_t(x) = \sum_{r \geq 1} (\eta_{r+x}(t) - \eta_r(0)) \ . \tag{8.90}$$

We recall the notations we introduced for the long-time limits of the cumulant generating function and GDP-generating function, where $x_t = \lfloor \xi \sqrt{2t} \rfloor$:

$$\psi_Q(\lambda, \xi, t) = \ln \left\langle \mathrm{e}^{\lambda Q_t(x_t)} \right\rangle \underset{t\to\infty}{\sim} \hat{\psi}_Q(\lambda, \xi)\sqrt{2t} \ , \tag{8.91}$$

$$w_{Q;r}(\lambda, \xi, t) = \frac{\langle \eta_{x_t+r}(t)\, \mathrm{e}^{\lambda Q_t(x_t)} \rangle}{\langle \mathrm{e}^{\lambda Q_t(x_t)} \rangle} \underset{t\to\infty}{\sim} \Phi_Q \left(v = \frac{r}{\sqrt{2t}}, \xi, \lambda \right) \ . \tag{8.92}$$

As discussed in section 7.2.2, the knowledge of the quantities $Q_t(x)$ for all x makes it possible to recover the position of the tracer. Moreover, we have seen (equation (7.37)) that the long-time limit Φ of the GDP-generating function for the tracer observable is equal to the one of the integrated Φ_Q provided that we make the good choice of parameters.

As a consequence, the closed equations (8.51) are expected to hold for this observable as well, provided that we replace the boundary conditions by the one for the integrated current computed in section 7.2.1. To sum up, we have the following equations (we do not write the dependencies on λ, ξ). The boundary equations obtained from microscopic considerations:

$$\frac{\Phi_Q(0^+)(1 - \Phi_Q(0^-))}{\Phi_Q(0^-)(1 - \Phi_Q(0^+))} = \mathrm{e}^{\lambda} \ , \tag{8.93}$$

$$\Phi'_Q(0^\pm) = \mp 2\Psi \left(\frac{1}{1 - \mathrm{e}^{\mp\lambda}} - \Phi_Q(0^\pm) \right) \ , \tag{8.94}$$

which involves the quantity originating from the moving $x_t = \lfloor \xi \sqrt{2t} \rfloor$:

$$\Psi = \hat{\psi}_Q - \xi \ln[1 + (\mathrm{e}^{-\lambda} - 1)\Phi_Q(0^+)] \ . \tag{8.95}$$

We define similarly the rescaled derivatives of the generalised profiles:

$$\Omega_\pm(v) = 2\Psi \frac{\Phi'_Q(v)}{\Phi'_Q(0^\pm)} \qquad \text{for } v \gtrless 0 \ , \tag{8.96}$$

still obey the simple linear equation

$$\Omega_\pm(v) + \int_{\mathbb{R}^\mp} \mathrm{d}z \, K(v - z)\, \Omega_\pm(z) = K(v) \ , \tag{8.97}$$

with the kernel

$$K(v) = \frac{\omega_Q}{\sqrt{\pi}} \, \mathrm{e}^{-(v+\xi)^2 + \xi^2} \ , \tag{8.98}$$

In the case of a step initial density:

$$\lim_{v \to \pm\infty} \Phi_Q(v) = \rho_\pm \ , \tag{8.99}$$

Then, the boundary conditions (8.94) combined to the solution (8.62,8.63) where the Fourier variable k is taken equal to zero, yield:

$$1 + \int_0^\infty \Omega_+ = 1 + 2\Psi \frac{\rho_+ - \Phi_Q(0^+)}{\Phi'_Q(0^+)} = 1 - \frac{\rho_+ - \Phi_Q(0^+)}{\frac{1}{1-\mathrm{e}^{-\lambda}} - \Phi_Q(0^+)} = \exp\left[-Z_+(\omega, \xi)\right] \ , \tag{8.100}$$

$$1+\int_{-\infty}^{0}\Omega_{-}=1+2\Psi\frac{\Phi_Q(0^-)-\rho_-}{\Phi_Q'(0^-)}=1+\frac{\Phi_Q(0^-)-\rho_-}{\frac{1}{1-\mathrm{e}^{+\lambda}}-\Phi_Q(0^-)}=\exp\left[-Z_-(\omega,\xi)\right]\,. \tag{8.101}$$

Making the product of these two equations, then simplifying the left-hand side using the boundary condition (8.93), and the right-hand side using $Z_+(\omega,\xi)+Z_-(\omega,\xi)=-\ln(1+\omega_Q\mathrm{e}^{\xi^2})$ (because $\mathrm{erfc}(\xi\sqrt{n})+\mathrm{erfc}(-\xi\sqrt{n})=2$), we find

$$\omega_Q\mathrm{e}^{\xi^2}=\rho_-(1-\rho_+)(\mathrm{e}^{\lambda}-1)+\rho_+(1-\rho_-)(\mathrm{e}^{-\lambda}-1)\,, \tag{8.102}$$

and thus

$$\hat{\psi}_Q=-\frac{1}{2\sqrt{\pi}}\mathrm{Li}_{\frac{3}{2}}(-\omega_Q)+\xi\ln[1+(\mathrm{e}^{-\lambda}-1)\Phi_Q(0^+)]\,. \tag{8.103}$$

Combining this expression with the value

$$(\mathrm{e}^{-\lambda}-1)\Phi_Q(0^+)=(1+\rho_+(\mathrm{e}^{-\lambda}-1))\mathrm{e}^{Z_+(\omega_Q,\xi)}-1 \tag{8.104}$$

obtained from (8.62) at $k=0$, we finally get

$$\hat{\psi}_Q(\lambda,\xi)=\xi\ln[1+(\mathrm{e}^{-\lambda}-1)\rho_+]-\sum_{n\geq 1}\frac{(-\omega_Q\mathrm{e}^{\xi^2})^n}{2n}\left(\frac{\mathrm{e}^{-n\xi^2}}{\sqrt{n\pi}}-\xi\,\mathrm{erfc}(\sqrt{n}\xi)\right)\,. \tag{8.105}$$

This expression coincides exactly with the result of Ref. [100, 101]. That supports the exactness of our main equations (8.51), non-perturbatively in λ.

Furthermore, we additionally obtain the profiles $\langle\eta_{x_t+r}(t)Q_t(x_t)^n\rangle_c \underset{t\to\infty}{\simeq} \Phi_{Q;n}(v)$ which measure the correlations between the current and the density in the hydrodynamic limit. For instance, in the case $\xi=0$ (current through the origin),

$$\Phi_{Q;1}(v)=\frac{\rho(1-\rho)}{2}\,\mathrm{erfc}(v)\,, \tag{8.106a}$$

$$\Phi_{Q;2}(v)=\frac{\rho(1-\rho)(1-2\rho)}{2}\,\mathrm{erfc}(v)\,, \tag{8.106b}$$

$$\Phi_{Q;3}(v)=\frac{\rho(1-\rho)(1-3\rho+3\rho^2)}{2}\,\mathrm{erfc}(v)-3\frac{\rho^2(1-\rho)^2}{4}\,\mathrm{erfc}\left(\frac{v}{\sqrt{2}}\right)^2\,. \tag{8.106c}$$

These profiles are shown in Fig. 8.3, and present similar features to the ones obtained above for the tracer.

Conclusion

In conclusion, our exact closure provides a simple way to fully characterise, analytically, the spatial correlations in the SEP. The existence of such a closure is exceptional, since many-body problems usually involve an infinite hierarchy of equations. As a byproduct, we recover straightforwardly the cumulant generating function of the tracer's position and also the one of the integrated current through the origin. These quantities have been the focus of recent studies; in [99–101], they are obtained using the arsenal of integrable probabilities.

In addition to that, many recent results obtained by using the inverse scattering method [172, 195–198] can be rephrased into the same Wiener-Hopf equation (8.45), provided that one modifies the kernel K [168]. These connections hint at the diversity of use cases for the equation, suggesting that it could be a valuable tool for a more general study of single-file diffusion.

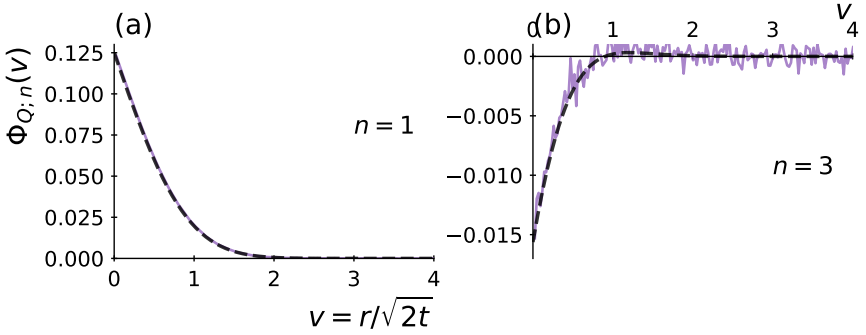

Figure 8.3: **Current in the SEP.** Generalised density profiles (GDP) $\Phi_{Q;n}(v)$ describing the correlations between the density and the current, at orders **(a)** $n = 1$ and **(b)** $n = 3$, at density $\rho = 0.5$, in the case $\xi = 0$. We do not show the profile $n = 2$ because it is zero for this density. Solid lines: GDP computed from the simulations of the SEP, at time $t = 900$. The averaging is performed over 10^8 realisations. Dashed lines: theoretical predictions (8.106a,8.106c).

Chapter 9

Extension to more general single-file systems

The SEP is a minimal model for single-file transport, in this sense it is a very simplified version of more realistic systems, such as molecules in nano-pores [73–75, 78]. However, we show here how the theory we developed for the SEP can be useful to study other models. The central result of this chapter (section 9.1) is the construction of a set of very general mappings between single-file systems at the hydrodynamic level (which, as we argue in appendix H.1, generate all possible mappings between single-file systems). We also analyse the action of these mapping on the tracer and integrated current observables. Then (section 9.2), as an illustration of the usefulness of these mappings, we use them to export results from the SEP to a wide variety of related systems.

Key results.

- Subsection 9.1.1: a general particles-gaps duality in single-file systems.
- Table 9.1.3: four general transformations that act on single-file systems. Combining these mappings, we relate many different models of single-file diffusion to the SEP (section 9.2).

9.1 Mapping single-file systems

In order to study and solve models of single-file diffusion, mappings between different models have proved to be of a great help in different contexts [89, 95, 96, 113, 114, 120–122, 177]. For example, it has been used to reduce the study of a biased tracer in the SEP to the study of the integrated current in another system with a biased site [119]. As we will see in chapter 10, it is much easier to study the integrated current in a system with a biased site than to study the position of a biased tracer; indeed, the biased site is at a fixed position, whereas the biased tracer is moving.

Relying on the fluctuating hydrodynamics description (6.14,6.15)

$$\partial_t \rho(x,t) + \partial_x j(x,t) = 0\,, \tag{9.1}$$

$$j(x,t) + D(\rho)\partial_x \rho(x,t) = \sqrt{\sigma(\rho)}\,\eta(x,t)\,, \tag{9.2}$$

we generalise these mappings to all single-file systems. We then go further by characterising entirely the systems which can be related one another (section 9.1.2 and appendix H.1).

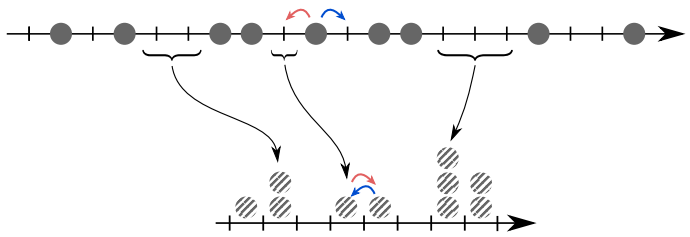

Figure 9.1: Mapping of the simple exclusion process (SEP, top) onto the zero range process (ZRP, bottom) [96, 117, 118]. The particles of the SEP can hop on neighbouring sites, only if they are empty. The sites of the ZRP correspond to the particles of the SEP. The number of particles on a site in the ZRP is the number of empty sites on the right of the corresponding particle in the SEP. For the SEP, we have represented by two arrows the possible jumps of an individual particle. We have represented in the ZRP the corresponding dynamics, illustrated by the two arrows corresponding to the jumps of the SEP particle.

9.1.1 The duality relation

The SEP is well known [96, 117, 118] to be linked to the Zero Range Process (ZRP, see 6.1.2) with constant hopping rates, by setting the occupations of the sites in the ZRP to be equal to the number of empty sites between the particles of the SEP (see figure 9.1 and its caption for a detailed description of the SEP-ZRP mapping). Using this same idea that a system of particles can be related to another system describing the spacing between the particles, we determine a general mapping from equations (9.1, 9.2) to another set of equations of the same form.

We start with density and current ρ, j verifying fluctuating hydrodynamics (9.1,9.2) for given transport coefficients $D(\rho)$ and $\sigma(\rho)$. Building on the intuition of systems of particles (see figure 9.2), we can define the "index" (it will be a real number here, and not an integer like in the SEP-ZRP microscopic mapping) $k(x,t)$ of particle at position x at time t by writing the number of particles between 0 and x as

$$k(x,t) - k(0,t) = \int_0^x \rho(x',t)\mathrm{d}x' \,. \tag{9.3}$$

That requires the knowledge of $k(0,t)$, which is the index of the particle located at $x = 0$. It can be determined by writing that the variation of $k(x,t)$ during a short time $\mathrm{d}t$ corresponds to the number of particles that crossed x from right to left, i.e. $-j(x,t)\mathrm{d}t$ (see figure 9.3 (a) for the intuition from particle system). Therefore,

$$\partial_t k(x,t) = -j(x,t) \,. \tag{9.4}$$

Note that this is coherent with definition (9.3) and the continuity relation (9.1). Taking the convention that at $t = 0$, the particle located at $x = 0$ has index $k(0,0) = 0$, equations (9.3, 9.4) fully determine $k(x,t)$ for all x and t.

This definition naturally fixes the position of the "p-th particle" $x_p(t)$ (for any real number p) by saying that the index of the particle at the position of the p-th particle is p:

$$k(x_p(t),t) = p \,. \tag{9.5}$$

In other words, $k(\cdot,t)$ and $x_{(\cdot)}(t)$ are reciprocal functions.

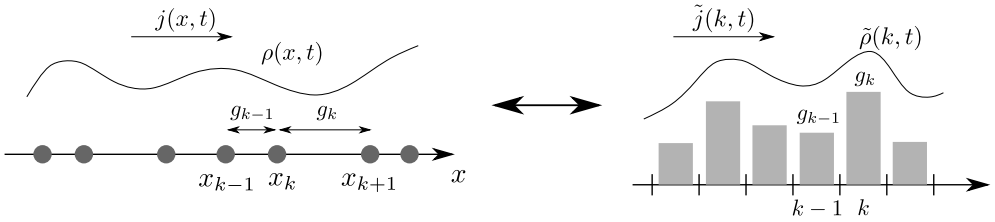

Figure 9.2: Duality relation between two equivalent descriptions of a particle system: through the positions of the particles (left) and the through the gaps between the particles (right). The particle system is described at the macroscopic level by a density field $\rho(x,t)$ and a current $j(x,t)$, while the dual system (gaps) is described by a density $\tilde{\rho}(k,t)$ and a current $\tilde{j}(k,t)$. These two descriptions are equivalent, and related by equations (9.10, 9.11). The inverse transformation is identical, and written explicitly in equations (9.20, 9.21). These two sets of fields (ρ, j) and $(\tilde{\rho}, \tilde{j})$ obey the equations of fluctuating hydrodynamics (9.1, 9.2), with transport coefficients respectively given by (D, σ) and $(\tilde{D}, \tilde{\sigma})$, which are related by the transformation (9.19).

We can now define the field of gaps $\tilde{\rho}(k,t)$ (the spacing between particles at the level of particle k) by saying that at time t, the density of particles at position x must be the inverse of the spacing between two particles around the index $k(x,t)$:

$$\rho(x,t) = \frac{1}{\tilde{\rho}(k(x,t),t)} \,, \tag{9.6}$$

The associated current $\tilde{j}(k,t)$ corresponds physically to the "flux of gap" through the particle k, which is thus given by the motion of this particle (see figure 9.3(b)). This justifies the definition:

$$\tilde{j}(k,t) = -\partial_t x_k(t) \,. \tag{9.7}$$

Deriving the definition (9.5) with respect to t, we get:

$$\begin{aligned} \partial_t x_p(t) \partial_x k(x_p(t),t) + \partial_t k(x_p(t),t) &= 0 \\ \partial_t x_p(t) \rho(x_p(t),t) - j(x_p(t),t) &= 0 \,, \end{aligned} \tag{9.8}$$

the definition (9.7) then yields:

$$\tilde{j}(k(x,t),t) = -\frac{j(x,t)}{\rho(x,t)} \,, \tag{9.9}$$

which can be rewritten using (9.6) as follows. Finally, we have defined $\tilde{\rho}$ and $\tilde{j}$ verifying:

$$\rho(x,t) = \frac{1}{\tilde{\rho}(k(x,t),t)} \,, \qquad j(x,t) = -\frac{\tilde{j}(k(x,t),t)}{\tilde{\rho}(k(x,t),t)} \,, \tag{9.10}$$

where

$$k(x,t) - k(0,t) = \int_0^x \rho(x',t) \mathrm{d}x' \,, \qquad \partial_t k(x,t) = -j(x,t) \,, \tag{9.11}$$

The key result is that these new fields $\tilde{\rho}$ and $\tilde{j}$ remarkably also verify fluctuating hydrodynamics equations (9.1,9.2) with new transport coefficients. Indeed, taking the time derivative

of equation (9.6) we get

$$\begin{aligned}\partial_t\rho(x,t) &= \partial_t\frac{1}{\tilde\rho(k,t)} + \partial_t k(x,t)\,\partial_k\frac{1}{\tilde\rho(k,t)}\\ &= -\frac{1}{\tilde\rho(k,t)^2}\left(\partial_t\tilde\rho(k,t) - j(x,t)\partial_k\tilde\rho(x,t)\right)\\ &= -\frac{1}{\tilde\rho(k,t)^2}\left(\partial_t\tilde\rho(k,t) + \frac{\tilde j(k,t)}{\tilde\rho(k,t)}\partial_k\tilde\rho(x,t)\right)\end{aligned} \tag{9.12}$$

where we have used (9.4) and (9.10). Similarly,

$$\partial_x\rho(x,t) = \partial_x k(x,t)\,\partial_k\frac{1}{\tilde\rho(k,t)} = -\frac{1}{\tilde\rho(k,t)^3}\partial_k\tilde\rho(k,t)\,, \tag{9.13}$$

$$\partial_x j(x,t) = -\frac{1}{\tilde\rho(k,t)}\partial_k\frac{\tilde j(k,t)}{\tilde\rho(k,t)} = -\frac{1}{\tilde\rho(k,t)^2}\left(\partial_k\tilde j(k,t) - \tilde j(k,t)\frac{\partial_k\tilde\rho(k,t)}{\tilde\rho(k,t)}\right)\,. \tag{9.14}$$

Plugging (9.12,9.14) into the continuity relation (9.1), we obtain a new continuity equation for the fields $\tilde\rho$ and $\tilde j$:

$$\partial_t\tilde\rho(k,t) + \partial_k\tilde j(k,t) = 0\,. \tag{9.15}$$

Similarly, using (9.13) into the expression of the current (9.2), we obtain

$$\tilde j(k,t) + D\left(\frac{1}{\tilde\rho}\right)\frac{1}{\tilde\rho^2(k,t)}\partial_k\tilde\rho(k,t) = -\tilde\rho(k,t)\sqrt{\sigma\left(\frac{1}{\tilde\rho}\right)}\,\eta(x_k(t),t) \tag{9.16}$$

Using (6.16), $\eta(x_k(t),t)$ is a Gaussian white noise related to the unit variance Gaussian noise $\eta(k,t)$:

$$\eta(x_k(t),t) \overset{\text{(law)}}{=} \sqrt{\frac{1}{\partial_k x_k(t)}}\,\eta(k,t) = \frac{1}{\sqrt{\tilde\rho(k,t)}}\eta(k,t)\,. \tag{9.17}$$

We thus get (using $\eta(k,t) \overset{\text{(law)}}{=} -\eta(k,t)$),

$$\tilde j(k,t) + \tilde D(\tilde\rho)\partial_k\tilde\rho(k,t) = \sqrt{\tilde\sigma(\tilde\rho)}\,\eta(k,t)\,, \tag{9.18}$$

where we have denoted

$$\tilde D(\tilde\rho) = \frac{1}{\tilde\rho^2}D\left(\frac{1}{\tilde\rho}\right)\,,\quad \tilde\sigma(\tilde\rho) = \tilde\rho\,\sigma\left(\frac{1}{\tilde\rho}\right)\,. \tag{9.19}$$

The dual system, which physically describes the dynamics of the gaps, therefore obeys the equations of fluctuating hydrodynamics (9.15,9.18), with transport coefficients $\tilde D$ and $\tilde\sigma$ which are related to the original coefficients D and σ of the particle system by the transformations (9.19). The known duality relation between the RAP and the KMP model, used in Refs. [89, 95, 114] is a special case of the duality relation described here, applied to the transport coefficients of these models, given in Table 6.1.

A quite unexpected feature of this duality is that it is an involution, meaning that if we apply it to the dual system (the system of gaps), we recover the initial system. This means that the inverse transformation of the current and density is identical:

$$\tilde\rho(k,t) = \frac{1}{\rho(x_k(t),t)}\,,\qquad \tilde j(k,t) = -\frac{j(x_k(t),t)}{\rho(x_k(t),t)}\,, \tag{9.20}$$

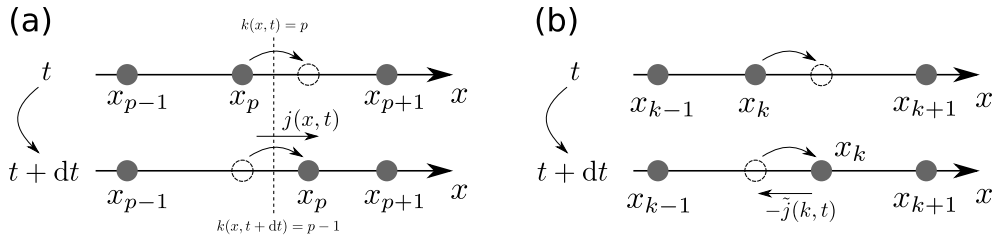

Figure 9.3: **(a)** The flux $j(x,t)$ of particles at position x at time t gives the variation of the index $k(x,t)$ of the closest particle to the left of x, see equation (9.4). **(b)** The flux $\tilde{j}(k,t)$ of gaps through particle k at time t gives the evolution of the position of this particle (9.7).

with

$$x_k(t) - x_0(t) = \int_0^k \tilde{\rho}(k',t)\mathrm{d}k' \,, \qquad \partial_t x_k(t) = -\tilde{j}(k,t) \,. \tag{9.21}$$

Finally, we stress the fact that this particle-gaps duality relation provides a justification to the use of Edwards-Wilkinson equation [199, 200] to describe the fluctuations of positions (and two-particles correlations) in a single-file system at equilibrium (flat initial density), see appendix H.2 for more details.

The duality relation associating $(\tilde{\rho},\tilde{j})$ to (ρ,j) will be referred to as **(Du)** in the following.

9.1.2 Translation and dilatations

We introduce 3 other transformations, acting on the fields ρ and j. We argue that these transformations, combined with the duality relation above, give *all possible* mappings between two single-file systems. This is shown in Appendix H.1.

- **Translation of density (T).** The first transformation consists in shifting the density by a constant c. We define new density and current fields as

$$\tilde{\rho}(x,t) = \rho(x,t) + c \,, \qquad \tilde{j}(x,t) = j(x,t) \,. \tag{9.22}$$

  These two fields still obey the equations of fluctuating hydrodynamics (9.1,9.2), upon changing the transport coefficients as

$$\tilde{D}(\tilde{\rho}) = D(\tilde{\rho} - c) \,, \qquad \tilde{\sigma}(\tilde{\rho}) = \sigma(\tilde{\rho} - c) \,. \tag{9.23}$$

- **Dilatation of the fields (Di).** This transformation multiplies the two fields by a constant c. We define

$$\tilde{\rho}(x,t) = c\,\rho(x,t) \,, \qquad \tilde{j}(x,t) = c\,j(x,t) \,, \tag{9.24}$$

  which obey the equations of fluctuating hydrodynamics (9.1,9.2), with the transport coefficients

$$\tilde{D}(\tilde{\rho}) = D\left(\frac{\tilde{\rho}}{c}\right) \,, \qquad \tilde{\sigma}(\tilde{\rho}) = c^2\,\sigma\left(\frac{\tilde{\rho}}{c}\right) \,. \tag{9.25}$$

- **Rescaling of time (Rt).** The last transformation corresponds to changing the time scale by a constant τ. We introduce

$$\tilde{\rho}(x,t) = \rho(x,\tau t) \,, \qquad \tilde{j}(x,t) = \tau\, j(x,\tau t) \,. \tag{9.26}$$

  Note that j needs to be rescaled by τ in order to satisfy the continuity equation (9.1). These new fields again obey the equations of fluctuating hydrodynamics (9.1,9.2), with the transport coefficients

$$\tilde{D}(\tilde{\rho}) = \tau\, D(\tilde{\rho}) \,, \qquad \tilde{\sigma}(\tilde{\rho}) = \tau\, \sigma(\tilde{\rho}) \,. \tag{9.27}$$

9.1.3 Transformation of observables

We now focus on the case of an infinite system, and consider the two observables which have been the focus of our study:

- The integrated current though a point x, $Q_t(x)$, which counts the total number of particles that crossed x from left to right (minus the number from right to left, and minus the number of particles initially between 0 and x) up to time t,

$$Q_t(x) = \int_0^t j(x,t')\mathrm{d}t' - \int_0^x \rho(x',0)\mathrm{d}x' = \int_x^\infty (\rho(x',t) - \rho(x',0))\mathrm{d}x' - \int_0^x \rho(x',0)\mathrm{d}x' \,. \tag{9.28}$$

- The position $x_k(t)$ of a the k-th particle (a tracer). We take the convention that the 0-th particle was initially placed at the origin $x_0(0) = 0$. It was defined in (9.5):

$$\int_0^{x_k(t)} \rho(x,t)\mathrm{d}x - k = \int_0^\infty (\rho(x,t) - \rho(x,0))\mathrm{d}x \,. \tag{9.29}$$

We study how the transformations presented above act on the two observables $x_k(t)$ and $Q_t(x)$. As in the previous sections, we consider a model described by the density ρ and current j, which is mapped to a new single-file system by one of the transformations defined above. The new system is described by a density $\tilde\rho$ and a flux $\tilde j$. We also denote $\tilde x_k(t)$ the position of a tracer in the new system, defined as in (9.29) with ρ replaced by $\tilde\rho$, and the flux through the origin in the new system is denoted $\tilde Q_t(x)$, defined as in (9.28).

- **Duality relation (Du).** We can express the position of the tracer in terms of the integrated current of the dual system, using equation (9.21):

$$x_k(t) = x_k(0) - \int_0^t \tilde j(k,t')\mathrm{d}t' = x_0(0) + \int_0^k \tilde\rho(k',t)\mathrm{d}k' - \int_0^t \tilde j(k,t')\mathrm{d}t' = -\tilde Q_t(k)\,, \tag{9.30}$$

since $x_0(0) = 0$. The position of a particle is exactly the opposite of the flux through the index of the particle in the dual model. Applying this relation to the dual system, we also obtain

$$\tilde x_k(t) = -Q_t(k) \,. \tag{9.31}$$

- **Translation (T).** This transformation conserves the current j, therefore the integrated current is changed by a constant, $\tilde Q_t(x) = Q_t(x) - cx$. For the positions $x_k(t)$, equation (9.29) gives

$$\int_0^{x_k(t)} (\tilde\rho(x,t) - c)\mathrm{d}x - k = \int_0^\infty (\tilde\rho(x,t) - \tilde\rho(x,0))\mathrm{d}x = \int_0^{\tilde x_0(t)} \tilde\rho(x,t)\mathrm{d}x - k \,. \tag{9.32}$$

This yields the relation

$$\int_{x_k(t)}^{\tilde x_k(t)} \tilde\rho(x,t)\mathrm{d}x = -c\, x_k(t) \,. \tag{9.33}$$

Another way to formulate it is $\tilde x_k(t) = x_{k - c\tilde x_k(t)}(t)$.

Original	Duality (Du)	Dilatation (Di)	Translation (T)	Rescaling (Rt)
$D(\rho)$	$\tilde{D}(\rho) = \frac{1}{\rho^2} D\left(\frac{1}{\rho}\right)$	$\tilde{D}(\rho) = D(\rho/c)$	$\tilde{D}(\rho) = D(\rho - c)$	$\tilde{D}(\rho) = \tau\, D(\rho)$
$\sigma(\rho)$	$\tilde{\sigma}(\rho) = \rho\, \sigma\left(\frac{1}{\rho}\right)$	$\tilde{\sigma}(\rho) = c^2\, \sigma(\rho/c)$	$\tilde{\sigma}(\rho) = \sigma(\rho - c)$	$\tilde{\sigma}(\rho) = \tau\, \sigma(\rho)$
ρ	$\tilde{\rho} = \frac{1}{\rho}$	$\tilde{\rho} = c\, \rho$	$\tilde{\rho} = \rho + c$	$\tilde{\rho} = \rho$
$x_k(t)$	$\tilde{x}_k(t) = -Q_t(k)$	$\tilde{x}_k(t) = x_{\frac{k}{c}}(t)$	$\tilde{x}_k(t) = x_{k - c\tilde{x}_k(t)}(t)$	$\tilde{x}_0(t) = x_0(t\tau)$
$Q_t(x)$	$\tilde{Q}_t(k) = -x_k(t)$	$\tilde{Q}_t(x) = c\, Q_t(x)$	$\tilde{Q}_t(x) = Q_t(x) - cx$	$\tilde{Q}_t(x) = Q_{t\tau}(x)$

Table 9.1: Transformation of the transport coefficients $D(\rho)$ and $\sigma(\rho)$, of the mean density ρ, and of the observables (i) position of a tracer $x_k(t)$ (9.29) and (ii) integrated current through a point x $Q_t(x)$ (9.28), under the different transformations ((Du) defined in 9.1.1, the others in 9.1.2).

- **Dilatation (Di).** This transformation multiplies both ρ and j by a constant c. Therefore, the integrated current is also multiplied by c, $\tilde{Q}_t = cQ_t$, while for the positions, equation (9.29) indicates

$$\int_0^{\tilde{x}_k(t)} \tilde{\rho}(x,t)\mathrm{d}x - k = \int_0^{\infty} (\tilde{\rho}(x,t) - \tilde{\rho}(x,0))\mathrm{d}x \tag{9.34}$$

$$\int_0^{\tilde{x}_k(t)} \rho(x,t)\mathrm{d}x - \frac{k}{c} = \int_0^{\infty} (\rho(x,t) - \rho(x,0))\mathrm{d}x. \tag{9.35}$$

  Therefore, $\tilde{x}_k(t) = x_{\frac{k}{c}}(t)$.

- **Rescaling of time (Rt).** This transformation only changes the time scale by a factor τ (and the current accordingly), such that both the integrated current and the positions of particles are only rescaled in time: $\tilde{Q}_t(x) = Q_{t\tau}(x)$ and $\tilde{x}_k(t) = x_k(t\tau)$.

These transformations are summarised in table 9.1.

9.2 Mapping the results from the SEP

We combine the four different transformations identified in part 9.1 in order to construct mappings from classical models presented in 6.1.2 to the SEP.

For a single-file system which is described at the hydrodynamic level by transport coefficients D and σ, we will focus on the study of a tracer initially at the origin, whose position is denoted $x_0(t)$ and of the integrated current through the origin $Q_t = Q_t(0)$. These quantities are defined from the hydrodynamic profile through equations (9.29, 9.28). As we argued in section 6.2.3, in the long time limit, according to MFT, they will match the tracer's position and integrated current defined from the microscopic system.

Similarly as we did for the SEP 7.1, we can define the generalised density profiles from the hydrodynamic profile $\rho(x,t)$ verifying fluctuating hydrodynamics (8.83, 9.2) (see 6.2.3 for

discussion):

$$w_r(\lambda,t)=\frac{\left\langle \rho(x_0(t)+r,t)\mathrm{e}^{\lambda x_0(t)}\right\rangle}{\left\langle \mathrm{e}^{\lambda x_0(t)}\right\rangle}\,,\quad w_{Q;r}(\lambda,t)=\frac{\left\langle \rho(r,t)\mathrm{e}^{\lambda Q_t}\right\rangle}{\left\langle \mathrm{e}^{\lambda Q_t}\right\rangle}\,. \tag{9.36}$$

In the long time limit, these profiles will also converge to scaling functions with a diffusive reduced variable $\frac{r}{\sqrt{t}}$.

We give below several examples of models that we map to the SEP. The method is the same for all of them, but the key point we want to underline is the wide diversity of phenomenology displayed by these models: point particles (RAP), particles with spatial extension (hard-rods), many-sites interactions (DEP), mass transfer process (KMP), several particles on a site (ZRP)... It is striking to see that, thanks to the mappings available in the hydrodynamic limit, all these models can be studied using our results for the SEP (chapter 8).

9.2.1 General quadratic mobility

The closed equation we have obtained for the SEP, corresponds to $D(\rho)=\frac{1}{2}$ and $\sigma(\rho)=\rho(1-\rho)$. These results can be extended to any single-file system with $D(\rho)=D_0$ constant and $\sigma''(\rho)$ constant with $\sigma(0)=0$, namely $\sigma(\rho)=2D_0\rho(a-b\rho)$. We consider step initial density ρ_- at the left of the origin, ρ_+ at the right.

The mapping from SEP to quadratic mobility system

We build a mapping from the considered system to the SEP by applying the dilatation (Di) both for this system and its dual, we get the following expressions for the transport coefficients of the transformed systems:

$$\begin{array}{ccccccccccc}
D_0 & \xrightarrow[c=1/a]{\text{(Di)}} & D_0 & \xrightarrow{\text{(Du)}} & \dfrac{D_0}{\rho^2} & \xrightarrow[c=1/b]{\text{(Di)}} & \dfrac{D_0}{b^2\rho^2} & \xrightarrow{\text{(Du)}} & \dfrac{D_0}{b^2}\,, \\
2D_0\rho(a-b\rho) & \xrightarrow[c=1/a]{\text{(Di)}} & 2D_0\rho(1-b\rho) & \xrightarrow{\text{(Du)}} & 2D_0\left(1-\dfrac{b}{\rho}\right) & \xrightarrow[c=1/b]{\text{(Di)}} & \dfrac{2D_0}{b^2}\left(1-\dfrac{1}{\rho}\right) & \xrightarrow{\text{(Du)}} & \dfrac{2D_0}{b^2}\rho(1-\rho)\,.
\end{array} \tag{9.37}$$

Using finally a rescaling of time (Rt), we recover the transport coefficients of the SEP

$$\begin{array}{ccc}
\dfrac{D_0}{b^2} & \xrightarrow[\tau=b^2/(2D_0)]{\text{(Rt)}} & \dfrac{1}{2}\equiv\tilde{D}(\rho)\,, \\
\dfrac{2D_0}{b^2}\rho(1-\rho) & \xrightarrow[\tau=b^2/(2D_0)]{\text{(Rt)}} & \rho(1-\rho)\equiv\tilde{\sigma}(\rho)\,,
\end{array} \tag{9.38}$$

Under these transformations, the average initial density of the system becomes

$$\rho_\pm \xrightarrow[c=1/a]{\text{(Di)}} \frac{\rho_\pm}{a} \xrightarrow{\text{(Du)}} \frac{a}{\rho_\pm} \xrightarrow[c=1/b]{\text{(Di)}} \frac{a}{b\rho_\pm} \xrightarrow{\text{(Du)}} \frac{b\rho_\pm}{a} \xrightarrow[\tau=b^2/(2D_0)]{\text{(Rt)}} \frac{b\rho_\pm}{a}\equiv\rho_{\mathrm{SEP},\pm}\,, \tag{9.39}$$

and the two observables become (on the first line, the integrated current through the origin of the transformed system is expressed in terms of the observables Q_t and $x_0(t)$ of the original system; on the second line, same for the tracer's position):

$$\begin{array}{ccccccccccc}
Q_t & \xrightarrow[c=1/a]{\text{(Di)}} & \dfrac{Q_t}{a} & \overset{\text{(Du)}}{\searrow\!\!\!\!\nearrow} & -x_0(t) & \xrightarrow[c=1/b]{\text{(Di)}} & -\dfrac{x_0(t)}{b} & \overset{\text{(Du)}}{\searrow\!\!\!\!\nearrow} & \dfrac{Q_t}{a} & \xrightarrow[\tau=\frac{b^2}{2D_0}]{\text{(Rt)}} & \dfrac{Q_{\frac{b^2t}{2D_0}}}{a}\equiv\tilde{Q}_t\,, \\
x_0(t) & \xrightarrow[c=1/a]{\text{(Di)}} & x_0(t) & & -\dfrac{Q_t}{a} & \xrightarrow[c=1/b]{\text{(Di)}} & -\dfrac{Q_t}{a} & & \dfrac{x_0(t)}{b} & \xrightarrow[\tau=\frac{b^2}{2D_0}]{\text{(Rt)}} & \dfrac{x_0(\frac{b^2t}{2D_0})}{b}\equiv\tilde{x}_0(t).
\end{array} \tag{9.40}$$

The hydrodynamic density $\rho(x,t)$ is expressed in function of the one of the SEP $\tilde{\rho}(x,t)$ in the following way:

$$\rho(x,t) = \frac{a}{b}\tilde{\rho}\left(\frac{x}{b}, \frac{2tD_0}{b^2}\right) \tag{9.41}$$

Using these relations, and results for the SEP (chapter 8), we get the following general solution for any quadratic mobility single-file system.

For the position of the tracer. At large times, the cumulant generating function of the position of the tracer behaves as

$$\ln\left\langle e^{\lambda x_0(t)}\right\rangle \underset{t\to\infty}{\sim} \hat{\psi}(\lambda)\sqrt{4D_0 t}\,. \tag{9.42}$$

The generalised profiles (9.36) also have a diffusive scaling

$$w_r(\lambda,t) \underset{t\to\infty}{\sim} \Phi\left(v = \frac{r}{\sqrt{4D_0 t}}, \lambda\right)\,. \tag{9.43}$$

We again define the functions

$$\Omega_\pm(v) = 2\hat{\psi}\frac{\Phi'(v)}{\Phi'(0^\pm)}\,, \tag{9.44}$$

which now verify the bilinear integral equations

$$\Omega_\pm(v) + b\int_{\mathbb{R}^\mp} \Omega_\pm(v\pm z)\Omega_\mp(\mp z)\mathrm{d}z = K(v)\,, \tag{9.45}$$

equivalent to the linear ones

$$\Omega_\pm(v) + b\int_{\mathbb{R}^\mp} \Omega_\pm(z)\,K(v-z)\mathrm{d}z = K(v)\,, \tag{9.46}$$

with the gaussian kernel $K(v) = \frac{\omega}{\sqrt{\pi}}\,\mathrm{e}^{-(v+\xi)^2+\xi^2}$ and $\xi = \frac{\mathrm{d}\hat{\psi}}{\mathrm{d}\lambda}(\lambda)$. The profile Φ can then be deduced by integration of $\Omega_\pm$, with the boundary conditions

$$\Phi'(0^\pm) \pm \hat{\psi} 2b\frac{\Phi(0^\pm)}{\mathrm{e}^{\pm b\lambda}-1} = 0\,, \tag{9.47}$$

$$\frac{a-b\Phi(0^+)}{a-b\Phi(0^-)} = \mathrm{e}^{-\lambda}\,, \quad \Phi(\pm\infty) = \rho_\pm\,. \tag{9.48}$$

And the solution for the cumulant generating function,

$$\hat{\psi} = -\frac{1}{2b\sqrt{\pi}}\mathrm{Li}_{\frac{3}{2}}\left(-b\omega\right)\,. \tag{9.49}$$

For the current through the origin. Similarly, we can also obtain the equations for the integrated current through the origin. The cumulant generating function scales as

$$\ln\left\langle \mathrm{e}^{\lambda Q_t}\right\rangle \underset{t\to\infty}{\sim} \hat{\psi}_Q(\lambda)\sqrt{4D_0 t}\,, \tag{9.50}$$

and the generalised profiles (9.36) as

$$w_{Q;r}(\lambda,t) \underset{t\to\infty}{\sim} \Phi_Q\left(v = \frac{r}{\sqrt{4D_0 t}}, \lambda\right)\,. \tag{9.51}$$

Defining $\Omega_\pm$ in the same way, these functions again satisfy the integral equation (9.46), with the gaussian kernel $K(v)$ (with $\xi = 0$ because we look at the current through the origin):

$$K(v) = \frac{\omega_Q}{\sqrt{\pi}}\, \mathrm{e}^{-v^2} \,. \tag{9.52}$$

This parameter ω_Q can be related to $\hat{\psi}_Q$ by

$$\hat{\psi}_Q = -\frac{1}{2b\sqrt{\pi}} \mathrm{Li}_{\frac{3}{2}}\left(-b\omega_Q\right) \,. \tag{9.53}$$

The profiles can again be deduced by integration of the solution $\Omega_\pm$ of (9.46), with the boundary conditions

$$\Phi_Q'(0^\pm) = \mp 2\hat{\psi}_Q \left(\frac{a}{1-\mathrm{e}^{\mp a\lambda}} - b\Phi_Q(0^\pm) \right) \,, \tag{9.54}$$

$$\frac{\Phi_Q(0^+)(a - b\Phi_Q(0^-))}{\Phi_Q(0^-)(a - b\Phi_Q(0^+))} = \mathrm{e}^{a\lambda} \,. \tag{9.55}$$

9.2.2 The Kipnis Marchioro Presutti model

As a first application of the generalised equation (9.46), we consider the Kipnis Marchioro Presutti (KMP) model [179, 201] which is a mass transfer model (6.1.2). This system is described by the transport coefficients

$$D(\rho) = D_0 \,, \quad \sigma(\rho) = \sigma_0 \rho^2 \,, \tag{9.56}$$

with $\sigma_0 = 2aD_0$ where a is the lattice spacing [115]. It is a model with constant diffusion and quadratic mobility, so it falls into the category studied above (9.2.1) and we can directly apply the results obtained there.

Position of a tracer

The KMP model is not a particle model, but one can still define the position of a tracer using equation (9.29). It represents a fictitious wall that separates the system into two regions in which the mass is conserved.

Following the procedure described in Section 8.3.1, we obtain the cumulants of the position of this tracer. For instance, in the case $\rho_+ = \rho_- = \rho$,

$$\frac{\langle x_0(t)^2 \rangle_c}{\sqrt{4D_0 t}} \underset{t\to\infty}{\sim} \hat{\kappa}_2^{(\mathrm{KMP})} = \frac{\sigma_0}{2D_0\sqrt{\pi}} \,, \tag{9.57}$$

$$\frac{\langle x_0(t)^4 \rangle_c}{\sqrt{4D_0 t}} \underset{t\to\infty}{\sim} \hat{\kappa}_4^{(\mathrm{KMP})} = \frac{\left(12 + \left(3\sqrt{2} - 8\right)\pi\right)\sigma_0^3}{8D_0^3\pi^{3/2}} \,. \tag{9.58}$$

We additionally get the generalised density profiles,

$$\Phi_1^{(\mathrm{KMP})}(v) = \frac{\rho\sigma_0}{4D_0} \operatorname{erfc}(v) \,, \tag{9.59}$$

$$\Phi_2^{(\mathrm{KMP})}(v) = \frac{\rho\sigma_0^2}{4D_0^2} \left(\operatorname{erfc}(v) - \frac{2}{\pi}\mathrm{e}^{-v^2} \right) \,, \tag{9.60}$$

$$\Phi_3^{(\mathrm{KMP})}(v) = \frac{\rho\sigma_0^3}{32D_0^3} \left(2\left(1 + \frac{6}{\pi}\right) \operatorname{erfc}(v) - 24\frac{\sqrt{\pi} - v}{\pi^{3/2}}\mathrm{e}^{-v^2} + 3\operatorname{erfc}\left(\frac{v}{\sqrt{2}}\right)^2 \right) \,. \tag{9.61}$$

These profiles are represented in Fig. 9.4.

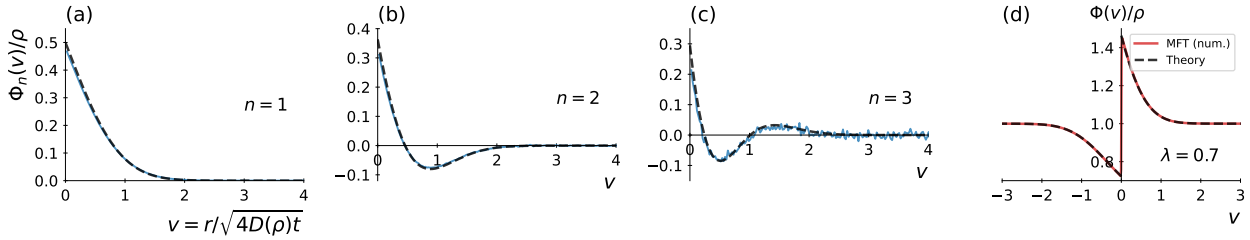

Figure 9.4: **KMP.** Generalised density profiles $\Phi_n^{(\mathrm{KMP})}(v)/\rho$ at orders **(a)** $n = 1$, **(b)** $n = 2$ and **(c)** $n = 3$ (the density ρ plays no role in this model). Solid lines: result of the simulations of the KMP model (see Appendix A) at time $t = 900$ on 500 sites. Dashed lines: theoretical predictions (9.59,9.60,9.61). **(d)** GDP-generating function at $\rho = 1$ and $\lambda = 0.7$, obtained from solving numerically the Wiener-Hopf equation (9.46) (dashed line), compared to the numerical solution (red solid line) of the MFT equations for KMP (similar to section 8.1.2).

Integrated current through the origin

Following an approach similar to section 8.3.3, with $\xi = 0$ since we look at the current through the origin, we find that

$$\omega_Q = \frac{\sigma_0 \rho^2 \lambda^2}{2D_0} , \tag{9.62}$$

which, combined with (9.53) yields

$$\hat{\psi}_Q^{(\mathrm{KMP})}(\lambda) = \frac{D_0}{\sqrt{\pi}\sigma_0} \mathrm{Li}_{\frac{3}{2}}\left(\left(\frac{\sigma_0 \rho \lambda}{2D_0}\right)^2\right) . \tag{9.63}$$

This expression coincides with the one given in [107]. We additionally obtain the profiles

$$\Phi_{Q;1}^{(\mathrm{KMP})}(v) = \frac{\rho^2 \sigma_0}{4D_0} \operatorname{erfc}(v) , \tag{9.64a}$$

$$\Phi_{Q;2}^{(\mathrm{KMP})}(v) = \frac{\rho^3 \sigma_0^2}{4D_0^2} \operatorname{erfc}(v) , \tag{9.64b}$$

$$\Phi_{Q;3}^{(\mathrm{KMP})}(v) = \frac{3\rho^4 \sigma_0^4}{32 D_0^3} \left(2 \operatorname{erfc}(v) + \operatorname{erfc}\left(\frac{v}{\sqrt{2}}\right)^2\right) . \tag{9.64c}$$

Note that, for this model, $\sigma'(0) = 0$, so the boundary condition (9.54) (with $a = 0$) is ill-defined. We have used the boundary condition deduced from (9.54) by taking the limit $\sigma'(0) \to 0$,

$$\Phi_Q'(0^\pm) = -2\hat{\psi}_Q \left(\frac{1}{\lambda} \pm \frac{\sigma_0}{4D_0} \Phi_Q(0^\pm)\right) . \tag{9.65}$$

9.2.3 The random average process

The random average process (RAP) [113, 170, 177] is a system of particles placed on an infinite line (6.1.2). We consider an initial mean density ρ. At random times, picked from an exponential distribution with rate $\frac{1}{2}$, a particle can move, either to the left or to the right, to a random fraction of the distance to the next particle. In the hydrodynamic limit, only the first two moments μ_1 and μ_2 of the distribution of this random fraction are relevant. The

transport coefficients depend on these two parameters only [113, 114]:

$$D(\rho) = \frac{\mu_1}{2\rho^2}\,, \quad \sigma(\rho) = \frac{1}{\rho}\frac{\mu_1\mu_2}{\mu_1-\mu_2}\,. \tag{9.66}$$

Applying the duality relation (Du) (9.19), we obtain that the dual system is described by the coefficients

$$\tilde{D}(\tilde{\rho}) = D_0 = \frac{\mu_1}{2}\,, \quad \tilde{\sigma}(\tilde{\rho}) = \sigma_0\tilde{\rho}^2\,, \quad \sigma_0 = \frac{\mu_1\mu_2}{\mu_1-\mu_2}\,, \tag{9.67}$$

which correspond to the KMP model, with a specific choice of the factors D_0 and σ_0 in the coefficients (see Table 6.1). Under this duality (Du), the density field $\rho^{(\mathrm{RAP})}(x,t)$ of the RAP can be expressed in terms of the one of the KMP $\rho^{(\mathrm{KMP})}(k,t)$ as:

$$\rho^{(\mathrm{RAP})}(x_k(t),t) = \frac{1}{\rho^{(\mathrm{KMP})}(k,t)}\,, \tag{9.68}$$

with $x_k(t)$ the position of the particle with label k at time t, which can be expressed from the density as

$$x_k(t) = x_0(t) + \int_0^k \rho^{(\mathrm{KMP})}(k',t)\mathrm{d}k'\,, \tag{9.69}$$

with x_0 the position of the tracer, defined from (9.29):

$$x_0(t) = \int_{-\infty}^0 (\rho^{(\mathrm{KMP})}(k',t) - \rho^{(\mathrm{KMP})}(k',0))\mathrm{d}k'\,. \tag{9.70}$$

As a consequence of this duality, the positions of particles in the RAP $x_k(t)$ are expressed in term of density $\rho^{(\mathrm{KMP})}(p,t)$ in the KMP. Since the density in the KMP evolves according to a constant diffusion coefficient D_0 (as opposed to $D(\rho) = D_0/\rho^2$ in the RAP), this explains why positions of particles are relatively easy to compute in the RAP.

As seen in section 9.1.3, the tracer's position in the RAP $x_0(t)$ can be expressed in terms of the integrated current $Q_t^{(\mathrm{KMP})}$ through the origin in the KMP model,

$$x_0(t) = -Q_t^{(\mathrm{KMP})}\,. \tag{9.71}$$

Therefore, one can easily relate the cumulant generating functions since

$$\begin{aligned}\hat{\psi}^{(\mathrm{RAP})}(\lambda) &= \lim_{t\to\infty}\frac{1}{\sqrt{4D(\rho)t}}\ln\left\langle \mathrm{e}^{\lambda x_0(t)}\right\rangle \\ &= \sqrt{\frac{D_0}{D(\rho)}}\lim_{t\to\infty}\frac{1}{\sqrt{4D_0t}}\ln\left\langle \mathrm{e}^{-\lambda Q_t^{(\mathrm{KMP})}}\right\rangle \\ &= \rho\,\hat{\psi}_Q^{(\mathrm{KMP})}(-\lambda)\,.\end{aligned} \tag{9.72}$$

Note that, due to the relation (9.68), and the RAP having mean density ρ, the KMP model has mean density $1/\rho$. The cumulant generating function $\hat{\psi}_Q^{(\mathrm{KMP})}$ must thus be evaluated at this density. From (9.63), this gives

$$\hat{\psi}^{(\mathrm{RAP})}(\lambda) = \frac{\rho(\mu_1-\mu_2)}{2\mu_2\sqrt{\pi}}\mathrm{Li}_{\frac{3}{2}}\left(\left(\frac{\mu_2\lambda}{\rho(\mu_1-\mu_2)}\right)^2\right)\,. \tag{9.73}$$

In addition to that, the generalised profiles can be obtained from the relation (9.68). Indeed, in the large time limit, the averages in equations (9.36) are dominated by a single

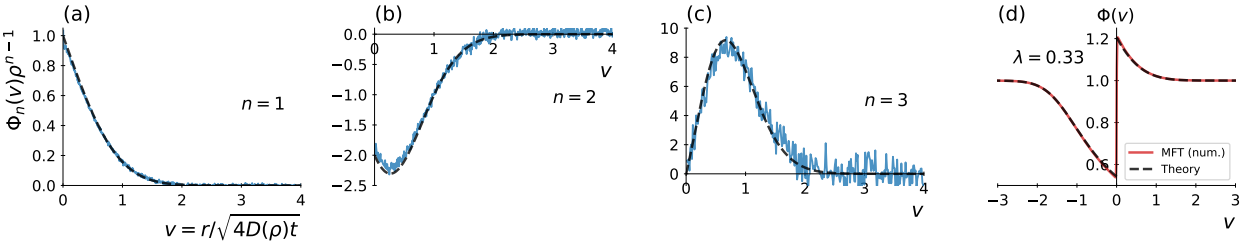

Figure 9.5: **RAP.** Generalised density profiles $\Phi_n^{(\mathrm{RAP})}(v)\rho^{n-1}$ at orders **(a)** $n=1$, **(b)** $n=2$ and **(c)** $n=3$ (the density ρ plays no role in this model). Solid lines: result of the simulations of the RAP (see appendix A) at time $t=4000$ with 5000 particles. Dashed lines: theoretical predictions (9.77,9.78,9.79). **(d)** GDP-generating function at $\rho=1$ and $\lambda=0.33$, obtained from solving numerically the Wiener-Hopf equation (9.46) and using the mapping (9.74) (dashed line), compared to the numerical solution (red solid line) of the MFT equations (similarly to 8.1.2).

realisation of the field $\rho(x,t)$, the typical realisation $(\rho_\star, j_\star)$ that optimises the MFT functional (identically as in 7.1.2, equations (7.12, 7.20)). Since all realisations verify (9.68), so does the typical one, which we denote $\rho_\star$. Hence,

$$\begin{aligned}\Phi^{(\mathrm{RAP})}\left(v=\frac{r(k)}{\sqrt{4D(\rho)t}}\right) &\underset{t\to\infty}{\simeq} \rho_\star^{(\mathrm{RAP})}(x_0(t)+r(k),t)\\ &= \frac{1}{\rho_\star^{(\mathrm{KMP})}(k,t)}\\ &\underset{t\to\infty}{\simeq} \frac{1}{\Phi_Q^{(\mathrm{KMP})}(u=k/\sqrt{4D_0t})}\,,\end{aligned} \tag{9.74}$$

where we have defined

$$r(k) \equiv x_k(t) - x_0(t) = \int_0^k \rho_\star^{(\mathrm{KMP})}\,, \tag{9.75}$$

which becomes

$$v(u) = \frac{r(k)}{\sqrt{4D(\rho)t}} = \sqrt{\frac{D_0}{D(\rho)}}\int_0^u \Phi_Q^{(\mathrm{KMP})}(u')\mathrm{d}u'\,. \tag{9.76}$$

Together with (9.74), expanding this relation in powers of λ, we can compute the profiles of the RAP from the ones obtained above on the KMP model (9.64), but evaluated at the density $1/\rho$. This gives for instance

$$\Phi_1^{(\mathrm{RAP})}(v) = \frac{\mu_2}{2(\mu_1-\mu_2)}\,\mathrm{erfc}(v)\,, \tag{9.77}$$

$$\Phi_2^{(\mathrm{RAP})}(v) = \frac{\mu_2^2}{2\pi\rho(\mu_1-\mu_2)^2}\left(\pi\,\mathrm{erfc}(v)^2 - 2\mathrm{e}^{-v^2} - 2\pi\left(1+v\frac{\mathrm{e}^{-v^2}}{\sqrt{\pi}}\right)\mathrm{erfc}(v) + 2\mathrm{e}^{-2v^2}\right)\,, \tag{9.78}$$

$$\begin{aligned}\Phi_3^{(\mathrm{RAP})}(v) =& \frac{3}{4\pi^2}\frac{\mu_1^3}{\rho^2(\mu_1-\mu_2)^3}\left(\pi^2\,\mathrm{erfc}(v)^3 + 2\sqrt{\pi}v\mathrm{e}^{-3v^2} - \pi^2\left(4+\frac{2v(3-v^2)}{\sqrt{\pi}}\mathrm{e}^{-v^2}\right)\mathrm{erfc}(v)^2\right.\\ &+ (2\pi^2+2\pi(3-2v^2)\mathrm{e}^{-2v^2} + 2\pi(2v^2+4\sqrt{\pi}v-3)\mathrm{e}^{-v^2})\,\mathrm{erfc}(v)\\ &\left.+ 2(4\pi+\sqrt{\pi}v)\mathrm{e}^{-v^2} - 4(2\pi+\sqrt{\pi}v)\mathrm{e}^{-2v^2}\right)\,.\end{aligned} \tag{9.79}$$

These profiles are represented in Fig. 9.5. Similarly, one could look at the integrated current in the RAP using results for the tracer in the KMP.

9.2.4 The double exclusion process

The double exclusion process (DEP) is similar to the SEP, but we consider that particles occupy two sites: the two neighbouring sites in the direction of a jump must be empty in order for the jump to occur (6.1.2). The transport coefficients are [175, 176]

$$D(\rho) = \frac{D_0}{(1-\rho)^2}\,, \qquad \sigma(\rho) = 2D_0\frac{\rho(1-2\rho)}{1-\rho}\,. \tag{9.80}$$

We consider an initial density $\rho \in [0, 1/2]$.

This model can be directly mapped onto the SEP by reducing the size of the particles to one lattice site. This is naturally done in the dual model (which describes the gaps between the particles) by removing a constant of 1 site to all the gaps. We can therefore construct this model by going to the dual of the DEP, translating the density by a constant -1 and going back to the particles using the duality relation (Du) again:

$$\begin{array}{ccccccc} D(\rho) = \dfrac{D_0}{(1-\rho)^2} & \xrightarrow{\text{(Du)}} & \dfrac{D_0}{(\rho-1)^2} & \xrightarrow[c=-1]{\text{(T)}} & \dfrac{D_0}{\rho^2} & \xrightarrow{\text{(Du)}} & D_0 = \tilde{D}(\rho)\,, \\ \sigma(\rho) = 2D_0\dfrac{\rho(1-2\rho)}{1-\rho} & \xrightarrow{\text{(Du)}} & 2D_0\left(1-\dfrac{1}{\rho-1}\right) & \xrightarrow[c=-1]{\text{(T)}} & 2D_0\left(1-\dfrac{1}{\rho}\right) & \xrightarrow{\text{(Du)}} & 2D_0\rho(1-\rho) = \tilde{\sigma}(\rho)\,, \end{array} \tag{9.81}$$

which are indeed the transport coefficients of the SEP (see table 6.1) with jump rate D_0. Note that we can straightforwardly extend this procedure to a system in which particles have a volume on n sites, by applying a translation of density (T) of $n-1$ for the dual. Under this series of transformations, the position of a tracer becomes (we do not write the action of (T) on the position of the tracer of the dual system because of its complexity); again, the first line represents the current in the transformed system in terms of the observables of the original system; the second line is the expression of the position of the tracer:

$$\begin{array}{ccccccc} Q_t & \xrightarrow{\text{(Du)}} & -x_0(t) & \xrightarrow[c=-1]{\text{(T)}} & -x_0(t) & \xrightarrow{\text{(Du)}} & -? \equiv \tilde{Q}_t\,, \\ x_0(t) & & -Q_t & \xrightarrow[c=-1]{\text{(T)}} & ? & & x_0(t) \equiv \tilde{x}_0(t)\,. \end{array} \tag{9.82}$$

In particular, the position of the tracer is the same in both models, and the density fields are related through

$$\rho^{(\mathrm{DEP})}(x_0(t) + x + n(x,t), t) = \frac{\rho^{(\mathrm{SEP})}(x_0(t)+x,t)}{1+\rho^{(\mathrm{SEP})}(x_0(t)+x,t)}, \tag{9.83}$$

where we defined the number of particles between the tracer and position x in the SEP:

$$n(x,t) = \int_0^x \rho^{(\mathrm{SEP})}(z,t)\mathrm{d}z\,. \tag{9.84}$$

As a consequence of (9.83), the corresponding initial density in the SEP is $\rho_{\mathrm{SEP}} = \frac{\rho}{1-\rho}$. Since the tracer's position is the same in both models, its cumulants in the DEP at density ρ are obtained from the known results in the SEP (8.74) evaluated at density ρ_{SEP}:

$$\left\langle x_0(t)^2 \right\rangle = \frac{2(1-2\rho)}{\rho}\sqrt{\frac{D_0 t}{\pi}}\,, \tag{9.85}$$

$$\left\langle x_0(t)^4 \right\rangle_c = \frac{2(1-2\rho)}{\pi\rho^3}\left(12(1-2\rho)^2 - \pi((23-6\sqrt{2})\rho^2 - 3(6-\sqrt{2})\rho + 3)\right)\sqrt{\frac{D_0 t}{\pi}}\,. \tag{9.86}$$

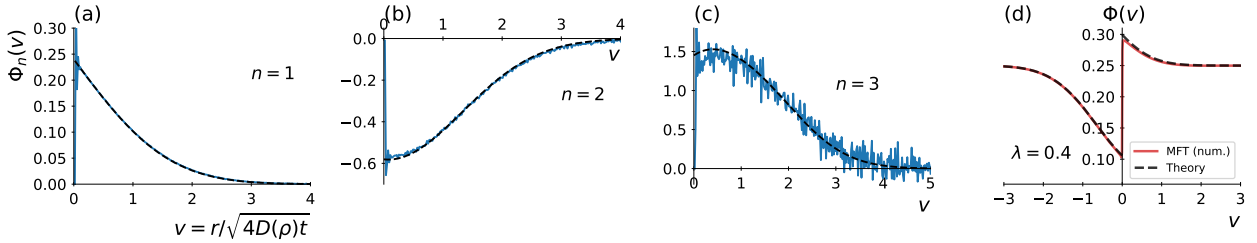

Figure 9.6: Generalised density profiles $\Phi_n^{(\mathrm{DEP})}(v)$ at orders **(a)** $n = 1$, **(b)** $n = 2$ and **(c)** $n = 3$ at density $\rho = 0.25$. Solid lines: result of the simulations of the DEP (see appendix A) at time $t = 3000$ on 20000 sites. Dashed lines: theoretical predictions (9.88,9.89). **(d)** GDP-generating function at $\rho = 0.25$ and $\lambda = 0.4$, obtained from solving numerically the Wiener-Hopf equation (9.46) and using the mapping (9.87) (dashed line), compared to the numerical solution (red solid line) of the MFT equations (similarly to 8.1.2).

Similarly as we did for the RAP, the relation (9.83) holds for the optimal profiles denoted $\rho_\star$ in the averages defining the GDP (9.36)

$$\begin{aligned}\Phi^{(\mathrm{DEP})}\left(v = \frac{x + n(x)}{\sqrt{4D(\rho)t}}\right) &\underset{t\to\infty}{\simeq} \rho_\star^{(\mathrm{DEP})}(x_0(t) + x + n(x), t) \\ &= \frac{\rho_\star^{(\mathrm{SEP})}(x_0(t) + x, t)}{1 + \rho_\star^{(\mathrm{SEP})}(x_0(t) + x, t)} \\ &\underset{t\to\infty}{\simeq} \frac{\Phi^{(\mathrm{SEP})}(u = x/\sqrt{4D_0 t})}{1 + \Phi^{(\mathrm{SEP})}(u = x/\sqrt{4D_0 t})}\end{aligned} \tag{9.87}$$

We can expand (9.87) in orders of λ to get the generalized density profiles for the DEP from those of the SEP given in Section 8.3.2. At lowest orders, we get

$$\Phi_1^{(\mathrm{DEP})}(v) = \frac{1}{2}(1-\rho)(1-2\rho)\mathrm{erfc}(v)\,, \tag{9.88}$$

$$\begin{aligned}\Phi_2^{(\mathrm{DEP})}(v) = &\frac{(1-\rho)(1-2\rho)}{4\pi\rho}\Big(2\sqrt{\pi}\rho(1-2\rho)v\,\mathrm{e}^{-v^2}\,\mathrm{erfc}(v) - 2\rho(1-2\rho)\mathrm{e}^{-2v^2} \\ &-2(1-2\rho)(2-\rho)\mathrm{e}^{-v^2} + \pi\,\mathrm{erfc}(v)((2\rho-1)\rho\,\mathrm{erfc}(v) - 3\rho + 1)\Big)\,,\end{aligned} \tag{9.89}$$

The profile $\Phi_3^{(\mathrm{DEP})}$ can be written similarly, but the expression is lengthy so we do not reproduce it here. These profiles are represented in Fig. 9.6. Note that if we denote by $\eta_r(t)$ the occupation of site r in the DEP and $X_t \in \mathbb{Z}$ the position of the tracer, we have, for $v = r/\sqrt{4D(\rho)} = r(1-\rho)/\sqrt{4D_0}$:

$$\Phi^{(\mathrm{DEP})}(v) \underset{t\to\infty}{\sim} \frac{\left\langle \eta_{X_t + r} e^{\lambda X_t}\right\rangle}{\left\langle e^{\lambda X_t}\right\rangle}. \tag{9.90}$$

For the two last models, we will only give the cumulants of the tracer's position, even though the profiles can be obtained as well with the same procedure.

9.2.5 The gas of hard rods

We consider a system of rods of length ℓ, which perform a Brownian motion, with the condition that two rods cannot overlap (6.1.2). The main interest of this model compared to

the point-like Brownian particles is that the system of hard rods has a maximal density $1/\ell$. It is the one dimensional version of the hard sphere gas. Its transport coefficients are given by [82]

$$D(\rho) = \frac{D_0}{(1-\ell\rho)^2}\,, \qquad \sigma(\rho) = 2D_0\rho\,. \tag{9.91}$$

We can map the gas of hard rods onto the model of point-like Brownian particles by decreasing the size of the rods by their length ℓ, in a similar way as for the DEP:

$$\begin{array}{ccccccc} D(\rho) = \dfrac{D_0}{(1-\ell\rho)^2} & \xrightarrow{\text{(Du)}} & \dfrac{D_0}{(\rho-\ell)^2} & \xrightarrow[c=-\ell]{\text{(T)}} & \dfrac{D_0}{\rho^2} & \xrightarrow{\text{(Du)}} & D_0 = \tilde{D}(\rho)\,, \\ \sigma(\rho) = 2D_0\rho & \xrightarrow{\text{(Du)}} & 2D_0 & \xrightarrow[c=-\ell]{\text{(T)}} & 2D_0 & \xrightarrow{\text{(Du)}} & 2D_0\rho = \tilde{\sigma}(\rho)\,. \end{array} \tag{9.92}$$

$D(\rho)$ and $\sigma(\rho)$ are the transport coefficients for the gas of hard rods [82], and this series of transformation indeed yields the coefficients $\tilde{D}$ and $\tilde{\sigma}$ of the gas of Brownian particles (see Table 6.1). Under these transformations (see Table 9.1), the position of the tracer is unchanged (in each column we give the observables of the current system in terms of the observables of the original system; the first line corresponds to the integrated current, the second line is the position of the tracer):

$$\begin{array}{ccccccc} Q_t & \overset{\text{(Du)}}{\nearrow\!\!\searrow} & -x_0(t) & \xrightarrow[c=-\ell]{\text{(T)}} & -x_0(t) & \overset{\text{(Du)}}{\nearrow\!\!\searrow} & -? \equiv \tilde{Q}_t\,, \\ x_0(t) & & -Q_t & \xrightarrow[c=-\ell]{\text{(T)}} & ? & & x_0(t) \equiv \tilde{x}_0(t)\,, \end{array} \tag{9.93}$$

where we again do not write explicitly the complex transformation (9.33) of the position of the tracer under the transformation (T). The mean density of the system becomes

$$\rho \xrightarrow{\text{(Du)}} \frac{1}{\rho} \xrightarrow[c=-\ell]{\text{(T)}} \frac{1}{\rho} - \ell \xrightarrow{\text{(Du)}} \frac{\rho}{1-\rho\ell} \equiv \rho_{\rm B}\,. \tag{9.94}$$

Since the tracer's position is unchanged by this transformation, its cumulant generating function in the hard-rods gas at density ρ is equal to the cumulant generating function $\psi_T^{(\rm B)}$ of the tracer in the Brownian model (which is the same as the low-density limit of the SEP 8.1.1), evaluated at the density ρ_B (9.94). In particular, expanding in powers of λ, we get the first cumulants:

$$\left\langle x_0(t)^2 \right\rangle = \frac{2(1-\ell\rho)}{\rho}\sqrt{\frac{D_0 t}{\pi}}\,, \qquad \left\langle x_0(t)^4 \right\rangle_c = \frac{6(4-\pi)}{\pi}\left(\frac{1-\ell\rho}{\rho}\right)^3\sqrt{\frac{D_0 t}{\pi}}\,. \tag{9.95}$$

9.2.6 The zero range process

Here, we consider one specific ZRP, which corresponds to the simplest case, in which the hopping rate are constant, so they depend neither on the site nor on the number of particles on it. We denote by $n_k(t)$ the number of particles on site k at time t. Note that this ZRP is different from a system of independent particles, as in this case the hopping rate on site k would be proportional to n_k. At the macroscopic level, this system is described by the transport coefficients [86, 119]

$$D(\rho) = \frac{D_0}{(1+\rho)^2}\,, \qquad \sigma(\rho) = \frac{2D_0\rho}{1+\rho}\,. \tag{9.96}$$

This model is remarkable because it is an example of system whose transport coefficients are left unchanged by the duality transformation (Du). This property will be useful below. This

model is well-known to be related to the SEP [117, 118], and this relation was used explicitly in [119]. The mapping is the following: to each site k is associated a particle at position x_k. The occupation of site k in the ZRP is given by the number of empty sites in the SEP between particles $k+1$ and k (see Fig. 9.1). Inversely, the distance between particles $k+1$ and k is given by $n_k + 1$. Therefore, the SEP can be obtained from the ZRP by combining the translation of density (T) and the duality relation (Du):

$$\begin{aligned} D(\rho) = \frac{D_0}{(1+\rho)^2} &\xrightarrow[c=1]{\text{(T)}} \frac{D_0}{\rho^2} \xrightarrow{\text{(Du)}} D_0 = \tilde{D}(\rho)\,, \\ \sigma(\rho) = \frac{2D_0\rho}{1+\rho} &\xrightarrow[c=1]{\text{(T)}} \frac{2D_0}{\rho}(\rho-1) \xrightarrow{\text{(Du)}} 2D_0\rho(1-\rho) = \tilde{\sigma}(\rho)\,. \end{aligned} \tag{9.97}$$

Under theses transformations the observables become:

$$\begin{array}{ccccc} Q_t & \xrightarrow{\text{(T)}} & Q_t & \overset{\text{(Du)}}{\searrow\!\!\!\!\!\!\nearrow} & ? \equiv \tilde{Q}_t\,, \\ x_0(t) & \xrightarrow{\text{(T)}} & ? & & -Q_t \equiv \tilde{x}_0(t)\,. \end{array} \tag{9.98}$$

The mean density of the ZRP is transformed as

$$\rho \xrightarrow[c=1]{\text{(T)}} \rho+1 \xrightarrow{\text{(Du)}} \frac{1}{\rho+1} = \rho_{\text{SEP}}\,. \tag{9.99}$$

Using (9.98, 9.99), the n-cumulant of the integrated current through the origin in the ZRP at density ρ is equal to the one of the tracer's position in the SEP at the density ρ_{SEP} multiplied by $(-1)^n$. For instance (8.74),

$$\langle Q_t^2 \rangle = 2\rho\sqrt{\frac{D_0 t}{\pi}}\,, \quad \langle Q_t^4 \rangle_c = 2\rho\frac{12\rho^2 + \pi(1+3(2-\sqrt{2})\rho - 3\rho^2)}{\pi}\sqrt{\frac{D_0 t}{\pi}}\,. \tag{9.100}$$

The ZRP we consider here is an example self dual system:

$$\begin{aligned} D(\rho) = \frac{D_0}{(1+\rho)^2} &\xrightarrow{\text{(Du)}} \frac{D_0}{(1+\rho)^2} = D(\rho)\,, \\ \sigma(\rho) = \frac{2D_0\rho}{1+\rho} &\xrightarrow{\text{(Du)}} \frac{2D_0\rho}{1+\rho} = \sigma(\rho)\,. \end{aligned} \tag{9.101}$$

The corresponding action on the observables is an exchange of integrated current and flux (with a sign):

$$\begin{array}{ccc} Q_t & \overset{\text{(Du)}}{\searrow\!\!\!\!\!\!\nearrow} & -x_0(t) \equiv \tilde{Q}_t\,, \\ x_0(t) & & -Q_t \equiv \tilde{x}_0(t)\,, \end{array} \tag{9.102}$$

and the initial mean density is mapped in the following way:

$$\rho \xrightarrow{\text{(Du)}} \frac{1}{\rho} = \tilde{\rho}\,. \tag{9.103}$$

This mapping thus implies the striking relation:

$$\left\langle e^{\lambda Q_t} \right\rangle_\rho = \left\langle e^{-\lambda x_0(t)} \right\rangle_{\rho^{-1}}\,, \tag{9.104}$$

where the first average is taken at initial density ρ and the second one at initial density ρ^{-1}. For instance, using (9.100),

$$\langle x_0(t)^2 \rangle = \frac{2}{\rho}\sqrt{\frac{D_0 t}{\pi}}\,, \quad \langle x_0(t)^4 \rangle_c = 2\frac{12 + \pi(\rho^2 + 3(2-\sqrt{2})\rho - 3)}{\rho^3\pi}\sqrt{\frac{D_0 t}{\pi}}\,. \tag{9.105}$$

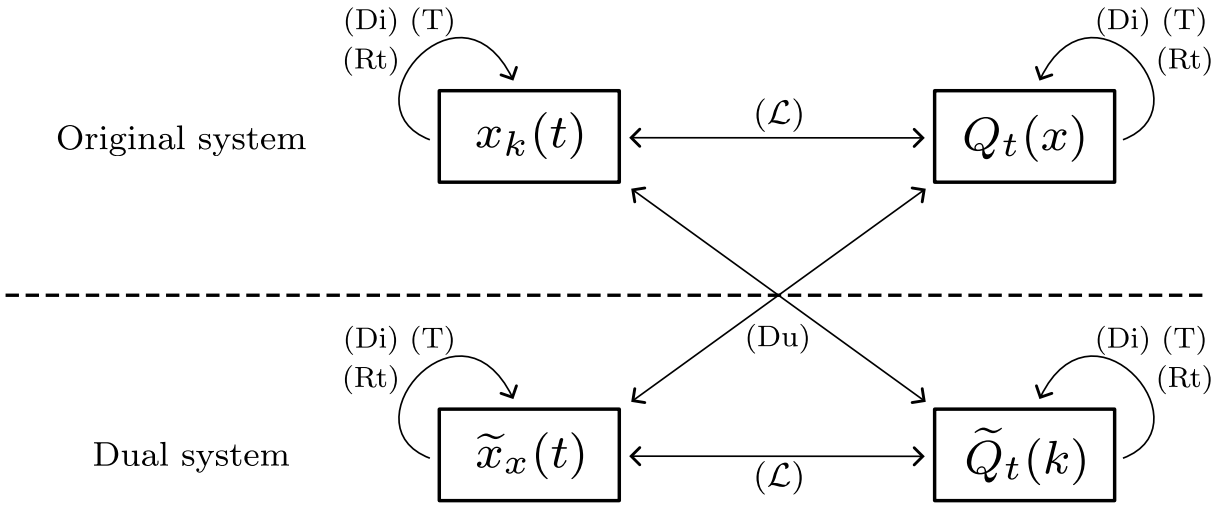

Figure 9.7: The transformations (T), (Di), and (Rt) connect a family of observables $\mathcal{O} \in \{(x_k(t))_k, (Q_t(x))_x\}$ to the same family in a related system, whereas the transformation (Du) connects a family $\mathcal{O}$ to the other family in the dual system (in fact it extchanges the families). The transformation $(\mathcal{L})$ connects the family of particles positions $(x_k(t))_k$ to the family of integrated currents $(Q_t(x))_x$ in the same system.

Conclusion

In conclusion, we see that the closed equation we found for the SEP in chapter 8 can be used (thanks to the mappings) to compute the GDP in several other models. This supports the idea that the GDP are relevant observables to tackle general systems of particles in interaction, not only from the physical point of view (as they describe the interplay between a tracer and the bath), but also from a technical point of view, since they verify a closed equation which applies to several systems, beyond the SEP.

To this point, it has become clear that the observables of position and current are intimately related in the context of single-file diffusion (summary in figure 9.7):

- There is the well known relation (6.2) between the position of a particle in a system and the integrated current through different points of this *same* system. This relation (and its translation in terms of Legendre transform 7.2.2) is denoted by $(\mathcal{L})$ in figure 9.7.

- Generalising known mappings between some microscopic models, we introduced general mappings in the hydrodynamic limit in 9.1. We showed that one of these mappings, the duality (Du) relates positions of particles in a given system to the integrated current through different points in another, *dual* system. The other mappings (Di), (T) and (Rt) relate these observables in different corresponding systems.

These rich relationships not only make it possible to export results on a quantity to compute many other quantities, but also, most importantly, impose strong symmetries that must be verified by any general formula characterising single-file diffusion. Using these symmetries could be a powerful way to study general properties of single-file diffusion.

Chapter 10

Biased tracer

In this chapter, we will study the case where the tracer is submitted to an external driving force. This situation is encountered for instance in active microrheology, which is a technique used to probe the properties of living or colloidal systems by forcing the displacement of a tracer through the medium [90, 91]. More generally, it constitutes a minimal one-dimensional model for nonequilibrium transport in confined crowded environments, which has received a growing attention [92, 93] (see also [63, 67, 89, 94, 95] for models combining tracer driving and bath-induced crowding).

We first propose a general procedure to derive hydrodynamic equations describing single-file systems with a bias. Then, we test this theory by comparing it to known results and numerical simulations for some specific models.

Finally, we apply this approach to the SEP with a driven tracer (only the tracer is biased) to obtain new analytical results. So far, the only analytical results at arbitrary density concern the means of both the position of the tracer and the lattice occupation numbers in its frame of reference (i.e. the density profiles) [119, 126, 127], which have recently been determined also on finite periodic systems [122, 128]. Since the seminal works [119, 126, 127] that date back to almost three decades, the results concerning higher-order cumulants have been limited to the high-density limit [129, 130], and to specific situations (equilibrium fluctuations 10.2.3 studied in [131]). At arbitrary density, even the determination of the variance of the position of the tracer, which is crucial to quantify its fluctuations, remains a fully open problem.[1]

Key results.

- Section 10.1: general procedure to describe single-file systems with a biased tracer (or local bias at a fixed point). The next section (10.2) mainly consists in a check of the validity of the procedure on a few examples.
- Section 10.3: we obtain the first non trivial correction (order 2 in the driving force) to the variance of a tracer in the SEP when the tracer is subject to a driving force.

[1] In parallel of our work, similar results appeared in [132]. However, we believe that our treatment is slightly more general (compare their bias matching condition (41) and ours (10.1), and resulting MFT boundary conditions (41,45) and ours (10.19)). Moreover, on the application to the SEP, a model of major importance, the explicit results by Dandekar and Mallick focus on the high-density limit of the problem, while our results are valid at arbitrary density.

10.1 Hydrodynamic description for a biased system

Our goal is to adapt the MFT in order to take into account at the hydrodynamic level bias which is added explicitly in the microscopic system, for example, the SEP with a biased tracer (figure 10.1). According to the duality relation 9.1.1, it is equivalent to consider a biased tracer in a given system and a biased current through the origin in the dual system. For example, the SEP with a biased tracer would correspond to a ZRP with biased bond (coloured arrows in figure 9.1). That is why we will study these two situations.

How to model a microscopic bias in a hydrodynamic description whereas everything is rescaled (6.2), and we loose all the details of the microscopic dynamics? The bias matching condition answers this question.

10.1.1 Bias matching condition

We consider an arbitrary one dimensional diffusive system, namely for which we can define a diffusion coefficient $D(\rho)$ and a mobility $\sigma(\rho)$. The hydrodynamic description relies on the existence of local equilibrium in the microscopic system (see appendix D for more detailed discussion). Local equilibrium means that locally, around a point x, the microscopic system is distributed according to its stationary measure at mean density $\rho(x,t)$. Therefore, in order to implement the bias at the macroscopic level, we need to understand the properties of the stationary measures of the biased system.

Since the number of particles is conserved by the dynamics, there is a family of stationary measures parameterised by the density of the system (identically to what we argue in appendix D). In the case where there is a bias, we expect in addition that the mean density is discontinuous at the location of the bias. For example, a biased tracer will push particles in front of it, so the density at equilibrium should be higher in front of the tracer than behind it. Hence, for each stationary measure, we expect a mean density to the left of the bias ρ_- different from the one to the right ρ_+. From physical intuition, we expect that the force to which is subjected the tracer (coming from the bias) can be compensated by a force coming from an imbalance of density on each side of the tracer, leading to a vanishing mean displacement. For a given density on the left ρ_-, the force from the bias is exactly compensated by one density on the right ρ_+. In other words, stationary ρ_-, ρ_+ verify a relation

$$B(\rho_-, \rho_+) = 0. \tag{10.1}$$

As a consequence, in order to implement the microscopic bias at the hydrodynamic level, we impose a boundary condition on the density field at the position of the bias, which is the one verified by the left and right densities of the stationary measures (10.1). In the case of the biased tracer the bias is located at the position of the tracer X_t, which can be recovered from the hydrodynamic density $\rho(x,t)$ by conservation of the number of particles to the right of the tracer:

$$\int_0^{X_t} \rho(x,t)\mathrm{d}x = \int_0^{\infty} \rho(x,t) - \rho(x,0)\mathrm{d}x. \tag{10.2}$$

The bias matching condition, which involves only hydrodynamic quantities, reads:

$$\boxed{B_T\left(\rho(X_t^-,t), \rho(X_t^+,t)\right) = 0}. \tag{10.3}$$

In the case where the bias is located at a fixed point (usually the origin, see example below of a biased bond between two sites), the bias matching condition takes a simple form:

$$\boxed{B\left(\rho(0^-,t), \rho(0^+,t)\right) = 0}. \tag{10.4}$$

This procedure, which requires to study the stationary measures of the biased system may seem unnecessarily complicated. One could imagine to find the relation (10.1) simply from the condition that the velocity of the tracer must vanish, without knowing anything about the stationary measure (except of course the mean densities ρ_-, ρ_+). In appendix I.1.1, we give an example to show that in general, one needs to know more features of the stationary measures (such as some correlations in addition the the mean densities).

To illustrate the bias relations (10.3, 10.4), we give the example of the SEP with a biased tracer 10.1.1, and of a mass transfer process with biased bond 10.1.1. The study of the stationary measures is done in appendix I.1, here we simply give and illustrate the bias conditions.

Example of the SEP with a biased tracer

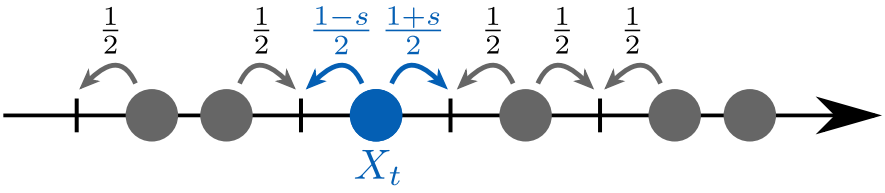

Figure 10.1: The Symmetric Exclusion Process (SEP) with a driven tracer (blue) at position X_t.

The master equation for the probability to find, at time t, the tracer at position X and the bath in configuration (η_r) ($\eta_r = 1$ if site r is occupied by a bath particle, 0 otherwise) is:

$$\partial_t P(X,\eta,t) = \frac{1}{2}\sum_{r\neq X,X-1}\left[P(X,\eta^{r,+},t) - P(X,\eta,t)\right] + \sum_{\mu=\pm1}\frac{1+\mu s}{2}\left\{(1-\eta_X)P(X-\mu,\eta,t) - (1-\eta_{X+\mu})P(X,\eta,t)\right\}. \quad (10.5)$$

In appendix I.1.2, we show that the explicit writing of the general bias condition (10.3) in the specific case of the SEP with a biased tracer is

$$\boxed{(1+s)(1-\rho(X_t^+,t)) - (1-s)(1-\rho(X_t^-,t)) = 0}. \quad (10.6)$$

We can verify that indeed, the mean position of the tracer is constant if the densities in its vicinity verify this relation. From the master equation, we have:

$$\partial_t \langle X_t\rangle = \frac{1+s}{2}(1-\langle\eta_{X_t+1}\rangle) - \frac{1-s}{2}(1-\langle\eta_{X_t-1}\rangle). \quad (10.7)$$

If the mean occupation is equal to the mean density[2] $\langle\eta_{X_t\pm1}\rangle = \rho(X_t^\pm,t)$, then indeed, from (10.6) we have $\partial_t\langle X_t\rangle = 0$.

Biased bond in a mass transfer process

In fact, a specific bias matching condition was introduced for the first time in [114] in the particular case of a mass transfer process with a bias. Here we recover this condition by applying the general procedure described above.

[2]Saying $\langle\eta_{X_t\pm1}\rangle = \rho(X_t^\pm,t)$ is true in the SEP because the stationary measures are product Bernoulli measures of density $\rho(X_t^\pm,t)$. We refer to appendix I.1 for further discussion.

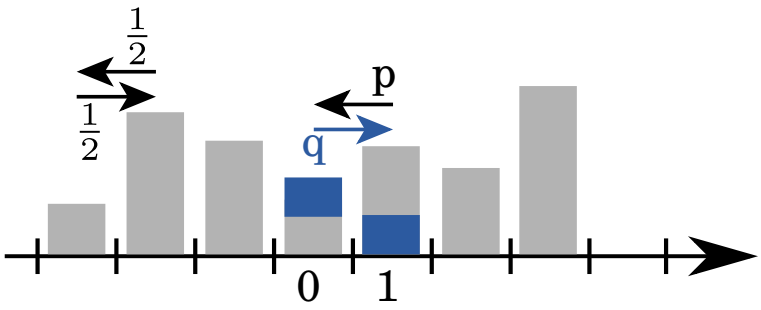

Figure 10.2: Mass transfer process with biased bond $(0,1)$. On each bond $(x, x+1)$ with $x \neq 0$, site x transfers half its mass to site $x+1$ with rate $\frac{1}{2}$ and site $x+1$ transfers half its mass to site x with rate $\frac{1}{2}$. On the biased bond, site 0 transfers half its mass to site 1 with rate q and site 1 transfers half its mass to site 0 with rate p. The system is described by the masses on each site $r \in \mathbb{Z}$, denoted $\eta_r \in \mathbb{R}^+$.

The master equation for the probability density $P(\eta, t)$ to find the system in configuration η at time t is (see [89] for an extensive study of mass transfer processes):

$$\partial_t P(\eta,t) = \frac{1}{2}\sum_{r\neq 0}[2P(\eta^r,t) - 2P(\eta,t)] + 2(p + (q-p)\mathbb{1}_{\mathbb{R}^+}(\eta_1 - \eta_0))P(\eta^0,t) - (p+q)P(\eta,t). \tag{10.8}$$

The configuration η^r is defined as follows:

- For all $x \neq r, r+1$, $\eta^r_x = \eta_x$
- If $\eta_{r+1} > \eta_r$, then $\eta^r_r = 2\eta_r$ and $\eta^r_{r+1} = \eta_{r+1} - \eta_r$.
- If $\eta_{r+1} \leq \eta_r$, then $\eta^r_{r+1} = 2\eta_{r+1}$ and $\eta^r_r = \eta_r - \eta_{r+1}$.

The explicit writing of the general equation (10.4) in the present system (see appendix I.1.2 for proof) is the bias matching condition used in [114]:

$$\boxed{p\rho(0^+,t) - q\rho(0^-,t) = 0}. \tag{10.9}$$

We can verify, similarly to what we did above for the biased tracer, that, this time, the mean of the integrated current through the bond $(0,1)$ denoted by Q_t is constant if the densities verify the bias relation. From the master equation:

$$\partial_t \langle Q_t \rangle = q\left\langle \frac{\eta_0}{2}\right\rangle - p\left\langle \frac{\eta_1}{2}\right\rangle. \tag{10.10}$$

Identifying the mean mass and the density[3] $\langle \eta_0 \rangle = \rho(0^-,t)$ and $\langle \eta_1 \rangle = \rho(0^+,t)$, and using (10.9), we have $\partial_t \langle Q_t \rangle = 0$.

10.1.2 MFT equations for a biased system

In order to get a macroscopic description of a biased one-dimensional diffusive system with transport coefficients $D(\rho)$ and $\sigma(\rho)$, we combine the fluctuating hydrodynamic description (6.2.3), valid at any point where the system follows an unbiased dynamics,

$$\partial_t \rho + \partial_x j = 0, \tag{10.11}$$

$$j + D(\rho)\partial_x \rho = \sqrt{\sigma(\rho)}\eta(x,t), \tag{10.12}$$

[3] Here also, it is true according to the known stationary measures, see appendix I.1.2.

with a bias matching condition derived from the microscopic dynamics according to the procedure detailed above.

In the case of a system with a biased tracer, the condition must be implemented at the position of the tracer, which is moving. Thanks to the duality relation (9.1.1), we can map this moving tracer problem onto the study of the integrated current through the origin (which is fixed) in a dual model (such that the integrated current through the origin in the dual system is equal to the position of the tracer in the original system). The bias condition for the tracer (10.3) can be expressed in terms of the density field $\tilde{\rho}(x,t)$ of the dual system:

$$B_T\left(\frac{1}{\tilde{\rho}(0^-,t)},\frac{1}{\tilde{\rho}(0^+,t)}\right)=0. \tag{10.13}$$

That is why we will focus on the integrated current through the origin in a system with a bias condition at the origin:

$$B\left(\rho(0^-,t),\rho(0^+,t)\right)=0. \tag{10.14}$$

Since there cannot be an infinite accumulation of particles at a point, the current $j(x,t)$ must be continuous at the origin (otherwise an infinite $\partial_x j$ would lead to a diverging density at 0):

$$j(0^-,t)=j(0^+,t). \tag{10.15}$$

The integrated current through the origin between initial time and time t will be denoted

$$Q_t[\rho]=\int_0^\infty \rho(x,t)-\rho(x,0)\mathrm{d}x. \tag{10.16}$$

The optimal density and current

Similarly to what we did in section 7.1.2 for the SEP, the long time limit of the cumulant generating function of the integrated current through the origin $\ln\left\langle e^{\lambda Q_t}\right\rangle$, and the long time limit of the associated GDP-generating function $\frac{\left\langle \rho(x,t)e^{\lambda Q_t}\right\rangle}{\left\langle e^{\lambda Q_t}\right\rangle}$ can be computed using a path integral formulation of MFT (6.7):

$$\ln\left\langle e^{\lambda Q_t}\right\rangle \underset{t\to\infty}{\sim} \ln\int \mathcal{D}[\rho,j]\exp\left(-\sqrt{t}\left(\int_0^1\int_{-\infty}^\infty \frac{\left(j+D(\rho)\partial_x\rho\right)^2}{2\sigma(\rho)}\mathrm{d}x\mathrm{d}t+F[\rho(x,0)]-\lambda Q_1[\rho]\right)\right) \tag{10.17}$$

where we integrate over ρ, j verifying (10.11, 10.14, 10.15). The functional $F[\rho(x,0)]$ encodes the probability on the annealed initial condition (6.8) with mean density profile $\rho_0(x)$. In the long time limit, the path integral will be dominated by the path of least action (minimising the argument of the exponential). Like in section 8.1.2, we solve the optimisation problem under the constraints (10.11, 10.14, 10.15) by introducing a Lagrangian $\mathcal{L}$ and a Lagrange multiplier $\hat{\rho}$ enforcing the conservation (10.11).

We denote by (q,j^*,p) the solution to the optimisation problem under constraint for $(\rho,j,\hat{\rho})$. In appendix I.2.1, show that they verify the classical MFT equations:

$$\begin{aligned}
\partial_t q &= \partial_x(D(q)\partial_x q)-\partial_x\left(\sigma(q)\partial_x p\right),\\
\partial_t p &= -D(q)\partial_x^2 p-\frac{\sigma'(q)}{2}(\partial_x p)^2,\\
p(x,0) &= \lambda\Theta(x)+\int_{\rho_0(x)}^{q(x,0)}\frac{2D(r)}{\sigma(r)}\mathrm{d}r,\\
p(x,1) &= \lambda\Theta(x).
\end{aligned} \tag{10.18}$$

In addition to that, the optimal fields are shown to verify the following boundary conditions, which are specific to the biased case:

$$\boxed{\begin{aligned} B\left(q(0^-,t),q(0^+,t)\right) &= 0,\\ \left[D(q)\partial_x q-\sigma(q)\partial_x p(x,t)\right]_{x=0^-}^{0^+} &= 0,\\ p(0^+,t)-p(0^-,t) &= 0,\\ \partial_- BD(q)\partial_x p(0^+,t)+\partial_+ BD(q)\partial_x p(0^-,t) &= 0. \end{aligned}} \tag{10.19}$$

The derivatives $\partial_\pm B$ are evaluated at $(q(0^-,t),q(0^+,t))$.

These equations, based on MFT, are very general, since they only require to know how the bias affects the density of the bath in the vicinity of the drive in the stationary regime, through the bias condition (10.14). This condition can be computed analytically for simple models, but also sampled numerically or experimentally for more realistic systems.

New mapping for the MFT equations

In the case of the SEP with biased tracer, the transport coefficients $D(\rho)=1/2$ and $\sigma(\rho)=\rho(1-\rho)$ are relatively simple, in particular the diffusion coefficient is constant. However, the theory presented above is valid for a bias located at the origin. That is why we must apply it to the dual of the SEP under the duality relation 9.1.1, since this transformation maps the tracer's position in the SEP to the integrated current through the origin in the dual system. Unfortunately, this dual system has more complicated transports coefficients:

$$\tilde{D}(\tilde{\rho})=\frac{1}{\tilde{\rho}^2}D(1/\tilde{\rho})=\frac{1}{2\tilde{\rho}}\,,\quad \tilde{\sigma}(\tilde{\rho})=\tilde{\rho}\sigma(1/\tilde{\rho})=1-\frac{1}{\tilde{\rho}}. \tag{10.20}$$

This yields non-linear diffusion equations. In order to circumvent this difficulty, we introduce a new general mapping directly at the level of MFT equations (10.18). It is inspired by the duality 9.1.1, but it is not the same since the current $\tilde{j}=-\tilde{D}(\tilde{q})\partial_x\tilde{q}+\sigma(\tilde{q})\partial_x\tilde{p}$ is not mapped accordingly, where we denoted by $(\tilde{q},\tilde{j},\tilde{p})$ the optimal fields for the integrated current cumulant generating function (10.17) in the dual system. We develop this mapping in appendix I.2.2.

10.2 Application to a few examples

The goal of this section is to test and validate the hydrodynamic equations derived above with specific examples of models. We compare the predictions from the hydrodynamic equations with results from Monte Carlo simulations. Our first example is a very rich model, the KLS. As a second example, we present a model for which the hydrodynamic equations are exactly solvable. Finally, we give the general solution for the integrated current (and tracer's position) and the associated correlation profiles in the case where the initial condition is a stationary measure (equilibrium fluctuations). We apply to our two last examples, the SEP with biased tracer (see 10.1.1) and the mass transfer process with biased bond (see 10.1.1). As we proceed to show, applying the procedure developed in section 10.1 yields results which exactly match Monte Carlo simulations.

10.2.1 The KLS model with biased tracer

The KLS model is a lattice model, described by occupation numbers $(\eta_r(t))$ where $\eta_r(t)=1$ if there is a particle on site r and 0 otherwise. The dynamics is described by jump rates

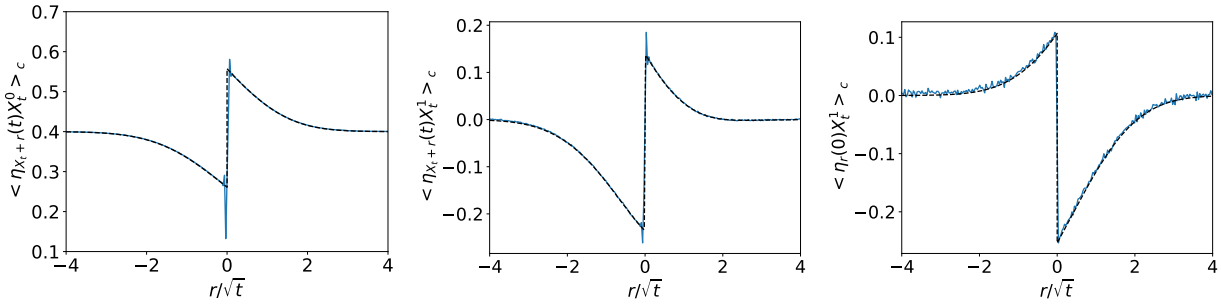

Figure 10.3: We simulated the KLS with parameter $\epsilon = 0.5, \delta = -0.3$, average initial density $\rho = 0.4$ and biased tracer with $a = 0.7, b = 1 - a$, with final time $t = 1000$. Left: density profiles. Middle: correlation profiles. Right: correlation between initial density at site r and position of the tracer at time t. Blue lines: Monte Carlo simulations (4000 sites, 10^7 simulations). Dashed lines: numerical resolution of equations (10.18).

which depend on the neighbouring configuration of the particle attempting the jump (see definition 6.1.2). Here we consider a biased tracer, namely its jump rates to the right are multiplied by a, and to the left by b. Since this model displays a rich phenomenology, with interactions inducing non-zero correlations at large distance (although decaying exponentially), it constitutes a challenging test, validating the robustness of our procedure.

The transport coefficients of the KLS are [176]:

$$D(\rho) = \frac{1}{\nu^3} \frac{\nu[1+\delta(1-2\rho)] - \epsilon\sqrt{4\rho(1-\rho)}}{\rho(1-\rho)\sqrt{(2\rho-1)^2 + 4\rho(1-\rho)e^{-4\beta}}}, \quad \sigma(\rho) = \frac{2}{\nu^3}\left(\nu[1+\delta(1-2\rho)] - \epsilon\sqrt{4\rho(1-\rho)}\right), \tag{10.21}$$

where $\nu = \dfrac{1 + \sqrt{(1-2\rho)^2 + 4\rho(1-\rho)e^{-4\beta}}}{\sqrt{4\rho(1-\rho)}}$ and $e^{-4\beta} = \dfrac{1-\epsilon}{1+\epsilon}$.

To find the bias condition, we look for the equilibrium measures for $\tau_r = \eta_{X_t+r}$, the occupations in the reference frame of the tracer. If fact, the dynamics of (τ_r) is reversible with respect to any Ising measure of the following family [175]:

$$\begin{aligned}\mathbb{P}(\tau_r) = &\exp\left(+\beta(1-2\tau_{-1}) + \beta(1-2\tau_1)\right) \\ &\times \prod_{r<0} \frac{1}{\lambda_-} \exp\left(-\beta(1-2\tau_r)(1-2\tau_{r-1}) - h_-(1-2\tau_r)\right) \\ &\times \prod_{r>0} \frac{1}{\lambda_+} \exp\left(-\beta(1-2\tau_r)(1-2\tau_{r+1}) - h_+(1-2\tau_r)\right),\end{aligned} \tag{10.22}$$

where $\lambda_\pm = e^{-\beta}\cosh h_\pm + \sqrt{e^{-2\beta}\sinh^2 h + e^{2\beta}}$ (it is the largest eigenvalue of the transfer matrix of the associated Ising measure), $e^{-4\beta} = \frac{1-\epsilon}{1+\epsilon}$ (this ensures reversibility with respect to transitions of rate $1 \pm \epsilon$), and $a\left(\frac{e^{-h_+}}{\lambda_+}\frac{\lambda_-}{e^{-h_-}}\right) = b$ (this ensures reversibility with respect to a displacement of the tracer, which would have the effect of removing a site in front of the tracer, and adding one behind it).

The parameter $h_\pm$ is related to the average density $\rho_\pm = \lim_{N\to\infty} \frac{\sum_{r=0}^{\pm N}\langle\tau_r\rangle}{N}$ (we also take a spacial average because the sites are correlated) through [175] $h(\rho) = \operatorname{argsh}\left[\frac{e^{-2\beta}|1-2\rho|}{2\sqrt{\rho(1-\rho)}}\right]$. Therefore, the bias condition takes the form:

$$B_T(\rho(X_t^-,t), \rho(X_t^+,t)) = a\frac{e^{-h(\rho(X_t^+,t))}}{\lambda(\rho(X_t^+,t))} - b\frac{e^{-h(\rho(X_t^-,t))}}{\lambda(\rho(X_t^-,t))} = 0. \tag{10.23}$$

In order to apply the MFT equations (10.18) to this model, we consider its dual 9.1.1 with corresponding bias relation (10.13). Given the complexity of the transport coefficients involved, the equations are intractable analytically, so we perform a numerical resolution of the equations, displayed in figure 10.3. The optimal density field $\rho^*(x,t)$ for the KLS with a biased tracer is obtained from the one of its dual $q(x,t)$ solution of (10.18) through relation (9.20):

$$\rho^*(x_k(t),t) = \frac{1}{q(k,t)}\,, \quad x_k(t) = x_0(t) + \int_0^k q(k',t)\mathrm{d}k'. \tag{10.24}$$

Note that the MFT formalism interestingly also gives access to the correlations between initial occupation numbers $\eta_r(0)$ and final position of the tracer (figure 10.3, on the right). If we denote by ρ_1^* the first order in lambda of $\rho^* = \rho_0^* + \lambda\rho_1^* + O(\lambda^2)$, then we have:

$$\langle \eta_r(0) X_t \rangle_c = \langle \eta_r(0)(X_t - \langle X_t \rangle) \rangle \underset{t\to\infty}{\sim} \rho_1^*\left(\frac{r}{\sqrt{t}}, t\right) \tag{10.25}$$

As we can see in figure 10.3, we find an excellent agreement between predictions from our procedure and Monte Carlo simulation.

10.2.2 An exactly solvable biased tracer model

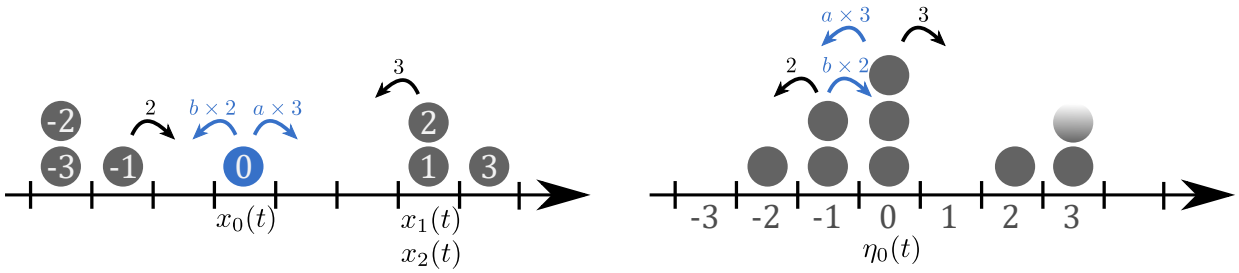

Figure 10.4: On the left, an example of realisation of the model. On the right, the corresponding system of gaps: site r contains $\eta_r(t) = x_{r+1}(t) - x_t(t)$ particles.

We consider a model of particles on the infinite one-dimensional lattice. The positions of the particles at time t are denoted $(x_k(t))_{k\in\mathbb{Z}}$, and the initial position of the tracer is the origin: $x_0(0) = 0$. The dynamics is described as follows:

- For $k \neq 0$, the particle k can jump to site $x_k(t)+1$ with rate $x_{k+1}(t) - x_k(t)$ (namely the rate is proportional to the distance to the next particle, like harmonic interactions between particles), and to site $x_k(t) - 1$ with rate $x_{k-1}(t) - x_k(t)$.
- The tracer (particle 0) is biased, it can jump to site $x_0(t)+1$ with rate $a(x_1(t) - x_0(t))$, and to site $x_0(t) - 1$ with rate $b(x_{-1}(t) - x_0(t))$.

We can also consider the gaps between particles $\eta_r(t) = x_{k+1}(t) - x_k(t)$. The dynamics of the gaps is described by a ZRP 6.1.2, where site r can transfer a particle to site $r \pm 1$ with rate $\eta_r(t)$ (for each neighbour), except if the transfer occurs at the biased bond $(-1, 0)$ in which case the rates are multiplied by a or b according to figure 10.4.

On the hydrodynamic level, this systems of gaps (η_r) is related to the original system of particles (x_k) through the particles-gaps duality 9.1.1. This system of gaps is in fact equivalent

to the independent walkers model (because a site bearing n particles gives a particle to a neighbouring site with a rate proportional to n) and its transport coefficients are given by [86]:

$$\tilde{D}(\tilde{\rho}) = 1\,, \quad \tilde{\sigma}(\tilde{\rho}) = 2\tilde{\rho}. \tag{10.26}$$

As a consequence, using duality 9.1.1, the transport coefficients of the original system of particles are:

$$D(\rho) = \frac{1}{\rho^2}\,, \quad \sigma(\rho) = 2. \tag{10.27}$$

Similarly to the example of a biased bond in a mass transfer process 10.1.1, the evolution equations on the mean gaps $\langle \eta_r(t) \rangle$ are closed:

$$\begin{aligned} \partial_t \langle \eta_r(t) \rangle =& (1 - \delta_{r,0} - \delta_{r,-11}) \left(\langle \eta_{r+1}(t) \rangle + \langle \eta_{r-1}(t) \rangle - 2 \langle \eta_r(t) \rangle \right) \\ &+ \delta_{r,-1} \left(\langle \eta_{-2}(t) \rangle + a \langle \eta_0(t) \rangle - (1+b) \langle \eta_{-1}(t) \rangle \right) \\ &+ \delta_{r,0} \left(\langle \eta_1(t) \rangle + b \langle \eta_{-1}(t) \rangle - (1+a) \langle \eta_0(t) \rangle \right). \end{aligned} \tag{10.28}$$

The stationary solutions are $\langle \eta_r(t) \rangle = \rho_- \left(1 + \left(\frac{b}{a} - 1\right) \mathbb{1}_{\mathbb{N}}(r)\right)$, hence the bias matching condition for the hydrodynamic profile $\tilde{\rho}(x,t)$ of the system of gaps:

$$B(\tilde{\rho}(0^-,t), \tilde{\rho}(0^+,t)) = a\tilde{\rho}(0^+,t) - b\tilde{\rho}(0^-,t) = 0. \tag{10.29}$$

Resolution of the MFT equations with boundary conditions for the system of gaps

Since the transport coefficients of system of gaps (10.26) (the dual system) are simple, we can solve the associated MFT equations (10.18) with boundary conditions (10.19) for the integrated current through the origin. This is done in appendix I.3.1, for step initial condition with density ρ_- to the left of the origin and ρ_+ to the right. Note that this corresponds in the original system of particles $(x_k(t))$ to an initial density of ρ_-^{-1} to the left of the tracer and ρ_+^{-1} to the right.

The long time limit of the generalised density profiles $\phi_Q(v) = \lim_{t\to\infty} \dfrac{\left\langle \eta_{\lfloor v\sqrt{4t} \rfloor} e^{\lambda Q_t} \right\rangle}{\left\langle e^{\lambda Q_t} \right\rangle}$ (where Q_t is the integrated current through the origin) is obtained by taking the MFT optimal profile q (solution of (10.18, 10.19)) at time $t = 1$ (see section 7.1.2). From the resolution in appendix I.3.1, we get:

$$\phi_Q(v > 0) = \rho_+ - \operatorname{erfc}(v) \left(-b e^{\lambda} \rho_- + a \rho_+ \right), \tag{10.30}$$

$$\phi_Q(v < 0) = \rho_- - \operatorname{erfc}(-v) \left(b \rho_- - e^{-\lambda} a \rho_+ \right). \tag{10.31}$$

Finally, the long time limit of the cumulant generating function can be easily computed using the identity $\dfrac{\mathrm{d} \ln \left\langle e^{\lambda Q_t} \right\rangle}{\mathrm{d}\lambda} = \dfrac{\left\langle Q_t e^{\lambda Q_t} \right\rangle}{\left\langle e^{\lambda Q_t} \right\rangle} \underset{t\to\infty}{\sim} \sqrt{t} \displaystyle\int_0^\infty q(x,1) - q(x,0) \mathrm{d}x$, since the weighed average $\dfrac{\left\langle \bullet e^{\lambda Q_t} \right\rangle}{\left\langle e^{\lambda Q_t} \right\rangle}$ is dominated by the optimal profile q in the long time limit. This yields:

$$\ln \left\langle e^{\lambda Q_t} \right\rangle \underset{t\to\infty}{\sim} \sqrt{4t} \frac{\left(e^{\lambda} - 1\right)(1-a)\rho_- + \left(e^{-\lambda} - 1\right) a \rho_+}{\sqrt{\pi}}. \tag{10.32}$$

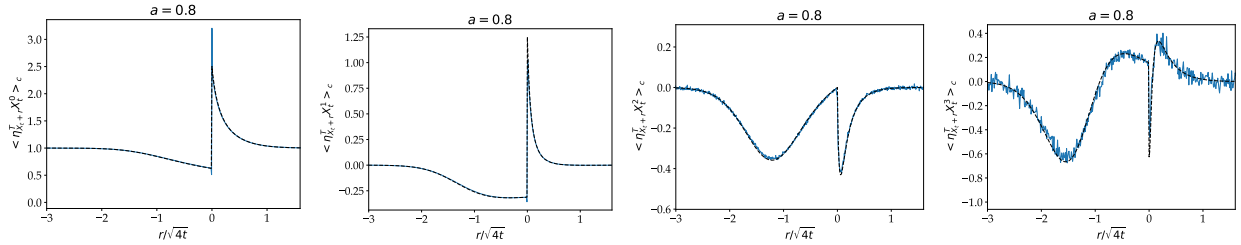

Figure 10.5: The solution to equation (10.37) is expanded up to order 3 in λ (dashed line) and compared to Monte Carlo simulations (1600 particles, final time $t = 4000$ for $\left\langle \eta^T_{x_0(t)+r} x_0(t)^3 \right\rangle_c$ and $t = 10000$ for the others, 6×10^8 simulations). The initial density is $\rho = 1$. We noted $X_t = x_0(t)$.

Closed equations for the system of particles with a biased tracer

Finally, we can get back to the original system of particles $(x_k(t))$ using the duality 9.1.1. The key result for this simple model is that we can show that the long time limit of the GDP-generating function still verifies a closed equation, very similar to what we had for the unbiased tracer in the dilute limit of the SEP 8.1.1.

The position of the tracer is the opposite of the integrated current through the origin in the system of gaps, so $x_0(t) = -Q_t$. Thus we find for the cumulant generating function of the tracer:

$$\hat{\psi} = \lim_{t\to\infty} \frac{\ln \left\langle e^{\lambda x_0(t)} \right\rangle}{\sqrt{4t}} = \frac{\left(e^{-\lambda} - 1\right)(1-a)\rho_- + \left(e^{\lambda} - 1\right) a\rho_+}{\sqrt{\pi}}. \tag{10.33}$$

The long time limit Φ of the GDP-generating function is defined by:

$$\frac{\left\langle \eta^T_{x_0(t)+r} e^{\lambda x_0(t)} \right\rangle}{\left\langle e^{\lambda x_0(t)} \right\rangle} \underset{t\to\infty}{\sim} \phi\left(v = \frac{r}{\sqrt{4t}}, \lambda\right), \tag{10.34}$$

where $\eta^T_r(t) = \sum_{k\in\mathbb{Z}} \delta_{r,x_k(t)}$. It is related to the generalised profiles of the dual system through (9.20):

$$\phi(v(k), \lambda) = \frac{1}{\phi_Q(k, -\lambda)}, \tag{10.35}$$

$$v(k) = \int_0^k \phi_Q(k', -\lambda) \mathrm{d}k'. \tag{10.36}$$

As a consequence, from the solution (10.31), it follows that ϕ verifies the following closed equation:

$$\boxed{\partial_v \left(\frac{\phi'}{\phi^2}\right) + 2\left(v + \nu \frac{\hat{\psi}_T}{e^{\nu\lambda} - 1}\right)\phi' = 0}, \tag{10.37}$$

where $\nu = \mathrm{sign}(v)$, with the boundary conditions:

$$\phi(\pm\infty) = \rho^T_{\pm}, \tag{10.38}$$

$$a\phi(0^+) - be^{\lambda}\phi(0^-) = 0, \tag{10.39}$$

$$\frac{\phi'(0^+)}{\phi(0^+)^3} - \frac{2\hat{\psi}}{1 - e^{\lambda}} = 0, \tag{10.40}$$

$$\frac{\phi'(0^-)}{\phi(0^-)^3} + \frac{2\hat{\psi}}{1 - e^{-\lambda}} = 0. \tag{10.41}$$

Here we denoted $\rho_\pm^T$ the initial densities of particles to the left and to the right of the tracer.

The solution to these equations is in perfect agreement with Monte Carlo simulations up to order 3 in λ (figure 10.5).

The closed equation (10.37) is obtained through the hydrodynamics approach, but it would be instructive to obtain it directly from the microscopic dynamics of the model.

10.2.3 Equilibrium fluctuations in a general system

When the initial density to the left ρ_- and to the right ρ_+ of a biased tracer are such that $B_T(\rho_-, \rho_+) = 0$, the mean displacement is zero. Intuitively, this means that the step of density exactly compensates the drive applied to the tracer. In this situation, which has been studied previously in the SEP [131], the first non-zero cumulant of the tracer's position is its mean squared displacement. Strikingly, this quantity can be computed in great generality from MFT equations (10.18) and boundary conditions (10.19) by expanding these equations in function of λ and solving them at order 1 (see appendix I.3.2). Here we give the analytical results, obtained by using a Green function similar to (I.38).

Biased integrated current

We consider a system with transport coefficients D and σ, with a bias at the origin:

$$B(\rho(0^-, t), \rho(0^+, t)) = 0. \tag{10.42}$$

Initially, the system is at equilibrium, namely the initial density ρ_- to the left of the origin and the one ρ_+ to the right verify:

$$B(\rho_-, \rho_+) = 0. \tag{10.43}$$

As a consequence, the average density remains constant $\rho(x, t) = \rho_- + \Theta(x)(\rho_+ - \rho_-)$. The first non trivial generalised density profile is therefore the correlation profile:

$$g_x(t) = \langle \rho(x, t) Q_t \rangle \underset{t\to\infty}{\sim} \Phi_1\left(\frac{r}{\sqrt{t}}\right) \tag{10.44}$$

We denote $B_\pm = \frac{\partial B(\rho_-,\rho+)}{\partial \rho_\pm}$ ($= \partial_\pm B(\rho_-, \rho_+)$ with $\partial_\pm B$ previously defined), $D_\pm = D(\rho_\pm)$ and $\sigma_\pm = \sigma(\rho_\pm)$. We have for $v > 0$:

$$\boxed{\Phi_1(v) = \frac{\pi\left(B_-^2 D_+ \sqrt{\frac{D_+}{D_-}}\sigma_- + B_+^2 D_- \sigma_+\right) \operatorname{erfc}\left(\frac{v}{2\sqrt{D_+}}\right) - B_- \sqrt{\frac{D_+}{D_-}} \left(B_- D_+ \sigma_- + B_+ D_- \sigma_+\right) \operatorname{Ei}\left(-\frac{v^2}{4D_+}\right)}{2\pi D_+ \left(B_+\sqrt{D_-} - B_-\sqrt{D_+}\right)^2}}. \tag{10.45}$$

Note the presence of the exponential integral function Ei, which has a logarithmic divergence at 0, which seems to be associated with a very slow convergence (figure 10.6). The variance reads:

$$\boxed{\left\langle Q_t^2 \right\rangle \underset{t\to\infty}{\sim} \frac{2\sqrt{t}\left(\frac{B_-^2 D_+ \sigma_-}{\sqrt{D_-}} + \frac{B_+^2 D_- \sigma_+}{\sqrt{D_+}}\right)}{\sqrt{\pi}\left(B_+\sqrt{D_-} - B_-\sqrt{D_+}\right)^2}} \tag{10.46}$$

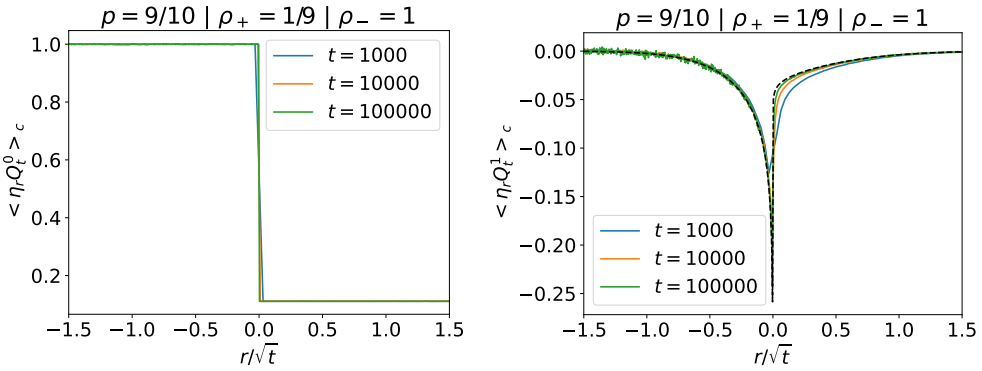

Figure 10.6: Equilibrium fluctuations of the integrated current through the origin for the mass transfer process with biased bond 10.1.1 ($D = 1/4, \sigma(\rho) = \rho^2/2, q = 1 - p$). Lines: Monte Carlo simulations of duration t. Dashed line: formula (10.45).

Biased tracer

Applying duality 9.1.1, we can extend the previous result for systems with transport coefficients D and σ and a biased tracer with bias condition:

$$B_T(\rho(X_t^-, t), \rho(X_t^+, t)) = 0. \tag{10.47}$$

Initially, the system is at equilibrium, with initial density ρ_- to the left of the origin and ρ_+ to the right with:

$$B_T(\rho_-, \rho_+) = 0. \tag{10.48}$$

The mean position of the tracer remains zero, and we can compute the correlation profile:

$$g_x(t) = \langle \rho(x,t) X_t \rangle \underset{t\to\infty}{\sim} \Phi_1\left(\frac{r}{\sqrt{t}}\right) \tag{10.49}$$

We use the same shorthand notations $B_\pm = \frac{\partial B_T(\rho_-,\rho+)}{\partial \rho_\pm}$, $D_\pm = D(\rho_\pm)$ and $\sigma_\pm = \sigma(\rho_\pm)$. We have for $v > 0$:

$$\boxed{\Phi_1(v) = \frac{\pi\rho_+ \left(B_-^2 D_+ \sqrt{\frac{D_+}{D_-}}\sigma_- + B_+^2 D_- \sigma_+\right) \operatorname{erfc}\left(\frac{v}{2\sqrt{D_+}}\right) - B_- \sqrt{\frac{D_+}{D_-}} \left(B_- D_+ \rho_+ \sigma_- + B_+ D_- \rho_- \sigma_+\right) \operatorname{Ei}\left(-\frac{v^2}{4D_+}\right)}{2\pi D_+ \left(B_- \sqrt{D_+}\rho_- - B_+ \sqrt{D_-}\rho_+\right)^2}} \tag{10.50}$$

and the variance of the tracer:

$$\boxed{\left\langle X_t^2 \right\rangle = \frac{2\left(B_-^2 \rho_-^2 \sigma_- \sqrt{D_+} + B_+^2 \rho_+^2 \sigma_+ \sqrt{D_-}\right)\sqrt{t}}{\sqrt{\pi}\left(B_-^2 \sqrt{D_- D_+}\rho_-^4 - B_- B_+ \rho_+ \rho_- \left(D_- \rho_-^2 + D_+ \rho_+^2\right) + B_+^2 \sqrt{D_- D_+}\rho_+^4\right)}}. \tag{10.51}$$

These results are very general, and, together with the exactly solvable model 10.2.2, they constitute a first basis in trying to extend the closed equation approach (chapter 8) to the case of a biased tracer.

10.3 The simple exclusion process with a biased tracer

As we recalled in the introduction of this chapter, the study of the SEP with a biased tracer 10.3 has turned out to be a difficult problem [119, 126, 131, 188]. Thanks to the method

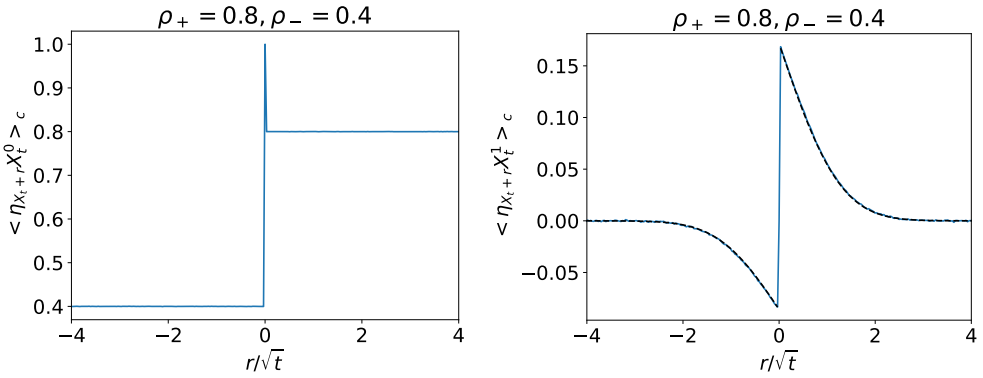

Figure 10.7: Equilibrium fluctuations of the tracer's position in the biased SEP 10.3 ($D = 1/2, \sigma(\rho) = \rho(1-\rho)), q = 1-p, p = 0.75$). Lines: Monte Carlo simulations of duration $t = 1000$. Dashed line: formula (10.50). Note that the exponential integral has a vanishing pre-factor in this case.

developed in this chapter, based on equations (10.18) with boundary conditions (10.19), we are able to make progress on this problem. In fact, in this section, we will not used directly equations (10.18) with boundary conditions (10.19). We will use the equations (I.25, I.26), which are obtained from them by applying the new mapping we mentioned in paragraph 10.1.2.

We determine the long time limit of the bath-tracer density profiles and cumulants of the tracer position at linear order in the driving force and at arbitrary density. We also go beyond linear response by determining the second cumulant of the tracer position and the corresponding density profile at second order in the driving force. We thus provide the first non-trivial contribution of the driving force to the variance of the tracer position at arbitrary density.

We would like to follow an approach similar to what we did for the symmetric tracer (chapters 7, 8), based on the GDP-generation function, defined identically:

$$w_r(t) = \frac{\left\langle \eta_{X_t+r} \mathrm{e}^{\lambda X_t} \right\rangle}{\left\langle \mathrm{e}^{\lambda X_t} \right\rangle} \underset{t\to\infty}{\sim} \Phi\left(v = \frac{r}{\sqrt{2t}}\right), \tag{10.52}$$

which is related in the long-time limit to the cumulant generating function

$$\ln \left\langle \mathrm{e}^{\lambda X_t} \right\rangle \underset{t\to\infty}{\sim} \hat{\psi}(\lambda)\sqrt{2t}\,, \quad \hat{\psi}(\lambda) = \sum_{n=0}^{\infty} \frac{\lambda^n}{n!} \hat{\kappa}_n \tag{10.53}$$

through the same boundary equations as in the symmetric case (7.44) [103, 133]:

$$\Phi'(0^{\pm}) \pm \frac{2\hat{\psi}}{\mathrm{e}^{\pm\lambda} - 1} \Phi(0^{\pm}) = 0\,. \tag{10.54}$$

As a consequence of the MFT large deviation principle, the GDP-generating function is related to the optimal density profile (see section 7.1.2) q solution of equations (I.25), with transport coefficients of the SEP $D = 1/2, \sigma(\rho) = \rho(1-\rho)$ and the bias matching condition (10.6):

$$\Phi(v) = q(v\sqrt{2}, 1). \tag{10.55}$$

Therefore, expanding these equations (I.25) in the variable λ (writing $q = \sum \lambda^n q_n$ and $\pi = \sum \lambda^n \pi_n$), we can solve for the first orders in λ: Φ_0, Φ_1, Φ_2.

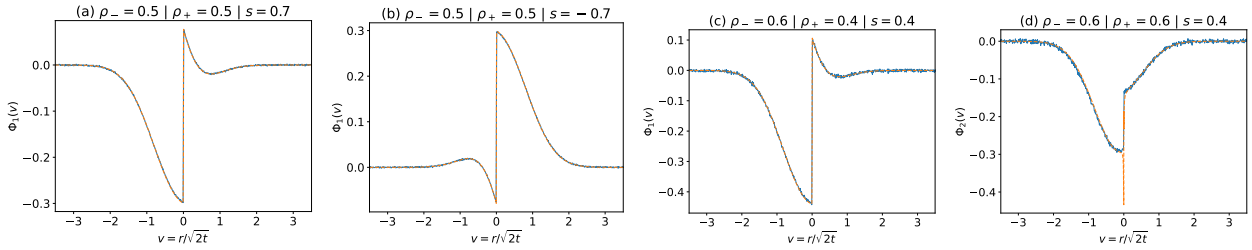

Figure 10.8: Profiles Φ_1 and Φ_2 obtained from the numerical resolution of the MFT equations (I.25) (orange dashed lines), compared to Monte Carlo simulations (blue solid lines), final time 6000, 10^7 simulations for (a), (b) and (c) and $9 \cdot 10^7$ for (d), of the SEP with a driven tracer, for various values of the bias and the density. The discrepancy at $v = 0$ on panel (d) comes from the numerical errors on Φ_1 near the discontinuity at the origin, which are amplified at the second order Φ_2.

10.3.1 Numerical resolution

We show in figure 10.8 the profiles at order 1 and 2 in λ obtained from the numerical resolution of the MFT equations (I.25), which are in perfect agreement with results from microscopic Monte Carlo simulations, for a broad range of parameters. In particular, we consider strong biases, and densities which are far from the extreme low- and high-density limits. Note that the approach can be extended to the paradigmatic case where the initial density of particles is step-like ($\rho = \rho_+$ in front of the tracer and $\rho = \rho_-$ behind the tracer) [99, 100]. Finally, the plots show that our MFT procedure 10.1 captures non-trivial dependencies of the correlation profiles on the rescaled distance.

10.3.2 New analytical results

We now turn to the analytical resolution of equations (I.25), perturbatively in the intensity of the bias s, with flat initial density ρ.

Linear order in s

We first note that, for any bias, at zeroth order in λ, we retrieve the exact results previously obtained for the mean occupation profiles in the frame of reference of the driven tracer [119, 126]. However, for the next orders (Φ_n with $n \geq 1$), no explicit analytical solution of the MFT problem at arbitrary density is available. We then resort to an expansion in powers of the bias s, and define for each order n:

$$\Phi_n(v) \underset{s\to 0}{=} \Phi_n^{(0)}(v) + s\Phi_n^{(1)}(v) + s^2\Phi_n^{(2)}(v) + \dots \tag{10.56}$$

where $\Phi_n^{(0)}$ corresponds to the known symmetric case (chapter 8). At linear order in the bias s, we find (we give the expressions for $v > 0$, as the ones for $v < 0$ can be deduced from the symmetry $v \to -v$, $\lambda \to -\lambda$ and $s \to -s$ which imposes $\Phi_n^{(m)}(-v) = (-1)^{n+m}\Phi_n^{(m)}(v)$.)

$$\Phi_1^{(1)}(v) = \frac{1-\rho}{2\rho}\left((2-3\rho)\operatorname{erfc}(v) - (1-\rho)\frac{6}{\pi}\mathrm{e}^{-v^2}\right) \tag{10.57}$$

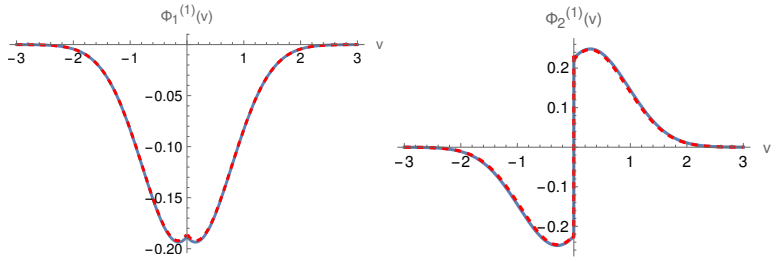

Figure 10.9: Generalised density profiles $\Phi_n^{(1)}(v)$ at first order in the bias s, at density $\rho = 0.6$, obtained from the numerical resolution of the MFT equations (10.18) (dashed red lined), compared to the analytical expressions (10.57) and (10.58) (solid blue). Left: profile $\Phi_1^{(1)}$. Right: profile $\Phi_2^{(1)}$.

$$\Phi_2^{(1)}(v) = \frac{(1-\rho)(1-2\rho(1-\rho))}{2\rho^2}\operatorname{erfc}(v) + \frac{(1-\rho)^2(4-3\rho)}{\pi\rho^2}\operatorname{erfc}(v) - \frac{(1-\rho)^2}{\rho}\operatorname{erfc}\left(\frac{v}{\sqrt{2}}\right)^2 - \frac{(1-\rho)^2}{2\rho^2}G(\sqrt{2}\,v) + \frac{8(1-\rho)^3}{\pi^{3/2}\rho^2}v\,\mathrm{e}^{-v^2} - \frac{4(1-\rho)^2(1-2\rho)}{\pi\rho^2}\mathrm{e}^{-v^2} - \frac{(1-\rho)^2}{\pi^{3/2}\rho^2}v\,\mathrm{e}^{-\frac{v^2}{2}}\,\mathrm{K}_0\left(\frac{v^2}{2}\right), \tag{10.58}$$

where $G(x) = \frac{1}{\pi}\sqrt{\frac{2}{\pi}}\int_x^\infty \mathrm{e}^{-z^2/4}\mathrm{K}_0\left(\frac{z^2}{4}\right)\mathrm{d}z$, and K_0 is a modified Bessel function of zeroth order. A key point is that, contrary to the first order in λ, $\Phi_2^{(1)}$ is a *non-analytic* function of the rescaled distance v, displaying a logarithmic singularity at the origin. This appears to be a specificity of the driven case, since, in the symmetric case, all Φ_n are analytical functions of the rescaled distance (chapter 10). The functions $\Phi_1^{(1)}(v)$ and $\Phi_2^{(1)}(v)$ are plotted in figure 10.9 and display perfect agreement with the numerical resolution of the MFT equations. The profile $\Phi_1(v)$ measures the correlation between the density at a rescaled distance v from the tracer, and the position of the tracer [103]. When there is no driving force, $\Phi_1^{(0)}(v > 0) > 0$, therefore a fluctuation of X_t towards the right is correlated with an increase of the density in front of the tracer, indicating an accumulation of particles in front of the tracer. Here, we find that the linear correction to these correlations due to the presence of the drive, $\Phi_1^{(1)}(v)$, is negative, indicating that a positive driving force reduces these correlations, while a negative drive increases them.

In addition to fully characterising the bath-tracer correlations, the generalized density profiles Φ_n also lead to the cumulants of the tracer's position. This is made possible by the key relation derived above [equation (10.54)]. We get for the rescaled cumulants:

$$\hat{\kappa}_1 = s\frac{1-\rho}{\rho\sqrt{\pi}} + \mathcal{O}(s^2), \quad \hat{\kappa}_2 = \frac{1-\rho}{\rho\sqrt{\pi}} + \mathcal{O}(s^2), \tag{10.59}$$

$$\hat{\kappa}_3 = \frac{s}{\pi^{3/2}\rho^3}\left[(1-\rho)\left(12(1-\rho)^2 - \pi\left(\left(8-3\sqrt{2}\right)\rho^2 - 3\left(4-\sqrt{2}\right)\rho + 3\right)\right)\right] + \mathcal{O}(s^2)\,. \tag{10.60}$$

We notice that, up to order $n = 3$, $\hat{\kappa}_n = s\,\hat{\kappa}_{n+1}^{(s=0)} + \mathcal{O}(s^2)$, which implies that

$$\psi(\lambda, t) \underset{t\to\infty}{\sim} \psi^{(s=0)}(\lambda, t) + s\,\frac{\mathrm{d}\psi}{\mathrm{d}\lambda}^{(s=0)} + \mathcal{O}(s^2, \lambda^4)\,. \tag{10.61}$$

On top of that, we checked from the high-density solution obtained in [129, 130] that, when $\rho \to 1$, equation (10.61) holds at any order in λ, and at arbitrary time. This points towards the generality of this relation.

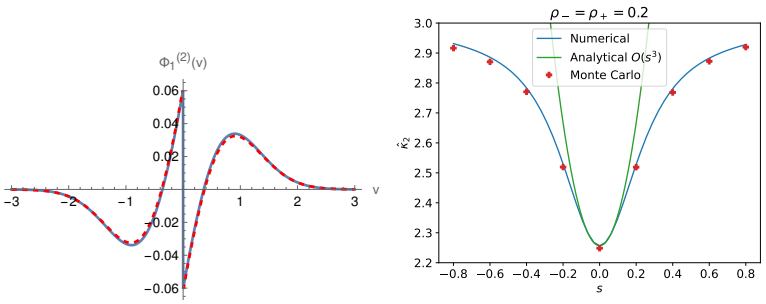

Figure 10.10: Left: Profile $\Phi_1^{(2)}(v)$ at $\rho = 0.6$ (10.62) (solid blue), compared to the numerical resolution of the MFT equations (10.18) (dashed red). Right: rescaled cumulant $\hat{\kappa}_2$ as a function of the bias s, obtained from the numerical resolution of the MFT equations (solid blue), compared to the small bias expansion (10.63) (solid green line). The points are obtained from Monte Carlo simulations (15.8 million simulations, final time 100000). Note that the correction in s^2 to $\hat{\kappa}_2$ is always positive, for all the values of the density ρ.

Beyond linear response

We next show that explicit analytical results can be obtained beyond linear response which, as we proceed to show, can be quantitatively and even qualitatively significant. In addition, even if our previous expressions provide the leading order in the bias s, they do not bring non-trivial information for even cumulants, since the first non-zero correction to the unbiased case is actually of order s^2 for symmetry reasons. We thus compute the profile Φ_1 at quadratic order in the bias, and get

$$\Phi_1^{(2)}(v) = \frac{(1-2\rho)(1-\rho)^2}{2\rho^2}\operatorname{erfc}(v) + \frac{(3-\rho)(1-\rho)^2}{\pi\rho^2}\operatorname{erfc}(v) - \frac{(1-\rho)^2}{2\rho}\operatorname{erfc}\left(\frac{v}{\sqrt{2}}\right)^2 - \frac{(1-\rho)^2}{2\rho^2}G(\sqrt{2}\,v) + \frac{5(1-\rho)^3}{\pi^{3/2}\rho^2}v\,\mathrm{e}^{-v^2} - \frac{(3-5\rho)(1-\rho)^2}{\pi\rho^2}\mathrm{e}^{-v^2} - \frac{(1-\rho)^2}{\pi^{3/2}\rho^2}v\,\mathrm{e}^{-\frac{v^2}{2}}\,\mathrm{K}_0\left(\frac{v^2}{2}\right). \tag{10.62}$$

Interestingly, we note that, even at order 1 in λ (and not only at order 2 as in the linear response analysis discussed above), the density profile is in fact non-analytic at the origin. We stress that this qualitatively different feature emerges beyond linear response.

In addition, the expression of $\Phi_1^{(2)}$ yields the s^2 order of $\hat{\kappa}_2 = \hat{\kappa}_2|_{s=0} + s^2\,\Delta\hat{\kappa}_2^{(2)} + \mathcal{O}(s^3)$, with

$$\boxed{\Delta\hat{\kappa}_2^{(2)} = \frac{(1-\rho)^2(7-5\rho-\pi((\sqrt{2}-3)\rho+2))}{\pi^{3/2}\rho^3}}. \tag{10.63}$$

This result constitutes the first determination of the bias-dependence of the variance of a driven tracer in the SEP for an arbitrary density, a problem which has remained open for more than 25 years.

The function $\Phi_1^{(2)}(v)$ is plotted in figure 10.9 and displays very good agreement with the results obtained from the numerical resolution of equations (10.18). We also display the dependence of the second cumulant as a function of the bias for a given value of the density $\rho = 0.2$, which shows good agreement with both microscopic Monte Carlo simulations and the numerical resolution as long as the bias is small enough. This cumulant displays an important variation with the bias ($\sim 30\%$), emphasising the quantitative importance of studying the problem beyond linear response (which would predict zero variation).

Conclusion

To conclude, we introduced a general procedure to obtain a macroscopic, hydrodynamic description for biased systems (either a biased particle or a biased bond). Then we tested this procedure on different examples, which displayed a perfect agreement with Monte Carlo simulations. Finally, applying this procedure to the SEP, we obtained the first new analytical result since more than twenty years for the variance of the position of a biased tracer, beyond linear response.

In further studies, we would like to extend the closed-equation approach for the symmetric SEP (chapters 7 and 8) to the case of a biased tracer. The results we obtained here for the SEP 10.2.3, the general result for the equilibrium fluctuations 10.2.3, the closed equations for a specific model 10.2.2, and further calculations using the procedure 10.1 constitute a first basis to this aim.

Conclusion and open questions

As a conclusion, we sum up the main steps of our approach to the study of tracer diffusion (and integrated current, which is, as we have shown, a closely related observable) in one dimension. We started from the observation that, although strong correlations between particles were known to be the signature of one-dimensional transport compared to higher dimensions, these correlations had not been characterised precisely. These correlations are at the origin of the anomalous scaling of the cumulants of the position of the tracer.

We first focused on the case of the SEP, which is paradigmatic model. To characterise the correlations between a tracer and the bath, we relied on the generalised density profiles, an observable introduced in previous works [103, 133]. Our major result is the discovery of a strikingly simple closed equation verified by these quantities (chapter 8), which makes it possible to close the infinite hierarchy of equations generated by the many-body interactions in the SEP.

Then, relying on a hydrodynamic description of one dimensional systems, we introduce mappings which enable us to relate different systems. Using these mappings, we generalised our results for the SEP to many other systems, displaying varied phenomenology.

Finally, we considered the case of a biased tracer. We introduced a general procedure to describe, at the hydrodynamic level, single-file systems with a bias. Applying this procedure to the SEP with a biased tracer, we obtained new analytical results on this model.

To finish with, we here mention some open questions that will be interesting to investigate:

- **Physical proof of the closed equation (8.41).** For now, this equation has been obtained by us by inferring a structure we uncovered from perturbative calculations. Afterwards, it has been found using the inverse scattering transform [172]. Is there a way to derive it from less analytical and more physical argument?

- **General structure of equations for single-file diffusion.** In chapter 9, we developed general mappings between single-file systems. As a consequence, these systems are related together by a symmetry group. Studying the properties of this group and of equations left invariant by its action could give valuable information on the structure of more general equations characterising single-file diffusion.

- **Exact solution for biased problems.** In chapter 10, we presented a simple model with a biased tracer which we solved exactly. Can we provide an exact solution for a system with more complicated transport coefficients, similar to what was obtained for the SEP with symmetric tracer?

Appendix A

Methods of numerical simulations

We use kinetic Monte Carlo algorithms in order to simulate a Markov process $s(t)$ in continuous time on a finite state space. To define the process $s(t)$, one must specify:

- The finite state space E.
- The initial distribution μ on the state space E. The initial state $s(0)$ is drawn from this distribution.
- For each pair of states $(a, b) \in E^2$, a rate r_{ab} (homogeneous to an inverse of a time) of transition from state a to b.

The probability $\mathbb{P}(a, t)$ to find the system in state a at time t evolves according to the Markovian evolution:

$$\frac{\mathrm{d}\mathbb{P}(a,t)}{\mathrm{d}t} = \sum_{b\in E} r_{ba}\mathbb{P}(b,t) - r_{ab}\mathbb{P}(a,t). \tag{A.1}$$

The initial condition is $\mathbb{P}(a, 0) = \mu(a)$. Because of exponential size of the space state, it is not conceivable to solve this equation. Instead, we sample random variables X_t such that $\mathbb{P}(X_t = a) = \mathbb{P}(a, t)$. The goal of this appendix is to explain different ways to build such an X_t computationally.

A.1 Decomposition of exponential laws

The fundamental result at the basis of the algorithm is the following. Let U_0 be a random variable following distribution μ, define $\tau_0 = 0$, and fix a big number $M \in \mathbb{R}$. Define a sequence of random variables $(U_n^a, T_n^a)_{(n,a)\in\mathbb{N}^*\times E}$ such that for all $(n, a) \in \mathbb{N}^* \times E$:

- $r_n^a \in \mathbb{R}^{+*}$ is a maximal jump rate such that $M \geq r_n^a \geq \sum_{b\neq a} r_{ab}$.
- T_n^a is a random variable following an exponential law of parameter r_n^a.
- U_n is a random variable which depends on U_{n-1} is equal to $b \in E \setminus \{U_{n-1}\}$ with probability $\frac{r_{U_{n-1}b}}{r_n^{U_n}}$ and is equal to U_{n-1} otherwise (*i.e.* with probability $1 - \frac{\sum_{b\neq a} r_{U_{n-1}b}}{r_n^{U_n}}$)

Then define for $n \in \mathbb{N}^*, \tau_n = \sum_{k=1}^{n} T_k^{U_{k-1}}$. The choice $r_n^a \leq M$ ensures that almost surely the sequence (τ_n) is not bounded. Build the process $S(t) = \sum_{n=0}^{\infty} U_n \mathbb{1}_{[\tau_n,\tau_{n+1}[}(t)$ (it means $S(t)$ spends time $T_{n+1}^{U_n}$ in state U_n then goes to U_{n+1}).

Then, we show that the probability $\mathbb{P}(S(t)=a)$ verifies equation (A.1). For any $t\in\mathbb{R}^+$, note N_t the random variable such that $t\in[\tau_{N_t},\tau_{N_t+1}[$ ($N_t<+\infty$ almost surely because we imposed $r_n^a\leq M$ for all $(n,a)\in\mathbb{N}^*\times E$). For $t'>t$:

$$\begin{aligned}\mathbb{P}(S(t')=a)=&\mathbb{P}(U_{N_{t'}}=a)\\ =&\mathbb{P}(\{U_{N_{t'}}=a,N_{t'}=N_t\}\cup\{U_{N_t'}=a,N_{t'}=N_t+1\})\\ &+\mathbb{P}(U_{N_{t'}}=a|N_{t'}\geq N_t+2)\mathbb{P}(N_{t'}\geq N_t+2).\end{aligned}\tag{A.2}$$

We have partitioned on the three possible events $\{N_{t'}=N_t\}$, $\{N_{t'}=N_t+1\}$ and $\{N_{t'}\geq N_t+2\}$. By definition $\{t<\tau_{N_t+1}\}$ is a certain event (probability one) and $\tau_{N_t+2}\geq\tau_{N_t+1}$ always, so we have the following relations between events (up to negligible sets)

$$\begin{aligned}\{N_{t'}\geq N_t+2\}=&\{\tau_{N_t+2}\leq t'\}\\ =&\{\tau_{N_t+2}\leq t',\tau_{N_t+1}<t',t<\tau_{N_t+1}\}\\ \subset&\{\tau_{N_t+2}-\tau_{N_t+1}\leq t'-t,\tau_{N_t+1}<t',t<\tau_{N_t+1}\}\\ \subset&\left\{T_{N_t+2}^{U_{N_t+1}}\leq t'-t\right\}\cap\left\{T_{N_t+1}^{U_{N_t}}\leq t'-\tau_{N_t},T_{N_t+1}^{U_{N_t}}>t-\tau_{N_t}\right\}.\end{aligned}\tag{A.3}$$

Partitioning on all possible values for τ_{N_t}, U_{N_t} and U_{N_t+1} and thanks to the bound $M\geq r_n^a$ we imposed $\forall(n,a)\in\mathbb{N}^*\times E$, we have the following estimation:

$$\begin{aligned}|\mathbb{P}\left(N_{t'}\geq N_t+2\right)|\leq&\left(1-e^{-M(t'-t)}\right)^2\\ =&O\left((t'-t)^2\right).\end{aligned}\tag{A.4}$$

Basically, we use the crucial property of any exponential law T that $\mathbb{P}(T>t|T>\tau)=\mathbb{P}(T>t-\tau)$ (no aging). We finally evaluate the other term $P=\mathbb{P}(\{U_{N_{t'}}=a,N_{t'}=N_t\}\cup\{U_{N_t'}=a,N_{t'}=N_t+1\})$:

$$\begin{aligned}P=&\sum_{n=0}^{\infty}\mathbb{P}\left(\{N_t=n,U_{N_{t'}}=a,\tau_{N_t+1}>t'\}\cup\{N_t=n,U_{N_{t'}}=a,\tau_{N_t+1}\leq t'<\tau_{N_t+2}\}\right)\\ =&\sum_{n=0}^{\infty}\mathbb{P}\left(N_t=n,U_n=a,\tau_{n+1}>t'\right)+\mathbb{P}\left(N_t=n,U_{n+1}=a,\tau_{n+1}\leq t'<\tau_{n+2}\right)\\ =&\sum_{n=0}^{\infty}\mathbb{P}\left(\tau_n\leq t<\tau_n+T_{n+1}^a,U_n=a,T_{n+1}^a>t'-\tau_n\right)\\ &+\sum_{b\in E}\mathbb{P}\left(N_t=n,U_n=b,U_{n+1}=a,\tau_{n+1}\leq t'<\tau_{n+2}\right)\\ =&\sum_{n=0}^{\infty}\mathbb{P}\left(\tau_n\leq t<\tau_n+T_{n+1}^a,U_n=a\right)\mathbb{P}\left(T_{n+1}^a>t'-t\right)+\sum_{b\in E}\mathbb{P}\left(N_t=n,U_n=b,U_{n+1}=a\right)\\ &\times\mathbb{P}\left(T_{n+1}^b\leq t'-t\right)\mathbb{P}\left(t'<\tau_{n+2}|N_t=n,U_n=b,U_{n+1}=a,\tau_{n+1}\leq t'\right)\\ =&\sum_{n=0}^{\infty}\mathbb{P}\left(N_t=n,U_n=a\right)e^{-r_{n+1}^a(t'-t)}+\sum_{b\in E}\mathbb{P}\left(N_t=n,U_n=b\right)\mathbb{P}\left(U_{n+1}=a|U_n=b\right)\\ &\times(1-e^{-r_{n+1}^b(t'-t)})\mathbb{P}\left(t'<\tau_{n+2}|N_t=n,U_n=b,U_{n+1}=a,\tau_{n+1}\leq t'\right).\end{aligned}\tag{A.5}$$

We have:

$$\begin{aligned}&\mathbb{P}\left(t'<\tau_{n+2}|N_t=n,U_n=b,U_{n+1}=a,\tau_{n+1}\leq t'\right)\geq\mathbb{P}\left(T_{n+2}^a>t'-t\right)\\ &\mathbb{P}\left(t'<\tau_{n+2}|N_t=n,U_n=b,U_{n+1}=a,\tau_{n+1}\leq t'\right)=1+O(t'-t)\end{aligned}\tag{A.6}$$

So when $t' \to t$ (the O are uniform in n, a, b thanks to the choice of M):

$$\begin{aligned}
P &= \sum_{n=0}^{\infty} \mathbb{P}\left(N_t = n, U_n = a\right)\left(1 - r_{n+1}^a(t'-t) + O\left((t'-t)^2\right)\right) + \sum_{b\in E} \mathbb{P}\left(N_t = n, U_n = b\right) \\
&\quad \times \mathbb{P}\left(U_{n+1} = a | U_n = b\right)\left(r_{n+1}^b(t'-t) + O\left((t'-t)^2\right)\right)\left(1 + O(t'-t)\right) \\
&= \sum_{n=0}^{\infty} \mathbb{P}\left(N_t = n, U_n = a\right)\left(1 - r_{n+1}^a(t-t') + \left(1 - \frac{\sum_{b\neq a} r_{ab}}{r_{n+1}^a}\right) r_{n+1}^a(t'-t)\right) \\
&\quad + \sum_{b\neq a} \mathbb{P}\left(N_t = n, U_n = b\right) \frac{r_{ba}}{r_{n+1}^b}\left(r_{n+1}^b(t'-t)\right) + O\left((t'-t)^2\right) \\
&= \left(1 - \sum_{b\neq a} r_{ab}(t'-t)\right) \sum_{n=0}^{\infty} \mathbb{P}\left(N_t = n, U_n = a\right) \\
&\quad + r_{ba}(t'-t) \sum_{n=0}^{\infty} \sum_{b\neq a} \mathbb{P}\left(N_t = n, U_n = b\right) + O\left((t'-t)^2\right) \\
&= \left(1 - \sum_{b\neq a} r_{ab}(t'-t)\right) \mathbb{P}\left(S(t) = a\right) + \sum_{b\neq a} r_{ba}(t'-t)\mathbb{P}\left(S(t) = b\right) + O\left((t'-t)^2\right) \qquad \text{(A.7)}
\end{aligned}$$

We have replaced $\mathbb{P}\left(U_{n+1} = a | U_n = b\right)$ by its definition (and split the sum on b into $b = a$ and $b \neq a$). Finally, the expression of $\mathbb{P}(S(t') = a)$ (A.2), with the explicit computation of (A.7) and the estimate (A.4), proves that $\mathbb{P}(S(t) = a)$ verifies (A.1). This result constitutes the core of our methods of simulation.

A.2 Kinetic Monte Carlo algorithm

We show how to use the result above to efficiently sample a Markov process, by simply drawing sequentially random variables U_k and $T_n^{U_{k-1}}$. An important point is that we are free to choose r_n^a (the rate at which we leave state a) and this will lead to two different algorithms.

- If $r_n^a = \sum_{b\neq a} r_{ab}$, this is a rejection free algorithm. At each step of the simulation the system changes state.
- If $r_n^a > \sum_{b\neq a} r_{ab}$, this is an algorithm with rejection. We authorize the algorithm to perform a test in order to know if it must leave current state or not.

We illustrate both algorithms with the KLS (see 6.1.2) model on a ring of L sites with N particles. The current state in the KLS will be represented by two arrays:

- An array of size N, $\mathrm{pos}[k] \in [\![0, L-1]\!]$ indicates the position of particle k.
- An array of size L, $\mathrm{occ}[x] \in [\![0, 1]\!]$ indicates if site x is empty (value 0) or occupied (value 1).

In both algorithms, we start at $t = 0$ with the system in a state a.

A.2.1 Rejection-free algorithm

Suppose the system is in given state described by arrays pos and occ (corresponding to $a = U_{n-1}$ in the theoretical result A.1) at time t (corresponding to $T_{n-1}^{U_{n-2}}$).

- The first step is to build an array r containing the rates of all accessible states. In our KLS example, for each particle $k \in [\![0, N-1]\!]$, depending on the occupation numbers of its neighbouring sites, we determine its jump rates to the left and to the right among the possibilities 0 (if the site is occupied), $1 \pm \delta$, $1 \pm \epsilon$ (see figure 6.9 for the corresponding configurations). We affect to $r[2k]$ the value of the jump rate to the right and to $r[2k+1]$ the value of the jump rate to the left. We then compute r_{tot} (which correspond to r_n^a in the theoretical resultA.1) as the sum of the values in the array r.

- Then we draw a random variable Δt (corresponding to T_n^a in the theoretical result A.1) from an exponential law of parameter r_{tot} and increment the current time t by this quantity (*i.e.* $t \leftarrow t + \Delta t$).

- To known which transition must be performed (U_n in A.1), we finally draw a random variable s from uniform law on $[0, r_{\text{tot}}]$. We find the index i such that $s \in [r[0] + ... + r[i-1], r[0] + ... + r[i][$ (this can be done efficiently by dichotomy). If there is $k \in [\![0, N-1]\!]$ such that $i = 2k$, then particle k moves to the right, and if there is k such that $i = 2k+1$ then particle k moves to the left (we update pos and occ accordingly).

We repeat this procedure until the desired final time t_f is reached (*i.e.* $t \geq t_f$). Note that in the next step, there is no need to reevaluate the whole array r, only values of the rates $r[2k-2]$ to $r[2k+3]$ may have changed if k is the index of the last particle which has jumped.

A.2.2 Algorithm with rejection

The difference here is that at each step of the simulation, it is possible to reject a transition, namely no particle moves. We can use this possibility to get rid of the array r. Here we give an example of how to proceed, but this algorithm is very flexible so there may be many other ways.

We fix $r_{\text{tot}} = 2N \times \max\{1 \pm \delta, 1 \pm \epsilon\}$ at the very beginning of the simulation, and we will not change it. This choice ensure that, whatever the current state, r_{tot} will be higher than the sum of transition rates ($r_n^a \geq \sum_{b \neq a} r_{ab}$ in theoretical result A.1).

Suppose the system is in given state described by arrays pos and occ (corresponding to $a = U_{n-1}$ in the theoretical result A.1) at time t (corresponding to $T_{n-1}^{U_{n-2}}$).

- Here, no need to evaluate the transition rates, the first step is to directly draw a random variable Δt (corresponding to T_n^a in the theoretical result A.1) from an exponential law of parameter r_{tot} and increment the current time t by this quantity (*i.e.* $t \leftarrow t + \Delta t$).

- Next, we chose a particle $k \in [\![0, N-1]\!]$ at random (uniform law on $[\![0, N-1]\!]$) and a Bernoulli variable of parameter $1/2$, which we denote by d. If $d = 0$, particle k will attempt a jump to the left, and if $d = 1$, to the right. To know if the attempt must be realised or not, we evaluate, in the current state given by pos and occ, (from the rules of the KLS, see definition 6.1.2) the jump rate $r_{k,d} \in \{0, 1 \pm \delta, 1 \pm \epsilon\}$ of particle k in direction d. Then we draw s from a uniform law on $[0, \max\{1 \pm \delta, 1 \pm \epsilon\}]$. If $s \leq r_{k,d}$, the jump is accepted, otherwise it is rejected.

The procedure is repeated until final time t_f is reached.

Why does this correctly simulate the KLS ? With this procedure, for all accessible states, denoted by (k, d) ($(k, 0)$ refers to the state obtained by moving particle k to the left and $(k, 1)$ the one obtained by moving it to the right), the probability to accept the transition to state (k, d) is:

$$\frac{1}{N} \times \frac{1}{2} \times \frac{r_{k,d}}{\max\{1 \pm \delta, 1 \pm \epsilon\}} = \frac{r_{k,d}}{r_{\text{tot}}}. \tag{A.8}$$

According to the theoretical result A.1, this transition probability (A.8) (it corresponds to $\frac{r_{U_{n-1}b}}{r_n^{U_n}}$) ensures that the procedure correctly simulate the desired Markov process.

Note that, if we are not interested about the whole time-trajectory, but only the final state, we can here take advantage of the constant rate r_{tot}. Indeed, the number N_{steps} of times an exponential clock of rate r_{tot} rings during a duration t_f is distributed according to a Poisson law of parameter $r_{\text{tot}}t_f$. Therefore, instead of drawing an exponential law at each step, one can just draw once, at the beginning, the number of steps N_{steps} from a Poisson law, and then perform the procedure described above N_{steps} times, without having to care about current time.

As a major difference with the previous algorithm, we evaluate only one transition rate at each step instead of six. The price to pay is that the total transition rate r_{tot} is always bigger than the real rate for leaving the current state, meaning that to get to a given final time, it will take more steps with the algorithm with rejection.

A.3 Simulation of the run-and-tumble tracer

For the simulations of the run-and-tumble particle in dimension 2 or more (part I), we use a different algorithm. The simulations were performed by Alessandro Sarracino. It relies on the fact that the continuous time dynamics of the Markov process (A.1) can be approximated by a discrete time Markov chain.

One chooses a time step $\mathrm{d}t$, which must be small in front of all the transition times:

$$\forall a \neq b \in E, \mathrm{d}t \ll \frac{1}{r_{ab}} \tag{A.9}$$

At a given time step, if the current state is denoted by $a \in E$, then for each state $b \neq a$, we draw an independent Bernoulli random variable of parameter $r_{ab}\mathrm{d}t$. If it is one, then the state at the next time step will be b, otherwise, it remains a.

Since we have chosen a small time step (A.9), the probability that two transitions occur at the same step can be made arbitrarily small. Nevertheless, in most cases, it is possible to deal with simultaneous transitions. For example, in the case of our run-and-tumble tracer in crowded environment, it is possible to move several particles at the same time, provided that they don't interact together (in other words if they are far enough from each other).

Then, if the system arrives in state a at step N, the probability to go to state b after n steps is $(1 - r_{ab}\mathrm{d}t)^{n-1}r_{ab}\mathrm{d}t$. In the limit where $\mathrm{d}t$ is small and $n\mathrm{d}t$ is kept equal to a fixed duration t, this probability is equivalent to $r_{ab}e^{-r_{ab}t}\mathrm{d}t$, which is exactly the density of the exponential law of parameter r_{ab}.

As a consequence, the N-th step of this discrete time dynamics approximates the continuous time dynamics at time $N\mathrm{d}t$, and the smaller $\mathrm{d}t$, the better the approximation.

Appendix B

Details of calculations of part I

Here, we precise some methods and analytical expressions involved the analytical resolution, based on the decoupling approximation 3.1, of our model of run-and-tumble particle on a lattice with a bath of mobile obstacles (part I).

B.1 Derivation of evolution equations from the master equation

Mean position of the tracer. The mean position of the tracer is defined by

$$\langle X_t \rangle = \sum_{\chi,\boldsymbol{R},\eta} (\boldsymbol{R}\cdot\boldsymbol{e}_1) P_\chi(\boldsymbol{R},\eta;t). \tag{B.1}$$

If we take the time derivative of $\langle X_t\rangle$ and use the master equation (2.2), we get:

$$\begin{aligned}
\frac{\mathrm{d}\langle X_t\rangle}{\mathrm{d}t} =& \frac{1}{2d\tau^*}\sum_{\chi,\boldsymbol{R},\eta} R\left(\mathcal{L}_\chi P_\chi - \alpha P_\chi + \frac{\alpha}{2d-1}\sum_{\chi'\neq\chi} P_{\chi'}\right)(\boldsymbol{R},\eta;t)\\
=& \frac{1}{2d\tau^*}\sum_{\boldsymbol{R},\eta} R\frac{\alpha}{2d-1}\sum_{\chi}\sum_{\chi'}\left(P_{\chi'}(\boldsymbol{R},\eta;t) - P_\chi(\boldsymbol{R},\eta;t)\right) + \frac{1}{2d\tau^*}\sum_{\chi}\sum_{\boldsymbol{R},\eta} R\mathcal{L}_\chi P_\chi(\boldsymbol{R},\eta;t)\\
=& 0 + \frac{1}{2d\tau^*}\sum_{\chi}\sum_{\boldsymbol{R},\eta} R\left\{\sum_{\nu=1}^{d}\sum_{\boldsymbol{r}\neq\boldsymbol{R}-\boldsymbol{e}_\nu,\boldsymbol{R}}\left[P_\chi(\boldsymbol{R},\eta^{\boldsymbol{r},\nu};t) - P_\chi(\boldsymbol{R},\eta;t)\right]\right.\\
&\left. + \frac{2d\tau^*}{\tau}\sum_{\mu} p_\mu^{(\chi)}\left[\left(1-\eta_{\boldsymbol{R}}\right)P_\chi(\boldsymbol{R}-\boldsymbol{e}_\mu,\eta;t) - \left(1-\eta_{\boldsymbol{R}+\boldsymbol{e}_\mu}\right)P_\chi(\boldsymbol{R},\eta;t)\right]\right\},
\end{aligned} \tag{B.2}$$

where we denote $R = (\boldsymbol{R}\cdot\boldsymbol{e}_1)$. The first term will turn out to be zero because for any $\boldsymbol{r}$, $\eta \longrightarrow \eta^{\boldsymbol{r},\nu}$ is a bijection from the space of configurations to itself, so we can re-parameterise one of the sums on η. As a consequence, for any $\boldsymbol{R},\chi$,

$$\begin{aligned}
\sum_{\eta} R\sum_{\nu=1}^{d}\sum_{\substack{\boldsymbol{r}\neq\boldsymbol{R}\\ \boldsymbol{r}\neq\boldsymbol{R}-\boldsymbol{e}_\nu}}\left[P_\chi(\boldsymbol{R},\eta^{\boldsymbol{r},\nu};t) - P_\chi(\boldsymbol{R},\eta;t)\right] =& R\sum_{\nu=1}^{d}\sum_{\substack{\boldsymbol{r}\neq\boldsymbol{R}\\ \boldsymbol{r}\neq\boldsymbol{R}-\boldsymbol{e}_\nu}}\left[\sum_{\eta} P_\chi(\boldsymbol{R},\eta^{\boldsymbol{r},\nu};t) - \sum_{\eta} P_\chi(\boldsymbol{R},\eta;t)\right]\\
=& R\sum_{\nu=1}^{d}\sum_{\substack{\boldsymbol{r}\neq\boldsymbol{R}-\boldsymbol{e}_\nu\\ \boldsymbol{r}\neq\boldsymbol{R}}}\left[\sum_{\eta} P_\chi(\boldsymbol{R},\eta;t) - \sum_{\eta} P_\chi(\boldsymbol{R},\eta;t)\right]\\
=& 0.
\end{aligned} \tag{B.3}$$

For the second term, we re-parameterise the sum on $\boldsymbol{R}$:

$$\begin{aligned}
\frac{\mathrm{d}\langle X_t\rangle}{\mathrm{d}t} &= \sum_\chi \sum_\eta \frac{1}{\tau} \sum_\mu p_\mu^{(\chi)} \left\{ \sum_{\boldsymbol{R}} R\,(1-\eta_{\boldsymbol{R}})\, P_\chi(\boldsymbol{R}-\boldsymbol{e}_\mu,\eta;t) - \sum_{\boldsymbol{R}} R\,(1-\eta_{\boldsymbol{R}+\boldsymbol{e}_\mu})\, P_\chi(\boldsymbol{R},\eta;t) \right\} \\
&= \sum_\chi \sum_\eta \frac{1}{\tau} \sum_\mu p_\mu^{(\chi)} \left\{ \sum_{\boldsymbol{R}} (R+\boldsymbol{e}_\mu\cdot\boldsymbol{e}_1)\,(1-\eta_{\boldsymbol{R}+\boldsymbol{e}_\mu})\, P_\chi(\boldsymbol{R},\eta;t) - \sum_{\boldsymbol{R}} R\,(1-\eta_{\boldsymbol{R}+\boldsymbol{e}_\mu})\, P_\chi(\boldsymbol{R},\eta;t) \right\} \\
&= \sum_\chi \sum_\eta \frac{1}{\tau} \sum_\mu p_\mu^{(\chi)} \left\{ \sum_{\boldsymbol{R}} (\boldsymbol{e}_\mu\cdot\boldsymbol{e}_1)\,(1-\eta_{\boldsymbol{R}+\boldsymbol{e}_\mu})\, P_\chi(\boldsymbol{R},\eta;t) \right\} \\
&= \sum_\chi \sum_{\mu=\pm1} \frac{1}{\tau} p_\mu^{(\chi)} \mu \sum_{\eta,\boldsymbol{R}} (1-\eta_{\boldsymbol{R}+\boldsymbol{e}_\mu})\, P_\chi(\boldsymbol{R},\eta;t)
\end{aligned} \tag{B.4}$$

Mean squared position of a symmetric tracer. We consider the case where there is no external force: $F_E = 0$. The mean squared position of the tracer is defined by

$$\left\langle X_t^2 \right\rangle = \sum_{\chi,\boldsymbol{R},\eta} (\boldsymbol{R}\cdot\boldsymbol{e}_1)^2 P_\chi(\boldsymbol{R},\eta;t). \tag{B.5}$$

We first compute, from the master equation (2.2), the evolution equation of the mean squared displacement conditioned to the state χ, where we denote $R = \boldsymbol{R}\cdot\boldsymbol{e}_1$:

$$\begin{aligned}
\frac{\mathrm{d}}{\mathrm{d}t}\left\langle {X_t}^2 \right\rangle_\chi =& 2d \sum_{\boldsymbol{R},\eta} \frac{1}{2d\tau^*} \left\{ \sum_{\mu=1}^{d} \sum_{\boldsymbol{r}\neq\boldsymbol{R}-\boldsymbol{e}_\mu,\boldsymbol{R}} R^2 \left[P_\chi(\boldsymbol{R},\eta^{\boldsymbol{r},\mu};t) - P_\chi(\boldsymbol{R},\eta;t) \right] \right. \\
&+ \frac{2d\tau^*}{\tau} \sum_\mu p_\mu^{(\chi)} R^2 [(1-\eta_{\boldsymbol{R}})\, P_\chi(\boldsymbol{R}-\boldsymbol{e}_\mu,\eta;t) - \left(1-\eta_{\boldsymbol{R}+\boldsymbol{e}_\mu}\right) P_\chi(\boldsymbol{R},\eta;t)] \\
&\left. -\alpha R^2 P_\chi(\boldsymbol{R},\eta;t) + \frac{\alpha}{2d-1} \sum_{\chi'\neq\chi} R^2 P_{\chi'}(\boldsymbol{R},\eta;t) \right\}
\end{aligned}$$

$$\begin{aligned}
\frac{\mathrm{d}}{\mathrm{d}t}\left\langle {X_t}^2 \right\rangle_\chi = 0 + \frac{1}{\tau} \sum_\mu p_\mu^{(\chi)} \Big[&\left\langle \left(1-\eta_{\boldsymbol{X}_t+\boldsymbol{e}_\mu}\right) \left(X_t^2 + 2X_t(\boldsymbol{e}_1\cdot\boldsymbol{e}_\mu) + (\boldsymbol{e}_1\cdot\boldsymbol{e}_\mu)\right)^2 \right\rangle_\chi \\
&- \left\langle X_t^2 \left(1-\eta_{\boldsymbol{R}+\boldsymbol{e}_\mu}\right) \right\rangle_\chi \Big] + \frac{\alpha/(2d\tau^*)}{2d-1} \sum_{\chi'\neq\chi} \left(\left\langle X_t^2 \right\rangle_{\chi'} - \left\langle X_t^2 \right\rangle_\chi \right).
\end{aligned} \tag{B.6}$$

We average the conditional averages to get the mean squared displacement:

$$\begin{aligned}
\frac{\mathrm{d}}{\mathrm{d}t}\left\langle {X_t}^2 \right\rangle =& \frac{1}{2d} \sum_\chi \frac{1}{\tau} \left\{ p_1^{(\chi)} \left[1-k_{\boldsymbol{e}_1}^{(\chi)}(t)\right] + p_{-1}^{(\chi)} \left[1-k_{\boldsymbol{e}_{-1}}^{(\chi)}(t)\right] \right\} - \frac{2}{\tau} \left[p_1^{(\chi)} \widetilde{g}_{\boldsymbol{e}_1}(t) - p_{-1}^{(\chi)} \widetilde{g}_{\boldsymbol{e}_{-1}}(t) \right] \\
&+ \frac{1}{2d} \sum_\chi \frac{2\left\langle X_t \right\rangle_\chi}{\tau} \left[p_1^{(\chi)} \left(1-k_{\boldsymbol{e}_1}^{(\chi)}(t)\right) - p_{-1}^{(\chi)} \left(1-k_{\boldsymbol{e}_{-1}}^{(\chi)}(t)\right) \right].
\end{aligned} \tag{B.7}$$

We recall the definitions of the conditional density profiles in the reference frame of the tracer (2.13) $k_{\boldsymbol{r}}^{(\chi)}(t) = \left\langle \eta_{\boldsymbol{X}_t+\boldsymbol{r}} \right\rangle_\chi$ and of the conditional correlation profiles (2.17) in the reference frame of the tracer $\widetilde{g}_{\boldsymbol{r}}^{(\chi)}(t) = \left\langle \left(X_t - \left\langle X_t \right\rangle_\chi \eta_{\boldsymbol{X}_t+\boldsymbol{r}} \right\rangle_\chi \right.$.

This equation involves the mean position of the tracer when the active force is in direction χ, $\langle X_t \rangle_\chi$. Its long time limit $X_\chi = \lim_{t\to\infty} \langle X_t \rangle_\chi$ can be determined by a computation similar to (B.2). In the long-time limit:

$$0 = \frac{\mathrm{d}}{\mathrm{d}t} \langle X_t \rangle_\chi = \frac{1}{\tau} \left\{ p_1^{(\chi)} \left[1 - k_{\boldsymbol{e}_1}^{(\chi)}\right] - p_{-1}^{(\chi)} \left[1 - k_{\boldsymbol{e}_{-1}}^{(\chi)}\right] \right\} + \frac{\alpha}{2d\tau^*} \left(-X_\chi + \frac{1}{2d-1} \sum_{\chi' \neq \chi} X_{\chi'} \right). \tag{B.8}$$

This gives a linear system of equations, which solutions are $X_\chi = 0$ for $\chi \neq \pm 1$ and:

$$X_1 = -X_{-1} = \frac{(2d-1)\tau^*}{\tau\alpha} \left\{ p_1^{(\chi)} \left[1 - k_{\boldsymbol{e}_1}^{(\chi)}\right] - p_{-1}^{(\chi)} \left[1 - k_{\boldsymbol{e}_{-1}}^{(\chi)}\right] \right\}. \tag{B.9}$$

B.2 Symmetries of the density and correlation profiles

Studying the symmetries of the jump rates $p_\mu^{(\chi)}$, we determine the symmetries verified bu the density profiles $h_\mu^{(\chi)} = \langle \eta_{X_t + \boldsymbol{r}} \rangle_\chi - \rho$ and the correlation profiles $\widetilde{g}_\mu^{(\chi)} = \left\langle (X_t - \langle X_t \rangle_\chi) \eta_{X_t + \boldsymbol{r}} \right\rangle_\chi$.

There are more symmetries in the case $F_E = 0$, since the tracer is then globally isotropic (note that however this isotropy is broken on short timescales because of the activity of the tracer).

Absence of external force. In this case ($F_E = 0$), we have many symmetries which simplify the problem. For any μ and $\chi \notin \{\mu, -\mu\}$:

$$\begin{aligned} h_\mu^{(\mu)} &= h_1^{(1)} \\ h_\mu^{(-\mu)} &= h_{-1}^{(1)} \\ h_\mu^{(\chi)} &= h_2^{(1)}, \end{aligned} \tag{B.10}$$

and for $\mu, \chi \notin \{-1, 1\}$:

$$\begin{aligned} \widetilde{g}_{-1}^{(-1)} &= -\widetilde{g}_1^{(1)} \\ \widetilde{g}_1^{(-1)} &= -\widetilde{g}_{-1}^{(1)} \\ \widetilde{g}_\mu^{(-1)} &= -\widetilde{g}_\mu^{(1)} = -g_2^{(1)} \\ \widetilde{g}_1^{(-\chi)} &= -\widetilde{g}_{-1}^{(-\chi)} = \widetilde{g}_1^{(\chi)} = -\widetilde{g}_{-1}^{(\chi)} \\ \widetilde{g}_{\pm\mu}^{(\pm\chi)} &= 0. \end{aligned} \tag{B.11}$$

Driven tracer. In the case of a non zero external force ($F_E \neq 0$), we have the following symmetries:

$$h_2^{(1)} = h_{-2}^{(1)}, \tag{B.12}$$

$$h_2^{(-1)} = h_{-2}^{(-1)}, \tag{B.13}$$

$$h_\chi^{(\chi)} = h_2^{(2)} \qquad \text{for any } \chi \neq \pm 1, \tag{B.14}$$

$$h_{-\chi}^{(\chi)} = h_{-2}^{(2)} \qquad \text{for any } \chi \neq \pm 1, \tag{B.15}$$

$$h_\mu^{(\chi)} = h_\mu^{(2)} \qquad \text{for any } \chi \neq \pm 1, \mu = \pm 1, \tag{B.16}$$

$$h_\mu^{(\chi)} = h_3^{(2)} \qquad \text{if } d \geq 3 \text{ for any } \chi \neq \pm 1, \mu \neq \pm 1, \pm\chi. \tag{B.17}$$

B.3 Expressions of the matrices for the conditional profiles

In the case of a symmetric tracer $F_E = 0$, we gave an analytical implicit equation verified by the conditional profiles (3.19, 3.20). The matrices involved in these equations are obtained from the Fourier transform equations (3.10) and (3.11).

B.3.1 Arbitrary density

The matrices are obtained from the Fourier transforms (3.10) and (3.11).

Density profiles

$$\mathbf{\Lambda} = \begin{pmatrix} \left(e^{\mathrm{i}q_1}-1\right)A_1^{(1)} & \left(e^{-\mathrm{i}q_1}-1\right)A_{-1}^{(1)} & 2\left(\cos\left(q_2\right)-1\right)A_2^{(1)} & 0 \\ \left(e^{-\mathrm{i}q_1}-1\right)A_1^{(1)} & \left(e^{\mathrm{i}q_1}-1\right)A_{-1}^{(1)} & 2\left(\cos\left(q_2\right)-1\right)A_2^{(1)} & 0 \\ \left(e^{\mathrm{i}q_2}-1\right)A_1^{(1)} & \left(e^{-\mathrm{i}q_2}-1\right)A_{-1}^{(1)} & 2\left(\cos\left(q_1\right)-1\right)A_2^{(1)} & 0 \\ \left(e^{-\mathrm{i}q_2}-1\right)A_1^{(1)} & \left(e^{\mathrm{i}q_2}-1\right)A_{-1}^{(1)} & 2\left(\cos\left(q_1\right)-1\right)A_2^{(1)} & 0 \end{pmatrix}, \tag{B.18}$$

and:

$$\boldsymbol{S} = 2\mathrm{i}\rho\frac{2d\tau^*}{\tau}\left[p_1^{(1)}(1-\rho-h_1^{(1)}) - p_{-1}^{(1)}(1-\rho-h_1^{(-1)})\right]\begin{pmatrix}\sin(q_1)\\ -\sin(q_1)\\ \sin(q_2)\\ -\sin(q_2)\end{pmatrix}. \tag{B.19}$$

Correlation profiles

$$\boldsymbol{E} = \begin{pmatrix} H^{(1)}\left((A_1^{(1)}-1)(e^{-\mathrm{i}q_1}-1) - (A_{-1}^{(1)}-1)(e^{\mathrm{i}q_1}-1)\right) \\ H^{(-1)}\left((A_{-1}^{(1)}-1)(e^{-\mathrm{i}q_1}-1) - (A_1^{(1)}-1)(e^{\mathrm{i}q_1}-1)\right) \\ -2\mathrm{i}(A_2^{(1)}-1)H^{(2)}\sin(q_1) \\ -2\mathrm{i}(A_2^{(1)}-1)H^{(-2)}\sin(q_1) \end{pmatrix} \tag{B.20}$$

$$\boldsymbol{X} = \frac{\alpha}{2d-1}\begin{pmatrix} X_{\chi\chi} = -\sum_{\chi'\neq\chi}\left(X_{\chi'}-X_\chi\right) \\ X_{\chi\chi'} = X_{\chi'} - X_\chi \end{pmatrix}_{\chi\chi'} \tag{B.21}$$

$$\begin{aligned}
\mathbf{\Lambda_G} = &-\frac{2d\tau^*}{\tau}\begin{pmatrix} H^{(1)}p_1^{(1)}(e^{-\mathrm{i}q_1}-1) & H^{(1)}p_{-1}^{(1)}(e^{\mathrm{i}q_1}-1) & 2H^{(1)}p_2^{(1)}(\cos(q_2)-1) & 0 \\ -H^{(-1)}p_{-1}^{(-1)}(e^{\mathrm{i}q_1}-1) & -H^{(-1)}p_1^{(-1)}(e^{-\mathrm{i}q_1}-1) & -2H^{(-1)}p_2^{(-1)}(\cos(q_2)-1) & 0 \\ 0 & 0 & 0 & 2H^{(2)}p_1^{(2)}(\cos(q_1)-1) \\ 0 & 0 & 0 & 2H^{(-2)}p_1^{(-2)}(\cos(q_1)-1) \end{pmatrix} \\
&-\rho\frac{2d\tau^*}{\tau}2\mathrm{i}\begin{pmatrix} \sin(q_1)p_1^{(1)} & -\sin(q_1)p_{-1}^{(1)} & 0 & 0 \\ \sin(q_1)p_{-1}^{(-1)} & -\sin(q_1)p_1^{(-1)} & 0 & 0 \\ 0 & 0 & 0 & 2\sin(q_1)p_1^{(2)} \\ 0 & 0 & 0 & 2\sin(q_1)p_1^{(-2)} \end{pmatrix} \\
&+\begin{pmatrix} \left(e^{\mathrm{i}q_1}-1\right)A_1^{(1)} & \left(e^{-\mathrm{i}q_1}-1\right)A_{-1}^{(1)} & 2\left(\cos\left(q_2\right)-1\right)A_2^{(1)} & 0 \\ -\left(e^{-\mathrm{i}q_1}-1\right)A_1^{(1)} & -\left(e^{\mathrm{i}q_1}-1\right)A_{-1}^{(1)} & -2\left(\cos\left(q_2\right)-1\right)A_2^{(1)} & 0 \\ 0 & 0 & 0 & 2\mathrm{i}A_2^{(1)}\sin(q_1) \\ 0 & 0 & 0 & 2\mathrm{i}A_2^{(1)}\sin(q_1) \end{pmatrix} \\
&-\frac{2d\tau^*}{\tau}\begin{pmatrix} \left(e^{\mathrm{i}q_1}-1\right)p_1^{(1)}h_1^{(1)} & \left(e^{-\mathrm{i}q_1}-1\right)p_1^{(-1)}h_1^{(-1)} & 2\left(\cos\left(q_2\right)-1\right)p_1^{(2)}h_1^{(2)} & 0 \\ -\left(e^{-\mathrm{i}q_1}-1\right)p_1^{(1)}h_1^{(1)} & -\left(e^{\mathrm{i}q_1}-1\right)p_1^{(-1)}h_1^{(-1)} & -2\left(\cos\left(q_2\right)-1\right)p_1^{(2)}h_1^{(2)} & 0 \\ 0 & 0 & 0 & 2p_1^{(2)}h_1^{(2)}\left(\cos(q_1)-1\right) \\ 0 & 0 & 0 & 2p_1^{(2)}h_1^{(2)}\left(\cos(q_1)-1\right) \end{pmatrix}
\end{aligned} \tag{B.22}$$

$$\boldsymbol{F} = -\begin{pmatrix} (A_1^{(1)}-1)\left(\rho e^{-\mathrm{i}q_1}+h_1^{(1)}\right)-(A_{-1}^{(1)}-1)\left(\rho e^{\mathrm{i}q_1}+h_{-1}^{(1)}\right) \\ (A_{-1}^{(1)}-1)\left(\rho e^{-\mathrm{i}q_1}+h_1^{(-1)}\right)-(A_1^{(1)}-1)\left(\rho e^{\mathrm{i}q_1}+h_{-1}^{(-1)}\right) \\ (A_2^{(1)}-1)\left(\rho e^{-\mathrm{i}q_1}+h_1^{(2)}\right)-(A_2^{(1)}-1)\left(\rho e^{\mathrm{i}q_1}+h_{-1}^{(2)}\right) \\ (A_2^{(1)}-1)\left(\rho e^{-\mathrm{i}q_1}+h_1^{(-2)}\right)-(A_2^{(1)}-1)\left(\rho e^{\mathrm{i}q_1}+h_{-1}^{(-2)}\right) \end{pmatrix}. \tag{B.23}$$

Then we perform the inverse Fourier transforms (where $[\cdot]_i$ means that we take the i-th line):

$$\boldsymbol{L} = \begin{pmatrix} \int_{\boldsymbol{q}} e^{-\mathrm{i}q_1}\left[\boldsymbol{M}^{-1}\boldsymbol{\Lambda_G}\right]_1 \\ \int_{\boldsymbol{q}} e^{\mathrm{i}q_1}\left[\boldsymbol{M}^{-1}\boldsymbol{\Lambda_G}\right]_1 \\ \int_{\boldsymbol{q}} e^{-\mathrm{i}q_2}\left[\boldsymbol{M}^{-1}\boldsymbol{\Lambda_G}\right]_1 \\ \int_{\boldsymbol{q}} e^{-\mathrm{i}q_1}\left[\boldsymbol{M}^{-1}\boldsymbol{\Lambda_G}\right]_3 \end{pmatrix} \quad \text{and} \quad \boldsymbol{B} = \begin{pmatrix} \int_{\boldsymbol{q}} e^{-\mathrm{i}q_1}\left[\boldsymbol{M}^{-1}(\boldsymbol{X}\cdot\boldsymbol{H}+\boldsymbol{E}+\boldsymbol{F})\right]_1 \\ \int_{\boldsymbol{q}} e^{\mathrm{i}q_1}\left[\boldsymbol{M}^{-1}(\boldsymbol{X}\cdot\boldsymbol{H}+\boldsymbol{E}+\boldsymbol{F})\right]_1 \\ \int_{\boldsymbol{q}} e^{-\mathrm{i}q_2}\left[\boldsymbol{M}^{-1}(\boldsymbol{X}\cdot\boldsymbol{H}+\boldsymbol{E}+\boldsymbol{F})\right]_1 \\ \int_{\boldsymbol{q}} e^{-\mathrm{i}q_1}\left[\boldsymbol{M}^{-1}(\boldsymbol{X}\cdot\boldsymbol{H}+\boldsymbol{E}+\boldsymbol{F})\right]_3 \end{pmatrix}. \tag{B.24}$$

B.3.2 Low and high-density limits

The matrices given above simplify at linear order in the density ρ in these limits. This yields linear systems (as opposed to the non-linear systems obtained before) verified by the linear dependence in ρ of the conditional density and correlation profiles.

Low density

We linearise at first order in ρ the matrices given above.

Density profiles.

$$\boldsymbol{\Lambda_0} = \begin{pmatrix} \left(e^{\mathrm{i}q_1}-1\right)a_1^{(1)} & \left(e^{-\mathrm{i}q_1}-1\right)a_{-1}^{(1)} & 2\left(\cos q_2-1\right)a_2^{(1)} & 0 \\ \left(e^{-\mathrm{i}q_1}-1\right)a_1^{(1)} & \left(e^{\mathrm{i}q_1}-1\right)a_{-1}^{(1)} & 2\left(\cos q_2-1\right)a_2^{(1)} & 0 \\ \left(e^{\mathrm{i}q_2}-1\right)a_1^{(1)} & \left(e^{-\mathrm{i}q_2}-1\right)a_{-1}^{(1)} & 2\left(\cos q_1-1\right)a_2^{(1)} & 0 \\ \left(e^{-\mathrm{i}q_2}-1\right)a_1^{(1)} & \left(e^{\mathrm{i}q_2}-1\right)a_{-1}^{(1)} & 2\left(\cos q_1-1\right)a_2^{(1)} & 0 \end{pmatrix}$$

and:

$$\boldsymbol{S_0} = 2\mathrm{i}\frac{2d\tau^*}{\tau}\left[p_1^{(1)}-p_{-1}^{(1)}\right]\begin{pmatrix} \sin q_1 \\ -\sin q_1 \\ \sin q_2 \\ -\sin q_2 \end{pmatrix} \tag{B.25}$$

Correlation profiles.

$$\boldsymbol{\mathcal{M}}_{\widetilde{\boldsymbol{g}},0} = \boldsymbol{1} + \begin{pmatrix} \int_{\boldsymbol{q}} e^{-\mathrm{i}q_1}\left[{\boldsymbol{M_0}}^{-1}\boldsymbol{\Lambda}_{\boldsymbol{G_0}}\right]_1 \\ \int_{\boldsymbol{q}} e^{\mathrm{i}q_1}\left[{\boldsymbol{M_0}}^{-1}\boldsymbol{\Lambda}_{\boldsymbol{G_0}}\right]_1 \\ \int_{\boldsymbol{q}} e^{-\mathrm{i}q_2}\left[{\boldsymbol{M_0}}^{-1}\boldsymbol{\Lambda}_{\boldsymbol{G_0}}\right]_1 \\ \int_{\boldsymbol{q}} e^{-\mathrm{i}q_1}\left[{\boldsymbol{M_0}}^{-1}\boldsymbol{\Lambda}_{\boldsymbol{G_0}}\right]_3 \end{pmatrix} \tag{B.26}$$

$$\boldsymbol{x}_{\widetilde{\boldsymbol{g}},0} = -\begin{pmatrix} \int_{\boldsymbol{q}} e^{-\mathrm{i}q_1}\left[{\boldsymbol{M_0}}^{-1}\left(\frac{1}{\rho}\boldsymbol{X}\cdot\boldsymbol{H}+\boldsymbol{E_0}+\boldsymbol{F_0}\right)\right]_1 \\ \int_{\boldsymbol{q}} e^{\mathrm{i}q_1}\left[{\boldsymbol{M_0}}^{-1}\left(\frac{1}{\rho}\boldsymbol{X}\cdot\boldsymbol{H}+\boldsymbol{E_0}+\boldsymbol{F_0}\right)\right]_1 \\ \int_{\boldsymbol{q}} e^{-\mathrm{i}q_2}\left[{\boldsymbol{M_0}}^{-1}\left(\frac{1}{\rho}\boldsymbol{X}\cdot\boldsymbol{H}+\boldsymbol{E_0}+\boldsymbol{F_0}\right)\right]_1 \\ \int_{\boldsymbol{q}} e^{-\mathrm{i}q_1}\left[{\boldsymbol{M_0}}^{-1}\left(\frac{1}{\rho}\boldsymbol{X}\cdot\boldsymbol{H}+\boldsymbol{E_0}+\boldsymbol{F_0}\right)\right]_3 \end{pmatrix} \tag{B.27}$$

where $[\cdot]_i$ means that we take the i-th line, and with

$$\boldsymbol{E_0} = \frac{1}{\rho}\begin{pmatrix} H^{(1)}\left((a_1^{(1)}-1)(e^{-\mathrm{i}q_1}-1)-(a_{-1}^{(1)}-1)(e^{\mathrm{i}q_1}-1)\right) \\ H^{(-1)}\left((a_{-1}^{(1)}-1)(e^{-\mathrm{i}q_1}-1)-(a_1^{(1)}-1)(e^{\mathrm{i}q_1}-1)\right) \\ -2\mathrm{i}(a_2^{(1)}-1)H^{(2)}\sin(q_1) \\ -2\mathrm{i}(a_2^{(1)}-1)H^{(-2)}\sin(q_1) \end{pmatrix}, \tag{B.28}$$

$$\boldsymbol{\Lambda_{G_0}} = \begin{pmatrix} \left(e^{\mathrm{i}q_1}-1\right)a_1^{(1)} & \left(e^{-\mathrm{i}q_1}-1\right)a_{-1}^{(1)} & 2\left(\cos\left(q_2\right)-1\right)a_2^{(1)} & 0 \\ -\left(e^{-\mathrm{i}q_1}-1\right)a_1^{(1)} & -\left(e^{\mathrm{i}q_1}-1\right)a_{-1}^{(1)} & -2\left(\cos\left(q_2\right)-1\right)a_2^{(1)} & 0 \\ 0 & 0 & 0 & 2\mathrm{i}a_2^{(1)}\sin(q_1) \\ 0 & 0 & 0 & 2\mathrm{i}a_2^{(1)}\sin(q_1) \end{pmatrix}, \tag{B.29}$$

and

$$\boldsymbol{F_0} = -\begin{pmatrix} (a_1^{(1)}-1)\left(e^{-\mathrm{i}q_1}+\frac{1}{\rho}h_1^{(1)}\right)-(a_{-1}^{(1)}-1)\left(e^{\mathrm{i}q_1}+\frac{1}{\rho}h_{-1}^{(1)}\right) \\ (a_{-1}^{(1)}-1)\left(e^{-\mathrm{i}q_1}+\frac{1}{\rho}h_1^{(-1)}\right)-(a_1^{(1)}-1)\left(e^{\mathrm{i}q_1}+\frac{1}{\rho}h_{-1}^{(-1)}\right) \\ (a_2^{(1)}-1)\left(e^{-\mathrm{i}q_1}+\frac{1}{\rho}h_1^{(2)}\right)-(a_2^{(1)}-1)\left(e^{\mathrm{i}q_1}+\frac{1}{\rho}h_{-1}^{(2)}\right) \\ (a_2^{(1)}-1)\left(e^{-\mathrm{i}q_1}+\frac{1}{\rho}h_1^{(2)}\right)-(a_2^{(1)}-1)\left(e^{\mathrm{i}q_1}+\frac{1}{\rho}h_{-1}^{(2)}\right). \end{pmatrix} \tag{B.30}$$

High density

In this case, we do not simply linearise expression from B.3.1. Instead, we diagonalise the matrix $\boldsymbol{M}(\boldsymbol{q})$, which can be done easily at high density. This makes it possible to derive expressions at any density d. The expressions involve the following quantities:

$$a = \zeta[\widehat{Q}(\mathbf{0}|\mathbf{0};\zeta) - \widehat{Q}(\boldsymbol{e}_1|\mathbf{0};\zeta)] \tag{B.31}$$

$$b = \zeta[\widehat{Q}(\mathbf{0}|\mathbf{0};\zeta) - \widehat{Q}(2\boldsymbol{e}_1|\mathbf{0};\zeta)] \tag{B.32}$$

$$b_0 = \widehat{Q}(\mathbf{0}|\mathbf{0};1) - \widehat{Q}(2\boldsymbol{e}_1|\mathbf{0};1) \tag{B.33}$$

$$c = \zeta\left[\widehat{Q}\left(\mathbf{0}\,|\mathbf{0};\zeta\right) - \widehat{Q}\left(\boldsymbol{e}_1+\boldsymbol{e}_\mu\,|\mathbf{0};\zeta\right)\right] \tag{B.34}$$

$$\beta = \zeta\widehat{Q}\left(\mathbf{0}\,|\mathbf{0};\zeta\right) \tag{B.35}$$

where $\zeta = \frac{2d-1}{2d-1+\alpha}$.

Density profiles.

$$\boldsymbol{\mathcal{M}}_{\boldsymbol{h},1} = \begin{pmatrix} 2d-c+bp_1\frac{2d\tau^*}{\tau} & b-c-bp_{-1}\frac{2d\tau^*}{\tau} & 0 \\ b-c-bp_1\frac{2d\tau^*}{\tau} & 2d-c+bp_{-1}\frac{2d\tau^*}{\tau} & 0 \\ 1 & 1 & 2d-2 \end{pmatrix} \tag{B.36}$$

$$\boldsymbol{x}_{\boldsymbol{h},1} = \frac{2d\tau^*}{\tau}(p_1^{(1)}-p_{-1}^{(1)})\begin{pmatrix} b \\ -b \\ 0 \end{pmatrix} \tag{B.37}$$

Correlation profiles

$$\boldsymbol{\mathcal{M}}_{\widetilde{\boldsymbol{g}},1} \equiv \begin{pmatrix} 2d & 2d & 4d^2-4d & 0 \\ 2d-1 & -1 & -(2d-2) & 0 \\ -1 & 2d-1 & -(2d-2) & 0 \\ 0 & 0 & 0 & 1 \end{pmatrix} + \frac{2d\tau^*}{\tau} \begin{pmatrix} 2p_1b_0 & 2p_{-1}b_0 & (4d-4)p_2b_0 & 0 \\ \frac{2d-2}{2d}p_1b & \frac{2d-2}{2d}p_{-1}b & -\frac{4d-4}{2d}p_2b & 0 \\ \frac{2d-2}{2d}p_1b & \frac{2d-2}{2d}p_{-1}b & -\frac{4d-4}{2d}p_2b & 0 \\ 0 & 0 & 0 & 0 \end{pmatrix}$$
$$- \begin{pmatrix} b_0 & b_0 & (2d-2)b_0 & 0 \\ \frac{2da-b}{2d} & \frac{(2d-1)b-2da}{2d} & -b\frac{2d-2}{2d} & 0 \\ \frac{(2d-1)b-2da}{2d} & \frac{2da-b}{2d} & -b\frac{2d-2}{2d} & 0 \\ a-c & c-a & 0 & (2d-2)a-b-(2d-4)c \end{pmatrix} \tag{B.38}$$

$$\boldsymbol{x}_{\widetilde{\boldsymbol{g}},1} = -\frac{2d\tau^*}{\tau} \begin{pmatrix} 0 \\ p_1(1-h_1^{(1)})(\beta-b) - p_{-1}(1+h_1^{(1)})\beta \\ p_{-1}(1+2_1^{(1)})(\beta-b) - p_1(1-h_1^{(1)})\beta \\ \left(p_1(1-h_1^{(1)}) - p_{-1}(1+h_1^{(1)})\right)(\beta-c) \end{pmatrix} + \frac{2d\tau^*}{\tau}(1-(p_1-p_{-1})h_1^{(1)}) \begin{pmatrix} b_0 \\ -\frac{b}{2d} \\ -\frac{b}{2d} \\ 0 \end{pmatrix} \tag{B.39}$$

Appendix C

Analysis of the qualitative argument

Thanks to the analytical formula given by the qualitative argument, we can perform some function analysis and extract scalings for the diffusion coefficient's dependence on the parameters of the problem. Here we restrict to the case of a symmetric run-and-tumble tracer $F_E = 0$.

According to the qualitative argument 3.4, the mean trapping time follows an exponential law of characteristic time $\tau_p^{(\chi)}$ given by

$$\frac{1}{\tau_p^{(\chi)}} = \frac{(2d-2)}{2d\tau^*} + \frac{1}{\tau_\alpha} + \frac{(1 - p_1^{(\chi)} - p_{-1}^{(\chi)})}{\tau}. \tag{C.1}$$

The diffusion coefficient is approached by:

$$D \simeq \frac{1}{4d} \sum_\chi \frac{p_1^{(\chi)} + p_{-1}^{(\chi)}}{\tau + \rho\tau_p^{(\chi)}} + \frac{(2d-1)\tau_\alpha}{4d^2} \sum_\chi \left\{ \frac{p_1^{(\chi)} - p_{-1}^{(\chi)}}{\tau + \rho\tau_p^{(\chi)}} \right\}^2. \tag{C.2}$$

C.1 Minimum of diffusion

We consider a fully directive run-and-tumble tracer $F_A \to \infty$. The diffusion coefficients (3.39) takes the simpler form:

$$\frac{1}{\tau_p} = \frac{(2d-2)}{2d\tau^*} + \frac{1}{\tau_\alpha}, \tag{C.3}$$

$$D \simeq \frac{1}{2d(\tau + \rho\tau_p)} \left(1 + \frac{(2d-1)\tau_\alpha}{d(\tau + \rho\tau_p)} \right). \tag{C.4}$$

To find the minimum, we consider the case where the tracer spends much time trapped $\rho\tau_p \gg \tau$ (for this regime to exist, we need a choice of parameters such that $\rho\tau^* \gg \tau$), we have the approximate expression:

$$D \simeq \frac{1}{2d\rho\tau_p} \left(1 + \frac{(2d-1)\tau_\alpha}{d\rho\tau_p} \right). \tag{C.5}$$

The minimum of this function is attained in τ_α^m:

$$\tau_\alpha^m = \tau^* \frac{d}{d-1} \sqrt{1 + \frac{d\rho}{2d-1}}, \qquad D_{\min} \simeq \frac{4d^2 - 6d + 2}{d^3\rho^2\tau^*}. \tag{C.6}$$

C.2 Maximum of diffusion

We still consider $F_A \to \infty$. For relatively small persistence time $\tau_\alpha \ll \tau^*$, the active tracer may exhibit a maximum of diffusivity (see the shape of the lower left curve on figure 4.5, or the green curve in the left plot of figure 4.3). In this limit $\tau_p \sim \tau_\alpha$, and therefore,

$$D \simeq \frac{1}{2d(\tau + \rho\tau_\alpha)} \left(1 + \frac{(2d-1)\tau_\alpha}{d(\tau + \rho\tau_\alpha)}\right). \tag{C.7}$$

The maximum of this function is reached for a value τ_α^M:

$$\tau_\alpha^M = \tau \frac{2d - 1 - d\rho}{\rho(2d - 1 + d\rho)}, \qquad D_{\max} = \frac{(2d - 1 + d\rho)^2}{8d^2(2d-1)\rho\tau}. \tag{C.8}$$

This is valid when $\tau_\alpha^M \ll \tau$, namely $\rho\tau^* \gg \tau$, which the same condition as for the minimum of diffusion. The slower the obstacles, the bigger the variations of the diffusion coefficient (the higher the trapping effects!).

C.3 Analytic criteria for existence of non monotony

In the case of infinite active force $F_A \to \infty$, a quite involved function analysis of equation (C.4) leads to the following analytic expression for the critical timescale of displacement of obstacles τ_c^* (with $\tau = 1$) above which there exists non monotony of the diffusion coefficient in function of the persistence time τ_α:

$$\tau_c^* \simeq \left(8 - \frac{8}{d}\right) \frac{1}{\rho}. \tag{C.9}$$

In the case of a finite active force $F_A \gg 1$, we can put forward the following argument. We neglect the effect of a finite F_A on the expression of D (C.4), and we only consider the change in the trapping time:

$$\begin{aligned} \frac{1}{\tau_p} &= \frac{(2d-2)}{2d\tau^*} + \frac{1}{\tau_\alpha} + \frac{1 - p_1^{(1)} - p_{-1}^{(1)}}{\tau} \\ &\simeq \frac{(2d-2)}{2d\tau^*} + \frac{1}{\tau_\alpha} + \frac{2d-2}{(2d-2+e^{F_A/2})\tau}. \end{aligned} \tag{C.10}$$

With this approach, we find that $\frac{(2d-2)}{2d\tau^*}$ and $\frac{2d-2}{(2d-2+e^{F_A/2})\tau}$ play equivalent roles. The critical surface (increase in active force F_A or in time τ^* or in density ρ implies apparition of non monotony in function of τ^α) is therefore the curve of equation:

$$\frac{(2d-2)\rho}{(16d-16)\,\tau} = \frac{(2d-2)}{2d\tau^*} + \frac{2d-2}{(2d-2+e^{F_A/2})\tau}. \tag{C.11}$$

As a direct consequence, under some critical density $\rho_C \simeq \dfrac{16(d-1)}{2d-2+e^{F_A/2}}$, there cannot be non monotony anymore, whatever the value of τ^*.

Appendix D

Hydrodynamic limit and local equilibrium

In this appendix, we give some details about how we can interpret the existence of hydrodynamic fields (section 6.2.3) in terms of local equilibrium in the microscopic system. This discussion relies mainly on physical intuitions, because the mathematical formulation of local equilibrium, and proofs in the general case are very challenging; see [182] (chapter 3), even in the simplest case where the considered microscopic system is a lattice model admitting invariant measures which are product of measures on each site, the precise definition of local equilibrium poses difficulties.

We study a system of particles on the infinite line. To make sense of the notion of local equilibrium, we first discuss the stationary measures of a finite version of this system (considering a finite version of the system is possible only if the evolution rules are local). Then we discuss the meaning of the macroscopic density field $\rho(x,t)$. Finally, we give an example where the local equilibrium is observed in numerical simulations.

D.1 Stationary measures and macroscopic density

We consider a very big (of size $L \gg 1$) finite version of the system studied, with periodic boundary conditions. Initially, we put $N = \rho L$ particles on the system. If we wait long enough, the system will converge to a stationary measure. Since the number of particle is conserved, the average density remains ρ at all time. Consequently, there is one stationary measure for any density ρ. We denote by $\langle\cdot\rangle_\rho$ the average with respect to the stationary measure of density ρ.

Now, we look at an infinite system $\mathcal{S}_{\text{whole}} = \mathbb{R}$ and take the hydrodynamic limit. The macroscopic density $\rho(x,t)$ corresponds, when the scaling parameter N goes to infinity, to the density of a mesoscopic system around xN, $\mathcal{S} = [xN, xN + \sqrt{N}]$ at time tN^2. The existence of a macroscopic density $\rho(x,t)$ comes from the fact that this mesoscopic system $\mathcal{S}$ is distributed, in the large N limit, according to the stationary measure at density $\rho(x,t)$ of the microscopic dynamics, whose averages are denoted by $\langle\cdot\rangle_{\rho(x,t)}$.

According to the fluctuating hydrodynamics formulation 6.2.3, this density $\rho(x,t)$ fluctuates with probabilities specified by the MFT large deviation principle (6.7). Heuristically, this can be described as "two levels of stochasticity":

- The macroscopic stochasticity, which deals with the fluctuations of the macroscopic density field $\rho(x,t)$.
- For a given realisation of the density $\rho(x,t)$, the microscopic system is not known

deterministically, but we know that each mesoscopic subsystem $\mathcal{S} = [xN, xN + \sqrt{N}]$ is distributed according to the stationary measure of density $\rho(x,t)$.

It is very unlikely that in the hydrodynamic limit ($N \to \infty$), the system is not distributed locally according to stationary measures ("super-exponential estimates" bounding the probability that local equilibrium does not exist is a key element of the proofs of hydrodynamic limits).

This gives a way to compute an average of the form $\frac{\left\langle F(Nx)e^{\lambda O_{N^2t}}\right\rangle}{e^{\lambda O_{N^2t}}}$, where O_{N^2t} is an observable (X_t or Q_t in our study) and $F(Nx)$ is a microscopic quantity, which depends on the state of the system in the vicinity of a point Nx (which scales with N), for example $F(N\xi) = \eta_{\lfloor \xi N \rfloor}(N^2t)\eta_{\lfloor \xi N \rfloor+1}(N^2t)$ in the SEP (F.14). Indeed, we know from the saddle-point method applied to the MFT large deviation principle (see section 7.1.2) that the macroscopic profile is concentrated around an optimal one ρ^*; in other words, the "macroscopic stochasticity" is killed. As a consequence, the only remaining stochasticity is the one on the microscopic distribution, that is why we can compute F using the stationary measure at density $\rho^*(x,t)$:

$$\frac{\left\langle F(Nx)e^{\lambda O_{N^2t}}\right\rangle}{e^{\lambda O_{N^2t}}} \underset{N\to\infty}{\sim} \langle F(0)\rangle_{\rho^*(x,t)}\,. \tag{D.1}$$

The fact that $F(xN)$ is computed in the mesoscopic system around xN appears only in the density $\rho^*(x,t)$ of the stationary measure used to compute the average of $F(0)$.

We now illustrate this convergence to local equilibrium with an example of microscopic model.

D.2 Example of the DEP

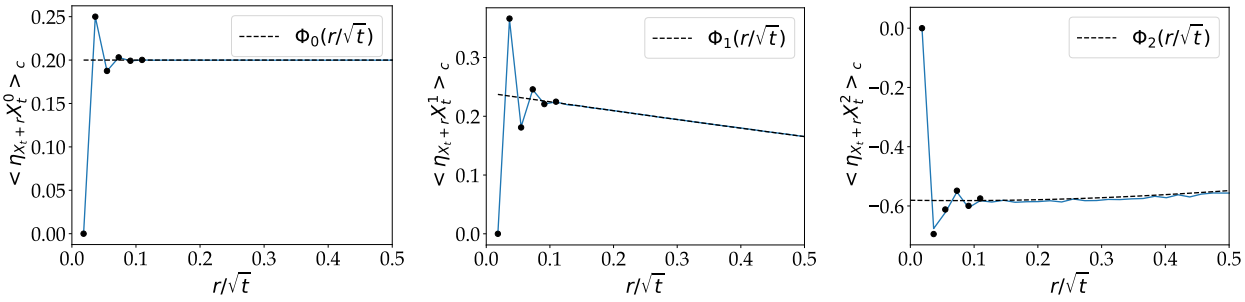

Figure D.1: Generalised profiles for the DEP at density $\rho = 0.2$. Blue lines: Monte Carlo simulations (20000 sites, 10^8 simulations, final time $t = 3000$). Black dashed lines: hydrodynamics profiles [equations (9.88, 9.89)]. Dots: microscopic distribution of particles computed according to the stationary measure [equation (D.3)].

In the DEP (Double Exclusion Process 6.1.2) with a tracer, we denote by $\eta_r(t)$ the occupation at site r and X_t the position of the tracer. If we plot the generalised profiles $\frac{\left\langle \eta_{X_t+r} e^{\lambda X_t}\right\rangle}{\left\langle e^{\lambda X_t}\right\rangle} = \sum \frac{\lambda^n}{n!} \left\langle \eta_{X_t+r} X_t^n \right\rangle_c$ (7.5), we see that they oscillate around the hydrodynamic profile $\Phi(v = r/\sqrt{t}, \lambda) = \sum \frac{\lambda^n}{n!} \Phi_n(v)$ in the vicinity of the tracer (figure D.1).

This is consistent with the local equilibrium. Indeed, the hydrodynamic profile $\Phi(0+, \lambda)$ expresses the density of the local equilibrium in the vicinity of the tracer particle. The stationary measures of the DEP are known (limit of the KLS [175, 176] where $\epsilon = 1$), in

particular, it is not a product measure; knowing that a site is occupied has an influence on the occupation of neighbouring sites. As argued previously, the system is distributed in the vicinity of the tracer according to the stationary measure of density $\Phi(0^+, \lambda)$. Since the tracer is always on site η_{X_t}, using equation (D.1), we have:

$$\frac{\left\langle \eta_{X_t+r} e^{\lambda X_t} \right\rangle}{\left\langle e^{\lambda X_t} \right\rangle} \underset{t\to\infty}{\sim} \langle \eta_r | \eta_0 = 1 \rangle_{\Phi(0^+,\lambda)} , \tag{D.2}$$

where $\langle \bullet | \eta_0 = 1 \rangle_{\Phi(0^+,\lambda)} = \dfrac{\langle \bullet \times \eta_0 \rangle_{\Phi(0^+,\lambda)}}{\langle \eta_0 \rangle_{\Phi(0^+,\lambda)}}$ is the average conditioned to site 0 being occupied. Finally, we have:

$$\frac{\left\langle \eta_{X_t+r} e^{\lambda X_t} \right\rangle}{\left\langle e^{\lambda X_t} \right\rangle} \underset{t\to\infty}{\sim} \Phi(0^+, \lambda) \left[1 - \left(-\frac{\Phi(0^+, \lambda)}{1 - \Phi(0^+, \lambda)} \right)^{r-1} \right] \tag{D.3}$$

This formula developed at first orders in λ is plotted in figure D.1.

Appendix E

Complements on Macroscopic Fluctuation Theory

In this appendix we provide compact proofs of different facts that were used in this thesis. The proofs E.1 and E.2 are based on arguments from [104, 202].

E.1 The equilibrium potential

In this appendix, we derive the large deviation functional F of the macroscopic empirical density $\rho(x,0)$ of a system which is initially distributed according to local equilibriums of density $\rho_0(x)$ slowly varying with x. This is what we call the annealed initial condition with density profile $\rho_0(x)$.

We consider that around a position r, any mesoscopic system is at equilibrium with a reservoir of density $\rho_0(r/N)$ (the reservoir is disconnected for $t>0$). We call mesoscopic a system which is infinitely small compared to the scaling parameter N, but which is large on the microscopic scale, for example $\mathcal{S}_r=[r,r+L]$ with $1\ll L=N^{1/4}\ll N$. Since $\mathcal{S}$ can exchange matter with the reservoir, the number of particles it contains, denoted by $n_{\mathcal{S}}$, follows the grand-canonical distribution (we take $k_BT=1$ for simplicity)

$$\mathbb{P}(n_{\mathcal{S}}=n)=\frac{e^{\mu_{\mathcal{S}}n}Z_L(n)}{Z_L^G(\mu_{\mathcal{S}})}, \tag{E.1}$$

where the chemical potential $\mu_{\mathcal{S}}$ is such that $\langle n_{\mathcal{S}}\rangle=\rho_0(r/N)L$. We denoted $Z_L(n)$ the partition function for the system of size L with n particles and $Z_L^G(\mu_{\mathcal{S}})$ the associated grand partition function at chemical potential $\mu_{\mathcal{S}}$. If we denote $F(L,n)$ the free energy of the system of size L with n particles, then we have in the thermodynamic limit $L\to\infty$:

$$\mathbb{P}(n_{\mathcal{S}}=n)=\frac{e^{\mu_{\mathcal{S}}n-F(L,n)}}{e^{-F(L,\langle n_{\mathcal{S}}\rangle)+\mu_{\mathcal{S}}\langle n_{\mathcal{S}}\rangle}}. \tag{E.2}$$

For large systems, the free energy is extensive $F(L,n)=Lf\left(\frac{n}{L}\right)$. The chemical potential is therefore an intensive quantity:

$$\begin{aligned}\mu_{\mathcal{S}}&=\frac{\mathrm{d}}{\mathrm{d}n}F(L,n)\\&=f'\left(\frac{n}{L}\right)\end{aligned} \tag{E.3}$$

The one dimensional line $\mathbb{R}=\cup_{k\in\mathbb{Z}}\mathcal{S}_{kL}$ is split into mesoscopic subsystems. If L is large, each mesoscopic systems $\mathcal{S}_{kL}$ can be considered independent since it communicates with other

systems at the extremities (2 points), whereas it is supposed in equilibrium with a reservoir in the bulk (length $L \gg 2$). Therefore, the probability to observe initially the systems $\mathcal{S}_{kL}$ at densities $\rho(r/N, 0)$ is given by the product of probabilities (E.2):

$$\prod_{k\in\mathbb{Z}} \mathbb{P}(n_{\mathcal{S}} = \rho(kL/N,0)L) = \exp\left(\sum_{k\in\mathbb{Z}} f'\left(\rho_0\left(\frac{kL}{N}\right)\right)\rho(kL/N,0)L - Lf\left(\rho\left(\frac{kL}{N},0\right)\right) + Lf\left(\rho_0\left(\frac{kL}{N}\right)\right) - f'\left(\rho_0\left(\frac{kL}{N}\right)\right)\rho_0\left(\frac{kL}{N}\right)L\right). \tag{E.4}$$

The sum can be replaced by an integral on $k \in \mathbb{R}$ by Euler-Maclaurin formula, because the derivative of the integrand with respect to k is small when N is big. Finally, we perform the change of variable $x = \frac{kL}{N}$, and we get the functional:

$$F[\rho(x,0)] = \int_{-\infty}^{+\infty} f(\rho(x,0)) - f(\rho_0(x)) - f'(\rho_0(x))(\rho(x,0) - \rho_0(x))\mathrm{d}x. \tag{E.5}$$

E.2 Relation between the transport coefficients

Since they characterise fluctuations and linear response of the transfer of matter between the two reservoirs, the transport coefficients are related through equilibrium quantities (fluctuation-dissipation theorem). This can be seen as a property of the Boltzmann-Gibbs distribution (which is the equilibrium distribution).

Consider the system (figure 6.12) made of two reservoirs at chemical potential μ and connected by a line, the total number of particles is very big, and considered constant. We denote $N_a(t)$ the number of particles in the left reservoir at time t. There is a (Markovian) dynamics invariant under time translations:

$$\mathbb{P}(N_a(t) = n_a) = \sum_n \mathbb{P}(N_a(0) = n)p(n \to n_a; t), \tag{E.6}$$

which admits the following Gibbs distribution as an invariant measure (F is the free energy):

$$\nu(n_a) = \frac{e^{\mu n_a - F(n_a)}}{\sum_n e^{\mu n - F(n)}}. \tag{E.7}$$

We denoted by $p(n \to n_a; t)$ the conditional probability that $N_a(T+t) = n_a$ given that $N_a(T) = n$.

The integrated current is given by the variation of the number of particles in the left reservoir $Q_t = -(N_a(t) - N_a(0))$. We consider the system at equilibrium (averages $\langle\cdot\rangle$ with respect to the equilibrium measure ν). Since it is a symmetric system (diffusive), we have $\langle Q_t\rangle = 0$. Like Brownian motion, the equilibrium dynamics is characterised by the second moment:

$$\begin{aligned} \left\langle Q_t^2\right\rangle &= \left\langle N_a(t)^2\right\rangle - 2\left\langle N_a(t)N_a(0)\right\rangle + \left\langle N_a(0)^2\right\rangle \\ \frac{\langle Q_t^2\rangle}{t} &\underset{t\to\infty}{\sim} -2\frac{\langle N_a(t)N_a(0)\rangle}{t}. \end{aligned} \tag{E.8}$$

We have used the fact that, at equilibrium, $\langle N_a(t)^2\rangle$ is constant.

Now, we suppose that the system is held in a near equilibrium situation where the chemical potential of the left reservoir $\mu_a \simeq \mu$ is slightly different from the one of the right reservoir $\mu_b = \mu$. We denote $\mu_a = \mu + \delta\mu$. The system follows the perturbed measure:

$$\begin{aligned}\nu_p(n_a) &= \frac{e^{\mu n_a - F(n_a) + \delta\mu n_a}}{\sum_n e^{\mu n - F(n) + \delta\mu n}} \\ &\simeq \nu(n_a)(1 + \delta\mu(n_a - \langle N_a \rangle)),\end{aligned} \tag{E.9}$$

at first order, since $\delta\mu$ is small, where $\langle\cdot\rangle$ is taken with respect to the equilibrium measure (E.7). In this perturbed setup, where the left-right symmetry is broken, the stochastic dynamics (E.6) leads to a nonzero mean current (the mean with respect to the perturbed measure ν_p is denoted $\langle\cdot\rangle_p$):

$$\begin{aligned}\langle Q_t \rangle_p &= \sum_{n_i, n_f} \nu_p(n_i) p(n_i \to n_f; t)(-n_f + n_i) \\ &= \sum_{n_i, n_f} \nu(n_i) p(n_i \to n_f; t)(-n_f + n_i) + \delta\mu \sum_{n_i, n_f} \nu(n_i)(n_i - \langle N_a \rangle) p(n_i \to n_f; t)(-n_f + n_i) \\ &= \langle -N_a(t) \rangle + \langle N_a(0) \rangle + \delta\mu \left(- \langle N_a(t) N_a(0) \rangle + \left\langle N_a(0)^2 \right\rangle - \langle N_a \rangle \left(- \langle N_a(t) \rangle + \langle N_a(0) \rangle \right) \right)\end{aligned}$$

$$\frac{\langle Q_t \rangle_p}{t} \underset{t \to \infty}{\sim} -\delta\mu \frac{\langle N_a(t) N_a(0) \rangle}{t}. \tag{E.10}$$

We used $\langle N_a(0) \rangle = \langle N_a(t) \rangle = \langle N_a \rangle$ (stationary measure). Comparing with (E.8), we get:

$$2\frac{\langle Q_t \rangle_p}{t} \underset{t \to \infty}{\sim} (\mu_a - \mu_b)\frac{\langle Q_t^2 \rangle}{t} \tag{E.11}$$

For large systems, the chemical potential is an intensive quantity, therefore μ_a and $\mu_b = \mu$ depend only on the densities ρ_a of the left reservoir and $\rho_b = \rho$ of the right reservoir. Since μ_a and μ_b are very close, we can write $\mu_a - \mu_b = \frac{\mathrm{d}\mu}{\mathrm{d}\rho}(\rho_a - \rho_b)$. Combined with the characterisation of the transport coefficients (6.9) and $\frac{\mathrm{d}\mu}{\mathrm{d}\rho} = f''(\rho)$ (E.3) (f is the free energy per unit volume), this yields the relation:

$$2D(\rho) = f''(\rho)\sigma(\rho). \tag{E.12}$$

Appendix F

Microscopic equations in the SEP

In this appendix we give some details about the derivation of the evolution equations of the GDP (7.17) of the integrated current. Then we explain how to take the long time limit of these equations using the scaling forms found in section 7.1.2.

We focus on the integrated current $Q_t(x_t)$. We fix a (positive for simplicity) value for ξ. We recall that $x_t = \lfloor \xi\sqrt{2t} \rfloor$.

F.1 Evolution equations for microscopic quantities

Because we consider a moving point of observation $x_t = \lfloor \xi\sqrt{2t} \rfloor$, the time evolution of the cumulant generating function is the sum of two contributions:

1. At times $t_n = (n/\xi)^2/2$, the increment of $x_{t_n^+} = x_{t_n^-} + 1$ causes a change of $Q_t(x_t)$, depending on the occupation $\eta_{x_{t_n^-}+1}$ of the site that is "leaving" the sum (7.15) at t_n. Therefore,
$$\left\langle \mathrm{e}^{\lambda Q_t(x_{t^+})} \right\rangle = \left\langle \mathrm{e}^{\lambda Q_t(x_{t^-}) - \lambda \eta_{x_t^-+1}} \right\rangle \text{ , for } t = t_n \,. \tag{F.1}$$
Taking the logarithm, and using that $\eta_x = 0$ or 1, we get
$$\ln \left\langle \mathrm{e}^{\lambda Q_t(x_t)} \right\rangle\Big|_{t=t_n^+} = \ln \left\langle \mathrm{e}^{\lambda Q_t(x_t)} \right\rangle\Big|_{t=t_n^-} + \ln(1 + (\mathrm{e}^{-\lambda} - 1) w_{Q;1}(t)) \,. \tag{F.2}$$

2. Between two increments of x_t, the stochastic dynamics of the SEP, from the master equation (7.1)
$$\partial_t \ln \left\langle \mathrm{e}^{\lambda Q_t(x_t)} \right\rangle = \frac{1}{2} \left[(\mathrm{e}^{\lambda} - 1) \frac{\left\langle \eta_{x_t}(1 - \eta_{x_t+1}) \mathrm{e}^{\lambda Q_t(x_t)} \right\rangle}{\left\langle \mathrm{e}^{\lambda Q_t(x_t)} \right\rangle} + (\mathrm{e}^{-\lambda} - 1) \frac{\left\langle \eta_{x_t+1}(1 - \eta_{x_t}) \mathrm{e}^{\lambda Q_t(x_t)} \right\rangle}{\left\langle \mathrm{e}^{\lambda Q_t(x_t)} \right\rangle} \right] , \tag{F.3}$$
for $t \neq t_n$.

Finally we have
$$\begin{aligned} \partial_t \ln \left\langle \mathrm{e}^{\lambda Q_t(x_t)} \right\rangle =& \frac{1}{2} \left[(\mathrm{e}^{\lambda} - 1) \frac{\left\langle \eta_{x_t}(1 - \eta_{x_t+1}) \mathrm{e}^{\lambda Q_t(x_t)} \right\rangle}{\left\langle \mathrm{e}^{\lambda Q_t(x_t)} \right\rangle} + (\mathrm{e}^{-\lambda} - 1) \frac{\left\langle \eta_{x_t+1}(1 - \eta_{x_t}) \mathrm{e}^{\lambda Q_t(x_t)} \right\rangle}{\left\langle \mathrm{e}^{\lambda Q_t(x_t)} \right\rangle} \right] \\ &+ \sum_n \delta(t - t_n) \ln[1 + (\mathrm{e}^{-\lambda} - 1) w_{Q;1}(t)] \,. \end{aligned} \tag{F.4}$$

Taking into account the two contributions as above, we compute the evolution of the GDP-generating function $\partial_t w_{Q;r}$:

1. At times $t_n = (n/\xi)^2/2$

$$\left.\frac{\left\langle \eta_{x_t+r} e^{\lambda Q_t(x_t)}\right\rangle}{\left\langle e^{\lambda Q_t(x_t)}\right\rangle}\right|_{t=t_n^+} = \left.\frac{\left\langle \eta_{x_t+r+1} e^{\lambda Q_t(x_t)-\lambda\eta_{x_t+1}}\right\rangle}{\left\langle e^{\lambda Q_t(x_t)-\lambda\eta_{x_t+1}}\right\rangle}\right|_{t=t_n^-}$$
$$= w_{Q;r}(t_n^-) + \left.\left(\frac{\left\langle \eta_{x_t+r+1}(1+(e^{-\lambda}-1)\eta_{x_t+1}) e^{\lambda Q_t(x_t)}\right\rangle}{\left\langle \mathrm{e}^{\lambda Q_t(x_t)}\right\rangle\left(1+(\mathrm{e}^{-\lambda}-1)w_{Q;1}(t)\right)} - w_{Q;r}(t)\right)\right|_{t=t_n^-}. \tag{F.5}$$

2. Between two increments, we use the product rule, for $t \neq t_n$:

$$\frac{\partial_t \left\langle \eta_{x_t+r} e^{\lambda Q_t(x_t)}\right\rangle}{\left\langle e^{\lambda Q_t(x_t)}\right\rangle} - w_{Q;r}\partial_t \ln\left\langle \mathrm{e}^{\lambda Q_t(x_t)}\right\rangle \tag{F.6}$$

with for $r \neq 0, 1$

$$\frac{\partial_t \left\langle \eta_{x_t+r} e^{\lambda Q_t(x_t)}\right\rangle}{\left\langle e^{\lambda Q_t(x_t)}\right\rangle} = \frac{1}{2}\Delta w_{Q;r} + \frac{\left\langle \eta_{x_t+r} e^{\lambda Q_t(x_t)}(e^{\lambda}-1)(\eta_{x_t} - e^{-\lambda}\eta_{x_t+1} + (e^{-\lambda}-1)\eta_{x_t}\eta_{x_t+1})\right\rangle}{2\left\langle e^{\lambda Q_t(x_t)}\right\rangle}, \tag{F.7}$$

and for $r = 0, 1$

$$\frac{\partial_t \left\langle \eta_{x_t} e^{\lambda Q_t(x_t)}\right\rangle}{\left\langle e^{\lambda Q_t(x_t)}\right\rangle} = \frac{w_{Q;-1} - w_{Q;0}}{2} + \frac{e^{-\lambda}w_{Q;1} - w_{Q;0}}{2} - (e^{-\lambda}-1)\frac{\left\langle \eta_{x_t}\eta_{x_t+1} e^{\lambda Q_t(x_t)}\right\rangle}{2\left\langle e^{\lambda Q_t(x_t)}\right\rangle}, \tag{F.8}$$

$$\frac{\partial_t \left\langle \eta_{x_t+1} e^{\lambda Q_t(x_t)}\right\rangle}{\left\langle e^{\lambda Q_t(x_t)}\right\rangle} = \frac{w_{Q;2} - w_{Q;1}}{2} + \frac{e^{\lambda}w_{Q;0} - w_{Q;1}}{2} - (e^{\lambda}-1)\frac{\left\langle \eta_{x_t}\eta_{x_t+1} e^{\lambda Q_t(x_t)}\right\rangle}{2\left\langle e^{\lambda Q_t(x_t)}\right\rangle}, \tag{F.9}$$

Before bringing everything together, it is important to see, because it gives information about the scalings in time, that (still for $t \neq t_n$)

$$\frac{\partial_t \left\langle \eta_{x_t} e^{\lambda Q_t(x_t)}\right\rangle}{\left\langle e^{\lambda Q_t(x_t)}\right\rangle} = \frac{w_{Q;-1} - w_{Q;0}}{2} - \frac{\partial_t \ln\left\langle \mathrm{e}^{\lambda Q_t(x_t)}\right\rangle}{e^{\lambda}-1}, \tag{F.10}$$

$$\frac{\partial_t \left\langle \eta_{x_t+1} e^{\lambda Q_t(x_t)}\right\rangle}{\left\langle e^{\lambda Q_t(x_t)}\right\rangle} = \frac{w_{Q;2} - w_{Q;1}}{2} - \frac{\partial_t \ln\left\langle \mathrm{e}^{\lambda Q_t(x_t)}\right\rangle}{e^{-\lambda}-1}, \tag{F.11}$$

Bringing everything together yields for example for $r = 0$:

$$\partial_t w_{Q;0} = \frac{\mathrm{e}^{-\lambda} - (\mathrm{e}^{-\lambda}-1)w_{Q;0}}{\mathrm{e}^{-\lambda}-1}\left(\partial_t \ln\left\langle \mathrm{e}^{\lambda Q_t(x_t)}\right\rangle - \sum_n \delta(t-t_n)\ln[1+(\mathrm{e}^{-\lambda}-1)w_{Q;1}(t)]\right)$$
$$+ \frac{w_{Q;-1} - w_{Q;0}}{2} + \sum_n \delta(t-t_n)\left(\frac{\mathrm{e}^{-\lambda}w_{Q;1}}{1+(\mathrm{e}^{-\lambda}-1)w_{Q;1}} - w_{Q;0}\right). \tag{F.12}$$

Remarkably, in the long time limit, equations (7.22, F.10, F.11) give non trivial information about the hydrodynamic profiles Φ_Q and cumulant generating function $\hat{\psi}_Q$.

F.2 Long-time limit of the equations

Here to lighten notations, we will simply write $\Phi_Q(v)$, instead of $\Phi_Q(v,\xi,\lambda)$.

To take the long-time limit of the evolution equations derived above, we inject the sclaings obtained in section 7.1.2 from MFT. In addition, there are two important points that we must understand, and which are tackled in the two following paragraphs.

The first thing we must understand is the long time limit of the cross correlation $\frac{\langle \eta_{x_t}\eta_{x_t+1}\mathrm{e}^{\lambda Q_t(x_t)}\rangle}{\langle \mathrm{e}^{\lambda Q_t(x_t)}\rangle}$. In fact when we apply the large deviation principle (like in (7.10)), we use the fact that the microscopic system in the vicinity of some site r converges to a local equilibrium at density $\rho^*(r/\sqrt{t},1)$ where ρ^* is the optimal hydrodynamic profile [124], defined by (7.20) for the integrated current, and which is related to the scaling function Φ_Q (further discussion of local equilibrium in appendix D). As a consequence (already used in (7.19)), we have the following limits:

$$w_{Q;0} \underset{t\to\infty}{\longrightarrow} \Phi_Q(0^-), \quad w_{Q;1} \underset{t\to\infty}{\longrightarrow} \Phi_Q(0^+), \tag{F.13}$$

because we will see that the GDP are discontinuous at the point x_t. Moreover, in the case of the SEP, the equilibrium measure at density ρ is the product measure of Bernoulli of parameter ρ on each site. In particular, the two site correlation $\frac{\langle \eta_{x_t}\eta_{x_t+1}\mathrm{e}^{\lambda Q_t(x_t)}\rangle}{\langle \mathrm{e}^{\lambda Q_t(x_t)}\rangle}$ converges over time to $\langle \eta_0(1-\eta_1)\rangle_H$ where $\langle\cdot\rangle_H$ is the average with respect to the product measure of Bernoulli of parameter $\Phi_Q(0^-)$ on sites $r\le 0$ and Bernoulli of parameter $\Phi_Q(0^+)$ on sites $r\ge 1$. Finally this gives:

$$\frac{\langle \eta_{x_t}\eta_{x_t+1}\mathrm{e}^{\lambda Q_t(x_t)}\rangle}{\langle \mathrm{e}^{\lambda Q_t(x_t)}\rangle} = \Phi_Q(0^-)\Phi_Q(0^+). \tag{F.14}$$

The second important point to understand in order to take the long time limit is that, due to the scaling $w_{Q;r}(t) \underset{t\to\infty}{\sim} \Phi_Q\left(\frac{r}{\sqrt{2t}}\right)$, $w_{Q;r}(t)$ varies slowly, namely with a rate $O(t^{-3/2})$. On the contrary, the average number of increments of x_t in a time window $\mathrm{d}t$ is $\xi\frac{\mathrm{d}t}{\sqrt{2t}}$, which is much bigger than the variation of Φ_Q. This justifies to write:

$$\sum_n \delta(t-t_n)\ln[1+(\mathrm{e}^{-\lambda}-1)w_{Q;1}(t)] \underset{t\to\infty}{\sim} \frac{\xi}{\sqrt{2t}}\ln[1+(\mathrm{e}^{-\lambda}-1)\Phi_Q(0^+)]. \tag{F.15}$$

More generally, if $f(t)$ varies slowly, we have:

$$\sum_n \delta(t-t_n)f(t) \underset{t\to\infty}{\sim} \frac{\xi}{\sqrt{2t}}f(t). \tag{F.16}$$

As a result of these observations, combined with the fact that because of the scaling of the cumulant generating function (7.19), $\partial_t \ln\left\langle \mathrm{e}^{\lambda Q_t(x_t)}\right\rangle \underset{t\to\infty}{\longrightarrow} 0$, the long time limit of the evolution equation (7.22) yields:

$$\boxed{\frac{\Phi_Q(0^+)(1-\Phi_Q(0^-))}{\Phi_Q(0^-)(1-\Phi_Q(0^+))} = \mathrm{e}^{\lambda}}. \tag{F.17}$$

This proves that the long time profile $\Phi_Q(v)$ is indeed discontinuous in 0 when $\lambda\neq 0$.

Now we look at the equation for $\partial_t w_{Q;0}$ (7.23). To take the long time limit we need a third ingredient that we did not discuss yet, which is the following expansion:

$$w_{Q;r+1}-w_{Q;r} \simeq \Phi_Q\left(\frac{r+1}{\sqrt{2t}}\right)-\Phi_Q\left(\frac{r}{\sqrt{2t}}\right) \simeq \frac{1}{\sqrt{2t}}\Phi_Q'\left(\frac{r}{\sqrt{2t}}\right). \tag{F.18}$$

Here the long time limit of equation (7.23) is trivial because $\partial_t w_{Q;r} = O(t^{-3/2})$, the sum over increments of x_t scales like $\frac{\xi}{\sqrt{t}}$ because the summand varies slowly (see equation (F.16)), and $w_{Q;-1} - w_{Q;0} \underset{t\to\infty}{\sim} \frac{1}{\sqrt{2t}}\Phi'_Q(0^-)$ which converges to zero. However, if we look a the order $\frac{1}{\sqrt{2t}}$, we find

$$0 = \left(\frac{1}{1-\mathrm{e}^{\lambda}} - \Phi_Q(0^-)\right)\Psi - \frac{\Phi'_Q(0^-)}{2} + \xi\left(\frac{\mathrm{e}^{-\lambda}\Phi_Q(0^+)}{1+(\mathrm{e}^{-\lambda}-1)\Phi_Q(0^+)} - \Phi_Q(0^-)\right), \tag{F.19}$$

where we have denoted

$$\Psi = \hat{\psi}_Q - \xi \ln[1+(\mathrm{e}^{-\lambda}-1)\Phi_Q(0^+)]. \tag{F.20}$$

In fact the last term in (F.19) is zero because of (7.25). Finally, doing the same for $\partial_t w_{Q;1}$, we find two boundary conditions:

$$\boxed{\Phi'_Q(0^{\pm}) = \mp 2\Psi\left(\frac{1}{1-\mathrm{e}^{\mp\lambda}} - \Phi_Q(0^{\pm})\right)}. \tag{F.21}$$

Appendix G

Interpretation of the closed equation

In this appendix, we give some physical insight into the cloed equations for the generalised profiles in the SEP (8.41, 8.43).

G.1 Projected dynamics

The closed equation (8.41, 8.43) can be interpreted as the long time limit of a decomposition of the evolution equation for the GDP-generating function $w_r(t)$ into a Markovian and a non-Markovian evolution. Indeed, let us write the evolution equation under the form:

$$\partial_t \langle w \rangle_r (t) = \frac{1}{2}\Delta w_r(t) + \partial_t \xi(t)(w_{r+1}(t) - w_r(t)) + N(r,t), \tag{G.1}$$

where $\xi(t) = \dfrac{\langle X_t e^{\lambda X_t} \rangle}{\langle e^{\lambda X_t} \rangle}$ and $N(r,t)$ is a non-Markovian dependance (with memory).

In the long time limit, under the scaling $v = r/\sqrt{2t}$, the time deivative $\partial_t \langle w \rangle_r (t)$, together with the Markovian part $\dfrac{1}{2}\Delta w_r(t) + \partial_t \xi(t)(w_{r+1}(t) - w_r(t))$ yield the left-hand side of our closed equation (8.41, 8.43) $\Phi''(v) + 2(v+\xi)\Phi'(v)$. Our closure can therofore be interpreted as the explicit form of the long time limit of the non-Markovian term, here for $v > 0$:

$$N(r,t) \underset{t\to\infty}{\sim} \int_0^\infty \mathrm{d}z\, \mathscr{G}(z) \frac{1 - \mathrm{e}^{\lambda}}{\Phi(0^+)} \Phi'(v)(v+z), \tag{G.2}$$

with the operator $\mathscr{G}(z) = z\Omega_-(-z)(1 - \mathscr{L}_-)$.

Here we presented the main idea in a schematic way, but it could be investigated further using a mode-coupling formalism.

G.2 Jump process

We prove that the two linear equations on $\Omega_\pm(v,\omega)$

$$\Omega_\pm(v,\omega) = \omega p(v) - \omega \int_{\mathbb{R}^\mp} p(v-z)\Omega_\pm(z,\omega)\mathrm{d}z, \tag{G.3}$$

where $p(v) = \dfrac{e^{-v^2}}{\sqrt{\pi}}$ are equivalent to the two bilinear equations (we do not write anymore the dependences of $\Omega_\pm$ on ω to lighten notations)

$$\Omega_\pm(v) = \omega p(v) - \omega \int_{\mathbb{R}^\mp} \Omega_\pm(v \pm z)\Omega_\mp(\mp z)\mathrm{d}z. \tag{G.4}$$

The idea, which comes from [193] consists in noticing that, since $\int_{\mathbb{R}} p(z)\mathrm{d}z = 1$ and $p(z) \geq 0$, $\Omega_\pm$ defined from equation (G.3) can be seen as generating functions of probabilities in a jump process:

$$\Omega_\pm(v) = -\sum_{n=1}^{+\infty}(-\omega)^n p_n^\pm(v), \tag{G.5}$$

where $p_n^\pm$ are defined from the following process. We consider a particle initially at $X_0 = 0$. At each step, it performs a jump on distance z distributed according to the probability density $p(z)$. Its position at step n is denoted by $X_n = Y_1 + ... + Y_n$, where Y_k are independent random variables with probability density $p(z)$.

We define $p_n^+(v)\mathrm{d}v$ as the probability that $X_1, ..., X_{n-1} < 0$ and $X_n \in [v, v + \mathrm{d}v[$ and $p_n^-(v)\mathrm{d}v$ is the probability $X_1, ..., X_{n-1} > 0$ and $X_n \in [v, \mathrm{d}v[$. We will denote:

$$p_n^+(v) = \mathbb{P}(X_1 < 0, ...X_{n-1} < 0, X_n = v), \tag{G.6}$$
$$p_n^-(v) = \mathbb{P}(X_1 > 0, ...X_{n-1} > 0, X_n = v). \tag{G.7}$$

Then, developing in powers of ω, we see that the fact that Ω_+ verify (G.4) is equivalent to having:

$$p_n^+(v) = \int_0^\infty p_{n-1}^+(v+z)p_1^-(-z) + p_{n-2}^+(v+z)p_2^-(-z) + ... + p_1^+(v+z)p_{n-1}^-(-z)\mathrm{d}z \tag{G.8}$$

As we proceed to show, this equation is true because it results from a partitioning on the step k for which X_k is the maximum of $\{X_1, ..., X_{n-1}\}$.

Let $k \in [\![1, n-1]\!]$, we have (because of independence of jumps):

$$\begin{aligned}\int_0^\infty p_{n-k}^+(v+z)p_k^-(-z)\mathrm{d}z &= \int_0^\infty \mathrm{d}z\mathbb{P}(X_1 \leq 0, ..., X_{n-k} = v+z)\mathbb{P}(X_1 \geq 0, ..., X_{k-1} \geq 0, X_k = -z)\\ &= \mathbb{P}(X_1 \geq 0, ..., X_{k-1} \geq 0, X_k \leq 0, X_{k+1} \leq X_k, ...X_{n-1} \leq X_k, X_n = v)\\ &= P_k. \end{aligned} \tag{G.9}$$

Then we rewrite the probabilities in terms of the jumps Y_i:

$$\begin{aligned}P_k = \int_{x_1,...x_k=0}^\infty \mathrm{d}^k\boldsymbol{x}\mathbb{P}(&Y_1 = x_1, Y_2 = x_2 - x_1, ..., Y_{k-1} = x_{k-1} - x_{k-2}, Y_k = -x_{k-1} - x_k,\\ &Y_{k+1} \leq 0, ..., Y_{k+1} + ... + Y_{n-1} \leq 0, Y_{k+1} + ... + Y_n = v + x_k)\end{aligned} \tag{G.10}$$

We use the independence of the jumps to reverse the order of the jumps from 1 to k; this does not change the probability:

$$\begin{aligned}P_k =& \int_{\boldsymbol{x}\in(\mathbb{R}^+)^k} \mathrm{d}^k\boldsymbol{x}\mathbb{P}(Y_1 = -x_{k-1} - x_k, Y_2 = x_{k-1} - x_{k-2}, ..., Y_{k-1} = x_2 - x_1, Y_k = x_1,\\ &\qquad Y_{k+1} \leq 0, ..., Y_{k+1} + ... + Y_{n-1} \leq 0, Y_{k+1} + ... + Y_n = v + x_k)\\ =& \int_{\boldsymbol{x}\in(\mathbb{R}^+)^k} \mathrm{d}^k\boldsymbol{x}\mathbb{P}(X_1 = -x_{k-1} - x_k, X_2 = -x_{k-2} - x_k, ..., X_{k-1} = -x_1 - x_k, X_k = -x_k,\\ &\qquad X_{k+1} \leq -x_k, ..., X_{n-1} \leq -x_k, X_n = v)\\ =&\mathbb{P}(X_1 \leq X_k, ..., X_{k-1} \leq X_k, X_k \leq 0, X_{k+1} \leq X_k, ...X_{n-1} \leq X_k, X_n = v).\end{aligned}$$

In other words:

$$P_k = \mathbb{P}\left(X_1 \leq 0, ..., X_{n-1} \leq 0, X_n = v, X_k = \max_{i\in[\![1,n-1]\!]} X_i\right). \tag{G.11}$$

Intuitively, this equality expresses the fact that saying that $X_k < 0$ is the maximum of the trajectory up to step $n-1$ is the same as saying that $X_{k+i} < X_k$ for $i \in [\![1, n-k-1]\!]$, and

Using the law of total probability we therefore have, as announced:

$$\mathbb{P}\left(X_1 \leq 0, ..., X_{n-1} \leq 0, X_n = v\right) = \sum_{k=1}^{n-1} P_k, \tag{G.12}$$

from which we conclude that Ω_+ verifies (G.4). The same reasoning give the result for Ω_-.

Appendix H

Discussion on the hydrodynamic duality relations

This appendix gives complementary information about the results mentioned in chapter 9.1. First, we prove that the mappings introduced in this chapter generate all possible mappings between single-file systems. Then, using the duality relation (Du), we prove that, in general, the variance and correlations of positions of particles in a single-file system can be fully characterised, in the hydrodynamic limit, by the Edwards-Wilkinson equation.

H.1 Characterisation of mappings between 1D diffusive systems

Here we investigate the possibility of existence of other mappings than the physical ones we presented ((Du), (Di), (T), (Rt)). We start from fields ρ and j verifying fluctuating hydrodynamics. We look for transformations of the following general form, linear with respect to the flux (the case of a non linear transformation of the flux generates difficulties concerning the random white noise):

$$\tilde{\rho}(k,t) = F(\rho(x_t(k), t/\tau)) \,, \tag{H.1}$$

$$\tilde{j}(k,t) = j(x_t(k), t/\tau) G(\rho(x_t(k), t/\tau)) \,, \tag{H.2}$$

In order that the new density $\tilde{\rho}$ and flux $\tilde{j}$ verify the conservation equation

$$\partial_t \tilde{\rho}(k,t) + \partial_k \tilde{j}(k,t) = 0 \,, \tag{H.3}$$

it is necessary that

$$\partial_k x_t(k) = \frac{F'(\rho(x_t(k'), t/\tau))}{\tau G(\rho(x_t(k'), t/\tau))} \,, \tag{H.4}$$

$$\partial_t x_t(k) = -j(x_t(k), t/\tau) \frac{G'(\rho(x_t(k), t/\tau))}{\tau G(\rho(x_t(k), t/\tau))} \,. \tag{H.5}$$

Then, from the stochastic Fourier law verified by (j, ρ) (9.2), we get the following stochastic Fourier law verified by $(\tilde{j}, \tilde{\rho})$

$$\tilde{j}(k,t) + \tilde{D}(\tilde{\rho}) \partial_k \tilde{\rho}(k,t) = \sqrt{\tilde{\sigma}(\tilde{\rho})} \eta_{t,k} \,, \tag{H.6}$$

where

$$\tilde{D}(x) = \tau \left(\frac{G^2}{F'^2} D \right) \circ F^{-1}(x) \,, \tag{H.7}$$

$$\tilde{\sigma}(x) = \tau^2 \left(\frac{|G|^3}{F'} \sigma \right) \circ F^{-1}(x) \,. \tag{H.8}$$

This mapping is not coherent for general F and G because of the compatibility condition $\partial_t \partial_k x_t(k) = \partial_k \partial_t x_t(k)$ which implies

$$\left(-\frac{jG' \circ \rho}{G \circ \rho} \partial_x \rho + \partial_t \rho \right) \left(\frac{F'' \circ \rho}{G \circ \rho} - \frac{F' \circ \rho G' \circ \rho}{(G \circ \rho)^2} \right) = - \frac{F' \circ \rho}{(G \circ \rho)^2} (-\partial_t \rho G' \circ \rho + j \partial_x \rho G'' \circ \rho) + \frac{(F' \circ \rho)(G' \circ \rho)^2}{(G \circ \rho)^3} j \partial_x \rho \,. \tag{H.9}$$

The factors in front of $j\partial_x \rho$ and $\partial_t \rho$ must vanish, so we get after simplifications,

$$G' F'' = F' G'' \,, \tag{H.10}$$

$$2 \frac{F' G'}{G} = F'' \,. \tag{H.11}$$

The only solutions to these equations are parameterised by $a, b, c, d \in \mathbb{R}$:

$$G(x) = \frac{1}{a + bx} \,, \tag{H.12}$$

$$F(x) = \begin{cases} c + \dfrac{d}{a + bx} & \text{if } b \neq 0 \,, \\ c + dx & \text{if } b = 0 \,. \end{cases} \tag{H.13}$$

The particular case $a = 0, b = -1, c = 0, d = -1, \tau = 1$ corresponds to the particles/gaps duality relation (Du). The transformation (T) is recovered by taking $a = 1, b = 0, d = 1, \tau = 1$ and (Di) by taking $a = 1/d, b = 0, c = 0, \tau = 1$. The time rescaling (Rt) is the case $a = \tau, b = 0, c = 0, d = 1$. Conversely, by composing the four transformations, we can reconstruct any possible transformation of the form (H.1,H.2,H.4,H.5). For the case $b = 0$ in (H.13), one can perform (in this order) (Du), (Di), (Du), (Di), (T), (Rt) and for the other case, (Di), (Du), (Di), (T), (Du), (T), (Rt) generates all the possibilities.

H.2 Edwards-Wilkinson equation for the fluctuations of position of tracers

In this appendix, we use the duality 9.1 in order to describe the correlations between the positions of the particles in the SEP using Edward-Wilkinson equations, similarly to what is done in [200]. We consider the SEP with flat initial density ρ_0, so that the mean density remains ρ along time.

We define the rescaled macroscopic density in the SEP, where $x_k(t)$ are the positions of particles at time t; $\rho(x,t) = \frac{1}{N} \sum_r \delta(x - x_k(tN^2)/N)$. Its dual field $\tilde{\rho}$ under transformation (Du) 9.1 verifies:

$$\partial_t \tilde{\rho} = \partial_k \left(\tilde{D}(\tilde{\rho}) \partial_k \tilde{\rho} \right) + \partial_k (\sqrt{\tilde{\sigma}(\tilde{\rho}) N^{-1}} \, \xi_{k,t}), \tag{H.14}$$

with $\tilde{D}(\tilde{\rho}) = \dfrac{1}{2\tilde{\rho}^2}$ et $\tilde{\sigma}(\tilde{\rho}) = 1 - \dfrac{1}{\tilde{\rho}}$ and mean density $\langle \tilde{\rho}(k,t) \rangle = 1/\rho_0$. Equation (H.14) in fact expresses the large deviations of the density field $\tilde{\rho}$. From it, we can extract a central limit theorem for the fluctuations field $\kappa(k,t)$ defined by:

$$\tilde{\rho}(k,t) = \frac{1}{\rho_0} + \frac{\kappa(k,t)}{\sqrt{N}}. \tag{H.15}$$

Injecting definition (H.15) in the large deviation principle (H.14) and considering dominant order in N (order $N^{-1/2}$), we get the stochastic linear partial differential equation:

$$\partial_t \kappa = \tilde{D}(1/\rho_0)\partial_k^2 \kappa + \partial_k(\sqrt{\tilde{\sigma}(1/\rho_0)}\xi_{x,t}). \tag{H.16}$$

According to equation (9.21), we can relate the displacement $d(k,t)$ of particles $x_{kN}(tN^2)$ in the SEP to the dual field $\tilde{\rho}$ and associated current $\tilde{j} = -\tilde{D}(\tilde{\rho})\partial_k\tilde{\rho} - \sqrt{\tilde{\sigma}(\tilde{\rho})N^{-1}}\ \xi_{k,t}$.

$$\begin{aligned} d(k,t) &= x_{kN}(tN^2)/N - k/\rho_0 \\ &= -\int_0^t \tilde{j}(0,t')\mathrm{d}t' + \int_0^k \tilde{\rho}(k',t)\mathrm{d}k' - k/\rho_0 \\ &= -\int_0^\infty \tilde{\rho}(k',t) - \tilde{\rho}(k',t)\mathrm{d}k' + \int_0^k \tilde{\rho}(k',t)\mathrm{d}k' - k/\rho_0 \end{aligned} \tag{H.17}$$

On average, $\langle d(k,t) \rangle = 0$, and if one looks at the fluctuation field $h(k,t)$ defined by:

$$d(k,t) = 0 + \frac{h(k,t)}{\sqrt{N}}, \tag{H.18}$$

then, from equations (H.15) and (H.17):

$$h(k,t) = -\int_0^\infty \kappa(k',t) - \kappa(k',0)\mathrm{d}k' + \int_0^k \kappa(k',t)\mathrm{d}k'. \tag{H.19}$$

As a consequence, $\partial_k h = \kappa$ and $\partial_t h = -\int_k^\infty \partial_t\kappa(k',t)\mathrm{d}k'$. Combined with (H.16) (supposing a vanishing current at infinity), this yields:

$$\partial_t h(k,t) = \frac{\rho_0^2}{2}\partial_k^2 h(k,t) + \sqrt{1-\rho_0}\ \xi_{k,t} \tag{H.20}$$

Finally, k represents the label of particles, we can go back to a spatial parameter by defining $x = k/\rho_0$, because the mean position of the k-th particle at density ρ_0 is indeed k/ρ_0. Performing this change of variable, without forgetting that $\xi_{\rho_0 x,t} = 1/\sqrt{\rho_0}\ \xi_{x,t}$:

$$\partial_t h(x,t) = \frac{1}{2}\partial_x^2 h(x,t) + \sqrt{\frac{1-\rho_0}{\rho_0}}\ \xi_{x,t}, \tag{H.21}$$

which is the equation proposed in [133, 200] based on heuristic arguments.

More generally, the fluctuations of positions of particles in any system of particles with transport coefficients D and σ, at mean density ρ_0, can by characterised by this equation:

$$\boxed{\partial_t h(x,t) = D(\rho_0)\partial_x^2 h(x,t) + \frac{\sqrt{\sigma(\rho_0)}}{\rho_0}\ \xi_{x,t}}, \tag{H.22}$$

which can be solved both for quenched and anealed initial conditions. If $x_k(t)$ is the position of particle k at time t, with $\langle x_k(t) \rangle = k/\rho_0$, then:

$$\boxed{\left\langle \frac{x_i(\tau) - \langle x_i(\tau)\rangle}{\sqrt{t}} \frac{x_j(\tau') - \langle x_j(\tau')\rangle}{\sqrt{t}} \right\rangle \underset{t\to\infty}{\sim} \left\langle h\left(\frac{i}{\sqrt{t}}, \frac{\tau}{t}\right) h\left(\frac{j}{\sqrt{t}}, \frac{\tau'}{t}\right) \right\rangle}. \tag{H.23}$$

Appendix I

Supplements on the hydrodynamic description of a biased system

In this appendix, we provide additional details and further discussion on points which where raised in section 10.1.

I.1 Examples of bias matching conditions

We first give an example to show why it is necessary to understand the properties of the stationary measures. Then we study the stationary measures in the example of the SEP with a biased tracer and a mass transfer process with a biased bond.

I.1.1 Vanishing velocity of a biased tracer is not enough

In the context of single-file systems with a biased tracer (chapter 10), one may be tempted to determine the bias matching condition (10.3) using the fact that the velocity of the tracer at equilibrium must vanish. We show here, with the example of the DEP, that it is necessary to know the stationnary measure to determine this condition.

We consider the DEP (Double Exclusion Process 6.1.2) with a baised tracer, namely the tracer attempts a jump to the right with rate p and to the left with rate q, the other particles remaining symmetric, with the constraint that there must always be one empty site between two particles. The means position of the tracer $\langle X_t \rangle$ verifies:

$$\partial_t \langle X_t \rangle = p(1 - \langle \eta_{X_t+2} \rangle) - q(1 - \langle \eta_{X_t-2} \rangle). \tag{I.1}$$

One may therefore imagine that, if there is a local equilibrium around the tracer, the mean density in front of and behind the tracer would be $\rho(X_t^{\pm}, t) = \langle \eta_{X_t \pm 2} \rangle$, leading to the bias condition:

$$p(1 - \rho(X_t^+, t)) - q(1 - \rho(X_t^-, t)) = 0. \tag{I.2}$$

This would be completely wrong since it neglects correlations that may exist between sites at equilibrium. Indeed, in the present case, the site of the tracer is always occupied, and since the DEP displays nonzero correlations between sites, $\langle \eta_{X_t-2} \rangle$ is in fact equal, like in equation (D.2), to the conditional average $\langle \eta_2 | \eta_0 = 1 \rangle_{(\rho_-, \rho_+)}$ with respect to an equilibrium measure of density ρ_- on negative sites and ρ_+ on positive sites.

The only way to compute this conditional average is to know precisely what is the stationary measure. In the example of the DEP, it can easily be obtained, for example, as the $\epsilon = 1$

case of the KLS (defined in 6.1.2, bias condition given in 10.2.1). The correct bias relation is therefore:

$$p\frac{1-2\rho(X_t^+,t)}{1-\rho(X_t^+,t)} - q\frac{1-2\rho(X_t^-,t)}{1-\rho(X_t^-,t)} = 0. \tag{I.3}$$

I.1.2 Example of the SEP with a biased tracer

We recall the master equation for the probability to find, at time t, the tracer at position X and the bath in configuration (η_r) ($\eta_r = 1$ if site r is occupied by a bath particle, 0 otherwise):

$$\begin{aligned}\partial_t P(X,\eta,t) = \frac{1}{2}\sum_{r\neq X,X-1}\left[P(X,\eta^{r,+},t) - P(X,\eta,t)\right] \\ + \sum_{\mu=\pm1}\frac{1+\mu s}{2}\left\{(1-\eta_X)P(X-\mu,\eta,t) - (1-\eta_{X+\mu})P(X,\eta,t)\right\}.\end{aligned} \tag{I.4}$$

The occupation numbers in the reference frame of the tracer are denoted by $\tau_r = \eta_{X_t+r}$. They obey the following master equation, where $\tau = \{\tau_r = 0,1\}$:

$$\begin{aligned}\partial_t \mathbb{P}(\tau,t) = \frac{1}{2}\sum_{r\neq 0,-1}\left[\mathbb{P}(\tau^{r,+},t) - \mathbb{P}(\tau,t)\right] \\ + \sum_{\mu=\pm1}\frac{1+\mu s}{2}\left\{(1-\tau_{-\mu})\mathbb{P}(T^\mu\tau,t) - (1-\tau_\mu)\mathbb{P}(\tau,t)\right\}.\end{aligned} \tag{I.5}$$

We denoted by $T^\mu\tau$ the configuration obtained from τ by translating occupation numbers of $-\mu$ for $r \neq \mu$, namely $(T^\mu\tau)_r = \tau_{r-\mu}$, and choosing $(T^\mu\tau)_\mu = 0$. The first line corresponds to an event of exchange of occupation numbers of two sites occupied by bath particles, and the second line to a displacement of the tracer particle. The first term in the right-hand side of (I.5) will vanish for probabilities of the form

$$\mathbb{P}(\tau,t) = \prod_{r<0}\rho_-^{\tau_r}(1-\rho_-)^{1-\tau_r}\prod_{r>0}\rho_+^{\tau_r}(1-\rho_+)^{1-\tau_r}. \tag{I.6}$$

For $(T^\mu\tau)$ with $\mu = \pm1$, we get:

$$\mathbb{P}(T^\mu\tau,t) = \prod_{r<0}\rho_-^{\tau_{r-\mu}}(1-\rho_-)^{1-\tau_{r-\mu}}\prod_{r>0}\rho_+^{\tau_{r-\mu}}(1-\rho_+)^{1-\tau_{r-\mu}} = \mathbb{P}(\tau,t)\times\frac{1-\rho_\mu}{\rho_\mu^{\tau_\mu}(1-\rho_\mu)^{1-\tau_\mu}}. \tag{I.7}$$

In order that the second term vanishes, we therefore need to have for any configuration τ:

$$\sum_{\mu=\pm1}\frac{1+\mu s}{2}\left\{(1-\tau_{-\mu})\frac{1-\rho_\mu}{\rho_\mu^{\tau_\mu}(1-\rho_\mu)^{1-\tau_\mu}} - (1-\tau_\mu)\right\} = 0. \tag{I.8}$$

This implies that (I.6) is a stationary measure if it verifies:

$$\sum_{\mu=\pm1}\frac{1+\mu s}{2}\mu(1-\rho_\mu) = 0. \tag{I.9}$$

In the hydrodynamic limit, there must exist a local equilibrium around the tracer particle. Therefore, in a small neighbourhood around the tracer, the occupations in the reference frame of the tracer follow a stationary measure of the form (I.6). Then, if we compute the mean densities $\lim_{N\to\infty}\sum_{r=1}^N\frac{\langle\tau_r\rangle}{N} = \rho(X_t^+,t)$ and $\lim_{N\to\infty}\sum_{r=1}^N\frac{\langle\tau_{-r}\rangle}{N} = \rho(X_t^-,t)$ according to the stationary measure (I.6), we get from (I.9) the matching condition obeyed by the hydrodynamic density profile:

$$\boxed{(1+s)(1-\rho(X_t^+,t)) - (1-s)(1-\rho(X_t^-,t)) = 0}, \tag{I.10}$$

which is the explicit writing of the general equation (10.3) in the specific case of the SEP.

Biased bond in a mass transfer process

Here we recover, by applying the general procedure described in 10.1, the bias condition which is given in [114] in a particular case.

We recall the master equation for the probability density $P(\eta, t)$ to find the system in configuration η at time t is (see [89] for an extensive study of mass transfer processes):

$$\partial_t P(\eta,t) = \frac{1}{2}\sum_{r\neq 0}[2P(\eta^r,t) - 2P(\eta,t)] + 2(p + (q-p)\mathbb{1}_{\mathbb{R}^+}(\eta_1 - \eta_0))P(\eta^0,t) - (p+q)P(\eta,t). \tag{I.11}$$

The configuration η^r is defined as follows:

- For all $x \neq r, r+1$, $\eta^r_x = \eta_x$
- If $\eta_{r+1} > \eta_r$, then $\eta^r_r = 2\eta_r$ and $\eta^r_{r+1} = \eta_{r+1} - \eta_r$.
- If $\eta_{r+1} \leq \eta_r$, then $\eta^r_{r+1} = 2\eta_{r+1}$ and $\eta^r_r = \eta_r - \eta_{r+1}$.

This process has the remarkable property that moments of the distributions associated to the probability density P verify closed equations [89]. In particular, for the mean mass, we find:

$$\begin{aligned}\partial_t \langle \eta_r(t)\rangle =& (1-\delta_{r,0}-\delta_{r,1})\frac{1}{2}\left(\frac{\langle\eta_{r+1}(t)\rangle}{2} + \frac{\langle\eta_{r-1}(t)\rangle}{2} - 2\frac{\langle\eta_r(t)\rangle}{2}\right)\\ &+ \delta_{r,0}\left(\frac{1}{2}\frac{\langle\eta_{-1}(t)\rangle}{2} + p\frac{\langle\eta_1(t)\rangle}{2} - \left(\frac{1}{2}+q\right)\frac{\langle\eta_0(t)\rangle}{2}\right)\\ &+ \delta_{r,1}\left(\frac{1}{2}\frac{\langle\eta_2(t)\rangle}{2} + q\frac{\langle\eta_0(t)\rangle}{2} - \left(\frac{1}{2}+p\right)\frac{\langle\eta_1(t)\rangle}{2}\right).\end{aligned} \tag{I.12}$$

The stationary solutions to this equation are of the form:

$$\langle \eta_r(t)\rangle = \rho_-\left(1 + \left(\frac{q}{p} - 1\right)\mathbb{1}_{\mathbb{N}^*}(r)\right), \tag{I.13}$$

for any $\rho_- > 0$. The hydrodynamic density must verify $\rho(0^-,t) = \lim_{N\to\infty}\sum_{r=0}^{N}\frac{\langle\eta_{-r}\rangle}{N} = \rho_-$ and $\rho(0^+,t) = \lim_{N\to\infty}\sum_{r=1}^{N}\frac{\langle\eta_r\rangle}{N} = \frac{q}{p}\rho_-$. This yields the bias matching condition used in [114]:

$$\boxed{p\rho(0^+,t) - q\rho(0^-,t) = 0}, \tag{I.14}$$

which is the explicit writing of the general equation (10.4) in the present system.

I.2 MFT equations for a biased system

Here we discuss the MFT equations (*i.e.* the deterministic coupled diffusion equations (10.18)) which can be obtained from the hydrodynamic description with a bias matching condition (which was absent in the symmetric case (8.21)).

I.2.1 Resolution of the optimisation problem

To find the path of least action under the constraints (10.11, 10.14, 10.15), we introduce the Lagrangian $\mathcal{L}$ and a Lagrange multiplier $\hat{\rho}$ enforcing the conservation equation (10.11):

$$\begin{aligned}\mathcal{L}(\rho,j,\hat{\rho}) &= \int_0^1\int_{-\infty}^{\infty}\frac{\left(j+D(\rho)\partial_x\rho\right)^2}{2\sigma(\rho)}+\hat{\rho}(\partial_t\rho+\partial_x j)\mathrm{d}x\mathrm{d}t+F[\rho(x,0)]-\lambda Q_1[\rho]\\ &= \int_0^1\int_{-\infty}^{\infty}\frac{\left(j+D(\rho)\partial_x\rho\right)^2}{2\sigma(\rho)}-\rho\partial_t\hat{\rho}-j\partial_x\hat{\rho}\mathrm{d}x\mathrm{d}t+\int_0^1\left[j\hat{\rho}(x,t)\right]_{x=0^+}^{x=0^-}\mathrm{d}t\\ &\quad+\int_{-\infty}^{\infty}\hat{\rho}(x,1)\rho(x,1)-\hat{\rho}(x,0)\rho(x,0)\mathrm{d}x+F[\rho(x,0)]-\lambda Q_1[\rho]. \end{aligned}\tag{I.15}$$

We performed integration by parts, and we did not suppose $\hat{\rho}$ continuous at 0. But, since j is continuous at 0:

$$\frac{\delta\mathcal{L}}{\delta j(0,t)}=\hat{\rho}(0^-,t)-\hat{\rho}(0^+,t).\tag{I.16}$$

The main difference with the unbiased case lies in the computation of the ρ derivative of the term

$$\mathcal{M}[\rho,j]=\int_0^1\int_{-\infty}^{\infty}\frac{\left(j+D(\rho)\partial_x\rho\right)^2}{2\sigma(\rho)}\mathrm{d}x\mathrm{d}t,\tag{I.17}$$

because of the bias matching condition (10.14) on ρ, which generates boundary terms in the integration by parts. Indeed, we compute $\delta\mathcal{M}=\mathcal{M}[\rho+\delta\rho,j]-\mathcal{M}[\rho,j]$:

$$\begin{aligned}\delta\mathcal{M} &= \int_0^1\int_{-\infty}^{\infty}\frac{2(\delta\rho D'(\rho)\partial_x\rho+D(\rho)\partial_x(\delta\rho))\left(j+D(\rho)\partial_x\rho\right)}{2\sigma(\rho)}-(\delta\rho)\sigma'(\rho)\frac{\left(j+D(\rho)\partial_x\rho\right)^2}{2\left(\sigma(\rho)\right)^2}\mathrm{d}x\mathrm{d}t\\ &= \int_0^1\int_{-\infty}^{\infty}(\delta\rho)\left[\frac{2D'(\rho)\partial_x\rho\left(j+D(\rho)\partial_x\rho\right)}{2\sigma(\rho)}-\sigma'(\rho)\frac{\left(j+D(\rho)\partial_x\rho\right)^2}{2\left(\sigma(\rho)\right)^2}\right.\\ &\quad\left.-\partial_x\left(D(\rho)\frac{2\left(j+D(\rho)\partial_x\rho\right)}{2\sigma(\rho)}\right)\right]\mathrm{d}x\mathrm{d}t+\int_0^1\left[(\delta\rho)D(\rho)\frac{\left(j+D(\rho)\partial_x\rho\right)}{\sigma(\rho)}(x,t)\right]_{x=0^+}^{0^-}\mathrm{d}t\end{aligned}\tag{I.18}$$

Because of the bias condition (10.14) verified by ρ and $\rho+\delta\rho$ (we only consider density fields verifying this relation), we have:

$$\delta\rho(0^-,t)\partial_-B(\rho(0^-,t),\rho(0^+,t))+\delta\rho(0^+,t)\partial_+B(\rho(0^-,t),\rho(0^+,t))=0,\tag{I.19}$$

where $\partial_\pm B=\frac{\partial B(\rho_-,\rho_+)}{\partial\rho_\pm}$. Therefore:

$$\begin{aligned}\left[(\delta\rho)D(\rho)\frac{\left(j+D(\rho)\partial_x\rho\right)}{\sigma(\rho)}(x,t)\right]_{x=0^-}^{0^+} &= \delta\rho(0^+,t)\left[\frac{D(\rho)\left(j+D(\rho)\partial_x\rho\right)}{\sigma(\rho)}(0^+,t)\right.\\ &\quad\left.+\frac{\partial_+B}{\partial_-B}D(\rho)\frac{\left(j+D(\rho)\partial_x\rho\right)}{\sigma(\rho)}(0^-,t)\right].\end{aligned}\tag{I.20}$$

Finally, we denote by (q,j^*,p) the solution to the optimisation problem under constraint for $(\rho,j,\hat{\rho})$. The vanishing of $\frac{\delta\mathcal{L}}{\delta j(x,t)}$ imposes $j^*=-D(q)\partial_x q+\sigma(q)\partial_x p$. Together with the conservation equation (10.11) and the vanishing of the derivatives $\frac{\delta\mathcal{L}}{\delta\rho(x,t)}$, $\frac{\delta\mathcal{L}}{\delta\rho(x,0)}$, $\frac{\delta\mathcal{L}}{\delta\rho(x,1)}$, this yields the classical MFT equations given in section 10.1.2 (10.18).

In addition to that, there are boundary conditions, which are specific to the biased case. They are obtained from the bias condition (10.14), the continuity of current (10.15) with $j^*=-D(q)\partial_x q+\sigma(q)\partial_x p$, the vanishing of $\frac{\delta\mathcal{L}}{\delta j(0,t)}$ (I.16), and the vanishing of $\frac{\delta\mathcal{L}}{\delta\rho(0^+,t)}$ (using (I.20)). They are given in section 10.1.2 (10.19).

I.2.2 New mapping for the MFT equations

We consider a system with transport coefficients $D(\rho)$ and $\sigma(\rho)$. We denote by (q, j, p) the optimal fields for the cumulant generating function of the tracer's position in this system (equation (10.17) where we replace Q_1 by X_1 defined in (10.2)).

We denote by $(\tilde{q}, \tilde{j}, \tilde{p})$ the optimal fields for the integrated current's cumulant generating function (10.17) in the dual system under the duality relation (Du) 9.1.1. The tracer's position in the original system is equal to the integrated current through the origin in the dual one. Therefore, the fields $(\tilde{q}, \tilde{j}, \tilde{p})$ verify MFT equations (10.18) and boundary conditions (10.19), with the dual transport coefficients $\tilde{D}$ and $\tilde{\sigma}$ (see table 9.1, (Du), for their expressions in terms of D, σ). The new mapping begins, identically to the duality 9.1.1, by relating the densities of the dual system and of the original one:

$$q(x_k(t), t) = \frac{1}{\tilde{q}(k, t)}, \tag{I.21}$$

$$x_k(t) = x_0(t) + \int_0^k \tilde{q}(k', t)\mathrm{d}k', \tag{I.22}$$

$$x_0(t) = -\int_0^t \tilde{j}(0, t)\mathrm{d}t = \int_0^t \tilde{D}(\tilde{q})\partial_k\tilde{q} - \tilde{\sigma}(\tilde{q})\partial_k\tilde{q}(0, t)\mathrm{d}t. \tag{I.23}$$

The difference is that instead of mapping the dual current $\tilde{j}$ to the original one j using the duality 9.1.1, which would correspond to $\partial_x p(x_k(t), t) = -\partial_k\tilde{p}(k, t)$, we rather define a new field:

$$\pi(x_k(t), t) = -\tilde{p}(k, t). \tag{I.24}$$

The main interest of this new field is that it does not involve derivatives, so there is no integration constant to fix in order to go from $\tilde{p}$ to π.

These new variables verify the following equations, where we indeed recovered the original transport coefficients $D(\rho)$ and $\sigma(\rho)$:

$$\begin{aligned}
\partial_t q &= \partial_x(D(q)\partial_x q) - \partial_x\left(\frac{\sigma(q)}{q}\partial_x\pi\right), \\
\partial_t\pi &= -D(q)\partial_x^2\pi + 2\frac{D(q)}{q}(\partial_x\pi)(\partial_x q) - \frac{\sigma(q) + q\sigma'(q)}{2q^2}(\partial_x\pi)^2, \\
\pi(x, T) &= -\lambda\Theta(x), \\
\pi(x, 0) &= -\lambda\Theta(x) + \int_{\rho_0(x)}^{q(x,0)} \frac{2rD(r)}{\sigma(r)}\mathrm{d}r,
\end{aligned} \tag{I.25}$$

and the modified boundary conditions at the position of the tracer in the original system $X_t = x_0(t)$ which can be recovered using equations (10.2):

$$\begin{aligned}
\pi(X_t^+, t) - \pi(X_t^-, t) &= 0, \\
B(1/q(X_t^+, t), 1/q(X_t^-, t)) &= 0, \\
\left[\frac{D(q)\partial_x q - \sigma(q)/q(\partial_x\pi)}{q}(x, t)\right]_{x=X_t^-}^{X_t^+} &= 0, \\
\partial_- BD(q)q\partial_x\pi(X_t^+, t) + \partial_+ BD(q)q\partial_x\pi(X_t^-, t) &= 0,
\end{aligned} \tag{I.26}$$

where $\partial_- B, \partial_+ B$ are evaluated at $\left(\frac{1}{q(X_t^-, t)}, \frac{1}{q(X_t^+, t)}\right)$. Note that equations (10.2) and (I.25) imply:

$$\frac{\mathrm{d}X_t}{\mathrm{d}t} = \frac{D(q)\partial_x q - \sigma(q)/q(\partial_x\pi)}{q}(x, t). \tag{I.27}$$

These equations will be particularly useful for our study of the SEP 10.3.

I.3 Resolution of the MFT equations

In this section, we first solve the MFT equation (10.18, 10.19) in a particular case. Then, we solve their expansion at order 1 in λ for arbitrary transport coefficients and bias relation (10.4), in the case where the system is initially at equilibrium.

I.3.1 Resolution for simple transport coefficients

If we consider transport coefficients $D = 1$ and $\sigma(\rho) = 2\rho$, we can easily solve the associated MFT equations (10.18) with boundary conditions (10.19) for the integrated current through the origin when the bias relation is $aq(0^+, t) - bq(0^-, t) = 0$. We consider step initial condition with density ρ_- to the left of the origin and ρ_+ to the right.

The usual method [102, 107] consists in perfoming a Cole-Hopf transformation by defining $P = e^p$ and $Q = qe^{-p}$, which then verify decoupled equations:

$$\partial_t P + \partial_x^2 P = 0, \tag{I.28}$$
$$\partial_t Q - \partial_x^2 Q = 0, \tag{I.29}$$

with boundary conditions:

$$aQ(0^+, t) = bQ(0^-, t), \tag{I.30}$$
$$\partial_x Q(0^+, t) - \partial_x Q(0^-, t) = 0, \tag{I.31}$$
$$a\partial_x P(0^-, t) = b\partial_x P(0^+, t), \tag{I.32}$$
$$P(0^-, t) = P(0^+, t), \tag{I.33}$$

and initial conditions:

$$P(x, 1) = \exp(\lambda\Theta(x)), \tag{I.34}$$
$$Q(x, 0) = \rho_\pm \exp(-\lambda\Theta(x)). \tag{I.35}$$

Given the form of the equations, we will suppose, in the following, $a + b = 1$ without loss of generality (we can always divide (I.30, I.32) by $(a + b)$).

For P, looking for a solution of the form $e^\lambda + \alpha \operatorname{erfc}\left(\frac{x}{2\sqrt{1-t}}\right)$ for $x > 0$ and $1 + \beta \operatorname{erfc}\left(-\frac{x}{2\sqrt{1-t}}\right)$ for $x < 0$, we find:

$$P(x > 0, t) = e^\lambda - \left(e^\lambda - 1\right) a \operatorname{erfc}\left(\frac{x}{2\sqrt{1-t}}\right), \tag{I.36}$$
$$P(x < 0, t) = 1 + \left(e^\lambda - 1\right) b \operatorname{erfc}\left(-\frac{x}{2\sqrt{1-t}}\right). \tag{I.37}$$

For Q, we use the same Green function as in [114] which enforces the discontinuity (I.30):

$$G(x, z, t) = \frac{\operatorname{sign}(x)(b-a)e^{-\frac{(|z|+|x|)^2}{4t}}}{2\sqrt{\pi}\sqrt{t}} + \frac{e^{-\frac{(x-z)^2}{4t}}}{2\sqrt{\pi}\sqrt{t}}. \tag{I.38}$$

This yields:

$$Q(x > 0, t) = e^{-\lambda}\left(\rho_+ - \operatorname{erfc}\left(\frac{x}{2\sqrt{t}}\right)\left(e^\lambda(a-1)\rho_- + a\rho_+\right)\right), \tag{I.39}$$
$$Q(x < 0, t) = \operatorname{erfc}\left(-\frac{x}{2\sqrt{t}}\right)\left(e^{-\lambda}a\rho_+ + (a-1)\rho_-\right) + \rho_-. \tag{I.40}$$

I.3.2 First order of MFT equations in the biased case

Writing expansions in the parameter λ:

$$q = q_0 + \lambda q_1 + O(\lambda^2)^2, \tag{I.41}$$
$$p = p_0 + \lambda p_1 + O(\lambda^2)^2, \tag{I.42}$$

and injecting them in MFT equations (10.18) with boundary conditions (10.19), we get at order 0:

$$p_0 = 0, \tag{I.43}$$
$$\partial_t q_0 = \partial_x (D(q_0)\partial_x q_0), \tag{I.44}$$
$$q_0(x,0) = \rho_0(x), \tag{I.45}$$
$$B\left(q_0(0^-,t), q_0(0^+,t)\right) = 0, \tag{I.46}$$
$$[D(q_0)\partial_x q_0(x,t)]_{x=0^-}^{0^+} = 0. \tag{I.47}$$

At order 1, we have:

$$\partial_t q_1 = \partial_x^2 (D(q_0)q_1) - \partial_x \left(\sigma(q_0)\partial_x p_1\right), \tag{I.48}$$
$$\partial_t p_1 = -D(q_0)\partial_x^2 p_1, \tag{I.49}$$
$$p_1(x,0) = \Theta(x) + q_1(x,0)\frac{2D(\rho_0(x))}{\sigma(\rho_0(x))}, \tag{I.50}$$
$$p_1(x,1) = \Theta(x), \tag{I.51}$$

with boundary conditions:

$$\partial_- B q_1(0^-,t) + \partial_+ B q_1(0^+,t) = 0, \tag{I.52}$$
$$[\partial_x (D(q_0)q_1) - \sigma(q_0)\partial_x p_1(x,t)]_{x=0^-}^{0^+} = 0, \tag{I.53}$$
$$p_1(0^+,t) - p_1(0^-,t) = 0, \tag{I.54}$$
$$\partial_- B D(q_0)\partial_x p_1(0^+,t) + \partial_+ B D(q_0)\partial_x p_1(0^-,t) = 0. \tag{I.55}$$

Here $\partial_\pm B$ are evaluated at $(q_0(0^-,t), q_0(0^+,t))$. In the case where the initial density $\rho_0(x) = \rho_- + (\rho_+ - \rho_-)\Theta(x)$ is an equilibrium measure, namely $B(\rho_-,\rho_+) = 0$, then it is straightforward to see that $q_0(x,t) = \rho_0(x)$ for all times t. As a consequence, the equations at order 1 simplify:

$$\partial_t q_1 = D(\rho_0(x))\partial_x^2(q_1) - \sigma(\rho_0(x)\partial_x^2 p_1, \tag{I.56}$$
$$\partial_t p_1 = -D(\rho_0(x))\partial_x^2 p_1, \tag{I.57}$$
$$p_1(x,0) = \Theta(x) + q_1(x,0)\frac{2D(\rho_0(x))}{\sigma(\rho_0(x))}, \tag{I.58}$$
$$p_1(x,1) = \Theta(x), \tag{I.59}$$

with boundary conditions:

$$\partial_- B q_1(0^-,t) + \partial_+ B q_1(0^+,t) = 0, \tag{I.60}$$
$$[D(\rho_0(x))\partial_x q_1 - \sigma(\rho_0(x))\partial_x p_1(x,t)]_{x=0^-}^{0^+} = 0, \tag{I.61}$$
$$p_1(0^+,t) - p_1(0^-,t) = 0, \tag{I.62}$$
$$\partial_- B D(q_0)\partial_x p_1(0^+,t) + \partial_+ B D(q_0)\partial_x p_1(0^-,t) = 0, \tag{I.63}$$

where now $\partial_\pm B$ are evaluated at (ρ_-, ρ_+), in particular, they are constant, which makes the resolution much simpler. The analytical resolution of these equations relies on two ingredients, largely inspired by [114]. First, p_1 is found under the form:

$$p_1(x>0,t) = 1 + a\,\mathrm{erfc}\left(\frac{x}{\sqrt{4D(\rho_+)(1-t)}}\right), \tag{I.64}$$

$$p_1(x<0,t) = b\,\mathrm{erfc}\left(\frac{-x}{\sqrt{4D(\rho_-)(1-t)}}\right). \tag{I.65}$$

Then the equation on q_1 is solved using a Green function similar to equation (I.38), also used in [114]. Here, it is more complicated because of the different diffusion coefficient on $\mathbb{R}^\pm$. The idea is to find a Green function $G(t,x,z)$ verifying the following properties:

$$\partial_t G - D(\rho_0(x))\partial_x^2 G = \delta(t)\delta(z-x), \tag{I.66}$$

$$\partial_- B G(0^-,t) + \partial_+ B G(0^+,t) = 0, \tag{I.67}$$

$$D(\rho_+)\partial_x G(0^+,t) - D(\rho_-)\partial_x G(0^-,t) = 0. \tag{I.68}$$

The first condition allows to get a solution to the non-homogeneous diffusion equation with initial condition and with different diffusion coefficients on $\mathbb{R}^\pm$. The other two conditions enforce the boundary relation at 0. We solved equations (I.68) to find G using a Laplace transform in time. This yielded for example for $x>0$:

$$G(t,x>0,z>0) = \frac{e^{-\frac{(x+z)^2}{4D_+ t}}\left(\partial_+ B D_-\left(e^{\frac{xz}{D_+ t}}-1\right) - \partial_- B\sqrt{D_- D_+}\left(e^{\frac{xz}{D_+ t}}+1\right)\right)}{2\sqrt{\pi}\sqrt{D_- D_+ t}\left(\partial_+ B\sqrt{D_-} - \partial_- B\sqrt{D_+}\right)}, \tag{I.69}$$

$$G(t,x>0,z<0) = \frac{\partial_- B\sqrt{\frac{D_+}{t}}e^{\frac{xz}{2t\sqrt{D_- D_+}} - \frac{D_- x^2 + D_+ z^2}{4D_- D_+ t}}}{\sqrt{\pi}\left(\partial_- B D_+ - \partial_+ B\sqrt{D_- D_+}\right)}, \tag{I.70}$$

where we denoted $D_\pm = D(\rho_\pm)$. Using these two ingredient, we obtain the result given in section 10.2.3.

Bibliography

[1] C. Bechinger, R. Di Leonardo, H. Löwen, C. Reichhardt, G. Volpe, and G. Volpe, Rev. Mod. Phys. **88**, 045006 (2016).

[2] A. Zöttl and H. Stark, J. Phys. Condens. Matter **28**, 253001 (2016).

[3] P. Romanczuk, M. Bär, W. Ebeling, B. Lindner, and L. Schimansky-Geier, European Physical Journal: Special Topics **202**, 1 (2012).

[4] J. Tailleur and M. E. Cates, Europhys. Lett. **86** (2009), 10.1209/0295-5075/86/60002.

[5] M. E. Cates and J. Tailleur, Europhys. Lett. **101**, 20010 (2013).

[6] K. Malakar, V. Jemseena, A. Kundu, K. V. Kumar, S. Sabhapandit, S. N. Majumdar, S. Redner, and A. Dhar, J. Stat. Mech. , 043215 (2018).

[7] M. J. Schnitzer, Physical Review E **48**, 2553 (1993).

[8] K. Martens, L. Angelani, R. Di Leonardo, and L. Bocquet, The European Physical Journal E **35**, 1 (2012).

[9] C. Kurzthaler, S. Leitmann, and T. Franosch, Scientific Reports **6**, 36702 (2016).

[10] U. Basu, S. N. Majumdar, A. Rosso, and G. Schehr, Physical Review E **98**, 1 (2018).

[11] U. Basu, S. N. Majumdar, A. Rosso, and G. Schehr, Physical Review E **100**, 62116 (2019).

[12] E. Bertin, M. Droz, and G. Grégoire, Physical Review E **74**, 022101 (2006).

[13] T. Vicsek and A. Zafeiris, Physics Reports **517**, 71 (2012).

[14] M. E. Cates and J. Tailleur, Ann. Rev. Condens. Matter Phys. **6**, 219 (2015).

[15] L. Conway, D. Wood, E. Tüzel, and J. L. Ross, Proceedings of the National Academy of Sciences of the United States of America **109**, 20814 (2012).

[16] N. A. Licata, B. Mohari, C. Fuqua, and S. Setayeshgar, Biophysical Journal **110**, 247 (2016).

[17] O. Sipos, K. Nagy, R. Di Leonardo, and P. Galajda, Phys. Rev. Lett. **114**, 258104 (2015).

[18] T. Bhattacharjee and S. S. Datta, Nature Communications **10**, 2 (2019).

[19] S. Makarchuk, V. C. Braz, N. A. Araújo, L. Ciric, and G. Volpe, Nature Communications **10** (2019).

[20] M. Brun-Cosme-Bruny, E. Bertin, B. Coasne, P. Peyla, and S. Rafaï, Journal of Chemical Physics **150** (2019).

[21] A. Guidobaldi, Y. Jeyaram, I. Berdakin, V. V. Moshchalkov, C. A. Condat, V. I. Marconi, L. Giojalas, and A. V. Silhanek, Physical Review E - Statistical, Nonlinear, and Soft Matter Physics **89**, 1 (2014).

[22] A. Morin, N. Desreumaux, J. B. Caussin, and D. Bartolo, Nature Physics **13**, 63 (2017), arXiv:1610.04404 .

[23] O. Chepizhko and F. Peruani, Physical Review Letters **111**, 1 (2013), arXiv:1310.0830 .

[24] A. Kaiser, H. H. Wensink, and H. Löwen, Physical Review Letters **108**, 1 (2012), arXiv:1202.0312 .

[25] C. Reichhardt and C. J. Olson Reichhardt, Physical Review E - Statistical, Nonlinear, and Soft Matter Physics **90**, 1 (2014).

[26] B. Bijnens and C. Maes, J. Stat. Mech. **2021**, 033206 (2021).

[27] O. Chepizhko and T. Franosch, arXiv (2020).

[28] G. Volpe and G. Volpe, Proceedings of the National Academy of Sciences of the United States of America **114**, 11350 (2017), arXiv:1706.07785 .

[29] M. Zeitz and H. Stark, Eur. Phys. J. E **40**, 23 (2017), arXiv:1611.07892 .

[30] T. Jakuszeit, O. A. Croze, and S. Bell, Physical Review E **99**, 1 (2019), arXiv:1807.04117 .

[31] L. Caprini, U. M. B. Marconi, C. Maggi, M. Paoluzzi, and A. Puglisi, Phys. Rev. Res. **2**, 023321 (2020).

[32] L. Caprini and U. M. B. Marconi, Soft matter **14**, 9044 (2018).

[33] L. Caprini, F. Cecconi, A. Puglisi, and A. Sarracino, Soft Matter **16**, 5431 (2020).

[34] F. Höfling and T. Franosch, Rep. Prog. Phys. **76**, 046602 (2013).

[35] M. J. Saxton, Biophysical Journal **52**, 989 (1987).

[36] J. D. Schmit, E. Kamber, and J. Kondev, Phys. Rev. Lett. **102**, 218302 (2009).

[37] N. Dorsaz, C. D. Michele, F. Piazza, P. D. L. Rios, G. Foffi, R. La, D. Fisica, and P. A. Moro, Phys. Rev. Lett. **105**, 120601 (2010).

[38] K. Nakazato and K. Kitahara, Prog. Theor. Phys. **64**, 2261 (1980).

[39] R. A. Tahir-Kheli and R. J. Elliott, Physical Review B **27**, 844 (1983).

[40] H. van Beijeren and R. Kutner, Phys. Rev. Lett. **55**, 238 (1985).

[41] H. N. Lekkerkerker and J. K. Dhont, The Journal of chemical physics **80**, 5790 (1984).

[42] J. Reichert, S. Mandal, and T. Voigtmann, Physical Review E **104**, 044608 (2021).

[43] T. Bertrand, Y. Zhao, O. Bénichou, J. Tailleur, and R. Voituriez, Physical Review Letters **120**, 198103 (2018), arXiv:1711.05209 .

[44] A. J. Wolfe and H. C. Berg, Proceedings of the National Academy of Sciences **86**, 6973 (1989).

[45] B. Mohari, N. A. Licata, D. T. Kysela, P. M. Merritt, S. Mukhopadhay, Y. V. Brun, S. Setayeshgar, and C. Fuqua, MBio **6** (2015), 10.1128/mBio.00005-15.

[46] A. Dehkharghani, N. Waisbord, and J. S. Guasto, Communications Physics **6**, 18 (2023).

[47] R. Kubo, Reports on Progress in Physics **29**, 255 (1966).

[48] U. M. B. Marconi, A. Puglisi, L. Rondoni, and A. Vulpiani, Physics Reports **461**, 111 (2008).

[49] R. Eichhorn, P. Reimann, and P. Hänggi, Phys. Rev. Lett. **88**, 190601 (2002).

[50] B. Cleuren and C. Van den Broeck, Physical Review E **65**, 030101 (2002).

[51] M. Kostur, L. Machura, P. Hänggi, J. Łuczka, and P. Talkner, Physica A **371**, 20 (2006).

[52] L. Machura, M. Kostur, P. Talkner, J. Łuczka, and P. Hänggi, Physical Review Letters **98**, 040601 (2007).

[53] D. Speer, R. Eichhorn, and P. Reimann, Physical Review E **76**, 051110 (2007).

[54] J. Cividini, D. Mukamel, and H. Posch, Journal of Physics A: Mathematical and Theoretical **51**, 085001 (2018).

[55] J. Wang, G. Casati, and G. Benenti, Physical Review Letters **124**, 110607 (2020).

[56] A. Sarracino, F. Cecconi, A. Puglisi, and A. Vulpiani, Physical review letters **117**, 174501 (2016).

[57] F. Cecconi, A. Puglisi, A. Sarracino, and A. Vulpiani, European Physical Journal E **40**, 81 (2017).

[58] B.-q. Ai, W.-j. Zhu, Y.-f. He, and W.-r. Zhong, Journal of Chemical Physics **149**, 164903 (2018).

[59] T. Chou, K. Mallick, and R. K. P. Zia, Reports on Progress in Physics **74**, 116601 (2011).

[60] K. Mallick, Physica A **418**, 17 (2015).

[61] O. Bénichou, P. Illien, G. Oshanin, A. Sarracino, and R. Voituriez, Phys. Rev. Lett. **113**, 268002 (2014).

[62] P. Illien, O. Bénichou, G. Oshanin, A. Sarracino, and R. Voituriez, Phys. Rev. Lett. **120**, 200606 (2018).

[63] O. Benichou, P. Illien, G. Oshanin, A. Sarracino, and R. Voituriez, Journal of Physics: Condensed Matter **30**, 443001 (2018).

[64] T. Bertrand, P. Illien, O. Bénichou, and R. Voituriez, New Journal of Physics **20** (2018), 10.1088/1367-2630/aaef6f, arXiv:1807.03993 .

[65] C. Lozano, J. R. Gomez-Solano, and C. Bechinger, Nature Materials **18**, 1118 (2019).

[66] P. Baerts, U. Basu, C. Maes, and S. Safaverdi, Physical Review E **88**, 052109 (2013).

[67] S. Leitmann and T. Franosch, Phys. Rev. Lett. **111**, 190603 (2013).

[68] M. Baiesi, A. L. Stella, and C. Vanderzande, Physical Review E **92**, 042121 (2015).

[69] O. Bénichou, P. Illien, G. Oshanin, A. Sarracino, and R. Voituriez, Phys. Rev. E **93**, 032128 (2016).

[70] C. Reichhardt and C. O. Reichhardt, Journal of Physics: Condensed Matter **30**, 015404 (2017).

[71] R. Zia, E. Praestgaard, and O. Mouritsen, American Journal of Physics **70**, 384 (2002).

[72] C. Maes, *Non-dissipative effects in nonequilibrium systems* (Springer, 2017).

[73] J. Köfinger, G. Hummer, and C. Dellago, Physical Chemistry Chemical Physics **13**, 15403 (2011).

[74] A. Horner and P. Pohl, Faraday discussions **209**, 9 (2018).

[75] N. Kavokine, R. R. Netz, and L. Bocquet, Annual Review of Fluid Mechanics **53**, 377 (2021).

[76] G. Hummer, J. C. Rasaiah, and J. P. Noworyta, nature **414**, 188 (2001).

[77] C. Y. Won and N. Aluru, Journal of the American Chemical Society **129**, 2748 (2007).

[78] R. H. Tunuguntla, R. Y. Henley, Y.-C. Yao, T. A. Pham, M. Wanunu, and A. Noy, Science **357**, 792 (2017).

[79] T. E. Harris, J. Appl. Probab. **2**, 323 (1965).

[80] K. Hahn, J. Kärger, and V. Kukla, Phys. Rev. Lett. **76**, 2762 (1996).

[81] Q.-H. Wei, C. Bechinger, and P. Leiderer, Science **287**, 625 (2000).

[82] B. Lin, M. Meron, B. Cui, S. A. Rice, and H. Diamant, Phys. Rev. Lett. **94**, 216001 (2005).

[83] B. Derrida, Phys. Rep. **301**, 65 (1998).

[84] B. Derrida, J. Lebowitz, and E. Speer, Journal of statistical physics **107**, 599 (2002).

[85] B. Derrida, B. Douçot, and P.-E. Roche, Journal of Statistical physics **115**, 717 (2004).

[86] T. Bodineau and B. Derrida, Phys. Rev. Lett. **92**, 180601 (2004).

[87] T. Bodineau and B. Derrida, Phys. Rev. E **72**, 066110 (2005).

[88] T. Bodineau and B. Derrida, Comptes Rendus Physique **8**, 540 (2007).

[89] J. Cividini, A. Kundu, S. N. Majumdar, and D. Mukamel, J. Phys. A **49**, 085002 (2016).

[90] P. Habdas, D. Schaar, A. C. Levitt, and E. R. Weeks, Europhys. Lett. **67**, 477 (2004).

[91] A. R. Bausch, F. Ziemann, A. A. Boulbitch, K. Jacobson, and E. Sackmann, Biophys. J. **75**, 2038 (1998).

[92] N. Leibovich and E. Barkai, Physical Review E **88**, 032107 (2013).

[93] L. Lizana, T. Ambjörnsson, A. Taloni, E. Barkai, and M. A. Lomholt, Physical Review E **81**, 051118 (2010).

[94] S. Leitmann and T. Franosch, Phys. Rev. Lett. **118**, 018001 (2017).

[95] J. Cividini, A. Kundu, S. N. Majumdar, and D. Mukamel, J. Stat. Mech: Theory Exp. **2016**, 053212 (2016).

[96] F. Spitzer, Adv. Math. **5**, 246 (1970).

[97] D. G. Levitt, Phys. Rev. A **8**, 3050 (1973).

[98] R. Arratia, Ann. Probab. **11**, 362 (1983).

[99] B. Derrida and A. Gerschenfeld, J. Stat. Phys. **136**, 1 (2009).

[100] T. Imamura, K. Mallick, and T. Sasamoto, Phys. Rev. Lett. **118**, 160601 (2017).

[101] T. Imamura, K. Mallick, and T. Sasamoto, Commun. Math. Phys. **384**, 1409 (2021).

[102] P. L. Krapivsky, K. Mallick, and T. Sadhu, J. Stat. Phys. **160**, 885 (2015).

[103] A. Poncet, A. Grabsch, P. Illien, and O. Bénichou, Phys. Rev. Lett. **127**, 220601 (2021).

[104] B. Derrida, Journal of Statistical Mechanics: Theory and Experiment **2007**, P07023 (2007).

[105] S. Sethuraman and S. Varadhan, Annals of Probability **41**, 1461 (2013).

[106] A. D. Polyanin and A. V. Manzhirov, *Handbook of integral equations* (CRC press, 2008).

[107] B. Derrida and A. Gerschenfeld, J. Stat. Phys. **137**, 978 (2009).

[108] P. Krapivsky and B. Meerson, Phys. Rev. E **86**, 031106 (2012).

[109] H. Spohn, Communications in mathematical physics **125**, 3 (1989).

[110] C. W. J. Beenakker and M. Büttiker, Phys. Rev. B **46**, 1889 (1992).

[111] H. Lee, L. S. Levitov, and A. Y. Yakovets, Phys. Rev. B **51**, 4079 (1995).

[112] A. Gerschenfeld, *Fluctuations de courant hors d'équilibre*, Ph.D. thesis, ENS (2012).

[113] J. Krug and J. Garcia, J. Stat. Phys. **99**, 31 (2000).

[114] A. Kundu and J. Cividini, Europhys. Lett. **115**, 54003 (2016).

[115] L. Zarfaty and B. Meerson, J. Stat. Mech: Theory Exp. **2016**, 033304 (2016).

[116] L. B. Shaw, R. K. P. Zia, and K. H. Lee, Phys. Rev. E **68**, 021910 (2003).

[117] M. R. Evans, Braz. J. Phys. **30**, 42 (2000).

[118] M. R. Evans and T. Hanney, J. Phys. A **38**, R195 (2005).

[119] C. Landim, S. Olla, and S. Volchan, Comm. Math. Phys. **192**, 287 (1998).

[120] G. Schönherr and G. Schütz, J. Phys. A: Math. Gen. **37**, 8215 (2004).

[121] J. Cividini, D. Mukamel, and H. Posch, Phys. Rev. E **95**, 012110 (2017).

[122] I. Lobaskin and M. R. Evans, J. Stat. Mech. **2020**, 053202 (2020).

[123] H. Spohn, *Large scale dynamics of interacting particles* (Springer Berlin, Heidelberg, 1991).

[124] L. Bertini, A. De Sole, D. Gabrielli, G. Jona-Lasinio, and C. Landim, Rev. Mod. Phys. **87**, 593 (2015).

[125] B. Derrida, J. Stat. Mech: Theory Exp. **2011**, P01030 (2011).

[126] S. Burlatsky, G. Oshanin, M. Moreau, and W. Reinhardt, Phys. Rev. E **54**, 3165 (1996).

[127] S. F. Burlatsky, G. S. Oshanin, A. V. Mogutov, and M. Moreau, Physics Letters A **166**, 230 (1992).

[128] A. Ayyer, Annales de l'Institut Henri Poincaré D (2022), 10.4171/AIHPD/157.

[129] P. Illien, O. Bénichou, C. Mejía-Monasterio, G. Oshanin, and R. Voituriez, Physical Review Letters **111**, 38102 (2013).

[130] A. Poncet, O. Benichou, and P. Illien, Physical Review E **103**, L040103 (2021).

[131] C. Landim and S. B. Volchan, Stochastic processes and their applications **85**, 139 (2000).

[132] R. Dandekar and K. Mallick, Journal of Physics A: Mathematical and Theoretical **55**, 435001 (2022).

[133] A. Poncet, *Dynamics and correlations of driven diffusive systems*, Ph.D. thesis, Sorbonne Université (2020).

[134] J. W. Gibbs, *Elementary principles in statistical mechanics: developed with especial reference to the rational foundations of thermodynamics* (C. Scribner's sons, 1902).

[135] A. Einstein, Annalen der physik **17**, 549 (1905).

[136] P. Langevin, Compt. Rendus **146**, 530 (1908).

[137] M. Von Smoluchowski, Annalen der physik **326**, 756 (1906).

[138] J. Tailleur and M. Cates, Physical review letters **100**, 218103 (2008).

[139] T.-D. Lee and C.-N. Yang, Physical Review **87**, 410 (1952).

[140] H. Van Beijeren, K. Kehr, and R. Kutner, Physical Review B **28**, 5711 (1983).

[141] U. Frisch, B. Hasslacher, and Y. Pomeau, Physical review letters **56**, 1505 (1986).

[142] D. H. Rothman and S. Zaleski, Reviews of Modern Physics **66**, 1417 (1994).

[143] P. Rizkallah, A. Sarracino, O. Bénichou, and P. Illien, Physical Review Letters **128**, 038001 (2022).

[144] P. Rizkallah, A. Sarracino, O. Bénichou, and P. Illien, Physical Review Letters **130**, 218201 (2023).

[145] R. Brown, The philosophical magazine **4**, 161 (1828).

[146] R. Chatterjee, N. Segall, C. Merrigan, K. Ramola, B. Chakraborty, and Y. Shokef, Journal of Chemical Physics **150** (2019), 10.1063/1.5085769, arXiv:1812.06146 .

[147] A. Ros, R. Eichhorn, J. Regtmeier, T. T. Duong, P. Reimann, and D. Anselmetti, Nature **436**, 928 (2005).

[148] R. Eichhorn, J. Regtmeier, D. Anselmetti, and P. Reimann, Soft Matter **6**, 1858 (2010).

[149] J. Luo, K. A. Muratore, E. A. Arriaga, and A. Ros, Analytical Chemistry **88**, 5920 (2016).

[150] A. Słapik, J. Łuczka, P. Hänggi, and J. Spiechowicz, Physical Review Letters **122**, 070602 (2019).

[151] T. Chou, K. Mallick, and R. K. P. Zia, Rep. Prog. Phys. **74**, 116601 (2011).

[152] K. W. Kehr, R. Kutner, and K. Binder, Physical Review B **23**, 4931 (1981).

[153] J. Cividini, D. Mukamel, and H. A. Posch, Physical Review E **95**, 012110 (2017).

[154] S. Pigeon, K. Fogelmark, B. Söderberg, G. Mukhopadhyay, and T. Ambjörnsson, Journal of Statistical Mechanics: Theory and Experiment **2017**, 123209 (2017).

[155] J.-P. Hansen and I. R. McDonald, *Theory of simple liquids: with applications to soft matter* (Academic press, 2013).

[156] O. Bénichou, A. Cazabat, J. De Coninck, M. Moreau, and G. Oshanin, Physical Review Letters **84**, 511 (2000).

[157] O. Bénichou, A. Cazabat, J. De Coninck, M. Moreau, and G. Oshanin, Physical Review B **63**, 235413 (2001).

[158] O. Bénichou, A. Bodrova, D. Chakraborty, P. Illien, A. Law, C. Mejía-Monasterio, G. Oshanin, and R. Voituriez, Phys. Rev. Lett. **111**, 260601 (2013).

[159] P. Illien, O. Bénichou, G. Oshanin, and R. Voituriez, Phys. Rev. Lett. **113**, 030603 (2014).

[160] B. D. Hughes, *Random Walks and Random Environments: Random walks, Volume 1* (Oxford University Press, Oxford, 1995).

[161] S. Jose, D. Mandal, M. Barma, and K. Ramola, Physical Review E **105**, 064103 (2022).

[162] M. Baiesi, C. Maes, and B. Wynants, Proc. R. Soc. A **467**, 2792 (2011).

[163] W. Götze and L. Sjögren, Transport theory and statistical physics **24**, 801 (1995).

[164] D. R. Reichman and P. Charbonneau, Journal of Statistical Mechanics: Theory and Experiment **2005**, P05013 (2005).

[165] A. Grabsch, A. Poncet, P. Rizkallah, P. Illien, and O. Bénichou, Sci. Adv. **8**, eabm5043 (2022).

[166] P. Rizkallah, A. Grabsch, P. Illien, and O. Bénichou, J. Stat. Phys. **2023**, 013202 (2023).

[167] A. Grabsch, P. Rizkallah, P. Illien, and O. Bénichou, Physical Review Letters **130**, 020402 (2023).

[168] A. Grabsch, P. Rizkallah, A. Poncet, P. Illien, and O. Bénichou, Phys. Rev. E **107**, 044131 (2023).

[169] S. Cambré, B. Schoeters, S. Luyckx, E. Goovaerts, and W. Wenseleers, Physical review letters **104**, 207401 (2010).

[170] R. Rajesh and S. N. Majumdar, Phys. Rev. E **64**, 036103 (2001).

[171] T. Sadhu and B. Derrida, J. Stat. Mech: Theory Exp. **2015**, P09008 (2015).

[172] K. Mallick, H. Moriya, and T. Sasamoto, Physical Review Letters **129**, 040601 (2022).

[173] K. Mallick, Physica A **418**, 17 (2015), proceedings of the 13th International Summer School on Fundamental Problems in Statistical Physics.

[174] T. Chou, K. Mallick, and R. K. Zia, Rep. Prog. Phys. **74**, 116601 (2011).

[175] J. S. Hager, J. Krug, V. Popkov, and G. M. Schütz, Phys. Rev. E **63**, 056110 (2001).

[176] Y. Baek, Y. Kafri, and V. Lecomte, Phys. Rev. Lett. **118**, 030604 (2017).

[177] P. Ferrari and L. Fontes, Electron. J. Probab. **3**, 1 (1998).

[178] S. Katz, J. L. Lebowitz, and H. Spohn, Journal of statistical physics **34**, 497 (1984).

[179] C. Kipnis, C. Marchioro, and E. Presutti, J. Stat. Phys. **27**, 65 (1982).

[180] A. Das, A. Kundu, and P. Pradhan, Phys. Rev. E **95**, 062128 (2017).

[181] E. Bertin, J.-P. Bouchaud, and F. Lequeux, Physical review letters **95**, 015702 (2005).

[182] C. Kipnis, S. Olla, and S. S. Varadhan, Communications on Pure and Applied Mathematics **42**, 115 (1989).

[183] L. Bertini, A. De Sole, D. Gabrielli, G. Jona-Lasinio, and C. Landim, Bull. Braz. Math. Soc. **37**, 611 (2006).

[184] L. Bertini, A. D. Sole, D. Gabrielli, G. Jona-Lasinio, and C. Landim, J. Stat. Mech: Theory Exp. **2007**, P07014 (2007).

[185] K. Kawasaki, Physica A: Statistical Mechanics and its Applications **208**, 35 (1994).

[186] D. S. Dean, Journal of Physics A: Mathematical and General **29**, L613 (1996).

[187] P. L. Krapivsky, K. Mallick, and T. Sadhu, J. Stat. Mech: Theory Exp. **2015**, P09007 (2015).

[188] P. Illien, O. Bénichou, C. Mejía-Monasterio, G. Oshanin, and R. Voituriez, Phys. Rev. Lett. **111**, 038102 (2013).

[189] M. Kollmann, Physical review letters **90**, 180602 (2003).

[190] C. A. Tracy and H. Widom, Journal of Statistical Physics **132**, 291 (2008).

[191] C. A. Tracy and H. Widom, Communications in Mathematical Physics **279**, 815 (2008).

[192] L. Arabadzhyan and N. Engibaryan, J. Sov. Math. **36**, 745 (1987).

[193] A. Krajenbrink and P. Le Doussal, Physical Review Letters **127**, 064101 (2021).

[194] D. B. Owen, Commun. Stat. Simul. Comput. **9**, 389 (1980).

[195] A. Krajenbrink and P. Le Doussal, Phys. Rev. Lett. **127**, 064101 (2021).

[196] E. Bettelheim, N. R. Smith, and B. Meerson, Phys. Rev. Lett. **128**, 130602 (2022).

[197] E. Bettelheim, N. R. Smith, and B. Meerson, J. Stat. Mech: Theory Exp. **2022**, 093103 (2022).

[198] A. Krajenbrink and P. Le Doussal, arXiv preprint arXiv:2204.04720 (2022).

[199] S. Majumdar and M. Barma, Physica A: Statistical Mechanics and its Applications **177**, 366 (1991).

[200] S. Gupta, S. N. Majumdar, C. Godrèche, and M. Barma, Physical Review E **76**, 021112 (2007).

[201] P. I. Hurtado and P. L. Garrido, J. Stat. Mech. **2009**, P02032 (2009).

[202] B. Derrida, L'annuaire du Collège de France. Cours et travaux , 47 (2019).